CHALMERS
UNIVERSITY OF TECHNOLOGY

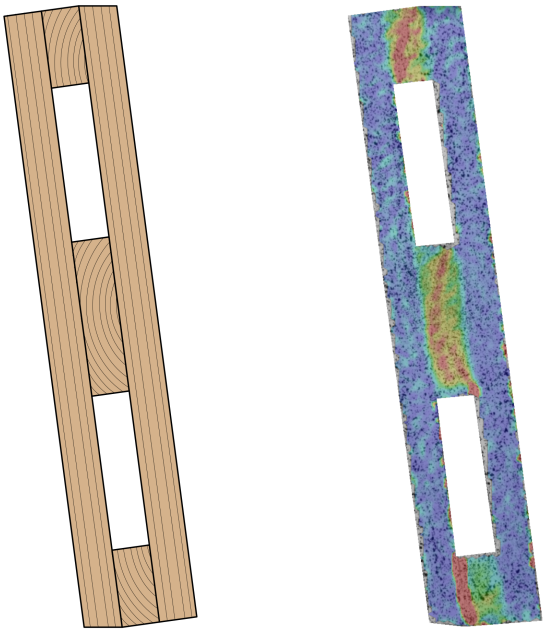

Next Generation CLT

Material optimisation of CLT with regard to structural performance by the introduction of air gaps in the cross-layers

Master's thesis in Structural Engineering and Building Technology

ANNA MOBERG

LINDA XIAO

DEPARTMENT OF ARCHITECTURE AND CIVIL ENGINEERING
CHALMERS UNIVERSITY OF TECHNOLOGY
Gothenburg, Sweden 2022
www.chalmers.se

Master's thesis 2022

Next Generation CLT

Material optimisation of CLT
with regard to structural performance
by the introduction of air gaps in the cross-layers

ANNA MOBERG
LINDA XIAO



CHALMERS
UNIVERSITY OF TECHNOLOGY

Department of Architecture and Civil Engineering
Division of Structural Engineering
Lightweight Structures
Chalmers University of Technology
Gothenburg, Sweden 2022

Next Generation CLT
Material optimisation of CLT
with regard to structural performance
by the introduction of air gaps in the cross-layers
ANNA MOBERG
LINDA XIAO

© ANNA MOBERG, LINDA XIAO, 2022.

Supervisor: Robert Jockwer and Yutaka Goto, Department of Architecture and Civil Engineering
Examiner: Robert Jockwer, Department of Architecture and Civil Engineering

Master's Thesis 2022
Department of Architecture and Civil Engineering
Division of Structural Engineering
Lightweight Structures
Chalmers University of Technology
SE-412 96 Gothenburg
Telephone +46 31 772 1000

Cover: Major strain distribution in a three-layer CLT panel with air gaps subjected to shear testing.

Typeset in LaTeX
Gothenburg, Sweden 2022

Next Generation CLT
Material optimisation of CLT
with regard to structural performance
by the introduction of air gaps in the cross-layers
ANNA MOBERG
LINDA XIAO
Department of Architecture and Civil Engineering
Chalmers University of Technology

Abstract

The construction industry is currently one of the major contributors to the greenhouse gas emissions and the search for more sustainable building materials has led to an increasing demand for CLT. However, the consumption of raw material for the production of CLT is excessively large in relation to the required structural capacity and the inefficient use of timber, in comparison to the required structural capacity, has led to the demand for material optimisation of CLT.

The aim of the thesis is to design a material-optimised CLT panel by introducing air gaps in the cross-layers. By designing and manufacturing a variety of three- and five-layer configurations with different air gap layouts and widths, and conducting strength tests on small scale test specimens, the shear capacity is determined and compared with the material reduction of the specimens. Furthermore, finite element analysis of each configuration is performed in order to predict the behaviour of the specimens and to complement the results from the physical strength tests.

From the testing, it was observed that the three-layer configurations mainly failed in the bondlines due to inadequate application of adhesive, whereas the five-layer configurations displayed an even distribution between failure due to panel shear, rolling shear, and deficient bondlines. Furthermore, a significant reduction in strength was noticed for the specimens with air gaps in comparison to the solid specimens and it was concluded to be a clear correlation between the reduction of material and the reduction in capacity. It was also observed that for the specimens with the same air gap widths, a centred air gap layout provided higher stiffness than a shifted air gap layout in general. However, it was concluded that the reduction of material influences the performance of the panel to a greater extent than the layout of the air gaps and the results were verified by the finite element models.

Keywords: Cross-laminated timber, CLT, timber, material optimisation, air gaps, shear strength, strength test

Next Generation CLT
Materialoptimering av KL-trä
med avseende på strukturell kapacitet
genom införandet av luftspalter i de tvärgående skikten
ANNA MOBERG
LINDA XIAO
Institutionen för arkitektur och samhällsbyggnadsteknik
Chalmers tekniska högskola

Sammanfattning

Byggbranschen står för närvarande för en stor andel av de globala utsläppen av växthusgaser och en strävan efter mer hållbara byggmaterial har lett till en ökad efterfrågan av korslimmat trä. Idag är dock förbrukningen av råmaterial för produktion av KL-trä obefogat hög i förhållande till den strukturella kapaciteten som krävs och den ineffektiva användningen av virke, i jämförelse med den nödvändiga kapaciteten, har lett till en efterfrågan av en materialoptimering av KL-trä.

Målet med arbetet är att designa en materialoptimerad KL-träpanel genom införandet av luftspalter i de tvärgående skikten. För att analysera hur luftspalterna och deras placeringar påverkar panelernas skjuvhållfasthet designades och tillverkades en stor variation av småskaliga provkroppar bestående av tre respektive fem skikt med olika kompositioner av luftspalter som testades med avseende på skjuvning. För att förutspå provkropparnas beteende och komplettera resultaten från de fysiska skjuvhållfasthetstesterna modellerades alla provkroppar enligt finita elementmetoden.

För konfigurationerna bestående av tre skikt skedde brott på grund av otillräckliga limfogar, medan brottmoden för konfigurationerna bestående av fem skikt varierade mellan panelskjuvning, rullskjuvning och bristfälliga limfogar. Vidare noterades en markant minskning av hållfastheten för provkropparna med luftspalter jämfört med de solida provkropparna och ett tydligt samband mellan minskningen av material och minskningen av skjuvkapacitet kunde observeras. Dessutom noterades det att för provkropparna med samma luftspaltsbredd resulterade en centrerad layout generellt sett i en högre skjuvkapacitet i jämförelse med en förskjuten layout. Det konstaterades dock att mängden minskat material har en större påverkan på panelens hållfasthet än luftspalternas placering, vilket verifierades av de finita elementmodellerna.

Nyckelord: Korslimmat trä, KL-trä, trä, materialoptimering, luftspalter, skjuvhållfasthet, hållfasthetstest

Acknowledgements

We would like to express our appreciation for our thoughtful supervisor and examiner Robert Jockwer for providing us with insightful knowledge and for his guidance and support throughout the thesis. We would also like to thank our supervisor Yutaka Goto for his encouragement and guidance.

Furthermore, we are sincerely grateful for Tabita Nilsson, Peter Lindblom, and Per Lundström for their assistance, guidance, and patience during the countless hours that were spent in the workshop. We would also like to thank Sebastian Almfeldt and Anders Karlsson in the Structures Lab for their support and tireless optimism. This thesis would not have been possible without them.

Anna Moberg, Gothenburg, June 2022
Linda Xiao, Gothenburg, June 2022

Contents

List of Figures **xvii**

List of Tables **xxiii**

Nomenclature **xxv**

1 Introduction **1**
1.1 Background . . . 1
1.2 Aim . . . 2
1.3 Methodology . . . 2
1.3.1 Preparation phase . . . 2
1.3.2 Manufacturing phase . . . 3
1.3.3 Experimental phase . . . 3
1.3.4 Evaluation phase . . . 3
1.4 Limitations . . . 3
1.5 State of the art . . . 4

2 Theory **5**
2.1 Properties of wood . . . 5
2.1.1 Structure of wood . . . 5
2.1.1.1 Microscopic structure . . . 5
2.1.1.2 Mesoscopic structure . . . 6
2.1.1.3 Macroscopic structure . . . 7
2.1.2 Natural characteristics of wood . . . 7
2.1.2.1 Knots . . . 7
2.1.2.2 Spiral grain . . . 8
2.1.2.3 Juvenile wood . . . 9
2.1.2.4 Reaction wood . . . 9
2.1.3 Physical properties . . . 10
2.1.3.1 Moisture . . . 10
2.1.3.2 Density . . . 10
2.1.3.3 Shrinkage and swelling . . . 11
2.1.3.4 Distortion . . . 11
2.1.4 Mechanical properties . . . 12
2.1.4.1 Tension . . . 13
2.1.4.2 Compression . . . 13
2.1.4.3 Shear . . . 14

2.1.4.4 Size effect . . . 15
2.2 Strength grading of timber . . . 16
2.2.1 Visual strength grading . . . 16
2.2.2 Machine strength grading . . . 16
2.2.2.1 Determination of density . . . 16
2.2.2.2 Determination of MOE . . . 17
2.3 Cross-Laminated Timber . . . 18
2.3.1 CLT as a construction material . . . 18
2.3.2 Manufacturing of CLT . . . 18
2.3.3 Consumption of CLT . . . 18
2.3.3.1 In Sweden . . . 19
2.3.3.2 Internationally . . . 19
2.4 Design of CLT . . . 20
2.4.1 Design in ultimate limit state . . . 20
2.4.2 Design in serviceability limit state . . . 20
2.4.3 Design factors . . . 20
2.4.4 System effect . . . 21
2.5 Strength testing of CLT . . . 22
2.5.1 Conditioning of test specimens . . . 22
2.5.2 Shear strength test . . . 23
2.5.3 Calculation of shear strength . . . 23
2.6 Finite element modelling in Abaqus . . . 25
2.6.1 Orthotropic modelling . . . 25
2.6.1.1 Material parameters . . . 25
2.6.1.2 Orthotropic elastic stiffness matrix . . . 27
2.6.2 Interaction . . . 28

3 Methodology 29
3.1 Preparation . . . 29
3.1.1 Designing of configurations . . . 29
3.1.1.1 Three-layer configurations . . . 29
3.1.1.2 Five-layer configurations . . . 30
3.1.1.3 Naming of specimens . . . 30
3.1.1.4 Determination of geometrical properties . . . 31
3.1.2 Conditioning of timber . . . 31
3.2 Strength grading of timber . . . 33
3.2.1 Visual grading . . . 33
3.2.2 Mechanical grading . . . 34
3.2.2.1 Determination of density . . . 34
3.2.2.2 Determination of dynamic modulus of elasticity . . . 35
3.3 Assigning of boards to configurations . . . 36
3.3.1 Average strength . . . 36
3.3.2 Low strength . . . 36
3.3.3 High strength . . . 36
3.4 Manufacturing of specimens . . . 37
3.4.1 Manufacturing method . . . 37

3.4.1.1 Sawing and planing . . . 37
3.4.1.2 Application of adhesive . . . 40
3.4.1.3 Vacuum pressing . . . 42
3.4.1.4 Finalisation . . . 43
3.4.2 Test manufacturing . . . 45
3.4.2.1 Solid test specimen . . . 45
3.4.2.2 Test specimen with air gaps . . . 46
3.4.3 Preparation of specimens . . . 47
3.5 Testing of specimens . . . 48
3.5.1 Test equipment . . . 48
3.5.1.1 Hydraulic press . . . 49
3.5.1.2 Fixtures . . . 49
3.5.1.3 ARAMIS optical system . . . 50
3.5.2 Shear strength test . . . 51
3.5.2.1 Loading rate . . . 51
3.5.2.2 Test method . . . 52
3.5.3 Trial test round . . . 54
3.5.3.1 Solid test specimen . . . 54
3.5.3.2 Test specimen with air gaps . . . 56
3.5.4 Analysing of results . . . 57
3.5.4.1 Shear strength . . . 57
3.5.4.2 Failure load ratio . . . 58
3.6 Finite element modelling in Abaqus . . . 59
3.6.1 Modelling of elements . . . 59
3.6.2 Material properties . . . 59
3.6.3 Interaction . . . 60
3.6.4 Load and boundary conditions . . . 60
3.6.4.1 Boundary conditions . . . 60
3.6.4.2 Load application . . . 61
3.6.4.3 Load scale factor . . . 61
3.6.5 Mesh . . . 62
3.6.6 Obtaining of results . . . 63
3.6.6.1 Creation of paths . . . 63
3.6.6.2 Extraction of data and plotting of results . . . 64
3.6.6.3 Calculation of utilisation ratios . . . 64

4 Results **65**
4.1 Conditioning of timber . . . 65
4.2 Strength grading of timber . . . 66
4.2.1 Board type A . . . 66
4.2.1.1 Density . . . 66
4.2.1.2 Dynamic MOE . . . 67
4.2.1.3 Relation between density and MOE . . . 68
4.2.2 Board type B . . . 69
4.2.2.1 Density . . . 69
4.2.2.2 Dynamic MOE . . . 70

4.2.2.3 Relation between density and MOE . . . 71
4.3 Assigning of boards to configurations . . . 72
4.3.1 Board type A . . . 72
4.3.2 Board type B . . . 73
4.4 Configurations . . . 74
4.4.1 Configuration I . . . 75
4.4.2 Configuration II . . . 76
4.4.3 Configuration III . . . 77
4.4.4 Configuration IV . . . 78
4.4.5 Configuration V . . . 79
4.4.6 Configuration VI . . . 80
4.4.7 Configuration VII . . . 81
4.4.8 Configuration VIII . . . 82
4.4.9 Configuration IX . . . 83
4.5 Testing of specimens . . . 84
4.5.1 Loss of ARAMIS test data . . . 84
4.5.2 Test specimens . . . 85
4.5.2.1 Solid test specimen . . . 85
4.5.2.2 Test specimen with air gaps . . . 88
4.5.3 Configuration I . . . 90
4.5.4 Configuration II . . . 94
4.5.5 Configuration III . . . 98
4.5.6 Configuration IV . . . 103
4.5.7 Configuration V . . . 105
4.5.8 Configuration VI . . . 107
4.5.9 Configuration VII . . . 109
4.5.10 Configuration VIII . . . 111
4.5.11 Configuration IX . . . 113
4.5.12 Compilation of results . . . 115
4.5.12.1 Shear strengths and failure modes . . . 116
4.5.12.2 Geometrical properties and failure load ratios . . . 117
4.6 Finite element modelling in Abaqus . . . 119
4.6.1 Load scale factor . . . 119
4.6.2 Calculation of design strength properties . . . 120
4.6.3 Configuration I . . . 121
4.6.4 Configuration II . . . 125
4.6.5 Configuration III . . . 129
4.6.6 Configuration IV . . . 133
4.6.7 Configuration V . . . 138
4.6.8 Configuration VI . . . 143
4.6.9 Configuration VII . . . 148
4.6.10 Configuration VIII . . . 153
4.6.11 Configuration IX . . . 158

5 Discussion **163**
5.1 Preparation and manufacturing . . . 163

5.1.1 Conditioning . . . 163
5.1.2 Manufacturing . . . 164
5.1.2.1 General method . . . 164
5.1.2.2 Adhesive . . . 164
5.2 Testing of specimens . . . 165
5.2.1 Three-layer configurations . . . 165
5.2.2 Five-layer configurations . . . 166
5.3 Finite element modelling in Abaqus . . . 168
5.3.1 Three-layer configurations . . . 168
5.3.2 Five-layer configurations . . . 169
5.3.2.1 Air gap layout . . . 169
5.3.2.2 Air gap width . . . 170

6 Conclusion **171**
6.1 Conditioning . . . 171
6.2 Manufacturing . . . 171
6.3 Strength of cross-layer lamellas . . . 172
6.4 Material reduction . . . 172
6.5 Air gap layout . . . 172
6.6 Finite element modelling . . . 172
6.7 Further work . . . 173

Bibliography **175**

A FFT Analyser manual **I**

B Matlab code (three-layer configuration example) **V**

C Matlab code (five-layer configuration example) **XIII**

D Configurations data **XXIII**

E Calculation of shear strength **XXVII**

F Calculation of failure load ratio **XXXI**

G Calculation of load scale factor **XXXVII**

H Figures from results **XLI**
H.1 Configuration I . . . XLI
H.2 Configuration II . . . XLVI
H.3 Configuration III . . . LI
H.4 Configuration IV . . . LVII
H.5 Configuration V . . . LXII
H.6 Configuration VI . . . LXVII
H.7 Configuration VII . . . LXXII
H.8 Configuration VIII . . . LXXVII
H.9 Configuration IX . . . LXXXII

List of Figures

2.1 The composition of a wood cell. 6
2.2 Earlywood and latewood. 6
2.3 The anatomy of a tree stem. 7
2.4 Common types of knots in boards. 8
2.5 A stem with straight grain vs spiral grain. 8
2.6 Reaction wood in coniferous and deciduous trees. 9
2.7 The four distortion modes. 12
2.8 The main directions of timber. 12
2.9 Stress-strain curve for wood loaded in tension parallel to the grain and perpendicular to the grain. 13
2.10 Stress-strain curve for wood loaded in compression parallel to the grain and perpendicular to the grain. 14
2.11 Shear in the three axial planes in a wood specimen. 14
2.12 Frequency test setup. 17
2.13 Shear test configuration for determination of rolling shear strength. . 23

3.1 Designing of three-layer configurations by varying the width of the air gaps. 30
3.2 Designing of five-layer configurations by varying the width of the air gaps and shifting the position of the lamellas. 30
3.3 Moisture measurement using a moisture meter. (February 16th 2022) 32
3.4 Moisture measurement of a specimen with air gaps. (May 6th 2022) . 32
3.5 The sorted boards after visual grading, board type A (30 mm) to the left and board type B (20 mm) to the right. (January 28th 2022) . . 33
3.6 Weighing of a board. (February 8th 2022) 34
3.7 Frequency measurement using FFT analyser. (February 8th 2022) . . 35
3.8 The circular saw used to saw all the specimens. (March 28th 2022) . 37
3.9 The planing machine used to obtain a right angle of the boards. (March 28th 2022) 38
3.10 The planing along the width and of the longitudinal edge. (March 28th 2022) 38
3.11 The parallel planing machine used to obtain parallel sides and edges of the boards. (March 28th 2022) 39
3.12 A batch of planed and sawn parts before assembling. (March 29th 2022) 39
3.13 The adhesive and the adhesive applicator. (March 30th 2022) 40

3.14 Application of adhesive on the longitudinal layers for a specimen constructed of boards of type A. (March 29th 2022) 40
3.15 Application of adhesive on the cross-layers for a specimen constructed of boards of type A. (March 30th 2022) 41
3.16 Application of adhesive on a specimen constructed of boards of type B. (April 12th 2022) 41
3.17 The vacuum press. (April 11th 2022) 42
3.18 Illustration of a finished three-layer specimen with sawn edges. 43
3.19 Illustration of a finished five-layer specimen with sawn edges. 44
3.20 Vacuum pressing of solid test specimen. (March 18th 2022) 45
3.21 Manufacturing of test specimen with air gaps. (March 21th 2022) . . 46
3.22 Vacuum pressing of test specimen with air gaps. (March 21th 2022) . 46
3.23 Spray painting of the specimens. (March 30th 2022) 47
3.24 Dabbing of black paint on the specimens. (March 30th 2022) 47
3.25 The hydraulic press used for the strength tests of the specimens. (May 5th 2022) 49
3.26 Fixtures and pressure plates. (May 5th 2022) 50
3.27 The ARAMIS optical system used for digital image correlation. (May 5th 2022) 50
3.28 Aligning of a specimen on the pressure plates in the hydraulic press. (April 6th 2022) 52
3.29 The setup of the strength testing of the specimens. (May 6th 2022) . 53
3.30 First test of the solid test specimen. (March 21th 2022) 54
3.31 Second test of the solid test specimen. (March 28th 2022) 55
3.32 Test of the test specimen with air gaps. (March 28th 2022) 56
3.33 Geometry of a configuration with an inclined edge, from which the solid extrusion was made in Abaqus. 59
3.34 Material orientation of the longitudinal layers vs the cross-layers in Abaqus. 60
3.35 Load application and boundary conditions of a configuration in Abaqus. 61
3.36 Mesh of a configuration in Abaqus. 62
3.37 Analysed paths for a three-layer configuration in Abaqus. 63
3.38 Analysed paths for a five-layer configuration in Abaqus. 64

4.1 The distribution of the determined density of boards of type A. . . . 66
4.2 The distribution of the determined MOE of boards of type A. 67
4.3 Relation between density and MOE of boards of type A. 68
4.4 Measured density of boards of type B. 69
4.5 Determined MOE of boards of type B. 70
4.6 Relation between density and MOE of boards of type B. 71
4.7 The selected boards of type A. 72
4.8 The distribution of assigned boards of type A. 72
4.9 The selected boards of type B. 73
4.10 The distribution of assigned boards of type B. 73
4.11 Illustration of the relation between a small scale test specimen and a full scale panel. 74

4.12 Drawing and illustration of Configuration I. 75
4.13 Drawing and illustration of Configuration II. 76
4.14 Drawing and illustration of Configuration III. 77
4.15 Drawing and illustration of Configuration IV. 78
4.16 Drawing and illustration of Configuration V. 79
4.17 Drawing and illustration of Configuration VI. 80
4.18 Drawing and illustration of Configuration VII. 81
4.19 Drawing and illustration of Configuration VIII. 82
4.20 Drawing and illustration of Configuration IX. 83
4.21 Results from the initial test of the solid test specimen. (March 21st 2022) 85
4.22 Results from the second test of the solid test specimen. (March 28th 2022) 86
4.23 Load-deformation curves for the solid test specimen. 87
4.24 Results from the test of the test specimen with air gaps. (March 28th 2022) 88
4.25 Close-up of the results from the test of the test specimen with air gaps. (March 28th 2022) 88
4.26 Load-deformation curve for the test specimen with air gaps. 89
4.27 Results from the test of Configuration I, in the order; average, low, and high strength. (April 6th 2022) 90
4.28 Load-deformation curves for Configuration I. 91
4.29 Strain distribution observed using ARAMIS right before and after failure for the average strength specimen of Configuration I. 92
4.30 Strain distribution observed using ARAMIS right before and after failure for the low strength specimen of Configuration I 92
4.31 Strain distribution observed using ARAMIS right before and after failure for the high strength specimen of Configuration I 93
4.32 Results from the test of Configuration II, in the order; average, low, and high strength. (April 6th 2022) 94
4.33 Load-deformation curves for Configuration II. 95
4.34 Strain distribution observed using ARAMIS right before and after failure for the average strength specimen of Configuration II. 96
4.35 Strain distribution observed using ARAMIS right before failure for the low strength specimen of Configuration II. 96
4.36 Strain distribution observed using ARAMIS right before and after failure for the high strength specimen of Configuration II. 97
4.37 Results from the test of Configuration III, in the order; average, low, and high strength. (April 6th 2022) 98
4.38 Load-deformation curves for Configuration III. 99
4.39 Strain distribution observed using ARAMIS right before and after failure for the average strength specimen of Configuration III. 100
4.40 Strain distribution observed using ARAMIS right before and after failure for the low strength specimen of Configuration III. 101
4.41 Strain distribution observed using ARAMIS right before and after failure for the high strength specimen of Configuration III. 102

4.42 Results from the test of Configuration IV, in the order; average, low, and high strength. (May 6th 2022) . . . 103
4.43 Load-deformation curves for Configuration IV. . . . 104
4.44 Results from the test of Configuration V, in the order; average, low, and high strength. (May 6th 2022) . . . 105
4.45 Load-deformation curves for Configuration V. . . . 106
4.46 Results from the test of Configuration VI, in the order; average, low, and high strength. (May 6th 2022) . . . 107
4.47 Load-deformation curves for Configuration VI. . . . 108
4.48 Results from the test of Configuration VII, in the order; average, low, and high strength. (May 6th 2022) . . . 109
4.49 Load-deformation curves for Configuration VII. . . . 110
4.50 Results from the test of Configuration VIII, in the order; average, low, and high strength. (May 6th 2022) . . . 111
4.51 Load-deformation curves for Configuration VIII. . . . 112
4.52 Results from the test of Configuration IX, in the order; average, low, and high strength. (May 6th 2022) . . . 113
4.53 Load-deformation curves for Configuration IX. . . . 114
4.54 Shear stress distribution of Configuration I in the LR-plane. . . . 121
4.55 Shear stress distribution of Configuration I in the RT-plane. . . . 121
4.56 Normal stress distribution of Configuration I in the RR-direction. . . 122
4.57 Stress distribution along paths in the longitudinal layer and in the cross-layer of Configuration I. . . . 122
4.58 The dominant shear stress and stress perpendicular to the grain in the longitudinal layer and in the cross-layer of Configuration I. . . . 123
4.59 Utilisation ratio of interaction in Configuration I. . . . 124
4.60 Shear stress distribution of Configuration II in the LR-plane. . . . 125
4.61 Shear stress distribution of Configuration II in the RT-plane. . . . 125
4.62 Normal stress distribution of Configuration II in the RR-direction. . . 126
4.63 Stress distribution along paths in the longitudinal layer and in the cross-layer of Configuration II. . . . 126
4.64 The dominant shear stress and stress perpendicular to the grain in the longitudinal layer and in the cross-layer of Configuration II. . . . 127
4.65 Utilisation ratio of interaction in Configuration II. . . . 128
4.66 Shear stress distribution of Configuration III in the LR-plane. . . . 129
4.67 Shear stress distribution of Configuration III in the RT-plane. . . . 129
4.68 Normal stress distribution of Configuration III in the RR-direction. . 130
4.69 Stress distribution along paths in the longitudinal layer and in the cross-layer of Configuration III. . . . 130
4.70 The dominant shear stress and stress perpendicular to the grain in the longitudinal layer and in the cross-layer of Configuration III. . . . 131
4.71 Utilisation ratio of interaction in Configuration III. . . . 132
4.72 Shear stress distribution of Configuration IV in the LR-plane. . . . 133
4.73 Shear stress distribution of Configuration IV in the RT-plane. . . . 133
4.74 Normal stress distribution of Configuration IV in the RR-direction. . 134

4.75 Stress distribution along paths in the upper longitudinal layer, the mid longitudinal layer, and the cross-layer of Configuration IV. 135
4.76 The dominant shear stress and stress perpendicular to the grain in the upper longitudinal layer, the mid longitudinal layer, and the cross-layer of Configuration IV. 136
4.77 Utilisation ratio of interaction in Configuration IV. 137
4.78 Shear stress distribution of Configuration V in the LR-plane. 138
4.79 Shear stress distribution of Configuration V in the RT-plane. 138
4.80 Normal stress distribution of Configuration V in the RR-direction. . . 139
4.81 Stress distribution along paths in the upper longitudinal layer, the mid longitudinal layer, and the cross-layer of Configuration V. 140
4.82 The dominant shear stress and stress perpendicular to the grain in the upper longitudinal layer, the mid longitudinal layer, and the cross-layer of Configuration V. 141
4.83 Utilisation ratio of interaction in Configuration V. 142
4.84 Shear stress distribution of Configuration VI in the LR-plane. 143
4.85 Shear stress distribution of Configuration VI in the RT-plane. 144
4.86 Normal stress distribution of Configuration VI in the RR-direction. . 144
4.87 Stress distribution along paths in the upper longitudinal layer, the mid longitudinal layer, and the cross-layer of Configuration VI. 145
4.88 The dominant shear stress and stress perpendicular to the grain in the upper longitudinal layer, the mid longitudinal layer, and the cross-layer of Configuration VI. 146
4.89 Utilisation ratio of interaction in Configuration VI. 147
4.90 Shear stress distribution of Configuration VII in the LR-plane. 148
4.91 Shear stress distribution of Configuration VII in the RT-plane. 149
4.92 Normal stress distribution of Configuration VII in the RR-direction. . 149
4.93 Stress distribution along paths in the upper longitudinal layer, the mid longitudinal layer, and the cross-layer of Configuration VII. . . . 150
4.94 The dominant shear stress and stress perpendicular to the grain in the upper longitudinal layer, the mid longitudinal layer, and the cross-layer of Configuration VII. 151
4.95 Utilisation ratio of interaction in Configuration VII. 152
4.96 Shear stress distribution of Configuration VIII in the LR-plane. . . . 153
4.97 Shear stress distribution of Configuration VIII in the RT-plane. . . . 154
4.98 Normal stress distribution of Configuration VIII in the RR-direction. 154
4.99 Stress distribution along paths in the upper longitudinal layer, the mid longitudinal layer, and the cross-layer of Configuration VIII. . . . 155
4.100 The dominant shear stress and stress perpendicular to the grain in the upper longitudinal layer, the mid longitudinal layer, and the cross-layer of Configuration VIII. 156
4.101 Utilisation ratio of interaction in Configuration VIII. 157
4.102 Shear stress distribution of Configuration IX in the LR-plane. 158
4.103 Shear stress distribution of Configuration IX in the RT-plane. 159
4.104 Normal stress distribution of Configuration IX in the RR-direction. . 159

4.105Stress distribution along paths in the upper longitudinal layer, the mid longitudinal layer, and the cross-layer of Configuration IX. 160
4.106The dominant shear stress and stress perpendicular to the grain in the upper longitudinal layer, the mid longitudinal layer, and the cross-layer of Configuration IX. 161
4.107Utilisation ratio of interaction in Configuration IX. 162

5.1 Comparison of failure load ratio and material reduction for three-layer configurations. 166
5.2 Comparison of failure load ratio and material reduction for five-layer configurations. 167

List of Tables

2.1 Dry density of common wood species in Scandinavia. (Holmberg and Sandberg, 1997) . . . 11
2.2 Shrinkage of common wood species in Scandinavia. (Holmberg and Sandberg, 1997) . . . 11
2.3 Partial factor values used in different countries. (Gustafsson, 2019) . 21
2.4 Values of k_{mod}. (Gustafsson, 2019) . . . 21
2.5 Linear elastic orthotropic material parameters for spruce comparing different studies (ρ in kg/m^3, E_{i} and G_{ij} in MPa). (Dahl, 2009) (Kohlhauser and Hellmich, 2012) (Niemz and Caduff, 2007) . . . 26
2.6 Characteristic strength values for C24 timber and CLT panels consisting of C24 boards. (Gustafsson, 2019) . . . 28

3.1 The properties used for the defining of the orthotropic material for all the configurations in Abaqus. . . . 59

4.1 Measured moisture content of the boards of type A and type B, respectively. . . . 65
4.2 Density distribution data of board type A. . . . 67
4.3 MOE distribution data of board type A. . . . 68
4.4 Density distribution data of board type B. . . . 69
4.5 MOE distribution data of board type B. . . . 70
4.6 Geometrical properties of Configuration I. . . . 75
4.7 Material properties of Configuration I. . . . 75
4.8 Geometrical properties of Configuration II. . . . 76
4.9 Material properties of Configuration II. . . . 76
4.10 Geometrical properties of Configuration III. . . . 77
4.11 Material properties of Configuration III. . . . 77
4.12 Geometrical properties of Configuration IV. . . . 78
4.13 Material properties of Configuration IV. . . . 78
4.14 Geometrical properties of Configuration V. . . . 79
4.15 Material properties of Configuration V. . . . 79
4.16 Geometrical properties of Configuration VI. . . . 80
4.17 Material properties of Configuration VI. . . . 80
4.18 Geometrical properties of Configuration VII. . . . 81
4.19 Material properties of Configuration VII. . . . 81
4.20 Geometrical properties of Configuration VIII. . . . 82
4.21 Material properties of Configuration VIII. . . . 82

4.22 Geometrical properties of Configuration IX. 83
4.23 Material properties of Configuration IX. 83
4.24 Test results from the testing of the solid test specimen. 86
4.25 Test results from the testing of the test specimen with air gaps. . . . 88
4.26 Test results from the testing of Configuration I. 90
4.27 Failure modes and calculated shear strengths of Configuration I. . . . 91
4.28 Test results from the testing of Configuration II. 94
4.29 Failure modes and calculated shear strengths of Configuration II. . . 95
4.30 Test results from the testing of Configuration III. 98
4.31 Failure modes and calculated shear strengths of Configuration III. . . 99
4.32 Test results from the testing of Configuration IV. 103
4.33 Failure modes and calculated shear strengths of Configuration IV. . . 104
4.34 Test results from the testing of Configuration V. 105
4.35 Failure modes and calculated shear strengths of Configuration V. . . 106
4.36 Test results from the testing of Configuration VI. 107
4.37 Failure modes and calculated shear strengths of Configuration VI. . . 108
4.38 Test results from the testing of Configuration VII. 109
4.39 Failure modes and calculated shear strengths of Configuration VII. . . 110
4.40 Test results from the testing of Configuration VIII. 111
4.41 Failure modes and calculated shear strengths of Configuration VIII. . 112
4.42 Test results from the testing of Configuration IX. 113
4.43 Failure modes and calculated shear strengths of Configuration IX. . . 114
4.44 Summary of the failure modes and calculated shear strengths of all the specimens. 116
4.45 The geometrical properties and results of the calculation of the failure load ratios for the three-layer specimens. 117
4.46 The geometrical properties and results of the calculation of the failure load ratio for the five-layer specimens. 118
4.47 Input data and results of the calculation of the load scale factor. . . . 119
4.48 Design strength properties used for the determination of the utilisation ratio. 120

Nomenclature

α, β	Angle
δ	Deformation
η_{A}	Pressure area ratio
η_{F}	Failure load ratio
η_{L}	Length ratio
η_{V}	Volume ratio
γ	Effective factor used in Abaqus
γ_{ij}	Shear strain in the ij-plane
γ_{M}	Partial factor
μ_{M}	Material reduction
ν_{ij}	Poisson's ratio in the ij-plane
ρ	Density
ρ_{12}	Density at 12 % moisture content
σ_{ii}	Stress in the ii-plane
σ_{ij}	Stress in the ij-plane
σ_{90}	Stress perpendicular to the grain
τ	Shear stress
τ_{LR}	Shear stress in the longitudinal-radial plane
τ_{LT}	Shear stress in the longitudinal-tangential plane
τ_{RT}	Shear stress in the radial-tangential plane
ε_{c}	Strain level corresponding to the characteristic compression strength parallel to the grain
$\varepsilon_{\mathrm{ii}}$	Strain in the ii-plane
$\varepsilon_{\mathrm{jj}}$	Strain in the jj-plane
ε_{u}	Ultimate strain level
A_{p}	Pressure area
b	Width
b_{airgap}	Width of air gap

D	Orthotropic elasticity stiffness matrix component
E_{i}	Modulus of elasticity in the i-direction
F	Load
f	Frequency
f_{b}	Bondline shear strength
$f_{\mathrm{c,0,k}}$	Characteristic compression strength parallel to the grain
$f_{\mathrm{c,90,d}}$	Design compression perpendicular to the grain
$f_{\mathrm{c,90,k}}$	Characteristic compression strength perpendicular to the grain
f_{d}	Design strength
f_{k}	Characteristic strength
$f_{\mathrm{r,EC}}$	Rolling shear strength according to Eurocode
$f_{\mathrm{r,k}}$	Characteristic shear strength in the plane perpendicular to the grain (rolling shear)
f_{r}	Modified rolling shear strength
$f_{\mathrm{t,0,k}}$	Characteristic tensile strength parallel to the grain
$f_{\mathrm{t,90,d}}$	Design tensile strength perpendicular to the grain
$f_{\mathrm{t,90,k}}$	Characteristic tensile strength perpendicular to the grain
$f_{\mathrm{v,d}}$	Design shear strength
$f_{\mathrm{v,EC}}$	Panel shear strength according to Eurocode
$f_{\mathrm{v,k}}$	Characteristic shear strength in the planes parallel to the grain (panel shear)
f_{v}	Modified panel shear strength
G_{ij}	Shear modulus in the ij-plane
$G_{\mathrm{r,EC}}$	Rolling shear modulus of rigidity according to Eurocode
$G_{\mathrm{v,EC}}$	Panel shear modulus of rigidity according to Eurocode
h	Total thickness
k_{h}	Modification factor accounting for the size effect
k_{mod}	Modification factor accounting for the load duration
k_{sys}	Modification factor accounting for the system effect
L	Length
L_{c}	Length of cross-layer interface
LSF	Load scale factor
m	Mass
m_{dry}	Dry mass
m_{u}	Mass at moisture content u

$MOE_{\mathrm{dyn,long}}$	Dynamic longitudinal modulus of elasticity
t	Thickness
u	Moisture content
V	Volume
v	Velocity of sound

1
Introduction

In a world currently facing a global climate crisis, with the construction industry responsible for a considerable portion of the greenhouse gas emissions, it is evident that measures must be taken to slow down the process. In the construction industry, there are many choices that can be made in order to navigate the course in a more sustainable direction and, in particular, the choice of building material is a significant decision. This has led to an increasing demand for sustainable building materials, such as cross-laminated timber.

The aim of this thesis is to develop a material-optimised CLT panel by introducing air gaps in the cross-layers. To analyse the structural behaviour of the modified panels, small scale specimens of various configurations are to be manufactured and subjected to shear loading, from which the shear capacity of each specimen is to be derived. Furthermore, the configurations are to be analysed using finite element analysis as a complement to the physical strength tests.

The introduction of air gaps in CLT panels is a topic that has been researched to a limited extent in the recent years. However, further work is necessary to implement the idea in practice.

1.1 Background

The construction industry is currently one of the major contributors to the greenhouse gas emissions and one of the key actors that are urged for change and improvement. In 2020, the construction industry alone was responsible for 37 % of the global energy-related CO_2 emissions and 36 % of the global energy usage (United Nations Environment Programme, 2021). It has been shown in numerous studies that the choice of building materials is a crucial decision that highly affects the environmental impact of a building, in particular when conventional building materials, such as concrete, are replaced with materials from renewable resources, such as timber (Andersen et al., 2021). Timber structures are becoming more common in Sweden, due to the carbon neutrality and renewability of the material and an increasing demand of timber, together with other sustainable building materials, can be observed in the construction industry.

Cross-laminated timber, also known as CLT, is a relatively new engineered wood product that has gained interest in recent years and considerably contributed to the

expansion of the technical possibilities of timber structures, in particular with regard to structural capacity. The alternately arranged layers of boards provide the CLT panel with high stiffness compared to its low self-weight. Furthermore, the efficient and highly adaptable manufacturing process, in combination with the low carbon footprint, make CLT a strong competitor to other conventional building materials. (Gustafsson, 2019)

However, the consumption of raw material for the production of CLT is excessively large in relation to the required structural capacity. Studies show that the cost of the raw material that is used for the manufacturing of CLT composes 20 % of the total manufacturing cost in the European industry (CBI, 2017). If the use of raw material is reduced, the construction cost will be reduced accordingly, and the material becomes more attractive and an even stronger competitor to other materials. Therefore, the demand for a material-optimised CLT panel is evident and the required load-bearing capacity is possible to achieve with less raw material at a lower cost by introducing air gaps in the cross-layers of the CLT panels.

1.2 Aim

The overall aim of the project is to develop a novel CLT panel for load-bearing structures in buildings. The novelty is characterised by the introduction of air gaps in the cross-layers of the panels to obtain an optimised composition that consumes less material, but still achieves a satisfying load-bearing capacity.

The main objectives of the project are to design a variety of configurations, where air gaps are introduced in the cross-layers with various widths and layouts. Furthermore, physical strength tests are to be conducted to determine the shear capacity of each specimen in order to compare the different configurations and identify how much material that can be reduced without compromising the structural capacity.

1.3 Methodology

The work is to be carried out both experimentally, by manufacturing and testing small scale specimens, and analytically, by modelling the specimens in a FE-software and predicting the behaviour, and the results are to be compared. The project is to be performed in four phases; preparation phase, manufacturing phase, experimental phase, and evaluation phase.

1.3.1 Preparation phase

During the preparation phase, related literature is to be studied in order to obtain a deeper knowledge regarding the properties of timber and CLT, as well as theory with regard to the designing and testing of CLT in relation to the aim of the work. Furthermore, a variety of configurations of modified CLT panels with air gaps in the cross-layers is to be designed and detailed planning of the manufacturing and

testing of the specimens is to be carried out.

Moreover, the timber that will be used for the manufacturing of the specimens is to be conditioned appropriately before strength grading of the boards is to be performed.

1.3.2 Manufacturing phase

The manufacturing is to be carried out in the Architecture workshop at Chalmers University of Technology. Initially, the boards are to be sawn and planed to the desired dimensions for each specimen using the machines in the workshop. The specimens are then to be assembled, according to the designed configurations, by applying adhesive in between each layer before placing them in the vacuum press for pressing.

1.3.3 Experimental phase

During the experimental phase, the rolling shear performance and stiffness of the manufactured specimens are to be tested in the Structures Lab at Chalmers University of Technology. Furthermore, finite element models are to be created in Abaqus to predict the stress distribution in the specimens.

1.3.4 Evaluation phase

After the testing of the specimens is completed, the test results are to be analysed and utilised to calculate the strength properties of the specimens. Furthermore, the results from the physical strength tests are to be compared with the predictions from the finite element models.

1.4 Limitations

The thesis is part of a larger research project called *Novel wood panel for efficient and healthy built environment* that is carried out at Chalmers University of Technology over a period of several years, in collaboration with Stora Enso as an industrial partner. The main project is organised in five work packages, where this thesis is a part of the third package with a focus on structural capacity analysis.

The main focus is to analyse the structural behaviour of CLT panels, meaning that other aspects, such as hygrothermal performance, environmental impact analysis, multi-performance optimisation, and panel design, will not be considered in this project.

The specimens will only be subjected to shear testing and the experiment will be carried out on a small scale. The CLT panels are limited to a maximum thickness of 115 mm, only allowing for configurations consisting of three and five layers to be

tested and analysed. Furthermore, the thickness of the layers within one configuration will not vary. For the three-layer configurations, 30 mm boards will be used and for the five-layer configurations, 20 mm boards will be used.

Moreover, the specimens will be evaluated using given climatic and loading conditions in Sweden, as well as according to Swedish construction standards. Only one species of wood will be used, specifically Scandinavian spruce.

The finite element modelling and analysis in Abaqus are only to be used as a complement to the results obtained from the physical strength tests, and therefore, no in depth analysis regarding the modelling in the software is made.

1.5 State of the art

The demand for an optimisation of the material consumption in CLT panels is continuously driving the development forward. Currently, research has been conducted where the possibilities of introducing air gaps in the cross-layers of CLT panels have been investigated parametrically and analytically. For example, Mayencourt et al. (2018) investigate the possibilites of minimising the volume of a CLT panel by the introduction of air gaps in the cross-layers, in combination with varying the thickness of the layers. By the application of physical testing, as well as analytical modelling, it was concluded that a slight modification of a standard CLT configuration could reduce the consumption of timber by 18 % without any significant decrease in the structural performance. Furthermore, there are numerous companies that have developed CLT panels with cavities in order to facilitate installations. However, the research is still limited and further studies are necessary to drive the development forward in order to implement the idea of introducing air gaps in CLT panels on a larger scale.

2
Theory

To analyse the behaviour of a cross-laminated timber panel, it is essential to understand the material that composes the layers of the panel, namely wood, and how its characteristics influence the properties of the material. As the physical and mechanical properties of wood vary, strength grading of the material is performed using various methods.

The introduction of cross-laminated timber, also known as CLT, as a building material in the 1990s revolutionised the construction industry with its numerous advantages in comparison to other materials. As a relatively new engineered wood product, there is no established method for the design of CLT. However, there are guidelines for the process of designing CLT. Furthermore, the procedure of shear testing of CLT to determine the strength is presented. Lastly, the finite element modelling in Abaqus is presented, along with the theory motivating the input data and the modelling in the software.

2.1 Properties of wood

The properties of wood are highly dependent on the structure of the material, and as an organic material, several characteristics appear naturally. In combination, the structural and the natural characteristics determine both the physical and the mechanical properties of wood.

2.1.1 Structure of wood

The distinctive structure provides the wood with its characteristic properties and ranges from the microscopic structure and the composition of a wood cell to the macroscopic structure and the anatomy of the tree stem.

2.1.1.1 Microscopic structure

Wood is composed of molecules of cellulose, hemicellulose, and lignin. The cellulose molecules are formed in crystalline strands, known as the microfibrils, and they are enclosed by hemicellulose and lignin molecules to form the wood cells. The cells are tube-shaped to allow for transportation of water and nutrition, and the cell walls are composed of four layers of microfibrils, with the microfibrils in each layer oriented at different angles, as illustrated in Figure 2.1.

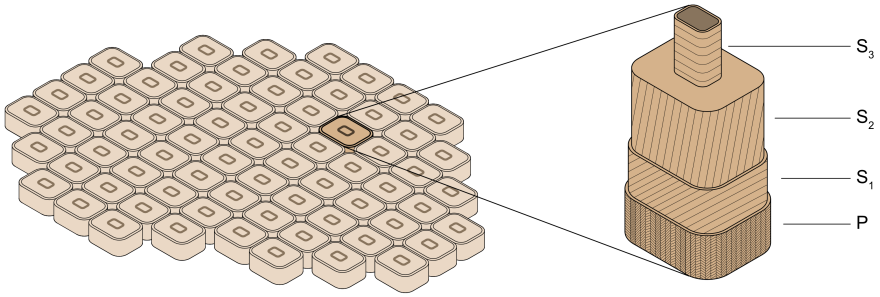

Figure 2.1: The composition of a wood cell.

The outermost layer is known as the primary wall, denoted by P, and consists of grains that are oriented irregularly in order to provide stability to the cell. The secondary wall is comprised of three layers, mainly consisting of microfibrils. The external layer, denoted by S_1, consists of microfibrils oriented nearly perpendicular to the longitudinal axis. The middle layer, denoted by S_2, is the thickest layer and, consequently, the major contributor of the properties of the wood cell. This layer is oriented virtually in the longitudinal direction of the cell. Similar to S_1, the internal layer, denoted by S_3, is comprised of microfibrils oriented almost perpendicular to the longitudinal axis, and both S_1 and S_3 contribute to the maintaining of the cell shape. (Johansson, 2016)

2.1.1.2 Mesoscopic structure

The exact composition of the cells varies both between different species, as well as within each tree. During the spring, the tree produces earlywood, which consists of cells with thin cell walls and large cell cavities to facilitate the transport of water and nutrition in the tree. During the summer and autumn, the tree instead produces latewood, which is comprised of cells with thicker cell walls that establish the strength needed to withstand external forces. The ratio between earlywood and latewood cells in the tree highly influence its mechanical properties. The cell walls of the latewood are in general five times as thick as the cell walls of the earlywood, as illustrated in Figure 2.2. (Johansson, 2016)

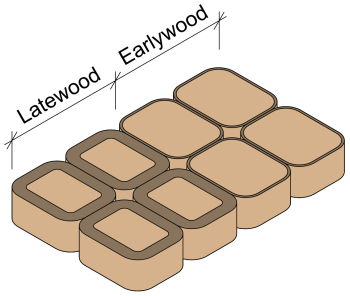

Figure 2.2: Earlywood and latewood.

2.1.1.3 Macroscopic structure

The centre of the stem is known as the pith. The pith is composed of parenchyma cells, which provide the stem with water. The layer outside the pith is called heartwood, which provides stability and strength to the tree and generally contains no living cells. The sapwood, which is the layer outside the heartwood, contains living and active wood cells that have a storing capacity and the ability to transport liquids in the stem. In pine species, the sapwood is commonly of a lighter colour than the heartwood, while in spruce species, the difference in colour can not be distinguished. The cells that are capable of cell division and, consequently, allow for further growth of the tree, are located in the cambium, which is the outermost area, located between the wood and the bark. The inner bark comprises living cells that transport nutrients to the cambium, meanwhile the outer bark is composed of dead cells with the purpose of protecting the stem. (Blaß and Sandhaas, 2017)

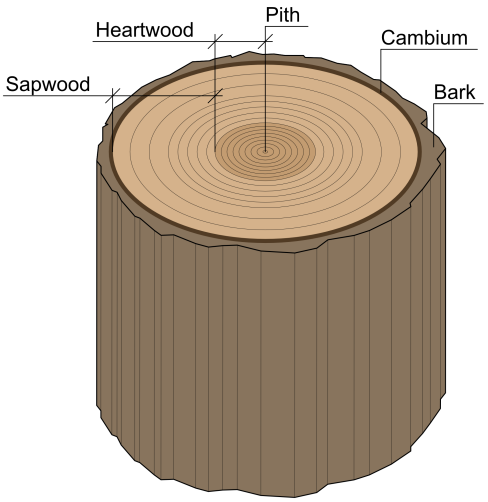

Figure 2.3: The anatomy of a tree stem.

2.1.2 Natural characteristics of wood

Due to the organic nature of wood, there are several characteristics that appear naturally, such as the occurrence of knots and the deviation and distortion of the fibres caused by the conditions of the surroundings, which all influence the properties of the material to a varying extent.

2.1.2.1 Knots

During the growth of trees, new branches are formed on the side of the stem, resulting in the occurrence of knots. When the tree continues to grow, some branches progressively become embedded in the stem, causing the orientation of the grain around the knot to be distorted and disconnected. Most mechanical properties are negatively affected by the presence of knots and the extent of the influence is mainly determined by the dimensions and position of individual knots rather than

the quantity of knots. There are several different types of knots that can appear when timber is sawn into boards, of which some are illustrated in Figure 2.4. (Blaß and Sandhaas, 2017) (Johansson, 2016)

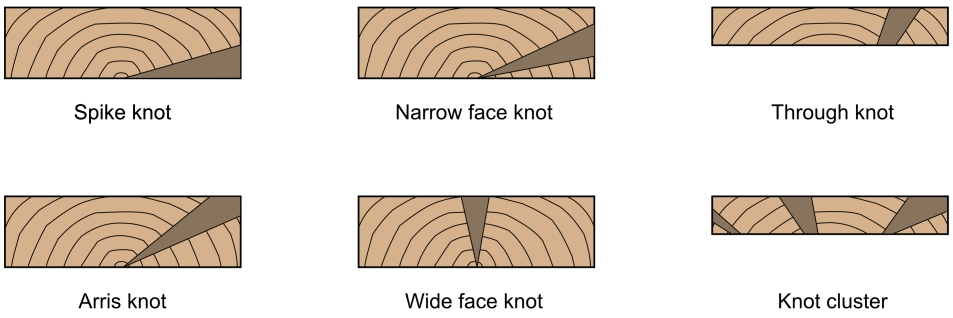

Figure 2.4: Common types of knots in boards.

2.1.2.2 Spiral grain

Spiral grain is a phenomenon that appears when the fibres grow in a spiral around the stem and not parallel to the stem axis, and is the result of the tree counteracting external loads, such as wind loads, see Figure 2.5. Since the strength of wood is highest in the longitudinal direction, see Section 2.1.4, all deviations in the fibre direction from the longitudinal axis result in a decrease in strength. Furthermore, the spiral-grained wood affects the hygroscopic behaviour and causes the wood to be more susceptible to distortion. (Blaß and Sandhaas, 2017)

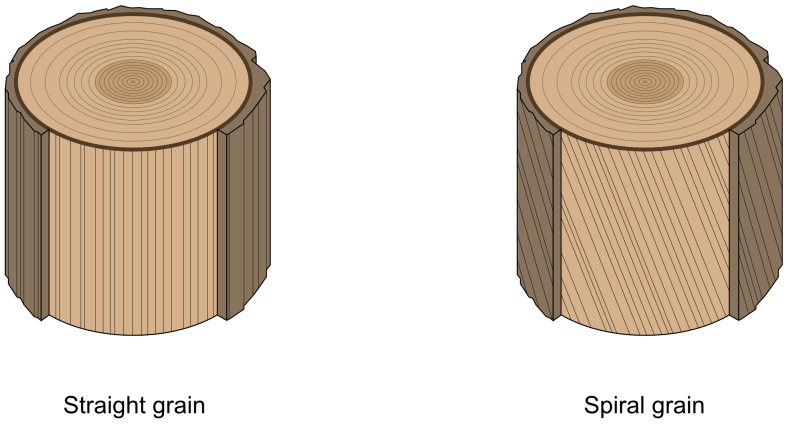

Figure 2.5: A stem with straight grain vs spiral grain.

2.1.2.3 Juvenile wood

During the first years of the life cycle of a tree, juvenile wood is formed around the pith in the stem. In the juvenile wood, the cell dimensions are gradually increasing and changes in the cell characteristics cause the properties to be less preferable than those of mature wood. Furthermore, juvenile wood contains fewer latewood cells which results in the density being about 10−15 % lower and the strength being 15−30 % lower than that of mature wood. (Johansson, 2016)

2.1.2.4 Reaction wood

When exposed to external forces, such as wind pressure, the tree strives to remain upright which causes reaction wood to be formed in order to deal with the internal stresses. Reaction wood is present in all types of trees and it is known as compression wood in coniferous trees and as tension wood in deciduous trees, as shown in Figure 2.6.

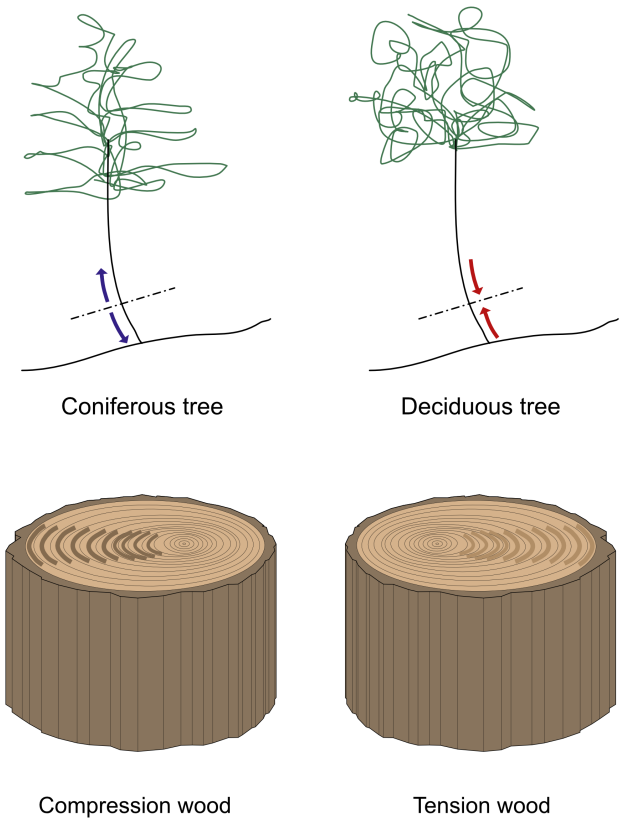

Figure 2.6: Reaction wood in coniferous and deciduous trees.

On a microscopical level, reaction wood consists of the same molecules as normal wood, but the ratio between the different types of molecules varies. The lignin to cellulose ratio is much higher in reaction wood in comparison to normal wood, while the amount of hemicellulose is unchanged. The difference influences the physical and mechanical properties of the material. (Johansson, 2016)

2.1.3 Physical properties

The physical properties of wood are a direct result of its anisotropic nature and unique cell structure. Wood is a hygroscopic material that is highly dependent on the moisture content and the orientation of the wooden fibres.

2.1.3.1 Moisture

Wood is a hygroscopic material that is directly dependent on the relative humidity of the surrounding air and the properties of wood are therefore highly influenced by the moisture content in the material.

The moisture content of wood is usually defined according to Equation 2.1.

$$u = \frac{m_{\mathrm{u}} - m_{\mathrm{dry}}}{m_{\mathrm{dry}}} \cdot 100 \ [\%] \tag{2.1}$$

where u is the moisture content, m_{u} is the weight of the wood at moisture content u, and m_{dry} is the dry weight of the wood.

When a dry piece of wood adsorbs water, the moisture is initially bound to the cell walls, but when all cell walls are saturated, the water begins to fill up the cell cavities instead. The point where the cell walls reach saturation is called the fibre saturation point, FSP, and is a threshold for when the mechanical properties of the wood no longer are affected by an increase in moisture content. For the wood species commonly used in Scandinavia as structural timber, such as pine and spruce, the fibre saturation point usually vary between 27 % and 33 %. (Johansson, 2016)

2.1.3.2 Density

The density of wood is defined according to Equation 2.2.

$$\rho = \frac{m}{V} \ \left[\frac{\mathrm{kg}}{\mathrm{m}^3}\right] \tag{2.2}$$

where ρ is the density, m is the weight, and V is the volume of the specimen.

Due to wood being highly dependent on its moisture content, the density is often defined as ρ_{12}, which is the density calculated at 12 % moisture content. According to EN 789 (2004), all types of strength testing are to be performed with wood specimens conditioned in an environment with a relative humidity of 65 ± 5 % and a temperature of 20 ± 2 °C. This corresponds to a moisture content of approximately 12 %. The density of some common wood species in Scandinavia is presented in Table 2.1. (Johansson, 2016)

Species	Latin	Dry density [kg/m^3]
Pine	*Pinus sylvestris L.*	450−500
Spruce	*Picea abies Karst.*	370−400
Larch	*Larix decidua Mill.*	520−600
Birch	*Betula verrucosa Ehrh.*	580−620
Ash	*Fraxinus ecxelsior L.*	530−780
Oak	*Quercus robur L.*	650−720

Table 2.1: Dry density of common wood species in Scandinavia. (Holmberg and Sandberg, 1997)

2.1.3.3 Shrinkage and swelling

When wood adsorbs moisture, the water is bonded to the surface of the microfibrils in the cell wall, which causes the space between the microfibrils to increase and the wood to swell. Depending on the orientation of the microfibrils, the swelling varies accordingly. The majority of the microfibrils is oriented in the longitudinal direction, which causes the major movements to be perpendicular to the longitudinal direction, i.e. in the transversal direction.

In general, the major shrinkage and swelling occurs in the tangential direction and the movements are about 30 times larger than those in the longitudinal direction. Additionally, the tangential movements are approximately twice as large as the movements in the radial direction. The shrinkage in different directions for some common wood species in Scandinavia is presented in Table 2.2. (Johansson, 2016)

Species	Latin	Shrinkage [%]		
		Longitudinal	Radial	Tangential
Pine	*Pinus sylvestris L.*	0.3	4.0	7.7
Spruce	*Picea abies Karst.*	0.2−0.3	3.6−4.2	7.8−8.8
Larch	*Larix decidua Mill.*	0.3	3.3−4.3	7.8−10.4
Birch	*Betula verrucosa Ehrh.*	0.6	5.3	7.8
Ash	*Fraxinus ecxelsior L.*	0.2	3.8−5.0	5.4−8.4
Oak	*Quercus robur L.*	0.4	4.0−5.0	7.8−10

Table 2.2: Shrinkage of common wood species in Scandinavia. (Holmberg and Sandberg, 1997)

2.1.3.4 Distortion

Due to local defects, the fibre orientation varies across the lengths. These variations cause the process of swelling and shrinking to be distributed unevenly across the lengths, which in turn causes distortion of the wood.

There are four types of distortion modes; cupping, bowing, twisting, and springing. From a structural perspective, twisting is the most problematic mode, followed by bowing and springing, since this causes a significant reduction in strength, while

the main problem with cupping is that it causes a substantial amount of material waste during the production. The four distortion modes are illustrated in Figure 2.7. (Johansson, 2016)

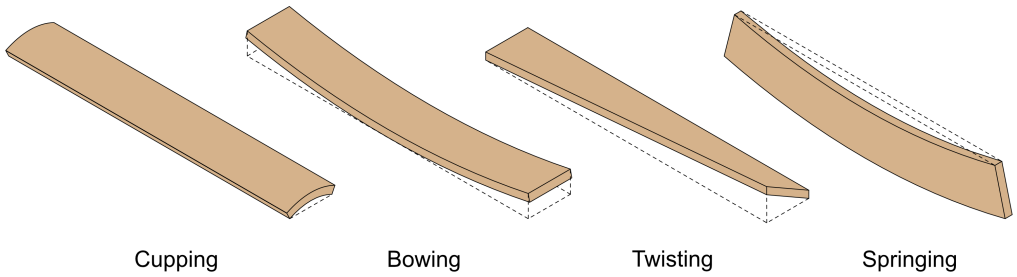

Figure 2.7: The four distortion modes.

2.1.4 Mechanical properties

Due to the anisotropic nature of timber, the properties of wood vary in different directions and the mechanical properties are dependent on the loading direction, see Figure 2.8. The three main directions are defined as follows:

- The longitudinal direction L, defined along the stem
- The radial direction R, defined from the pith to the peripheral bark
- The tangential direction T, defined along the annual rings

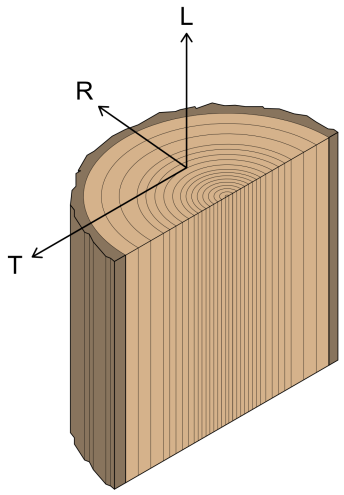

Figure 2.8: The main directions of timber.

2.1.4.1 Tension

If the wood is loaded in tension parallel to the grain, the relationship between the stress and the strain in the material is nearly linear until it reaches failure. The failure may be caused by either the fibres being dislocated, or the fibres breaking. The characteristic strength in tension parallel to the grain, denoted by $f_{t,0,k}$, is high and often around 100 MPa.

For wood loaded in tension perpendicular to the grain, the failure may also be caused by the fibres breaking. However, the characteristic strength in tension perpendicular to the grain, denoted by $f_{t,90,k}$, is much lower than the strength in tension parallel to the grain, and is usually less than 0.5 MPa. The stress-strain relationships for wood loaded in tension parallel to the grain and perpendicular to the grain, respectively, are presented in Figure 2.9. (Johansson, 2016)

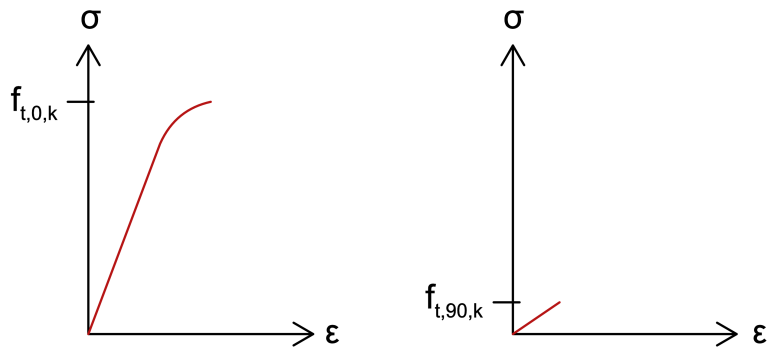

Figure 2.9: Stress-strain curve for wood loaded in tension parallel to the grain and perpendicular to the grain.

2.1.4.2 Compression

Wood loaded in compression parallel to the grain has a high characteristic strength, denoted by $f_{c,0,k}$, and it is usually around 80 MPa. When failure is reached, some fibres start to buckle and the load is redistributed into other fibres causing the strength to decrease and initiating a plasticising behaviour. The ultimate strain level ε_u is approximately three times as high as the strain level ε_c corresponding to the characteristic strength, see Figure 2.10.

When the wood is loaded in compression perpendicular to the grain, the load will cause the wood cells to be crushed, enabling the stress level to slightly increase. However, the characteristic strength in compression perpendicular to the grain, denoted by $f_{c,90,k}$, is low and around 3 to 5 MPa. The stress-strain relationships for wood loaded in compression parallel to the grain and perpendicular to the grain, respectively, are presented in Figure 2.10. (Johansson, 2016)

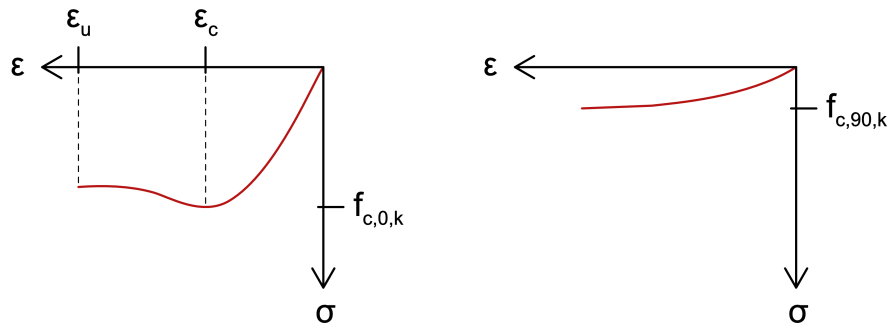

Figure 2.10: Stress-strain curve for wood loaded in compression parallel to the grain and perpendicular to the grain.

2.1.4.3 Shear

A wood specimen can be subjected to shear stresses in three planes; in the longitudinal-radial plane (denoted by τ_{LR}), in the longitudinal-tangential plane (denoted by τ_{LT}), and in the radial-tangential plane (denoted by τ_{RT}), as illustrated in Figure 2.11.

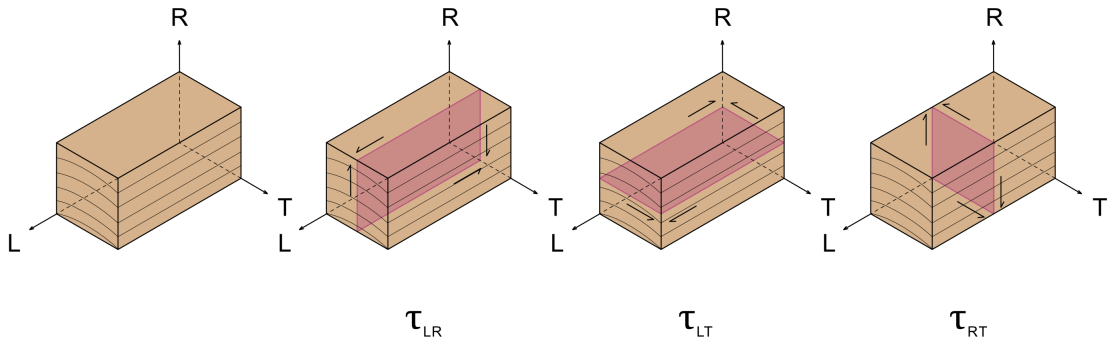

Figure 2.11: Shear in the three axial planes in a wood specimen.

The first two shear modes are parallel to the grain and their characteristic strength, denoted by $f_{\mathrm{v,k}}$, is around 5 to 8 MPa, while the latter mode is perpendicular to the grain and is called rolling shear. It is the weakest shear mode with a characteristic strength, denoted by $f_{\mathrm{r,k}}$, of about 3 to 4 MPa. It is usually not the designing mode for regular structural timber. However, for CLT and glulam beams with more advanced cross-sections, rolling shear is an important load case to consider. (Johansson, 2016)

2.1.4.4 Size effect

The size effect of a timber specimen is a phenomenon that occurs due to the fact that the strength of a timber specimen is highly dependent on the volume of the specimen. It has been observed in several tests that the strength of a test specimen increases as the size decreases, which can be described by the reduction of number of potential defects and failure points in the specimen when the size decreases. (Blaß and Sandhaas, 2017)

In Eurocode EN 1995-1-1 (2004), the size effect is considered by applying a modification factor k_{h} to increase the characteristic strength values for timber specimens of dimensions smaller than a reference value. The modification factor for solid timber is determined according to Equation 2.3.

$$k_{\mathrm{h}} = \min \begin{cases} \left(\frac{150}{h}\right)^{0.2} \\ \\ 1.3 \end{cases} \tag{2.3}$$

The modification factor for glued laminated timber is determined according to Equation 2.4.

$$k_{\mathrm{h}} = \min \begin{cases} \left(\frac{600}{h}\right)^{0.1} \\ \\ 1.1 \end{cases} \tag{2.4}$$

where h is the total thickness of the specimen in mm.

2.2 Strength grading of timber

Unavoidable variations in properties occur due to the natural characteristics of wood and it is therefore essential to grade the material in order to estimate its strength properties before proceeding with any application of the material. There are two types of strength grading; visual strength grading and machine strength grading, which are performed according to EN 14081-1 (2016).

2.2.1 Visual strength grading

The visual strength grading is based on visual detection of defects and its correlation to the strength of the material. The accuracy of this method, however, may be inadequate since the grading can only be based on visual defects, while internal defects are impossible to detect. For improvement of the accuracy, the visual strength grading can be combined with various scanning techniques. (Johansson, 2016)

2.2.2 Machine strength grading

The machine strength grading is based on non-destructive measuring of parameters in a machine that are used to predict the strength of the material. There are several different grading methods that are used to determine different material parameters.

2.2.2.1 Determination of density

The density within a piece of wood may differ due to local defects and the variation can be measured using x-ray, γ-rays, or microwaves. The natural characteristics of wood, as discussed in Section 2.1.2, highly influence the density and can cause the affected parts to show a different density than that of normal wood. (Johansson, 2016)

The average density of a timber specimen can be determined by using Equation 2.2 as presented in Section 2.1.3.2, where the mass m is measured using a scale and the volume V is determined according to Equation 2.5.

$$V = L \cdot b \cdot t \ [\mathrm{m}^3] \tag{2.5}$$

where L is the length, b is the width, and t is the thickness of the board in m.

2.2.2.2 Determination of MOE

By the introduction of vibrations into a board and the evaluation of the resonance frequency, the dynamic longitudinal modulus of elasticity, $MOE_{\text{dyn,long}}$, can be determined. The test is performed by placing the test board on two supports, where a microphone is placed by one end of the board and a hammer is used to hit the opposite end. The test setup for the frequency test is illustrated in Figure 2.12.

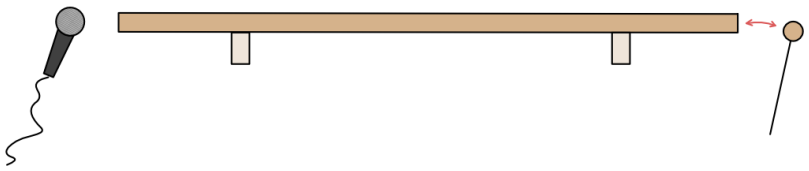

Figure 2.12: Frequency test setup.

The MOE can be calculated according to Equation 2.6.

$$MOE_{\text{dyn,long}} = \rho v^2 \ \text{[Pa]} \tag{2.6}$$

where ρ is the density of the material in kg/m^3 and v is the velocity of sound in m/s, which can be calculated according to Equation 2.7.

$$v = 2Lf \ \text{[m/s]} \tag{2.7}$$

where L is the length of the board in m and f is the longitudinal vibration frequency in Hz that is measured during the test.

The resonance frequency for dry wood samples can be roughly estimated by using Equation 2.8.

$$f = 2500/L \ \text{[Hz]} \tag{2.8}$$

where L is the length of the board in m. The measured longitudinal vibration frequency should be in the range of ± 20 % the predicted frequency. For reference, see the manual of the software FFT Analyser in Appendix A.

2.3 Cross-Laminated Timber

Cross-laminated timber, also known as CLT, is an engineered wood product that was developed in Austria in the 1990s. CLT is characterised by its odd number of boards in layers that are arranged alternately at right angles, which provides stiffness in two directions, allowing for the use of the material as large surface panels. The production is a straightforward and efficient process that allows for prefabrication to a large extent and the low self-weight allows for smooth transport and assembly. The consumption of CLT, both in Sweden and internationally, is continuously growing due to the demand for sustainable building materials and the numerous advantages of CLT, along with the pressing urge for change in the construction industry, will only lead to the continuous growth in production in the foreseeable future.

2.3.1 CLT as a construction material

A CLT panel is composed by an odd number of glued boards, usually between three and nine layers, where each layer is arranged at a right angle in relation to the adjacent layers. The alternately layered boards provide stiffness in two directions, making CLT a versatile building material that can be applied in all types of structural components. The high strength-to-weight ratio makes it suitable for different types of buildings, including high-rise complexes. Furthermore, the easily adaptable manufacturing process allows for almost any cross-section and geometry to be produced, which makes CLT a strong competitor to other conventional building materials. (Gustafsson, 2019)

2.3.2 Manufacturing of CLT

The manufacturing of CLT is a straight-forward process that is performed in accordance with EN 16351 (2015). Furthermore, the boards should be strength graded according to EN 14081-1 (2016), as presented in Section 2.2, before the manufacturing of the CLT panels.

The manufacturing process is initiated by the finger-jointing of boards to obtain longer boards. After the hardening of the glue in the joints, the boards are planed and assembled into large panels by gluing and pressing. After the pressing, the panels are refined in a CNC machine to prepare them for their ultimate purpose. Finally, the visible surfaces are polished and a final visual check of the panels is carried out before they are ready for transportation. (Gustafsson, 2019)

2.3.3 Consumption of CLT

The demand for sustainable building materials in the construction industry is increasing and CLT is one of the strong competitors with its carbon neutrality and renewability of the raw material. The production of CLT is constantly growing, with a majority of the production located in Europe. Sweden is one of the countries with a large production of CLT, together with countries in the Alpine region of Europe,

due to the great access to raw material.

2.3.3.1 In Sweden

For more than a hundred years, a law in Sweden forbid timber buildings with more than two storeys to be built due to the fear of timber being a highly combustible material that had led to disastrous city fires in the past. However, the law was removed in 1994, at a time when the interest in CLT as a building material was increasing and the material was introduced in the Swedish construction industry in the late 1990s. (Brandt, 2015)

Today, there are several manufacturers in Sweden and the production of CLT is continuously expanding. As of 2016, the production of CLT panels in Sweden was around 200,000 cubic metres each year and the growth of production and demand since then has increased. (Gustafsson, 2019)

2.3.3.2 Internationally

An increase in the demand for CLT can also be observed in the construction industry globally and the production is continuously growing. Currently, a majority of the CLT industry is concentrated in the Alpine region of Europe, including countries such as Austria, Germany, and Switzerland, from where the development of the material originated. As of 2019, the annual global production of CLT was approximately 1.44 million cubic metres and the Alpine countries were responsible for 70 % of the manufactured volume. (Muszynski et al., 2020)

2.4 Design of CLT

The design of CLT is currently not included in Eurocode 5, however, it is expected to be added in the near future. Meanwhile, two methods are currently in use; the designing of the cross-section based on the material properties of the individual lamellas in the CLT panel or the designing based on tables with material properties that are published by CLT manufacturers.

When designing CLT structures, the partial factor method is used to verify that the design value of the resistance is sufficient to manage the specified load effect. The structures must be designed in both ultimate limit state and in serviceability limit state and the design values are modified using different material factors that are specified for CLT.

2.4.1 Design in ultimate limit state

The design strength f_{d} can be calculated according to Equation 2.9.

$$f_{\mathrm{d}} = \frac{k_{\mathrm{mod}} \cdot f_{\mathrm{k}}}{\gamma_{\mathrm{M}}} \ [\mathrm{Pa}] \tag{2.9}$$

where k_{mod} is a modification factor accounting for the load duration (see Section 2.4.3), f_{k} is the characteristic strength in Pa, and γ_{M} is a partial factor that is material-dependent (see Section 2.4.3).

2.4.2 Design in serviceability limit state

In the serviceability limit state, the designing of the CLT is governed by the aim to obtain sufficient stiffness to avoid vibrations and deformation to a greater extent. The stiffness of CLT panels is influenced by different factors, including the load duration and moisture content of the material.

2.4.3 Design factors

Two design factors are used to modify the design resistance in order to establish a safe design.

The partial factor γ_{M} for CLT is in some countries taken as the same value as for glulam, while in other countries, the value for structural timber is used. Some values for the partial factor γ_{M} that are used for CLT in different countries are shown in Table 2.3.

Country	Partial factor γ_M
Sweden	1.25
Norway	1.15
Austria	1.25
Germany	1.3

Table 2.3: Partial factor values used in different countries. (Gustafsson, 2019)

For the modification factor k_{mod} that accounts for the load duration in relation to the service class, the same value is used for CLT as for glulam and structural timber due to numerous tests showing similar behaviours with regard to load duration. The values of the modification factor k_{mod} used for different combinations of load duration and service class are presented in Table 2.4.

Load duration class	P	L	M	S	I
Service class					
1	0.6	0.7	0.8	0.9	1.1
2	0.6	0.7	0.8	0.9	1.1
3	0.5	0.55	0.65	0.7	0.9

Table 2.4: Values of k_{mod}. (Gustafsson, 2019)

2.4.4 System effect

The system effect is a phenomenon that is present in CLT panels, where the combination of boards of different strengths decreases the risk of the weakest cross-sections to coincide in the same direction and layer. The characteristic bending and tensile strength of CLT can therefore be increased by applying a system effect factor k_{sys}, due to the fact that CLT consists of several boards subjected to bending or tension at the same time, which increases the strength of the whole panel. The system effect factor can be determined according to Equation 2.10.

$$k_{\text{sys}} = \min \begin{cases} 1.15 \\ \\ 1 + 0.1 \cdot b \end{cases} \tag{2.10}$$

where b is the effective width of the cross-section in m.

2.5 Strength testing of CLT

There are several methods for determining the shear strength of a CLT panel. In EN 16351 (2015), two different methods are suggested. The first method is similar to the one applied to regular structural timber and is comprised of a four-point bending test, from which the rolling shear strength can be derived. The second method is a shear test specifically developed for CLT where the CLT specimen is directly subjected to a shear loading configuration, from which the rolling shear strength can be derived according to EN 789 (2004). In this thesis, the rolling shear strength will be tested by the application of the second method only.

2.5.1 Conditioning of test specimens

As discussed in Section 2.1.3.2, the moisture content of a wood specimen is crucial for the determination of its mechanical properties. It is therefore important that all test specimens are conditioned correctly in accordance with the procedure presented in EN 408 (2010).

It is specified that all test specimens should be stored in a "standard environment", with a temperature of 20 ± 2 °C and a relative humidity of 65 ± 5 % until moisture equilibrium is reached. Furthermore, a conditioned test specimen should be transferred to the test area within one hour before the testing to ensure that the moisture conditions are unaffected.

If a test specimen is not conditioned in accordance with the procedure as presented above, it is instead suggested that a moisture content of 12 ± 3 % is sufficient.

2.5.2 Shear strength test

According to EN 16351 (2015), the rolling shear strength can be derived by conducting a shear test with the test configuration as is illustrated in Figure 2.13.

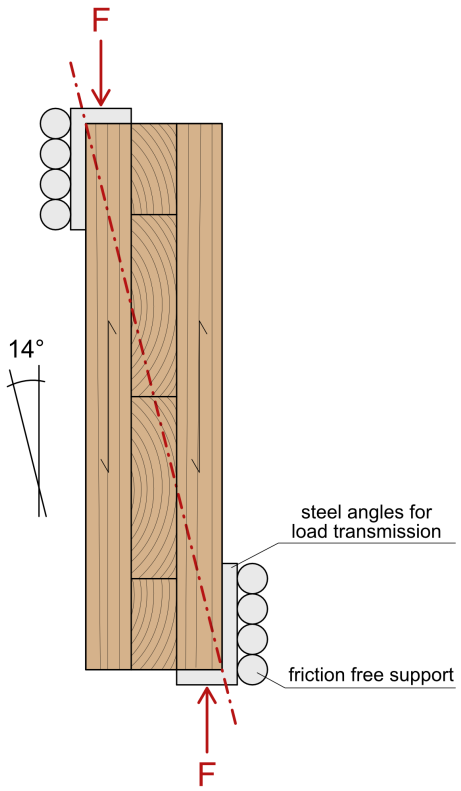

Figure 2.13: Shear test configuration for determination of rolling shear strength.

The load F should be applied at a constant rate and the loading rate should be adjusted so that the failure load is reached within 300 ± 120 seconds, in accordance with EN 789 (2004). The test specimen should have a width of at least 100 mm and the diagonal between two opposite corners of the specimen should be at an angle of 14 degrees.

2.5.3 Calculation of shear strength

The shear strengths can be derived from the results of the shear strength test performed in accordance with EN 789 (2004).

The panel shear strength $f_{\mathrm{v,EC}}$ is calculated according to Equation 2.11.

$$f_{\mathrm{v,EC}} = \frac{F_{\mathrm{max}}}{L \cdot h} \text{ [Pa]} \tag{2.11}$$

where F_{max} is the maximum load applied in N, L is the length of the specimen in m, and h is the total thickness of the specimen in m.

The panel shear modulus of rigidity $G_{\mathrm{v,EC}}$ is calculated according to Equation 2.12.

$$G_{\mathrm{v,EC}} = \frac{0.5(F_2 - F_1)}{(\delta_2 - \delta_1)} \cdot \frac{L_1}{L \cdot h} \text{ [Pa]} \tag{2.12}$$

where $F_2 - F_1$ is the load increment between $0.1F_{\mathrm{max}}$ and $0.4F_{\mathrm{max}}$, $\delta_2 - \delta_1$ is the increment in deformation corresponding to F_2 and F_1, respectively, L_1 is the gauge length in m, L is the length of the specimen in m, and h is the total thickness of the specimen in m.

The rolling shear strength $f_{\mathrm{r,EC}}$ is calculated according to Equation 2.13

$$f_{\mathrm{r,EC}} = \frac{F_{\mathrm{max}}}{L \cdot b} \text{ [Pa]} \tag{2.13}$$

where F_{max} is the maximum load applied in N, L is the length of the specimen in m, and b is the width of the specimen in m.

The rolling shear modulus of rigidity $G_{\mathrm{r,EC}}$ is calculated according to Equation 2.14.

$$G_{\mathrm{r,EC}} = \frac{(F_2 - F_1)}{(\delta_2 - \delta_1)} \cdot \frac{t}{L \cdot b} \text{ [Pa]} \tag{2.14}$$

where $F_2 - F_1$ is the load increment between $0.1F_{\mathrm{max}}$ and $0.4F_{\mathrm{max}}$, $\delta_2 - \delta_1$ is the increment in deformation corresponding to F_2 and F_1, respectively, t is the thickness of the specimen in m, L is the length of the specimen in m, and b is the width of the specimen in m.

2.6 Finite element modelling in Abaqus

The software Abaqus is used for finite element modelling and analysis. A wood material can be modelled as an orthotropic material, where the material parameters are dependent on three perpendicular directions. To simulate the orthotropy in Abaqus, an orthotropic elastic stiffness matrix can be defined. Furthermore, the composite action of the various stresses obtained by the finite element analysis can be analysed by checking the interaction between the stresses.

2.6.1 Orthotropic modelling

For the establishment of a simplified structural model, wood materials can be assumed to have a linear elastic behaviour during short term loading up to the point of failure. Furthermore, the material can be considered to be orthotropic, meaning that the mechanical properties are dependent on the direction, as described in Section 2.1.4, and the principal directions are defined by three orthogonal axes (Dahl, 2009). Therefore, in Abaqus, timber can be modelled as an orthotropic material with linear elastic material parameters.

2.6.1.1 Material parameters

For the orthotropic modelling of a material, twelve elastic constants can be used to describe the material; three moduli of elasticity E_{i}, three shear moduli G_{ij}, and six Poisson's ratios ν_{ij}. However, only three of the Poisson's ratios are independent and therefore, an orthotropic material is governed by nine independent material parameters. These can be determined experimentally by observing the stress and strain increments according to Equations 2.15 − 2.17.

$$E_{\mathrm{i}} = \frac{d\sigma_{\mathrm{ii}}}{d\varepsilon_{\mathrm{ii}}} \tag{2.15}$$

where σ_{ii} is the stress in the ii-plane and $\varepsilon_{\mathrm{ii}}$ is the strain in the ii-plane.

$$G_{\mathrm{ij}} = \frac{d\sigma_{\mathrm{ij}}}{d\gamma_{\mathrm{ij}}} \tag{2.16}$$

where σ_{ij} is stress in the ij-plane and γ_{ij} is the shear strain in the ij-plane.

$$\nu_{\mathrm{ij}} = -\frac{d\varepsilon_{\mathrm{jj}}}{d\varepsilon_{\mathrm{ii}}} \tag{2.17}$$

where $\varepsilon_{\mathrm{jj}}$ is the strain in the jj-plane and $\varepsilon_{\mathrm{ii}}$ is the strain in the ii-plane.

There are several methods to determine the Poisson's ratios ν_{ij} of a material, including mechanical tests and ultrasonic wave propagation. However, there are no standardised tests and many extensive studies are dated and based on different test methods. Therefore, the linear elastic orthotropic parameters of wood vary depending on the test methods used and a large range of values can be observed, see Table 2.5 for a comparison of values of linear elastic orthotropic material parameters for spruce from different studies. (Dahl, 2009) (Kohlhauser and Hellmich, 2012)

Ref.	ρ	$\mathbf{E_L}$	$\mathbf{E_R}$	$\mathbf{E_T}$	ν_{LR}	ν_{LT}	ν_{RT}	ν_{RL}	ν_{TL}	ν_{TR}	$\mathbf{G_{LR}}$	$\mathbf{G_{LT}}$	$\mathbf{G_{RT}}$
1	445	–	–	–	0.38	0.42	0.64	0.02	0.02	0.34	–	–	–
2	440	15919	686	392	0.43	0.54	0.42	0.02	0.01	0.24	617	760	36
2	500	16706	810	633	0.37	0.56	0.43	0.02	0.02	0.33	624	853	35
3	440	15900	690	390	0.44	0.38	0.47	0.03	0.01	0.25	620	770	36
4	370	9900	730	410	0.44	0.56	0.57	0.03	0.01	0.29	496	607	21
4	390	10700	710	430	0.38	0.51	0.51	0.03	0.03	0.31	500	620	23
4	390	10900	640	420	0.39	0.49	0.64	0.03	0.02	0.32	580	590	26
4	500	16600	850	690	0.36	0.52	0.43	0.02	0.02	0.33	630	840	37
Avg.	434	13804	731	481	0.40	0.50	0.51	0.03	0.02	0.30	581	720	31
Max.	500	16706	850	690	0.44	0.56	0.64	0.03	0.03	0.34	630	853	37
Min.	370	9900	640	390	0.36	0.38	0.42	0.02	0.01	0.24	496	590	21

Table 2.5: Linear elastic orthotropic material parameters for spruce comparing different studies (ρ in kg/m^3, E_i and G_{ij} in MPa). (Dahl, 2009) (Kohlhauser and Hellmich, 2012) (Niemz and Caduff, 2007)

The references that are shown in Table 2.5 are listed in reversed chronological order below.

1. Caduff, P., Niemz, D. (2007)
2. Kollmann, F., Côté, W. (1968)
3. Stamer, J. (1935)
4. Carrington, H. (1923)

2.6.1.2 Orthotropic elastic stiffness matrix

The linear elasticity of an orthotropic material can be defined using nine independent parameters in an orthotropic elastic stiffness matrix. In Abaqus, the elastic stiffness matrix for an orthotropic material is defined according to Equation 2.18. (Dassault Systèmes, 2020)

$$\boldsymbol{D} = \begin{bmatrix} D_{\mathrm{LLLL}} & D_{\mathrm{LLRR}} & D_{\mathrm{LLTT}} & 0 & 0 & 0 \\ & D_{\mathrm{RRRR}} & D_{\mathrm{RRTT}} & 0 & 0 & 0 \\ & & D_{\mathrm{TTTT}} & 0 & 0 & 0 \\ & & & D_{\mathrm{LRLR}} & 0 & 0 \\ & \text{Sym.} & & & D_{\mathrm{LTLT}} & 0 \\ & & & & & D_{\mathrm{RTRT}} \end{bmatrix} \tag{2.18}$$

where L denotes the longitudinal direction, R denotes the radial direction, and T denotes the tangential direction.

The parameters in Equation 2.18 are defined according to Equations 2.19 to 2.27.

$$D_{\mathrm{LLLL}} = E_{\mathrm{L}}(1 - \nu_{\mathrm{TR}}\nu_{\mathrm{RT}})\gamma \tag{2.19}$$

$$D_{\mathrm{RRRR}} = E_{\mathrm{R}}(1 - \nu_{\mathrm{LT}}\nu_{\mathrm{TL}})\gamma \tag{2.20}$$

$$D_{\mathrm{TTTT}} = E_{\mathrm{T}}(1 - \nu_{\mathrm{LR}}\nu_{\mathrm{RL}})\gamma \tag{2.21}$$

$$D_{\mathrm{LLRR}} = E_{\mathrm{L}}(\nu_{\mathrm{RL}} + \nu_{\mathrm{TL}}\nu_{\mathrm{RT}})\gamma \tag{2.22}$$

$$D_{\mathrm{LLTT}} = E_{\mathrm{L}}(\nu_{\mathrm{TL}} + \nu_{\mathrm{RL}}\nu_{\mathrm{TR}})\gamma \tag{2.23}$$

$$D_{\mathrm{RRTT}} = E_{\mathrm{R}}(\nu_{\mathrm{TR}} + \nu_{\mathrm{LR}}\nu_{\mathrm{TL}})\gamma \tag{2.24}$$

$$D_{\mathrm{LRLR}} = E_{\mathrm{R}}(\nu_{\mathrm{LR}} + \nu_{\mathrm{TR}}\nu_{\mathrm{LT}})\gamma \tag{2.25}$$

$$D_{\mathrm{LTLT}} = E_{\mathrm{T}}(\nu_{\mathrm{LT}} + \nu_{\mathrm{LR}}\nu_{\mathrm{RT}})\gamma \tag{2.26}$$

$$D_{\mathrm{RTRT}} = E_{\mathrm{T}}(\nu_{\mathrm{RT}} + \nu_{\mathrm{RL}}\nu_{\mathrm{LT}})\gamma \tag{2.27}$$

where γ is an effective factor calculated according to Equation 2.28.

$$\gamma = \frac{1}{1 - \nu_{\mathrm{LT}}\nu_{\mathrm{TL}} - \nu_{\mathrm{TR}}\nu_{\mathrm{RT}} - \nu_{\mathrm{RL}}\nu_{\mathrm{LR}} - 2\nu_{\mathrm{TL}}\nu_{\mathrm{RT}}\nu_{\mathrm{LR}}} \ [-] \tag{2.28}$$

2.6.2 Interaction

To calculate the resulting stresses in a specimen subjected to composite action, the interaction between shear stresses and stresses perpendicular to the grain can be obtained by Equation 2.29.

$$\frac{\left(f_{\mathrm{c,90,d}} + \sigma_{90}\right)^2}{\left(f_{\mathrm{c,90,d}} + f_{\mathrm{t,90,d}}\right)^2} + \frac{\tau^2}{f_{\mathrm{v,d}}^2} \cdot \left[1 - \left(\frac{f_{\mathrm{c,90,d}}}{f_{\mathrm{c,90,d}} + f_{\mathrm{t,90,d}}}\right)^2\right] \leq 1 \ [-] \tag{2.29}$$

where $f_{\mathrm{c,90,d}}$ is the design compression strength perpendicular to the grain, σ_{90} is the stress perpendicular to the grain, $f_{\mathrm{t,90,d}}$ is the design tensile strength perpendicular to the grain, τ is the shear stress, and $f_{\mathrm{v,d}}$ is the design shear strength. The stress perpendicular to the grain $\sigma_{90} = -\sigma_{c,90}$ in case of compression and $\sigma_{90} = \sigma_{t,90}$ in case of tension. (Steiger and Gehri, 2011)

The design strength values in Equation 2.29 are calculated using the characteristic strength values in Table 2.6 and Equation 2.9, see Section 2.4.1. For ordinary structural timber, the regular characteristic values of timber apply, whereas the corresponding values for CLT panels differ slightly due to the bi-axial effect of the cross-layers.

The characteristic values of C24 structural timber and the corresponding characteristic values for CLT panels consisting of C24 boards, is presented in Table 2.6.

Timber (C24)	**Value [MPa]**	**CLT (C24)**	**Value [MPa]**	
$f_{\mathrm{c,90,k}}$	2.5	$f_{\mathrm{c,90,R,k}}$	2.5	
$f_{\mathrm{t,90,k}}$	0.4	$f_{\mathrm{t,90,L,k}}$	0.4	
		$f_{\mathrm{t,90,T,k}}$	0.4	
$f_{\mathrm{v,k}}$	4.0	$f_{\mathrm{v,090,L\text{-}lay,k}}$	4.0	
		$f_{\mathrm{v,090,T\text{-}lay,k}}$	4.0	
$f_{\mathrm{r,k}}$	–	$f_{\mathrm{v,9090,L\text{-}lay,k}}$	1.1*	0.7**
	–	$f_{\mathrm{v,9090,T\text{-}lay,k}}$	1.1*	0.7**

Table 2.6: Characteristic strength values for C24 timber and CLT panels consisting of C24 boards. (Gustafsson, 2019)

∗) Used for CLT panels with edge-glued boards, or where the board thickness is less than 45 mm and the width-to-thickness ratio for the boards is equal to or greater than 4.

∗∗) Used for CLT panels where the boards are not edge-glued and where the width-to-thickness ratio for the boards is less than 4, or where grooves have been cut into the boards.

3
Methodology

In order to investigate the possibilities of introducing air gaps in the cross-layers of CLT panels, a wide variety of modified configurations was designed and small scale test specimens were manufactured and strength tested to analyse the reduction of shear capacity in relation to the material reduction.

The work of the thesis was divided into several phases. Initially, preparatory work was carried out, including the designing of the configurations that were to be investigated and the conditioning of the timber boards that were to be used for the manufacturing of the test specimens. Each board was strength graded and assigned to a specific configuration based on the determined strength properties. The manufacturing of the specimens was then conducted in several steps before the specimens were strength tested in shear using a hydraulic press and analysed with digital image correlation using a high resolution optic system. Furthermore, finite element modelling of each configuration that was manufactured and tested, was performed in order to predict the behaviour of the specimens and to complement the results from the physical strength tests.

3.1 Preparation

For the preparation before the manufacturing and testing of the specimens, the designing of the configurations was conducted for two types of panels and the conditioning of the timber boards was carried out in a climate chamber in the Building Materials Lab at Chalmers University of Technology.

3.1.1 Designing of configurations

A variety of configurations was designed based on the configurations suggested by the main research project, however, a few modifications were made in order to have a large diversity of cases to be able to make nuanced analyses.

3.1.1.1 Three-layer configurations

For the three-layer configurations, the only variation that can occur is in the cross-layer, where the variation occurs in the width of the introduced air gaps. The designing of the three-layer configurations was conducted by investigating different widths of the air gaps, denoted by b_{airgap}, as shown in Figure 3.1.

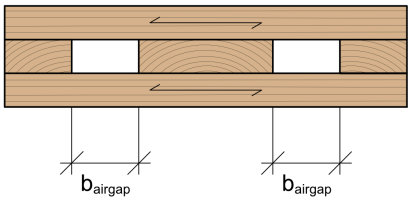

Figure 3.1: Designing of three-layer configurations by varying the width of the air gaps.

3.1.1.2 Five-layer configurations

For the five-layer configurations, there are several more possibilities of variation. The width of the air gaps may vary and the position of the lamellas in the two cross-layers can be aligned or shifted in relation to each other. The designing of the five-layer configurations was conducted by investigating different combinations of air gap widths, denoted by b_{airgap}, and varying positions of the lamellas, as shown in Figure 3.2.

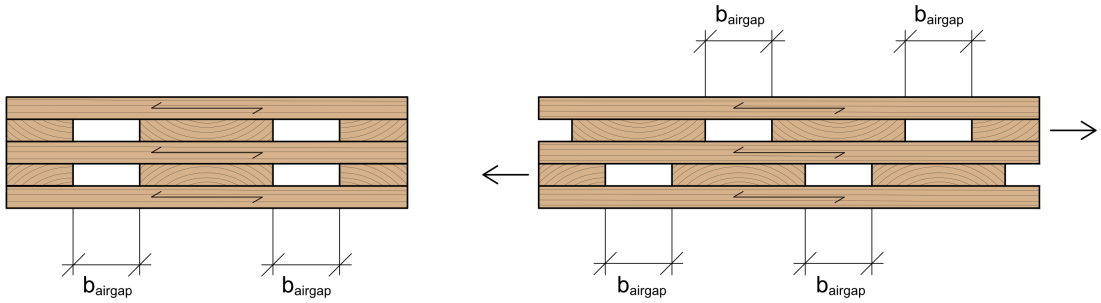

Figure 3.2: Designing of five-layer configurations by varying the width of the air gaps and shifting the position of the lamellas.

3.1.1.3 Naming of specimens

In order to differentiate the specimens during testing, each test specimen was named in accordance with the following system.

$$\text{CLT} - \text{a} - \text{b} - \text{c} - \text{d} - \text{e}$$

where

- a is the number of the configuration in Roman numerals, i.e. I, II, III etc.
- b is the number of layers, i.e. 3 or 5.
- c is the width of the air gaps in mm.
- d is the arrangement of the two cross-layers in relation to each other in the five-layer specimens, i.e. *C* as in centred (the cross-layers are aligned) or

S as in shifted (the cross-layers are shifted symmetrically in relation to each other). For the three-layer specimens, this letter is ignored since there is only one cross-layer.

e is the type of test specimen with regard to strength, i.e. *A* as in average strength, *L* as in low strength, and *H* as in high strength.

As an example, CLT-VII-5-120-C-L is a test specimen of Configuration VII composed of five layers, 120 millimeter air gaps, and centred cross-layers consisting of low strength boards.

3.1.1.4 Determination of geometrical properties

In order to be able to compare the various configurations geometrically, a volume ratio η_V was calculated according to Equation 3.1.

$$\eta_{\mathrm{V}} = \frac{V_{\mathrm{max}}}{V_{\mathrm{wood}}} \ [-] \tag{3.1}$$

where V_{max} is the maximum possible volume of the specimen and V_{wood} is the actual wood volume of the specimen.

The volume ratio η_{V} was then used to calculate a material reduction μ_{M} according to Equation 3.2.

$$\mu_{\mathrm{M}} = \Big(1 - \eta_{\mathrm{V}}\Big) \cdot 100 \ [\%] \tag{3.2}$$

where η_{V} is the volume ratio.

3.1.2 Conditioning of timber

The timber boards were received from the industrial partner of the project, Stora Enso, and placed in a climate chamber directly upon arrival to begin the process of acclimatisation towards reaching moisture equilibrium.

As discussed in Section 2.1.3.2, EN 789 (2004) suggests a moisture content of 12 % in the specimens for all types of strength testing of timber. The boards were therefore stored in a climate chamber with a relative humidity of 60 % and a temperature of 20 °C, which theoretically corresponds to a moisture content slightly lower than 12 %. In total, 60 boards with the average dimensions 2000x129x35 mm and 110 boards with the average dimensions 2000x127x25 mm were received for the project.

After three weeks in the climate chamber, the moisture content in the boards were measured using a moisture meter, as shown in Figure 3.3.



Figure 3.3: Moisture measurement using a moisture meter. (February 16th 2022)

The measurement was repeated six weeks after the initial measurement in order to ensure that the boards had reached moisture equilibrium and the manufacturing process could be initiated.

Since the method of the moisture measurement is destructive to some extent, the moisture content of some specimens was measured directly after the strength testing, instead of beforehand, to validate the moisture equilibrium. The moisture content was measured in the longitudinal layer of the specimens. In the specimens with air gaps, the moisture content was measured both above an air gap and above a cross-layer lamella, see Figure 3.4.

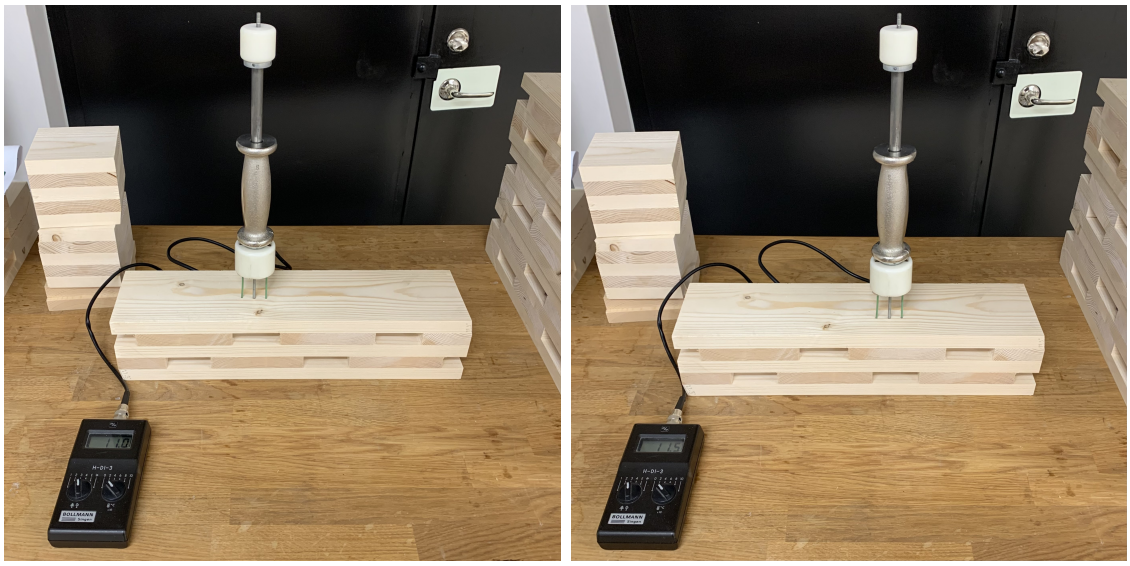

Figure 3.4: Moisture measurement of a specimen with air gaps. (May 6th 2022)

3.2 Strength grading of timber

In order to sort the timber boards with regard to their individual strengths, strength grading was performed in accordance with the method presented in Section 2.2, including visual grading and mechanical grading. The grading was performed for the two types of boards; board type A (with a thickness of 30 mm) and board type B (with a thickness of 20 mm). The boards were only sorted in relation to each other and not according to the standard strength classes C14−C40.

3.2.1 Visual grading

The visual grading of the boards was carried out directly upon arrival since this grading method is not dependent on the moisture content of the boards. The desired thickness for the layers used in the three- and five-layer panels was 30 mm and 20 mm, respectively. Since the thickness of the received boards was in average 35 mm and 25 mm, respectively, there was a tolerance of approximately 5 mm for all boards.

To be able to determine whether the boards would be usable, the visual grading was performed to detect visual defects that would affect the strength of the board noticeably. Among the considered defects were large amount of knots, holes that had originated from dry knots, severe distortion in terms of cupping, bending, twisting, or springing, and large fibre deviations. The boards were sorted into two piles; approved boards and partly usable boards, see Figure 3.5. The boards that were considered to have an excessive degree of distortion to be able to be planed within the tolerance of 3 mm, as well as the boards considered to have excessively large natural defects, were neglected.



Figure 3.5: The sorted boards after visual grading, board type A (30 mm) to the left and board type B (20 mm) to the right. (January 28th 2022)

3.2.2 Mechanical grading

The mechanical grading of the boards was carried out in two steps. Firstly, the density of the boards was calculated, and then, a resonance frequency response test was performed to determine the dynamic modulus of elasticity in the longitudinal direction of each board.

3.2.2.1 Determination of density

In order to calculate the density, all the boards were initially weighed to obtain their mass m using a scale, as shown in Figure 3.6.



Figure 3.6: Weighing of a board. (February 8th 2022)

The width b and thickness t of all boards were measured using a calliper. The length L of a few boards were measured, and it was evident that the length only varied a few millimeters at most, i.e. a magnitude of about 1/1000 of the length. Therefore, it was concluded to be negligible and the length was estimated to be 2000 mm for all boards. The density ρ was calculated according to Equation 3.3.

$$\rho = \frac{m}{V} \left[\frac{\text{kg}}{\text{m}^3}\right] \tag{3.3}$$

where V is the volume of the board in m^3, calculated according to Equation 3.4.

$$V = L \cdot b \cdot t \ [\text{m}^3] \tag{3.4}$$

where L is the length, b is the width, and t is the thickness of the board in m.

3.2.2.2 Determination of dynamic modulus of elasticity

For determining the dynamic modulus of elasticity in the longitudinal direction, the boards were placed on two small pieces of cork. A microphone was placed at one end of the board recording the frequency meanwhile a hardwood hammer was used to hit the other end of the board, and the first resonance frequency was measured using the software FFT analyser, see Figure 3.7.

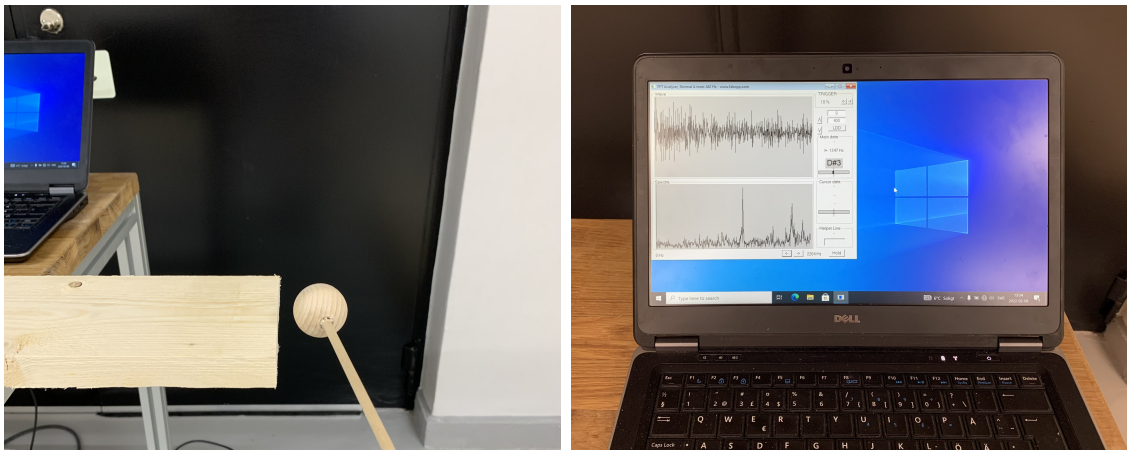

Figure 3.7: Frequency measurement using FFT analyser. (February 8th 2022)

The frequency f was determined according to the method presented in Section 2.2.2.2 and the dynamic modulus of elasticity in the longitudinal direction was calculated according to Equation 3.5.

$$MOE_{\text{dyn,long}} = 4\rho L^2 f^2 \text{ [Pa]} \tag{3.5}$$

where ρ is the density of the material in kg/m^3, L is the length of the board in m, and f is the measured resonance frequency in Hz.

3.3 Assigning of boards to configurations

For each configuration, three specimens were to be produced; one specimen of average strength, one specimen of low strength, and one specimen of high strength. For the specimens of low and high strength, the longitudinal layers were composed of boards of average strength, while the cross-layers were composed of boards of low and high strength, respectively, in relation to the average strength of the longitudinal layers. For the specimens of average strength, both the longitudinal layers and the cross-layers were composed of boards of average strength. The boards were selected based on both the density and the MOE. However, the density was regarded to be a more reliable indication of the board strength in comparison to the MOE and it was therefore concluded to be of more importance when assigning boards to the different specimens.

3.3.1 Average strength

For the average strength specimens and the longitudinal layers, the boards were selected to be around the average values for all the boards. Moreover, since there were several more configurations possible for the five-layer panels than the three-layer panels, a larger portion of boards of type B were needed to be used. The boards that were used for specimens within the same configuration were selected to have a similar strength in terms of both density and MOE, meanwhile the strength was allowed to vary between the different configurations due to the large amount of boards required to cover the need in production.

3.3.2 Low strength

The low strength boards of each configuration were assigned based on the average strength of the configuration. The average strength was calculated as the average of all the boards used for both the average strength specimen and for the longitudinal layers of the low and high strength specimens.

For the low strength specimens, the boards were selected to have a density and an MOE in the range between 10 to 20 % below the average strength.

3.3.3 High strength

The high strength boards of each configuration were assigned based on the average strength of the configuration. The average strength was calculated as the average of all the boards used for both the average strength specimen and for the longitudinal layers of the low and high strength specimens.

For the high strength specimens, the boards were selected to have a density and MOE in the range between 10 to 20 % above the average strength.

3.4 Manufacturing of specimens

The manufacturing of the specimens was carried out in the Architecture workshop at Chalmers University of Technology. The work was divided into several smaller batches to make the process more practicable and to minimise the risk of excessive drying of the wood during the manufacturing. Whenever the specimens were not being processed, they were stored in the climate chamber to ensure that the moisture content was kept at equilibrium. Furthermore, before the manufacturing process was initiated, two test specimens were produced to validate and improve the method.

3.4.1 Manufacturing method

The manufacturing method consisted of several steps. First, all the boards were sawn into shorter lengths in a circular saw. Then, the boards were planed in two different planing machines to obtain the desired widths and thicknesses before they were sawn to the desired lengths. The pieces were then assembled by applying adhesive between each layer before letting the adhesive harden in a vacuum press. Finally, the assembled specimens were refined in the circular saw.

3.4.1.1 Sawing and planing

Initially, all boards were cut in half in a circular saw in order to to make them more manageable and to prevent unnecessary material waste during the planing process. The boards were originally around two meters long and due to distortion being more noticeable in longer boards, it was necessary to shorten them before planing to limit the material waste, since the margins for planing of the boards into the desired dimensions were very limited. From the beginning, the average dimensions of the boards of type A were 129x35 mm and the average dimensions of the boards of type B were 127x25 mm, while after planing, the desired dimensions were 120x30 and 120x20, respectively. The circular saw that was used is shown in Figure 3.8.



Figure 3.8: The circular saw used to saw all the specimens. (March 28th 2022)

After the sawing, the boards were planed in the first planer that was used to obtain a right angle and where the thickness was reduced with 0.5 mm each round, see Figure 3.9.



Figure 3.9: The planing machine used to obtain a right angle of the boards. (March 28th 2022)

First, the boards were planed along their widths several times until they were flat, but leaving as much of a tolerance as possible for the rest of the planing procedure. The boards were then planed along one of the longitudinal edges to obtain a right angle between the edge and the plane side, as shown in Figure 3.10.

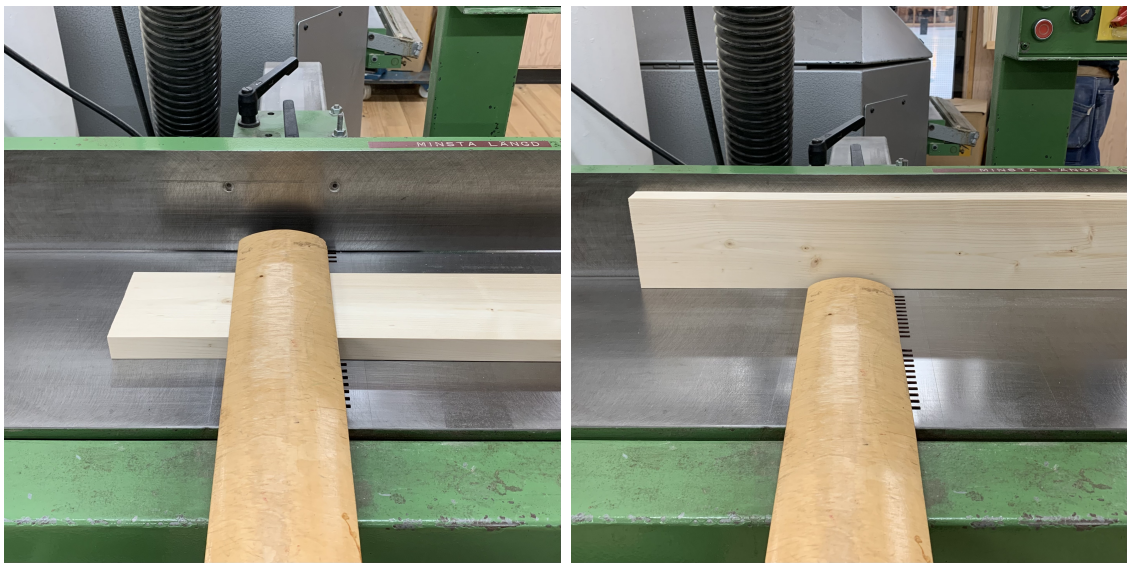

Figure 3.10: The planing along the width and of the longitudinal edge. (March 28th 2022)

In order to obtain parallel sides and edges, the boards were planed in the second planer until reaching the desired thicknesses and widths. Firstly, all boards were placed on the flat side and planed to their desired thickness. For the boards of type A, the final thickness was set to 30 mm and for the boards of type B, the final thickness was set to 20 mm. The boards were then placed on the flat edge and planed to a width of 120 mm. All boards that were intended to be used within the same configurations were planed in the same batch to minimise the risk of deviations in size that may cause issues during the gluing procedure. The planing machine that was used is shown in Figure 3.11.



Figure 3.11: The parallel planing machine used to obtain parallel sides and edges of the boards. (March 28th 2022)

The planed boards were then sawn in the circular saw to obtain all the parts needed to construct the various specimens. All the longitudinal parts were sawn to the desired dimensions according to the corresponding configuration with an additional length of 20 mm on each end. Furthermore, all edge parts of the cross-layers were sawn to the desired dimensions with an additional width of 20 mm on one side. The additional dimensions were added in order to be able to refine the final specimens to their desired dimensions without the risk of sawing them shorter than intended. One finished batch of planed and sawn parts before assembling is shown in Figure 3.12.



Figure 3.12: A batch of planed and sawn parts before assembling. (March 29th 2022)

3.4.1.2 Application of adhesive

For the assembly of the specimens, the adhesive that was used was Cascol Indoor wood adhesive and it was applied using an applicator, see Figure 3.13. Cascol Indoor wood adhesive is a fast drying, PVAC-based glue with an open time of around five minutes and a pressing time of around ten minutes (Casco®, 2019). This required the assembly process to be quick and effective to avoid hardening of the adhesive before the specimens were placed in the vacuum press.



Figure 3.13: The adhesive and the adhesive applicator. (March 30th 2022)

For the specimens with boards of type A, with a thickness of 30 mm, the adhesive was applied with the notched edge of the applicator to obtain an even distribution of adhesive. For the solid configurations without air gaps, the adhesive was applied on the longitudinal layers and the cross-layers were placed accordingly, see Figure 3.14.

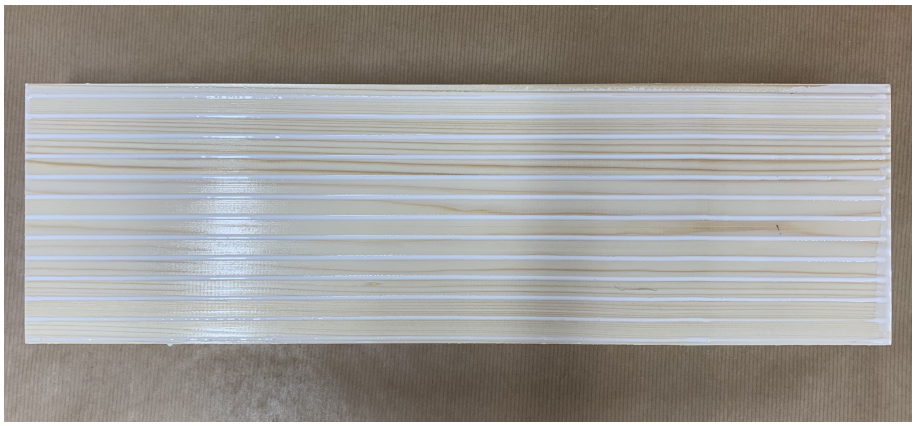

Figure 3.14: Application of adhesive on the longitudinal layers for a specimen constructed of boards of type A. (March 29th 2022)

For the configurations with air gaps, the adhesive was applied on the cross-layers, which were then placed on the longitudinal layers, in order to avoid excessive adhesive in the air gaps, see Figure 3.15.

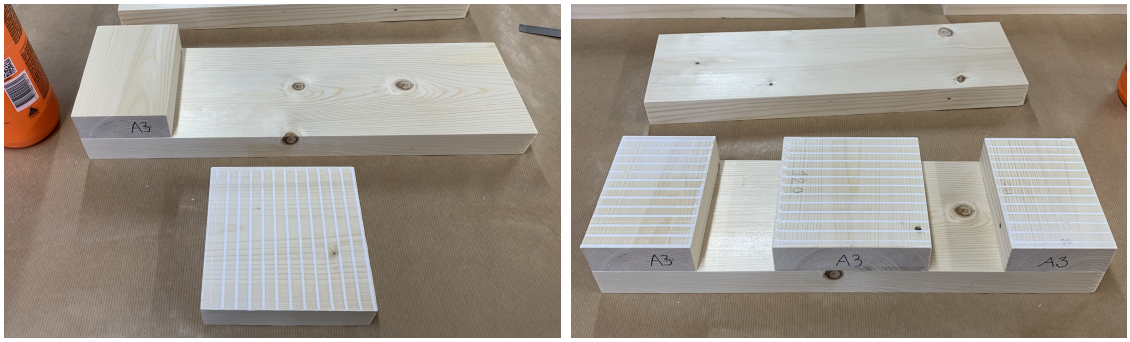

Figure 3.15: Application of adhesive on the cross-layers for a specimen constructed of boards of type A. (March 30th 2022)

As previously mentioned, the manufacturing of the different configurations was divided between several batches, of which the first batch consisted of all the three-layer configurations. This batch was both manufactured and tested before any five-layer configurations were produced and based on the test results from the first batch, the manufacturing process was altered prior to the production of the remaining batches. The alterations were made with regard to the application of the adhesive, as well as the procedure of pressing, and the reason for the alterations is further discussed in Section 5.1.2.

For the specimens with boards of type B, with a thickness of 20 mm, the adhesive was applied with the flat edge of the applicator to obtain an even layer of adhesive, as shown in Figure 3.16.

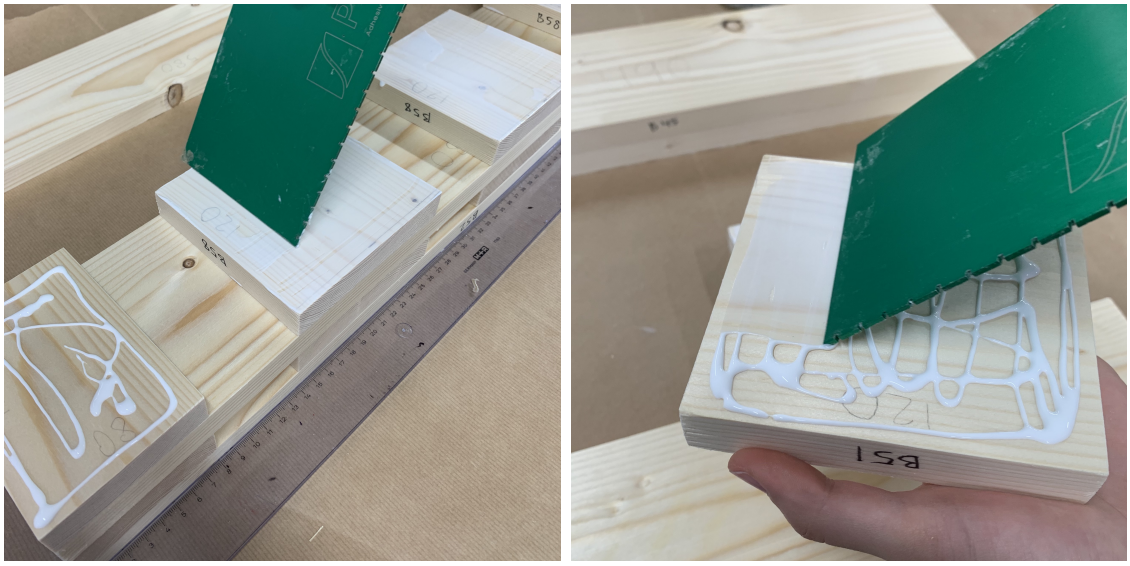

Figure 3.16: Application of adhesive on a specimen constructed of boards of type B. (April 12th 2022)

For the solid specimens, both with boards of type A and of type B, no edge-bonding was implemented, i.e. the adhesive was only applied on the surfaces between each layer and not on the surfaces between the lamellas in the cross-layers.

3.4.1.3 Vacuum pressing

After the assembly, the specimens were placed in a vacuum press and pressed until the glue had hardened. The vacuum press that was used had a pressing power of approximately 0.09 N/mm^2, see Figure 3.17.



Figure 3.17: The vacuum press. (April 11th 2022)

For the first batch of specimens, constructed of board type A with a thickness of 30 mm, all three specimens of each configuration were glued, assembled, and placed in the vacuum press at the same time. However, as mentioned in Section 3.4.1.2, the procedure was altered for the remaining batches of specimens. For the specimens of board type B, with a thickness of 20 mm, only one specimen was glued, assembled, and placed in the vacuum press at a time in order to minimise the risk of the glue hardening before it was subjected to pressure. All the specimens were placed in the vacuum press for a total of 40 minutes each.

3.4.1.4 Finalisation

In the final step of production, the pressed and hardened specimens were sawn in the circular saw to refine the edges and to obtain the desired dimensions. All specimens were sawn to a width of 110 mm. The specimens were then sawn on the opposite edges of the outer lamellas to an inclination that would correspond to a vertical axis between the opposite corners. This was done in order to be able to attach the specimens in the hydraulic press used for testing, as described further in Section 3.5.2.2.

For the three-layer specimens, constructed of board type A, the angle α was approximated according to Figure 3.18 and calculated according to Equation 3.6.

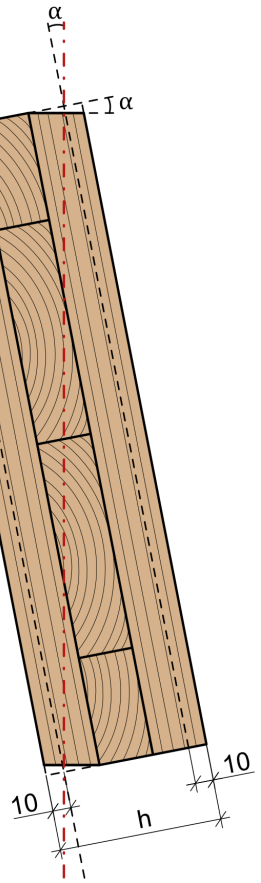

Figure 3.18: Illustration of a finished three-layer specimen with sawn edges.

$$\alpha = \arctan\left(\frac{h - 2 \cdot 10\,\text{mm}}{L}\right) \tag{3.6}$$

where h is the total thickness and L is the total length of the specimen in mm. The thickness was reduced with 10 mm on each side in order to better approximate the resulting vertical axis of the specimen, rather than calculating the angle based on an axis drawn between the original corners.

For the five-layer specimens, constructed of board type B, the angle β was approximated according to Figure 3.19 and calculated according to Equation 3.7.

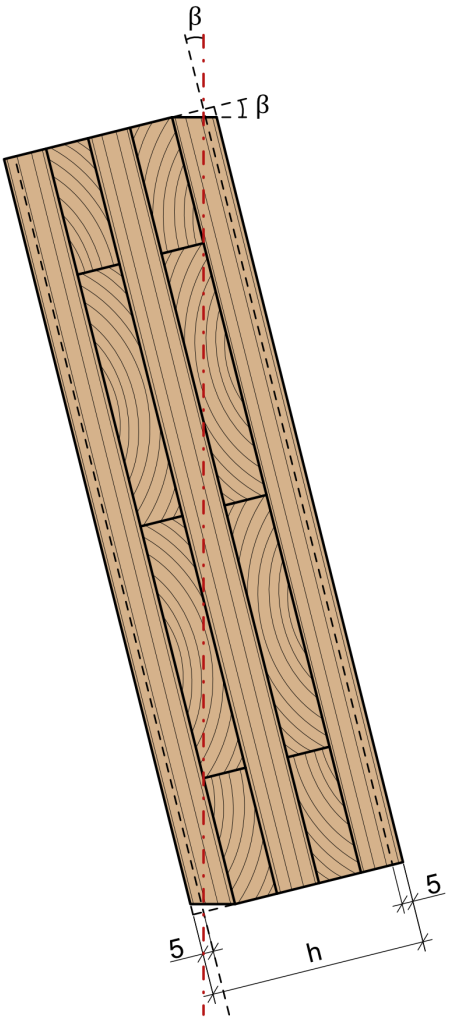

Figure 3.19: Illustration of a finished five-layer specimen with sawn edges.

$$\beta = \arctan\left(\frac{h - 2 \cdot 5\,\text{mm}}{L}\right) \tag{3.7}$$

where h is the total thickness and L is the total length of the specimen in mm. The thickness was reduced with 5 mm on each side in order to better approximate the resulting vertical axis of the specimen, rather than calculating the angle based on an axis drawn between the original corners.

3.4.2 Test manufacturing

Initially, a test manufacturing was performed in order to obtain a rough time estimation of all the steps in the manufacturing and to refine the manufacturing method. Two test specimens were produced; a five-layer solid specimen and a five-layer specimen with 120 mm aligned air gaps.

3.4.2.1 Solid test specimen

For the solid test specimen, all boards were planed to a thickness t of 20 mm and a width b of 120 mm. For the longitudinal layers, the boards were sawn to a length L of 600 mm and for the cross-layers, the boards were sawn to a length L of 120 mm. The layers were then assembled by applying adhesive, according to the method described in Section 3.4.1.2. After the assembling, the specimen was placed in the vacuum press for 80 minutes, see Figure 3.20.



Figure 3.20: Vacuum pressing of solid test specimen. (March 18th 2022)

3.4.2.2 Test specimen with air gaps

For the test specimen with air gaps, the same procedure was utilised as described in Section 3.4.2.1 with the difference that the boards in the cross-layers were placed with a distance of 120 mm when assembling, as shown in Figure 3.21.



Figure 3.21: Manufacturing of test specimen with air gaps. (March 21th 2022)

After assembling, the specimen was placed in the vacuum press for 80 minutes, see Figure 3.22.

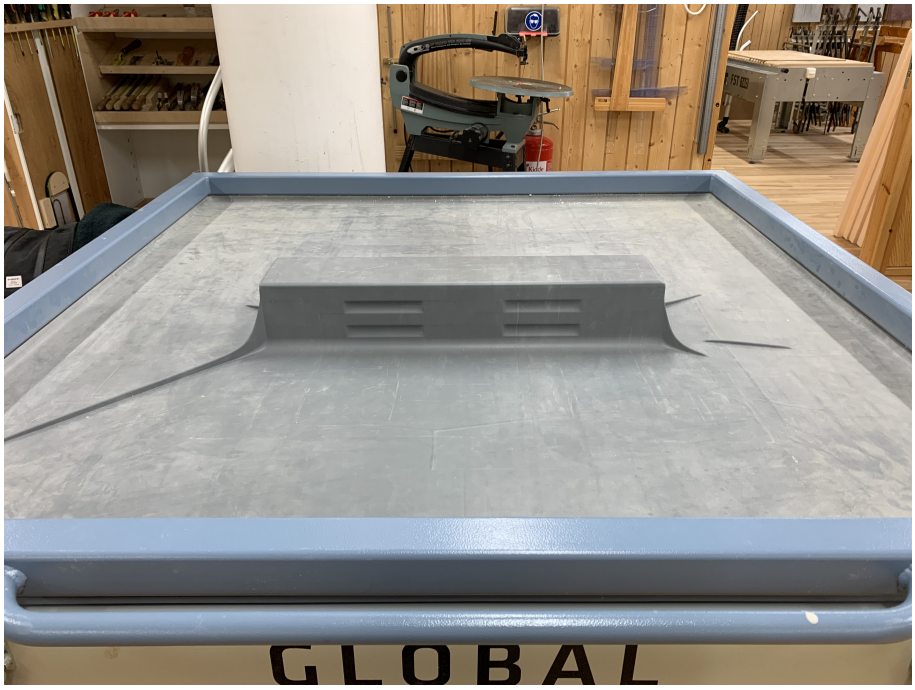

Figure 3.22: Vacuum pressing of test specimen with air gaps. (March 21th 2022)

3.4.3 Preparation of specimens

In order to utilise the optical system ARAMIS, one side of each specimen was painted with white and black paint in order to achieve a high contrast surface. Further information about the ARAMIS system is presented in Section 3.5.1.3.

Firstly, the specimens were spray coated with a thin layer of white paint on one side, as shown in Figure 3.23.



Figure 3.23: Spray painting of the specimens. (March 30th 2022)

Thereafter, black paint was dabbed on the specimens in order to establish a satisfactory pattern. The aim was to achieve a high contrast pattern consisting of small black dots, preferably no larger than 1 mm in diameter, and approximately 50 % white colour and 50 % black colour. The black paint was applied using small pieces of acrylic doormat, see Figure 3.24.



Figure 3.24: Dabbing of black paint on the specimens. (March 30th 2022)

3.5 Testing of specimens

The testing of the specimens was carried out in the Structures Lab at Chalmers University of Technology using a hydraulic press and the procedure was monitored using the high resolution optical system ARAMIS. The testing was conducted in two sessions, where the first session concluded the testing of all the three-layer configurations and the second session concluded the testing of all the five-layer configurations. Before the testing was initiated, two test specimens were subjected to a trial test round to validate the test method and to ensure that the test equipment operated as desired. Whenever the specimens were not being tested, they were stored in the climate chamber to ensure that the moisture content was kept at equilibrium.

3.5.1 Test equipment

The testing of the specimens was carried out using a hydraulic press and the test procedure was monitored with the utilisation of the high resolution optical system ARAMIS. Furthermore, to attach the specimens to the hydraulic press, two fixtures were manufactured; one for specimens constructed of board type A and one for specimens constructed of board type B.

3.5.1.1 Hydraulic press

The hydraulic press that was used to perform the strength tests of the specimens is shown in Figure 3.25 with a maximum force capacity of 250 kN.



Figure 3.25: The hydraulic press used for the strength tests of the specimens. (May 5th 2022)

3.5.1.2 Fixtures

Two fixtures were produced in order to be able to attach the specimens to the hydraulic press. The fixtures were composed of one solid part that was fastened into the press and one interchangeable plate that acted as the support for the specimens. Furthermore, two different pressure plates were produced to correspond to the dimensions of the pressure area of the specimens, i.e. a length of 120 mm, and two different widths; one width of 30 mm for the specimens constructed of board type A and one width of 20 mm for the specimens constructed of board type B. The pressure plates were produced to be slightly longer than the width of the specimens in order to ensure that the whole pressure area of the specimen was in contact with the load. For the fixtures and the pressure plates, see Figure 3.26.



Figure 3.26: Fixtures and pressure plates. (May 5th 2022)

3.5.1.3 ARAMIS optical system

Digital image correlation was implemented by using the high resolution optical system ARAMIS in order to monitor the changes in strain in the surfaces of the specimens, utilising the high contrast patterns of the specimen surfaces. The system was set to take one image per second, i.e. a frequency of 1 Hz, when the loading procedure was initiated. The ARAMIS system is shown in Figure 3.27.



Figure 3.27: The ARAMIS optical system used for digital image correlation. (May 5th 2022)

The software GOM Correlate Professional was used to establish a reference image of the test specimen in the hydraulic press and the surface with the high contrast pattern was selected to be analysed with regard to major strain. The analysis using the digital image correlation was initiated once the loading of the specimen in the hydraulic press began.

3.5.2 Shear strength test

For each specimen, a strength test was performed according to the method presented in Section 2.5.2.

3.5.2.1 Loading rate

As described in Section 2.5.2, the maximum load should be reached within 300 ± 120 seconds and the loading rate was adjusted for each specimen in order to meet this requirement. The loading rate is defined as the deformation in mm per minute.

For the testing of the three-layer configurations, a loading rate of 0.8 mm per minute was used for the first two specimens, i.e. the average and low strength specimen of Configuration I. However, since the loading time ended up being less than 300 ± 120 seconds, the loading rate was decreased to a deformation of 0.5 mm per minute for the remaining specimens.

For the testing of the five-layer configurations, the loading rate was adjusted for all the configurations and there was a minor variation in the time required to reach the maximum load depending on the different designs of the specimens. For the loading time and loading rate for each specimen, see Sections 4.5.3 to 4.5.11.

3.5.2.2 Test method

For each test procedure, the test specimen was attached to the hydraulic press by placing it on the bottom pressure plate and aligning the outer edge of the bottom pressure area with one edge of the pressure plate. The cylinder was then lowered and one edge of the top pressure plate was aligned with the outer edge of the upper pressure area of the specimen. For the alignment of the specimen on the pressure plates, see Figure 3.28.

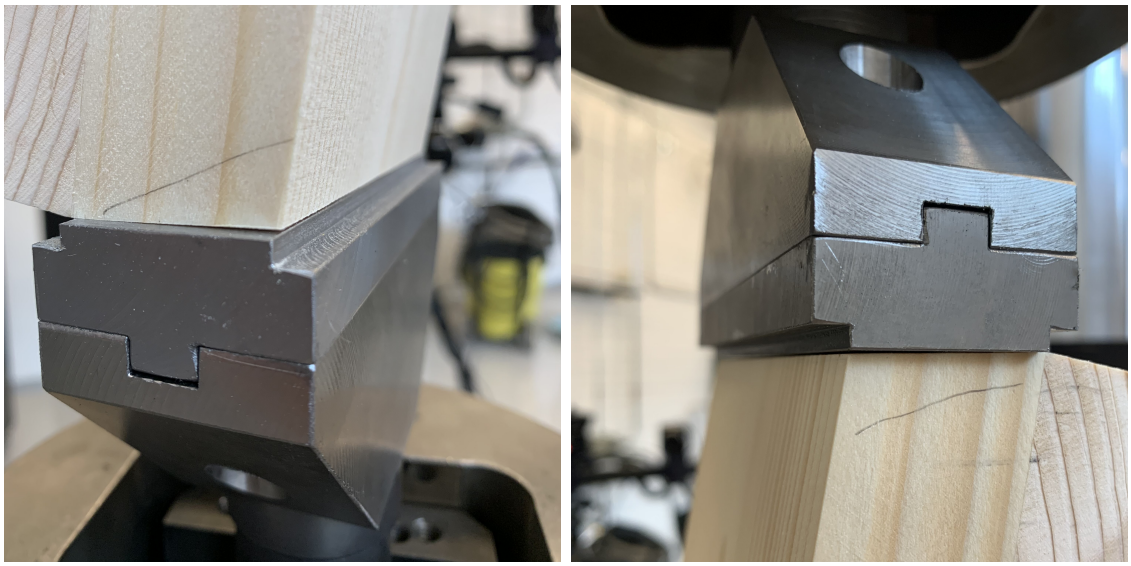

Figure 3.28: Aligning of a specimen on the pressure plates in the hydraulic press. (April 6th 2022)

After the attachment of the test specimen, the ARAMIS optical system was prepared in accordance with the method presented in Section 3.5.1.3 and the loading was initiated and operating until failure was reached. The test setup is shown in Figure 3.29.

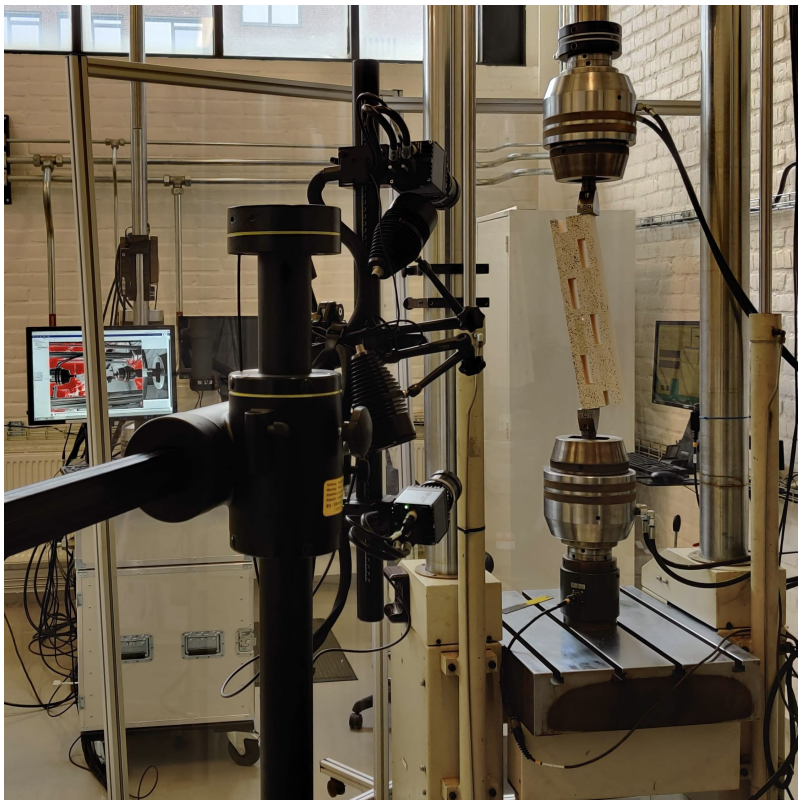

Figure 3.29: The setup of the strength testing of the specimens. (May 6th 2022)

3.5.3 Trial test round

A trial test round was performed on the two test specimens and the test method was refined based on the results.

3.5.3.1 Solid test specimen

The first test was performed with the solid test specimen with a loading rate based on a deformation of 0.5 mm per minute. For the attachment of the specimen in the hydraulic press, see Figure 3.30.



Figure 3.30: First test of the solid test specimen. (March 21th 2022)

After the initial test, the solid test specimen was shortened from a width of five cross-layers to a width of three cross-layers for a second test with twice the loading rate, i.e. a deformation of 1 mm per minute. The attachment of the specimen in the hydraulic press is shown in Figure 3.31.



Figure 3.31: Second test of the solid test specimen. (March 28th 2022)

3.5.3.2 Test specimen with air gaps

The test specimen with air gaps was tested with a loading rate of 1 mm per minute. For the attachment of the specimen in the hydraulic press, see Figure 3.32.



Figure 3.32: Test of the test specimen with air gaps. (March 28th 2022)

3.5.4 Analysing of results

The results from the tests of the specimens were used to determine the shear strength of each specimen. In order to compare the failure loads of the different specimens, the failure loads were reduced with regard to the specimen lengths. Furthermore, a failure load ratio was introduced and compared to the material reduction of the configuration.

3.5.4.1 Shear strength

The failure load obtained from each test of a specimen was used to calculate the shear strength based on the observed failure mode. The different failure modes that were accounted for were; panel shear failure, i.e. failure in the longitudinal layers, bondline failure, i.e. failure in the interface between the longitudinal layers and the cross-layer lamellas, and rolling shear failure, i.e. failure in the cross-layer lamellas. The shear strength was calculated by modifying Equations 2.11 and 2.13 in Section 2.5.3 in order to adapt them for the determination of shear strength in CLT panels and to include the specimens with air gaps.

For the specimens that failed in the longitudinal layer, the panel shear strength was calculated according to Equation 3.8.

$$f_{\mathrm{v}} = \frac{F_{\max}}{L \cdot b} \ [\mathrm{Pa}] \tag{3.8}$$

where $F_{\max}$ is the failure load in N, L is the length of the specimen in m, and b is the width of the specimen in m.

For the specimens that failed in the bondline, the bondline shear strength was calculated according to Equation 3.9.

$$f_{\mathrm{b}} = \frac{F_{\max}}{L_{\mathrm{c}} \cdot b} \ [\mathrm{Pa}] \tag{3.9}$$

where $F_{\max}$ is the failure load in N, L_{c} is the length of the cross-layer interface (i.e. the length of the bondlines) in m, and b is the width of the specimen in m.

For the specimens that failed in the cross-layers, the rolling shear strength was calculated according to Equation 3.10.

$$f_{\mathrm{r}} = \frac{F_{\max}}{L_{\mathrm{c}} \cdot b} \ [\mathrm{Pa}] \tag{3.10}$$

where $F_{\max}$ is the failure load in N, L_{c} is the length of the cross-layer interface in m, and b is the width of the specimen in m.

3.5.4.2 Failure load ratio

Since the lengths of the specimens vary, and the failure load is dependent on the length, the failure load of each specimen was adjusted with regard to a length ratio. The length ratio η_{L} was calculated between the length of each configuration and a reference length, according to Equation 3.11.

$$\eta_{\mathrm{L}} = \frac{L}{L_{\mathrm{ref}}} \ [-] \tag{3.11}$$

where L is the length of the configuration in question and L_{ref} is the reference length.

The adjusted failure loads were then calculated according to Equation 3.12.

$$F_{\mathrm{adjusted}} = \frac{F_{\mathrm{max}}}{\eta_{\mathrm{L}}} \ [N] \tag{3.12}$$

where F_{max} is the failure load in N and η_{L} is the length ratio for the configuration in question.

A failure load ratio was determined for each specimen by comparing the adjusted failure loads with a reference failure load. The failure load ratio η_{F} was calculated according to Equation 3.13.

$$\eta_{\mathrm{F}} = \frac{F_{\mathrm{adjusted}}}{F_{\mathrm{ref}}} \ [-] \tag{3.13}$$

where F_{adjusted} is the adjusted failure load of the specimen in question and F_{ref} is the reference failure load.

The failure load ratio was then used to compare the test results of the specimens with regard to the material reduction and the air gap layout of each configuration.

3.6 Finite element modelling in Abaqus

Each configuration that was manufactured and tested was modelled in Abaqus in order to predict the behaviour under shear loading and to complement the results from the physical strength tests. The configurations were modelled with average material properties and analysed using static analysis. No in-depth analysis was performed regarding the modelling.

3.6.1 Modelling of elements

Each element was modelled as a 3D deformable solid extrusion, where the thickness represents the width of the specimen. The longitudinal layers at the top and the bottom were modelled with inclined edges, as shown in Figure 3.33, to represent the inclined edges of the physical specimens, as presented in Section 3.4.1.4.

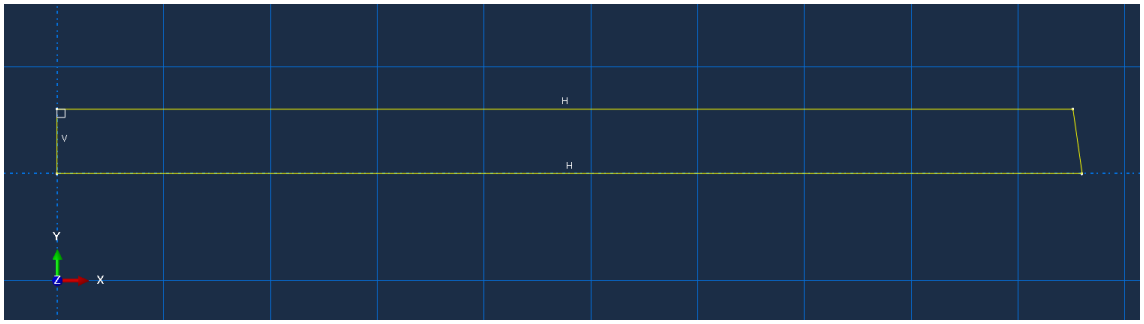

Figure 3.33: Geometry of a configuration with an inclined edge, from which the solid extrusion was made in Abaqus.

For the cross-layers, two types of elements were modelled; one with a width of 120 mm for the centre lamellas and one with a width of 60 mm for the edge lamellas.

3.6.2 Material properties

The material was modelled as an elastic orthotropic material. The material properties were determined using Table 2.5 in Section 2.6.1.1 and the average value of each property was used, see Table 3.1.

Property	ρ	$\mathbf{E_L}$	$\mathbf{E_R}$	$\mathbf{E_T}$	$\nu_{\mathbf{LR}}$	$\nu_{\mathbf{LT}}$	$\nu_{\mathbf{RT}}$	$\nu_{\mathbf{RL}}$	$\nu_{\mathbf{TL}}$	$\nu_{\mathbf{TR}}$	$\mathbf{G_{LR}}$	$\mathbf{G_{LT}}$	$\mathbf{G_{RT}}$
Value	434	13804	731	481	0.40	0.50	0.51	0.03	0.02	0.30	581	720	31

Table 3.1: The properties used for the defining of the orthotropic material for all the configurations in Abaqus.

The input values for the orthotropic elastic stiffness matrix **D** were calculated according to the equations presented in Section 2.6.1.2. The same material properties were used for all the configurations. The material was assigned to each part by creating a solid homogeneous section.

The material orientation for the longitudinal layers was assigned to coincide with the global coordinate system, whereas for the cross-layers, which are arranged perpendicular to the longitudinal layers, a local coordinate system was created and assigned for all the parts, as shown in Figure 3.34.

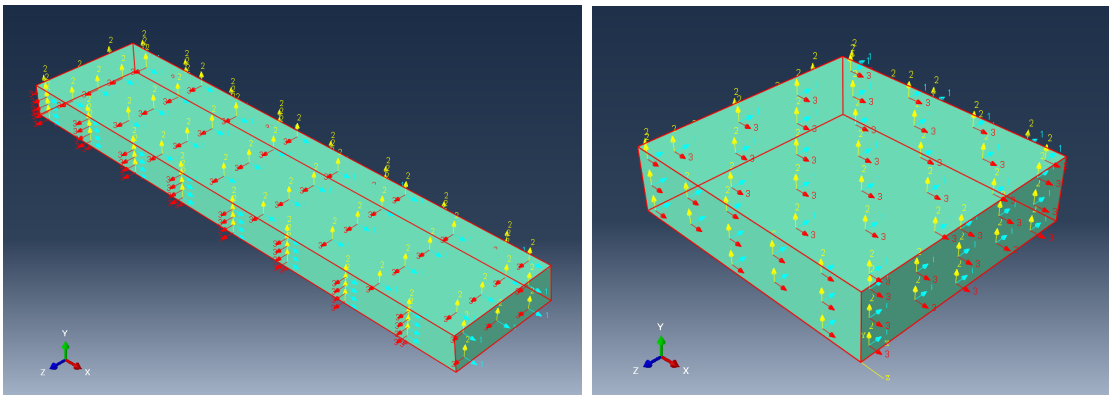

Figure 3.34: Material orientation of the longitudinal layers vs the cross-layers in Abaqus.

3.6.3 Interaction

The interaction between the parts of the cross-layers and the longitudinal layers was determined to be tie constraints. The constraints were applied on the interfacing surfaces of the different layers and the inner layers, i.e. the cross-layers, were chosen to be governed by the outer layers, i.e. the longitudinal layers. No interaction was set between the individual parts of the cross-layer, to simulate the physical test specimens, which were assembled without edge-bonding. Furthermore, no rotational degrees of freedom were tied.

3.6.4 Load and boundary conditions

The load type and boundary conditions were chosen in order to best correspond to the physical shear tests of the configurations. To be able to compare the results of the different FE models numerically, a scale factor was introduced for the application of the load.

3.6.4.1 Boundary conditions

The models were determined to be constrained in translation and the boundary conditions were applied on the outermost edges of the inclined surfaces, see Figure 3.35. The left edge of the lowermost longitudinal layer was fixed in all three axial directions, whereas the right edge of the uppermost longitudinal layer was fixed in only y- and z-direction. The boundaries were free to rotate around all three axes and the same boundary conditions were applied on all configurations.

3.6.4.2 Load application

The load was applied as a uniform pressure with a magnitude of 1 times the load scale factor, denoted by LSF, see Section 3.6.4.3. It was uniformly distributed on the inclined surfaces of the outer longitudinal layers, as shown in Figure 3.35.

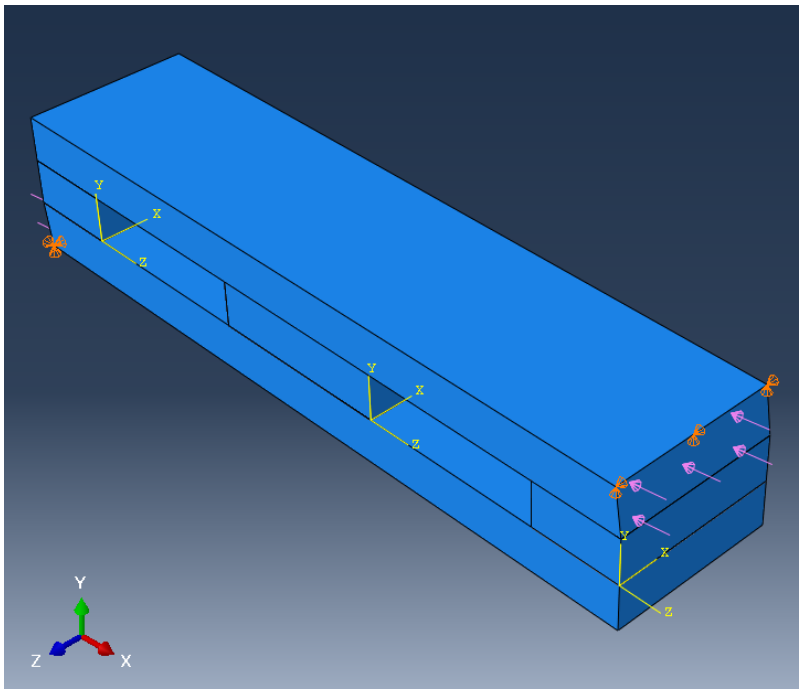

Figure 3.35: Load application and boundary conditions of a configuration in Abaqus.

3.6.4.3 Load scale factor

To be able to compare the results of the different FE models numerically, a scale factor was introduced for the application of the load to establish a linear relationship between the length of the configuration and the assumed strength. Since the area of the inclined surface, on which the load is applied, varies between the different configurations, a ratio was calculated between the pressure area of each configuration and a reference pressure area. The pressure area ratio η_{A} was calculated according to Equation 3.14.

$$\eta_{\mathrm{A}} = \frac{A_{\mathrm{p}}}{A_{\mathrm{p,ref}}} \ [-] \tag{3.14}$$

where A_{p} is the pressure area of the configuration in question and $A_{\mathrm{p,ref}}$ is the reference pressure area.

To calculate the load scale factor, the pressure area ratio η_A and the length ratio η_L, according to Equation 3.11 in Section 3.5.4.2, were combined into one factor, denoted by LSF. The load scale factor LSF was calculated according to Equation 3.15.

$$LSF = \eta_A \cdot \eta_L \ [-] \tag{3.15}$$

where η_A is the pressure area ratio and η_L is the length ratio.

3.6.5 Mesh

For the meshing of the models, a standard mesh configuration was chosen, resulting in hex-shaped mesh elements. The size of the elements was set to 5 mm for all configurations, which resulted in six mesh elements per lamella thickness of the three-layer configurations and four mesh elements per lamella thickness of the five-layer configurations. No convergence study of the mesh size was conducted. For the mesh of a configuration, see Figure 3.36.

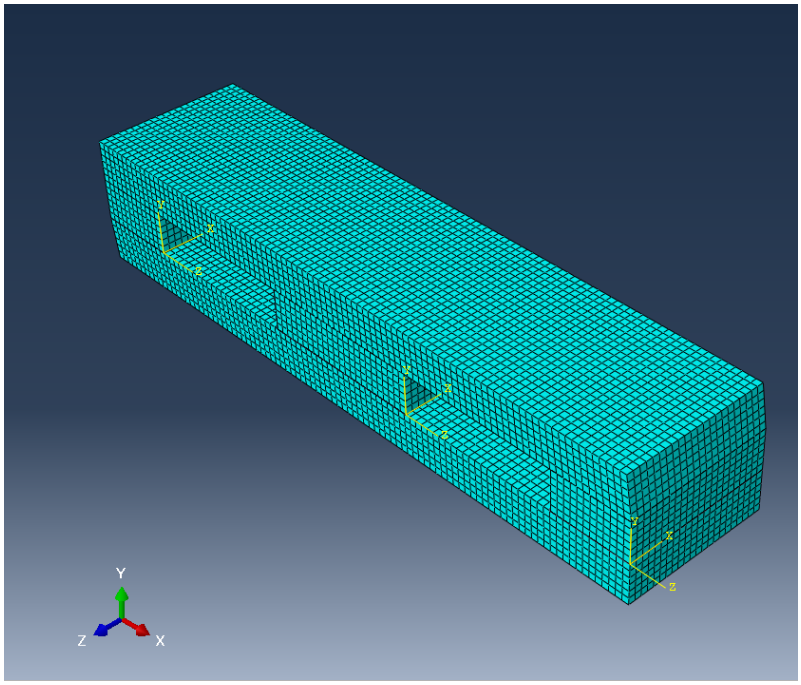

Figure 3.36: Mesh of a configuration in Abaqus.

3.6.6 Obtaining of results

The results of the finite element analysis were processed in several steps to obtain the desired information. Paths were created for the extraction of data and were used to plot the stress distributions, as well as to calculate the utilisation ratios of the interaction between shear stresses and stresses perpendicular to the grain. Furthermore, plots of the stress distributions were extracted from Abaqus.

3.6.6.1 Creation of paths

To be able to obtain the desired information from the finite element analysis, several paths were created for the extraction of data. Since the stress distribution is close to symmetrical around the centre line of the middle longitudinal layer, only the upper half of each configuration was analysed.

For the three-layer configurations, four paths were created; one in the centre of the upper longitudinal layer, one close to the lower edge of the upper longitudinal layer, one close to the upper edge of the cross-layer, and one in the centre of the cross-layer, see Figure 3.37.

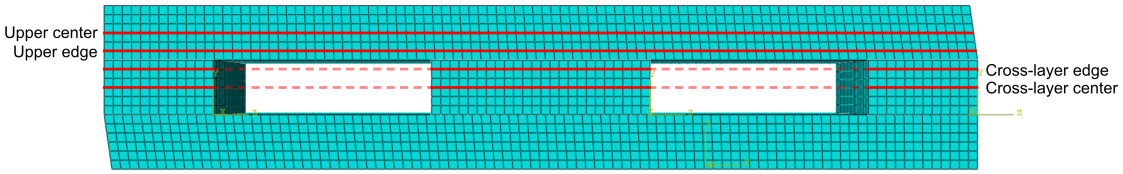

Figure 3.37: Analysed paths for a three-layer configuration in Abaqus.

For the five-layer configurations, seven paths were created; one in the centre of the upper longitudinal layer, one close to the lower edge of the upper longitudinal layer, one close to the upper edge of the cross-layer, one in the centre of the cross-layer, one close to the lower edge of the cross-layer, one close to the upper edge of the middle longitudinal layer, and one in the centre of the middle longitudinal layer, see Figure 3.37.

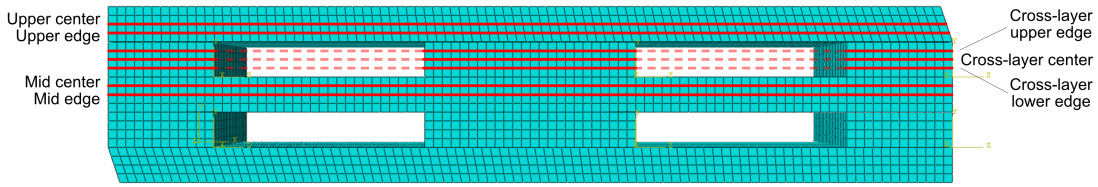

Figure 3.38: Analysed paths for a five-layer configuration in Abaqus.

To analyse the behaviour of the edges of the various layers, the paths close to the edges were analysed instead of the paths on the actual edges. This was done since no difference was observed in the results whether the edge path was created in the longitudinal lamella or in the cross-layer lamella, meaning that it was not possible to differentiate the behaviour in the edges unless the paths were separated.

3.6.6.2 Extraction of data and plotting of results

For each path, the stress distributions in the LR- and RT-plane, as well as in the R-direction, were extracted. The numerical data was then used to plot various graphs in Matlab, illustrating the stress distribution along the paths. Furthermore, the same stress distributions were also plotted and extracted directly in Abaqus.

3.6.6.3 Calculation of utilisation ratios

To calculate the resulting stresses in every path of each configuration, the interaction between the shear stresses and stresses perpendicular to the grain was obtained using Equation 2.29, see Section 2.6.2. The utilisation ratio for each path was then plotted for each configuration in Matlab.

4
Results

The results from the testing of the specimens are presented using the recommended test report details in accordance with EN 408 (2010). The result of the conditioning of the timber, including the moisture content of the test specimens directly after testing, is presented. The strength grading, i.e. the determination of density and longitudinal dynamic modulus of elasticity, for all the boards are also presented. Furthermore, the distribution of the boards, in terms of strength, that were used for the manufacturing of the test specimens and a description of all the configurations that were designed are presented. Lastly, the results from the strength testing of all the specimens, including the test data that was obtained as well as the calculations of the shear strength based on the test data, are presented, together with the FE analysis of the configurations.

4.1 Conditioning of timber

The conditioning of the timber in the climate chamber was concluded after three separate measurements of the moisture content in board type A and board type B, respectively. The moisture content in the boards of both board types from all measurements is presented in Table 4.1.

Moisture content [%]	**Board type A**	**Board type B**
After three weeks	~ 9.5	~ 9.9
Before manufacturing	~ 9.8	~ 10.7
After testing	$10.0 - 10.5$	$11.0 - 11.5$

Table 4.1: Measured moisture content of the boards of type A and type B, respectively.

As can be seen in Table 4.1, the boards of type A appears to have reached equilibrium at a moisture content of around 10 %, while the equilibrium moisture content of the boards of type B appears to be around 11 %. Furthermore, the moisture content of the test specimens after testing varied between 10.0 and 10.5 % for board type A and between 10.0 and 10.5 % for board type B depending on if the measurement was conducted in the surface layer above an air gap or above a cross-layer lamella.

4.2 Strength grading of timber

The strength grading of the timber was performed according to the method presented in Section 3.2 for board type A with a thickness of 30 mm and board type B with a thickness of 20 mm, respectively.

4.2.1 Board type A

The results from the strength grading of the boards of type A, with a thickness of 30 mm, are presented using histograms illustrating the distribution of the density and longitudinal dynamic MOE of the boards, as well as a scatter plot illustrating the relation between the density and the longitudinal dynamic MOE.

4.2.1.1 Density

The distribution of the determined density of the boards of type A is presented in Figure 4.1.

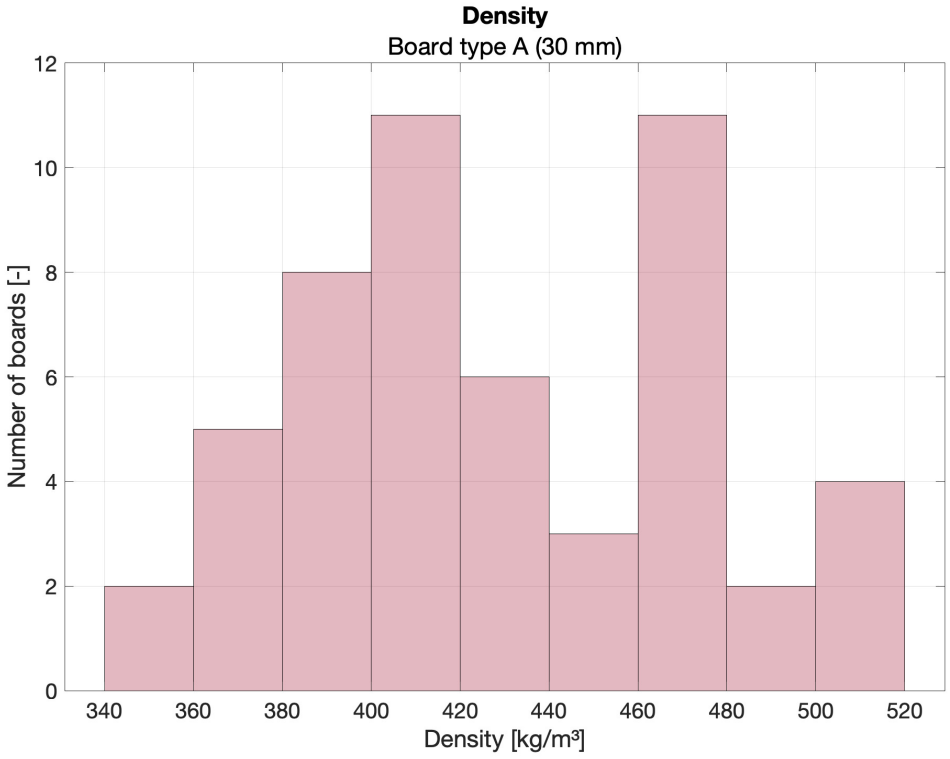

Figure 4.1: The distribution of the determined density of boards of type A.

It can be observed in Figure 4.1 that the density for the majority of the boards is in the range between 380 and 480 kg/m^3. However, no evident normal distribution can be observed. For board type A, the average and median density, as well as the maximum and minimum density, are presented in Table 4.2.

	Density [kg/m^3]
Average	428.32
Median	421.55
Maximum	519.00
Minimum	351.03

Table 4.2: Density distribution data of board type A.

It can be observed in Table 4.2 that the average and the median value of the density are almost coinciding. Furthermore, the difference between the maximum value and the average value is greater than between the minimum and the average value, indicating that there are more boards of lower density than of higher density.

4.2.1.2 Dynamic MOE

The distribution of the determined dynamic longitudinal MOE of the boards of type A is presented in Figure 4.2.

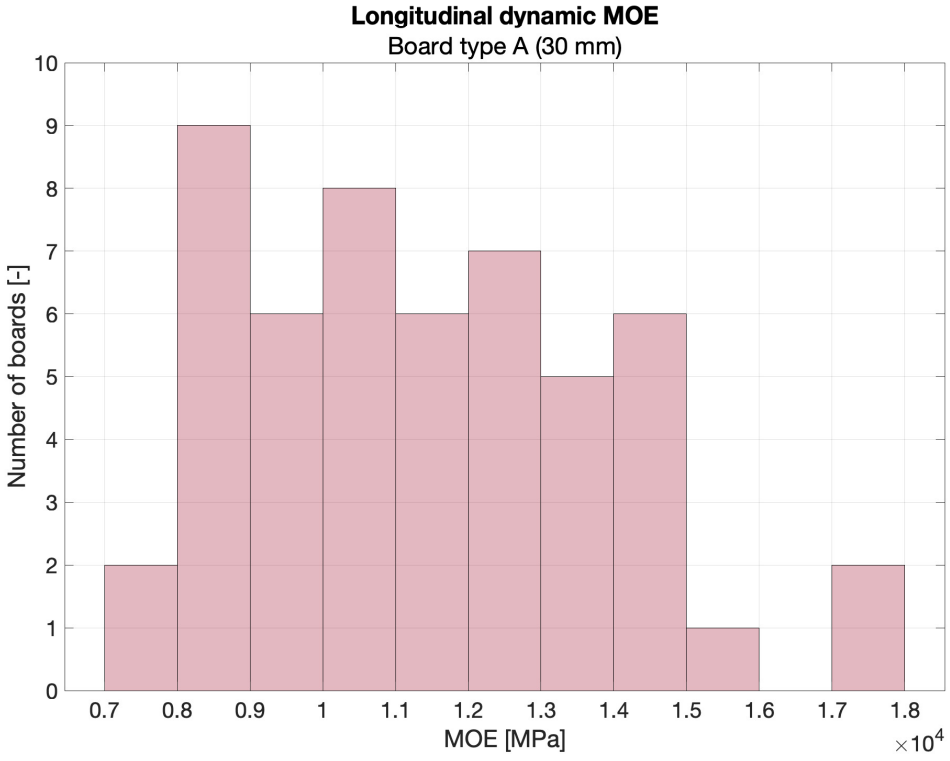

Figure 4.2: The distribution of the determined MOE of boards of type A.

As can be seen in Figure 4.2, the MOE for the majority of the boards is distributed between 8 000 and 15 000 MPa. No evident normal distribution can be observed. For board type A, the average and median MOE, as well as the maximum and minimum MOE, are presented in Table 4.3.

	Longitudinal MOE [MPa]
Average	11 450.39
Median	11 025.47
Maximum	17 866.08
Minimum	7 184.78

Table 4.3: MOE distribution data of board type A.

It can be observed in Table 4.3 that the median value is slightly lower than the average value. Furthermore, the difference between the maximum value and the average value is greater than between the minimum and the average value, indicating that there are more boards of lower MOE than of higher MOE.

4.2.1.3 Relation between density and MOE

The relation between the density and the longitudinal dynamic MOE for the boards of type A is presented in Figure 4.3.

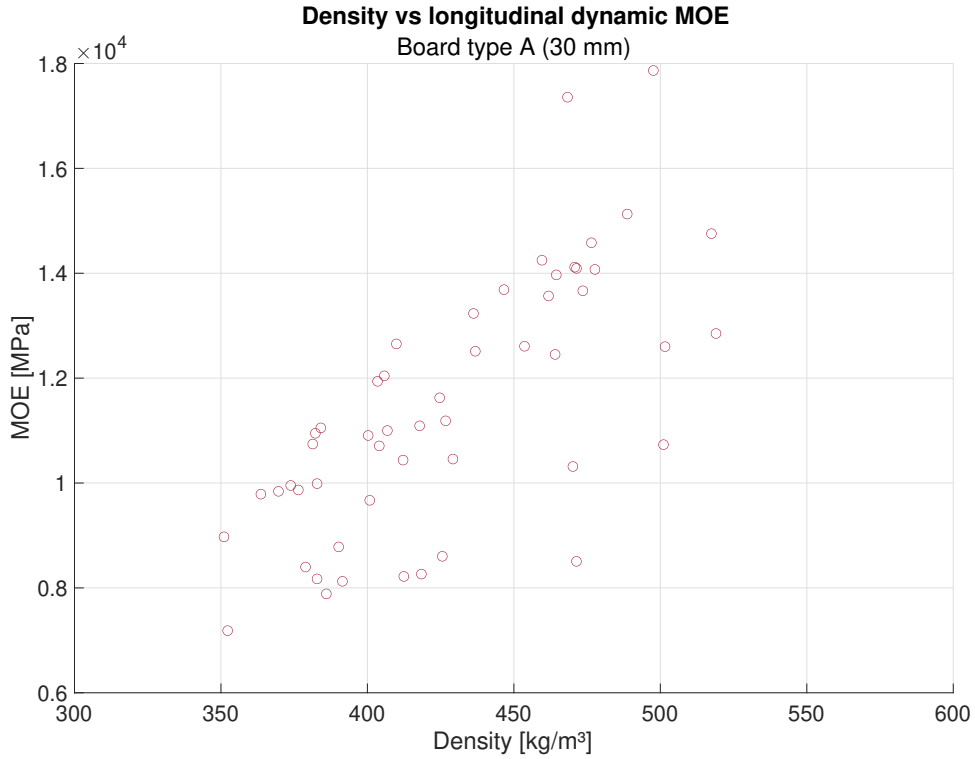

Figure 4.3: Relation between density and MOE of boards of type A.

A linear correlation can be observed between the density and the MOE, with a few deviations, indicating that the MOE is linearly dependent on the density. According to Equation 3.5, the MOE is proportional to the density, which is in agreement with the relation presented in Figure 4.3.

4.2.2 Board type B

The results from the grading of the boards of type B, with a thickness of 20 mm, are presented using histograms illustrating the distribution of the density and longitudinal dynamic MOE of the boards, as well as a scatter plot illustrating the relation between the density and the longitudinal dynamic MOE.

4.2.2.1 Density

The distribution of the measured density of the boards of type B is presented in Figure 4.4.

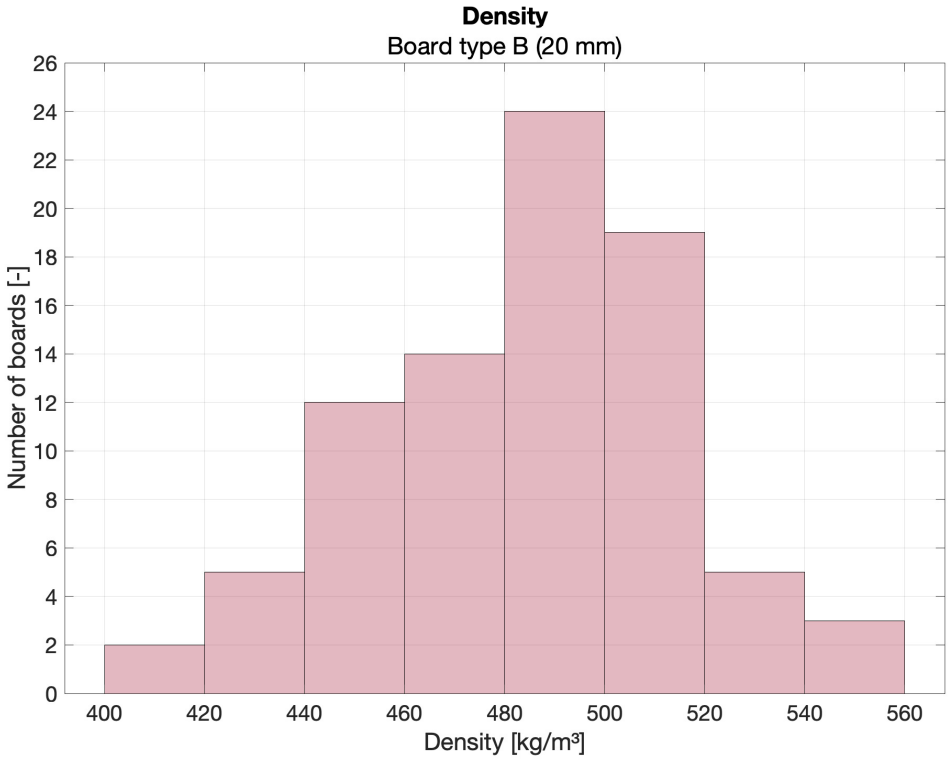

Figure 4.4: Measured density of boards of type B.

It can be observed in Figure 4.4 that the density of the boards is just about normally distributed around 480−500 kg/m^3. For board type B, the average and median density, as well as the maximum and minimum density, are presented in Table 4.4.

	Density [kg/m^3]
Average	484.46
Median	485.33
Maximum	557.08
Minimum	415.87

Table 4.4: Density distribution data of board type B.

As can be observed in Table 4.4, the average and median value of the density is almost coinciding and the difference between the average value and the maximum and minimum value, respectively, is approximately equal, indicating that the density is close to normally distributed.

4.2.2.2 Dynamic MOE

The distribution of the determined dynamic longitudinal MOE of the boards of type B is presented in Figure 4.5.

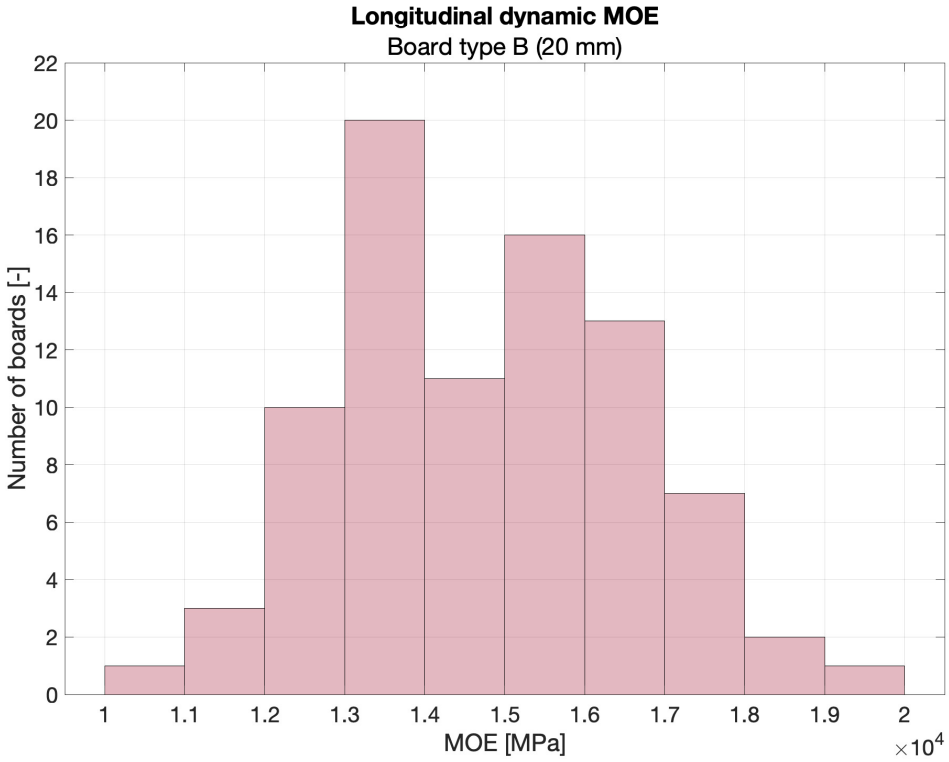

Figure 4.5: Determined MOE of boards of type B.

It can be observed that the MOE is close to normally distributed around 14 000 to 16 000 MPa, with a slight peak on the lower half. For board type B, the average and median MOE, as well as the maximum and minimum MOE, are presented in Table 4.5.

	Longitudinal MOE [MPa]
Average	14 737.45
Median	14 712.49
Maximum	19 041.22
Minimum	10 734.97

Table 4.5: MOE distribution data of board type B.

As can be observed in Table 4.5, the average and the median value almost coincides. The average value is slightly closer to the minimum value than the maximum value, indicating that there are more boards of lower MOE than of higher MOE.

4.2.2.3 Relation between density and MOE

The relation between the density and dynamic MOE for the boards of type A is presented in Figure 4.6.

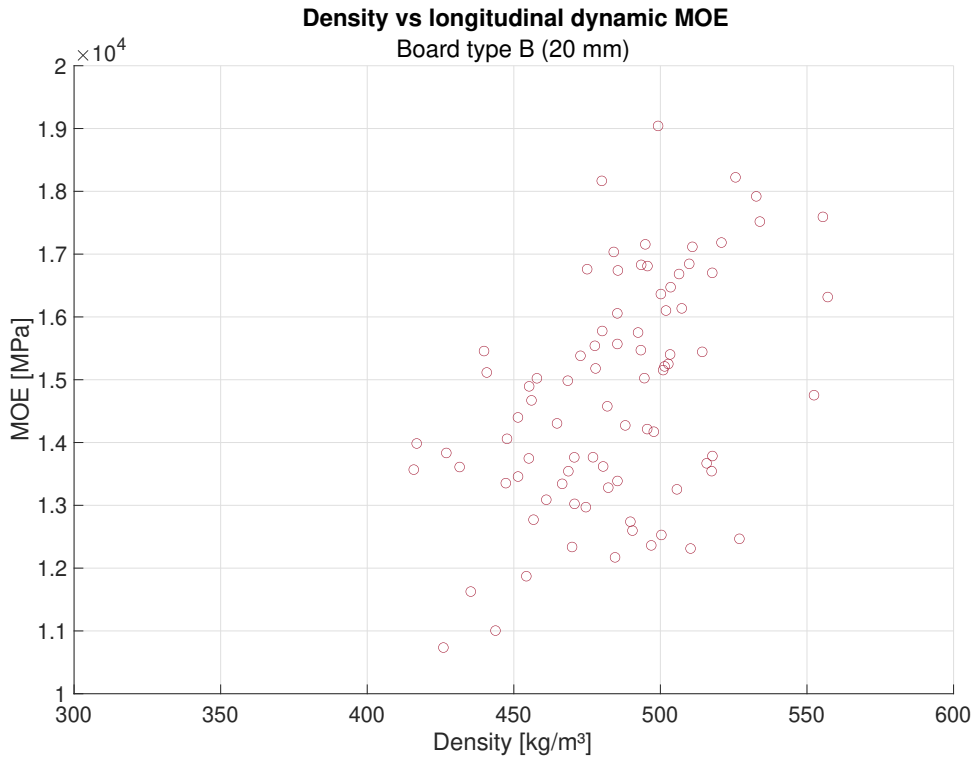

Figure 4.6: Relation between density and MOE of boards of type B.

For board type B, a linear correlation can be observed between the density and the MOE, with a few deviations, indicating that the MOE is linearly dependent on the density, which is in agreement with the theory.

4.3 Assigning of boards to configurations

The boards that were assigned for the manufacturing of the specimens, as well as the distribution of the boards in terms of strength are presented for board type A and B, respectively.

4.3.1 Board type A

In total, nine boards of type A were selected to be used for the construction of the three-layer configurations, see Figure 4.7.



Figure 4.7: The selected boards of type A.

The distribution of the assigned boards of type A with regards to the relation between density and MOE is presented in Figure 4.8.

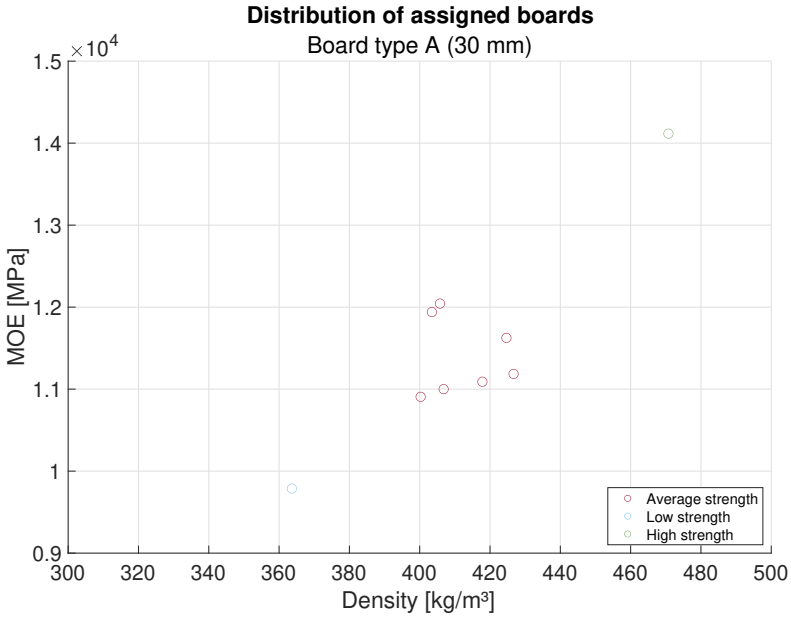

Figure 4.8: The distribution of assigned boards of type A.

4.3.2 Board type B

In total, 36 boards of type B were selected to be used for the construction of the five-layer configurations, see Figure 4.9.



Figure 4.9: The selected boards of type B.

The distribution of the assigned boards of type A with regards to the relation between density and MOE is presented in Figure 4.10.

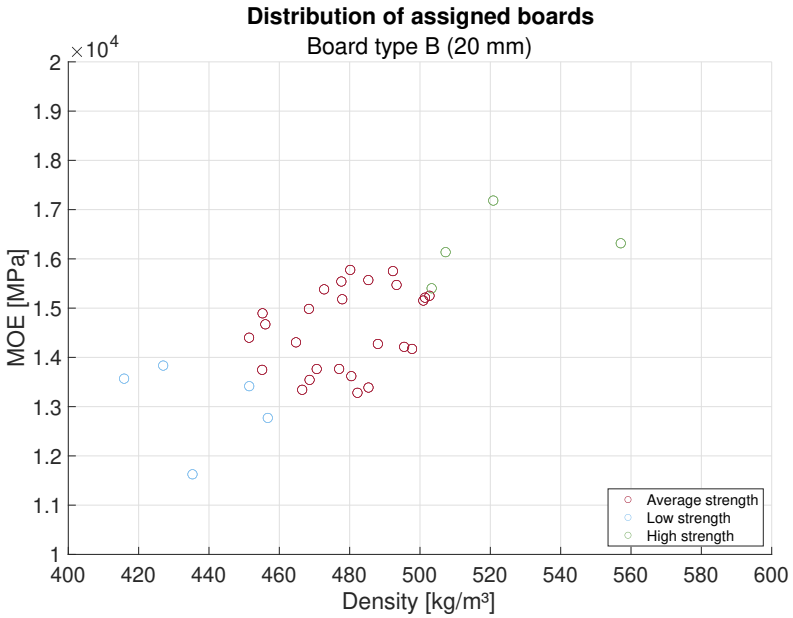

Figure 4.10: The distribution of assigned boards of type B.

4.4 Configurations

The designing of the configurations resulted in nine different configurations, where Configuration I to III are constructed of three layers of board type A (30 mm) and Configuration IV to IX are constructed of five layers of board type B (20 mm). All configurations have a width of 110 mm and cross-layers with lamella widths of 120 mm. The layout of the configurations were constructed so that each one would correspond to a small segment of a full scale panel, see Figure 4.11. Therefore, all the edge parts of the cross-layers have a width of a half lamella, i.e. 60 mm, to allow for symmetry. For the strength properties of the boards that were used for the specimens of each configuration, as well as the calculations of the differences in strength, see Appendix D.

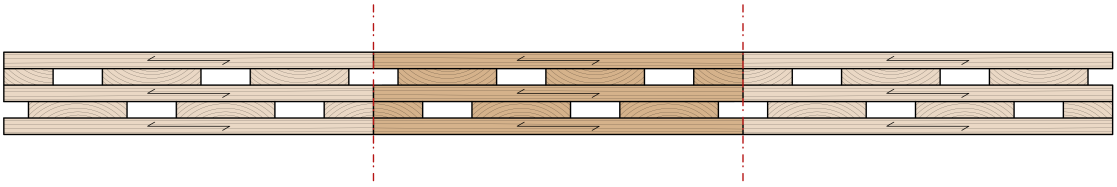

Figure 4.11: Illustration of the relation between a small scale test specimen and a full scale panel.

4.4.1 Configuration I

Configuration I is a regular solid three-layer configuration without air gaps, see Figure 4.12 and Table 4.6 for details.

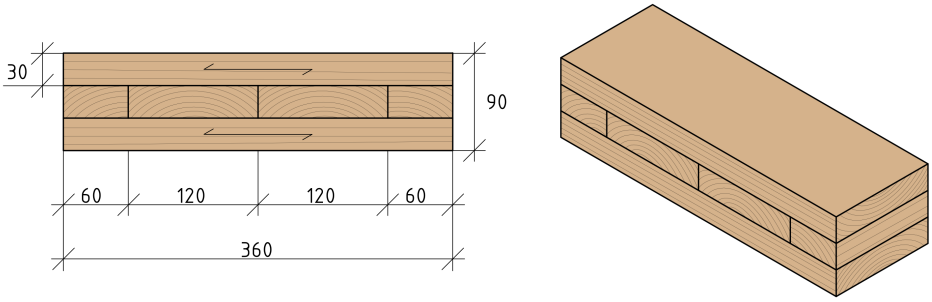

Figure 4.12: Drawing and illustration of Configuration I.

Air gap width b_{airgap} [mm]	0
Wood volume V_{wood} [mm^3]	3 564 000
Maximum possible volume V_{max} [mm^3]	3 564 000
Relative volume η_{V} [−]	1.00
Material reduction μ_{M} [%]	0.00

Table 4.6: Geometrical properties of Configuration I.

The difference in density and MOE between the average strength and the low and high strength boards used for Configuration I are presented in Table 4.7.

	Average strength	**Low strength**	**Decrease**	**High strength**	**Increase**
Density [kg/m^3]	426	364	14.6 %	471	10.6 %
MOE [MPa]	11 400	9 790	14.2 %	14 100	23.8 %

Table 4.7: Material properties of Configuration I.

4.4.2 Configuration II

Configuration II is a three-layer configuration, where air gaps are introduced in the cross-layer. The width of the air gaps are half the width of the lamella in the cross-layer, see Figure 4.13 and Table 4.8 for details.

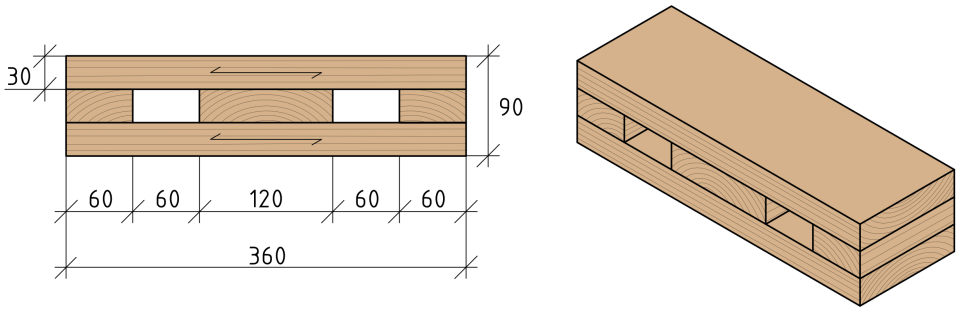

Figure 4.13: Drawing and illustration of Configuration II.

Air gap width b_{airgap} [mm]	60
Wood volume V_{wood} [mm^3]	3 168 000
Maximum possible volume V_{max} [mm^3]	3 564 000
Relative volume η_{V} [%]	0.89
Material reduction μ_{M} [%]	11.1

Table 4.8: Geometrical properties of Configuration II.

The difference in density and MOE between the average strength and the low and high strength boards used for Configuration II are presented in Table 4.9.

	Average strength	**Low strength**	**Decrease**	**High strength**	**Increase**
Density [kg/m^3]	405	364	10.1 %	471	16.4 %
MOE [MPa]	12 000	9 790	18.4 %	14 100	17.7 %

Table 4.9: Material properties of Configuration II.

4.4.3 Configuration III

Configuration III is a three-layer configuration, where air gaps with the same width as the lamella are introduced in the cross-layer, see Figure 4.14 and Table 4.10 for details.

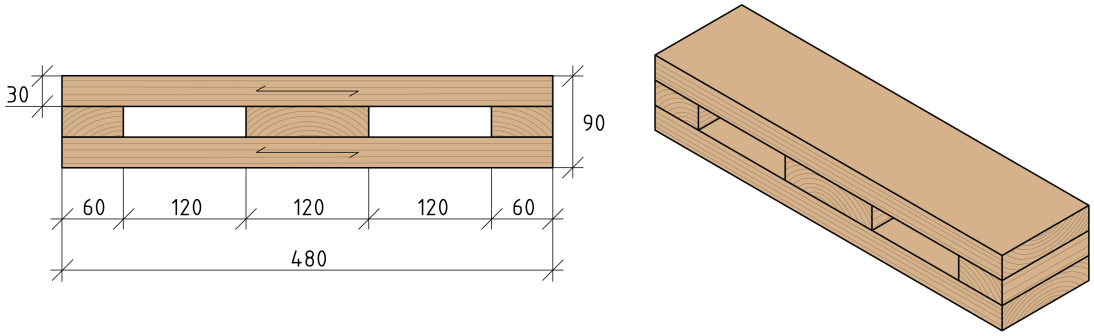

Figure 4.14: Drawing and illustration of Configuration III.

Air gap width b_{airgap} [mm]	120
Wood volume V_{wood} [mm^3]	3 960 000
Maximum possible volume V_{max} [mm^3]	4 752 000
Relative volume η_{V} [−]	0.83
Material reduction μ_{M} [%]	16.7

Table 4.10: Geometrical properties of Configuration III.

The difference in density and MOE between the average strength and the low and high strength boards used for Configuration III are presented in Table 4.11.

	Average strength	**Low strength**	**Decrease**	**High strength**	**Increase**
Density [kg/m^3]	408	364	10.9 %	471	15.3 %
MOE [MPa]	11 000	9 790	11.0 %	14 100	28.3 %

Table 4.11: Material properties of Configuration III.

4.4.4 Configuration IV

Configuration IV is a regular solid five-layer configuration without air gaps, see Figure 4.15 and 4.13 for details.

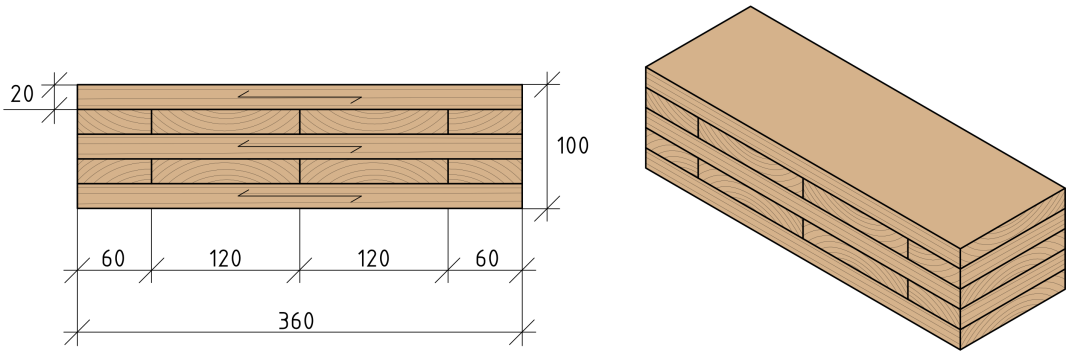

Figure 4.15: Drawing and illustration of Configuration IV.

Air gap width b_{airgap} [mm]	0
Wood volume V_{wood} [mm^3]	3 960 000
Maximum possible volume V_{max} [mm^3]	3 960 000
Relative volume η_{V} [−]	1.00
Material reduction μ_{M} [%]	0.00

Table 4.12: Geometrical properties of Configuration IV.

The difference in density and MOE between the average strength and the low and high strength boards used for Configuration IV are presented in Table 4.13.

	Average strength	**Low strength**	**Decrease**	**High strength**	**Increase**
Density [kg/m^3]	494	457	7.50 %	557	12.8 %
MOE [MPa]	14 200	12 800	10.2 %	16 300	14.8 %

Table 4.13: Material properties of Configuration IV.

4.4.5 Configuration V

Configuration V is a five-layer configuration with introduced air gaps in the cross-layers. The width of the air gaps are half the width of the lamellas in the cross-layers and the air gaps are aligned vertically in the cross-layers, see Figure 4.16 and Table 4.14 for details.

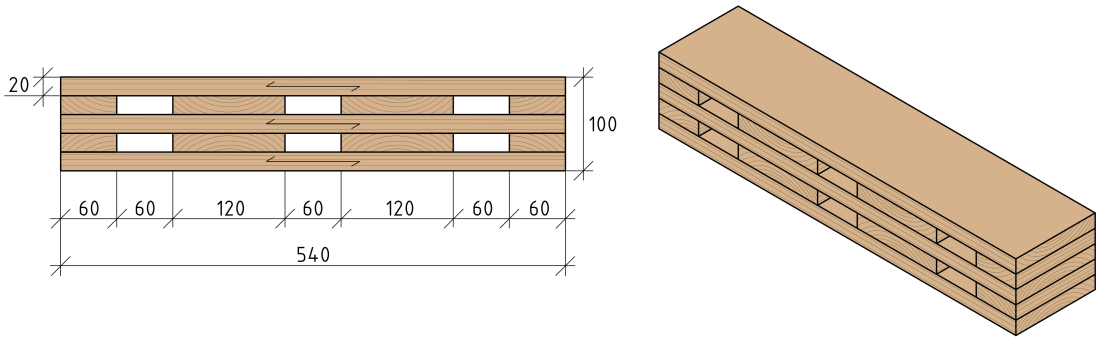

Figure 4.16: Drawing and illustration of Configuration V.

Air gap width b_{airgap} [mm]	60
Wood volume V_{wood} [mm^3]	5 148 000
Maximum possible volume V_{max} [mm^3]	5 940 000
Relative volume η_{V} [−]	0.87
Material reduction μ_{M} [%]	13.3

Table 4.14: Geometrical properties of Configuration V.

The difference in density and MOE between the average strength and the low and high strength boards used for Configuration V are presented in Table 4.15.

	Average strength	**Low strength**	**Decrease**	**High strength**	**Increase**
Density [kg/m^3]	488	427	12.5 %	521	6.77 %
MOE [MPa]	15 600	13 800	11.6 %	17 200	9.86 %

Table 4.15: Material properties of Configuration V.

4.4.6 Configuration VI

Configuration VI is a five-layer configuration, where air gaps are introduced in the cross-layers. The width of the air gaps are half the width of the lamellas in the cross-layers and the air gaps in one cross-layer are shifted 90 mm horizontally in relation to the air gaps in the other cross-layer, see Figure 4.17 and Table 4.16 for details.

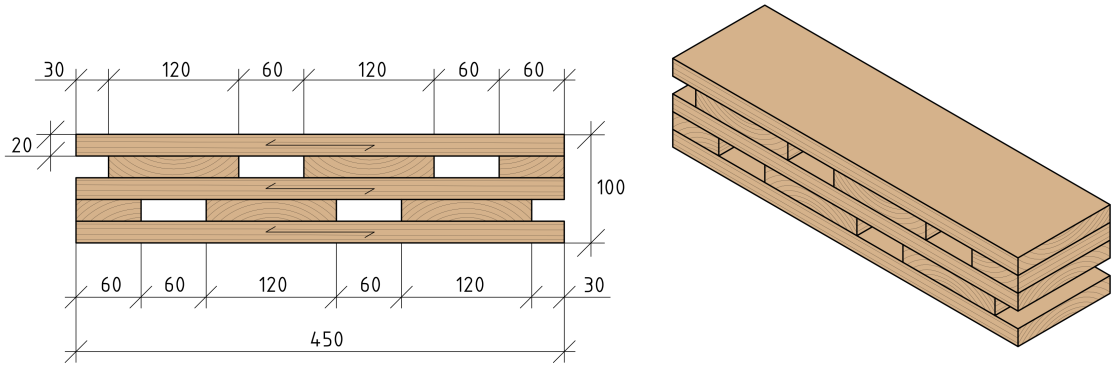

Figure 4.17: Drawing and illustration of Configuration VI.

Air gap width $b_{\mathbf{airgap}}$ [mm]	60
Wood volume $V_{\mathbf{wood}}$ [mm^3]	4 290 000
Maximum possible volume $V_{\mathbf{max}}$ [mm^3]	4 950 000
Relative volume $\eta_{\mathbf{V}}$ [−]	0.87
Material reduction $\mu_{\mathbf{M}}$ [%]	13.3

Table 4.16: Geometrical properties of Configuration VI.

The difference in density and MOE between the average strength and the low and high strength boards used for Configuration VI are presented in Table 4.17.

	Average strength	**Low strength**	**Decrease**	**High strength**	**Increase**
Density [kg/m^3]	476	427	10.3 %	521	9.40 %
MOE [MPa]	15 400	13 800	9.98 %	17 200	11.8 %

Table 4.17: Material properties of Configuration VI.

4.4.7 Configuration VII

Configuration VII is a five-layer configuration, where air gaps with the same width as the lamellas are introduced in the cross-layers. The air gaps are aligned vertically in the cross-layers, see Figure 4.18 and Table 4.18 for details.

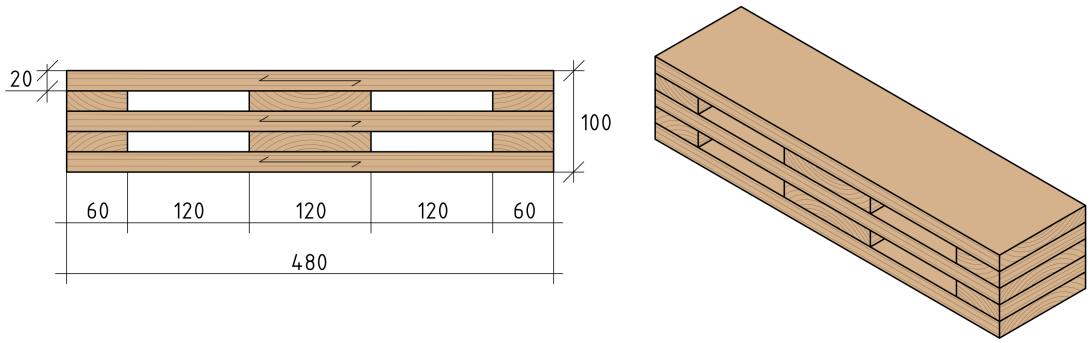

Figure 4.18: Drawing and illustration of Configuration VII.

Air gap width b_{airgap} [mm]	120
Wood volume V_{wood} [mm^3]	4 224 000
Maximum possible volume V_{max} [mm^3]	5 280 000
Relative volume η_{V} [−]	0.80
Material reduction μ_{M} [%]	20.0

Table 4.18: Geometrical properties of Configuration VII.

The difference in density and MOE between the average strength and the low and high strength boards used for Configuration VII are presented in Table 4.19.

	Average strength	**Low strength**	**Decrease**	**High strength**	**Increase**
Density [kg/m^3]	463	435	6.06 %	503	8.61 %
MOE [MPa]	13 500	11 600	14.2 %	15 400	13.7 %

Table 4.19: Material properties of Configuration VII.

4.4.8 Configuration VIII

Configuration VIII is a five-layer configuration, where air gaps are introduced in the cross-layers. The width of the air gaps are the same as the width of the lamellas in the cross-layers and the air gaps in one cross-layer are shifted 120 mm horizontally in relation to the air gaps in the other cross-layer, see Figure 4.19 and Table 4.20 for details.

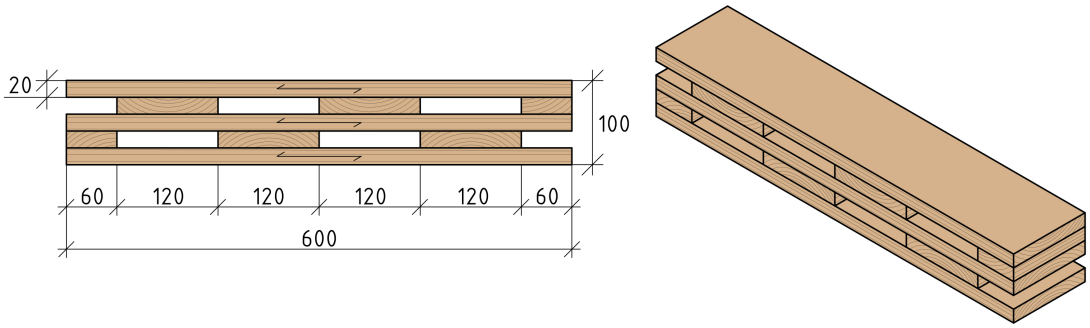

Figure 4.19: Drawing and illustration of Configuration VIII.

Air gap width b_{airgap} [mm]	120
Wood volume V_{wood} [mm^3]	5 280 000
Maximum possible volume V_{max} [mm^3]	6 600 000
Relative volume η_{V} [−]	0.80
Material reduction μ_{M} [%]	20.0

Table 4.20: Geometrical properties of Configuration VIII.

The difference in density and MOE between the average strength and the low and high strength boards used for Configuration VIII are presented in Table 4.21.

	Average strength	**Low strength**	**Decrease**	**High strength**	**Increase**
Density [kg/m^3]	479	435	9.15 %	503	5.05 %
MOE [MPa]	13 600	11 600	14.3 %	15 400	13.6 %

Table 4.21: Material properties of Configuration VIII.

4.4.9 Configuration IX

Configuration IX is a five-layer configuration, where air gaps are introduced in the cross-layers with a width of 80 mm, i.e. ⅔ of the width of the lamellas. The air gaps in one cross-layer are shifted 100 mm horizontally in relation to the air gaps in the other cross-layer, resulting in a 20 mm overlap between the lamellas in the different cross-layers, see Figure 4.20 and Table 4.22 for details.

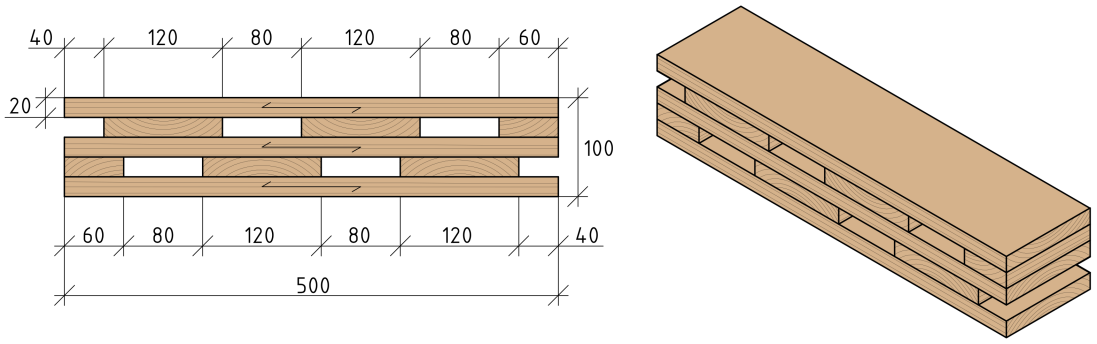

Figure 4.20: Drawing and illustration of Configuration IX.

Air gap width b_{airgap} [mm]	80
Wood volume V_{wood} [mm^3]	4 620 000
Maximum possible volume V_{max} [mm^3]	5 500 000
Relative volume η_{V} [−]	0.84
Material reduction μ_{M} [%]	16.0

Table 4.22: Geometrical properties of Configuration IX.

The difference in density and MOE between the average strength and the low and high strength boards used for Configuration IX are presented in Table 4.23.

	Average strength	**Low strength**	**Decrease**	**High strength**	**Increase**
Density [kg/m^3]	502	451	10.0 %	557	11.0 %
MOE [MPa]	15 200	13 400	11.8 %	16 300	7.31 %

Table 4.23: Material properties of Configuration IX.

4.5 Testing of specimens

In this section, the results from the strength testing of the specimens are presented. For the test specimens, the results are presented using photos of the specimens after failure and load-deformation curves. For the three-layer configurations, i.e. Configurations I to III, the results are presented using photos of the specimens after failure, load-deformation curves, calculations of shear strength, and images showing the major strain distribution, as obtained using ARAMIS. For the five-layer configurations, i.e. Configurations IV to IX, the results are presented using photos of the specimens after failure, load-deformation curves, and calculations of shear strength. For the plotting of the load-deformation curves of two example configurations, Configuration I and IV, see Appendix B and C, respectively. For the calculations of the shear strength of all the configurations, see Appendix E.

4.5.1 Loss of ARAMIS test data

Due to unfortunate circumstances, all the test data for the five-layer configurations from the digital image correlation using ARAMIS was encrypted and therefore, the results are not as comprehensive as originally intended.

The intention was to analyse the changes in the major strain distribution, as obtained from ARAMIS, and to determine the shear modulus, according to Equations 2.12 and 2.14 in Section 2.5.3, in order to obtain more extensive results regarding the shear capacity of the specimens. However, due to the loss of data for the five-layer configurations, only the test data for the three-layer configurations was available and since we believe that it would only be interesting to compare all the configurations, no calculations of the shear modulus were carried out and only the images showing the strain distribution of the three-layer specimens are presented.

4.5.2 Test specimens

The results from the trial testing of the test specimens were used to evaluate and optimise the manufacturing and testing method for the final specimens. No analysis using ARAMIS, nor any hand calculations were conducted for the test specimens.

4.5.2.1 Solid test specimen

The results from the initial test of the solid test specimen, with a width of five lamellas in the cross-layers, are shown in Figure 4.21.

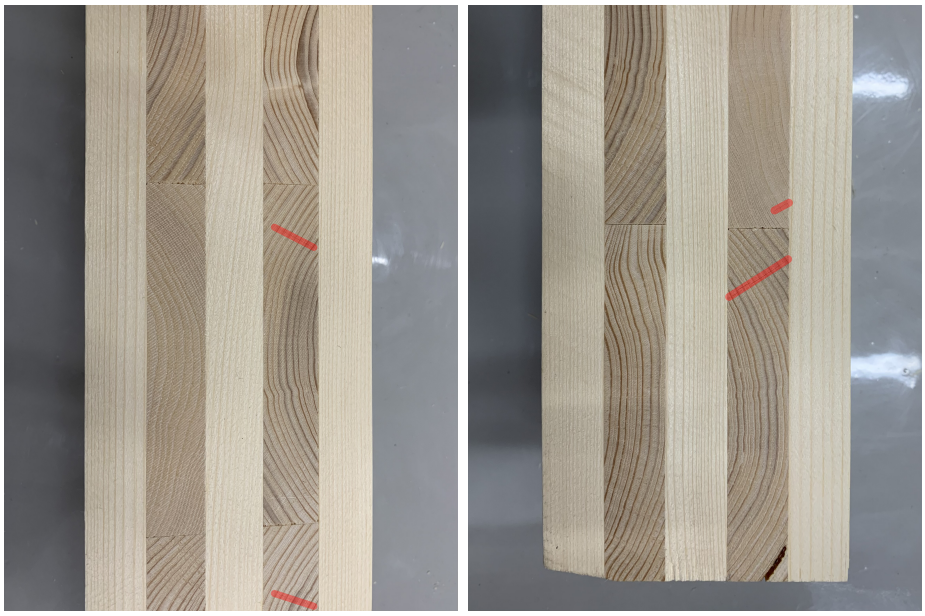

Figure 4.21: Results from the initial test of the solid test specimen. (March 21st 2022)

As can be seen in Figure 4.21, the only remaining visible cracks are shear cracks in the radial direction of the cross-layers, as highlighted in red.

The results from the second test of the solid test specimen, with a shortened width of three lamellas in the cross-layers, are shown in Figure 4.22.



Figure 4.22: Results from the second test of the solid test specimen. (March 28th 2022)

The crack distribution of the shortened test specimen is highlighted in red in Figure 4.22, where some distinct shear cracks in the radial direction of the cross-layers can be observed, as well as some cracks in the bondlines.

The test results for the solid test specimen are presented in Table 4.24.

Solid test specimen	**Failure load [kN]**	**Deformation [mm]**	**Time [s]**	**Loading rate [mm/min]**
Initial test	90.24	8.79	835	0.5
Second test	60.26	2.90	147	0.8

Table 4.24: Test results from the testing of the solid test specimen.

For the first test, a loading rate of a deformation of 0.5 mm per minute was applied. As can be seen in Table 4.24, the loading time exceeded the recommended maximum loading time due to no occurrence of failure and the specimen was unloaded after about 800 seconds. For the second test, twice the loading rate was applied, i.e. a deformation of 1.0 mm per minute, and the time of failure occurred before the recommended minimum loading time instead.

The load-deformation curves for the testing of the solid test specimen are illustrated in Figure 4.23.

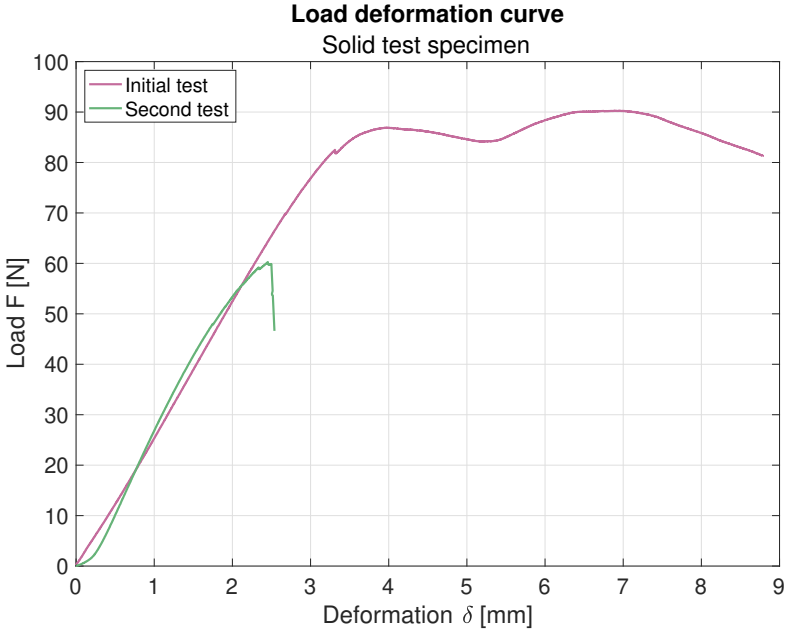

Figure 4.23: Load-deformation curves for the solid test specimen.

It can be observed in Figure 4.23 that the behaviour of the specimen in the first test was ductile, whereas the failure of the specimen in the second test was brittle. Furthermore, the failure load of the shortened test specimen, from the second test, was lower than the failure load of the specimen from first test.

4.5.2.2 Test specimen with air gaps

The results from the testing of the test specimen with air gaps are shown in Figures 4.24 and 4.25.

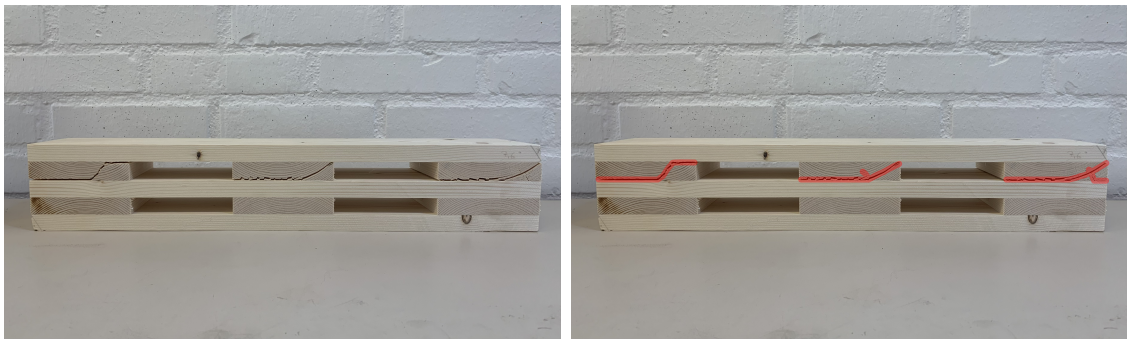

Figure 4.24: Results from the test of the test specimen with air gaps. (March 28th 2022)



Figure 4.25: Close-up of the results from the test of the test specimen with air gaps. (March 28th 2022)

It can be observed in Figures 4.24 and 4.25 that the specimen failed in the cross-layers, i.e. due to rolling shear. Furthermore, some shear cracks in the radial direction of one of the cross-layers can be observed, as highlighted in red in Figure 4.24.

The test results for the test specimen with air gaps are presented in Table 4.25.

Test specimen with air gaps	**Failure load [kN]**	**Deformation [mm]**	**Time [s]**	**Loading rate [mm/min]**
Test results	51.58	3.33	194	1.0

Table 4.25: Test results from the testing of the test specimen with air gaps.

A loading rate of a deformation of 1.0 mm per minute was applied and as can be seen in Table 4.25, the failure load was reached after 194 seconds, which is within the recommended range of time.

The load-deformation curve for the testing of the test specimen with air gaps is illustrated in Figure 4.26.

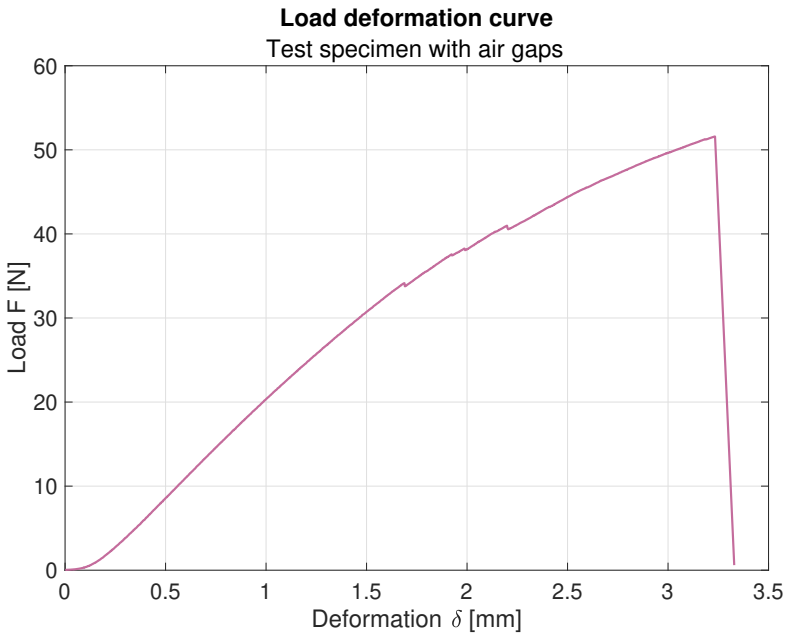

Figure 4.26: Load-deformation curve for the test specimen with air gaps.

It can be observed in Figure 4.26 that the failure of the test specimen with air gaps is of brittle character.

4.5.3 Configuration I

The results of the testing of Configuration I are shown in Figure 4.27.

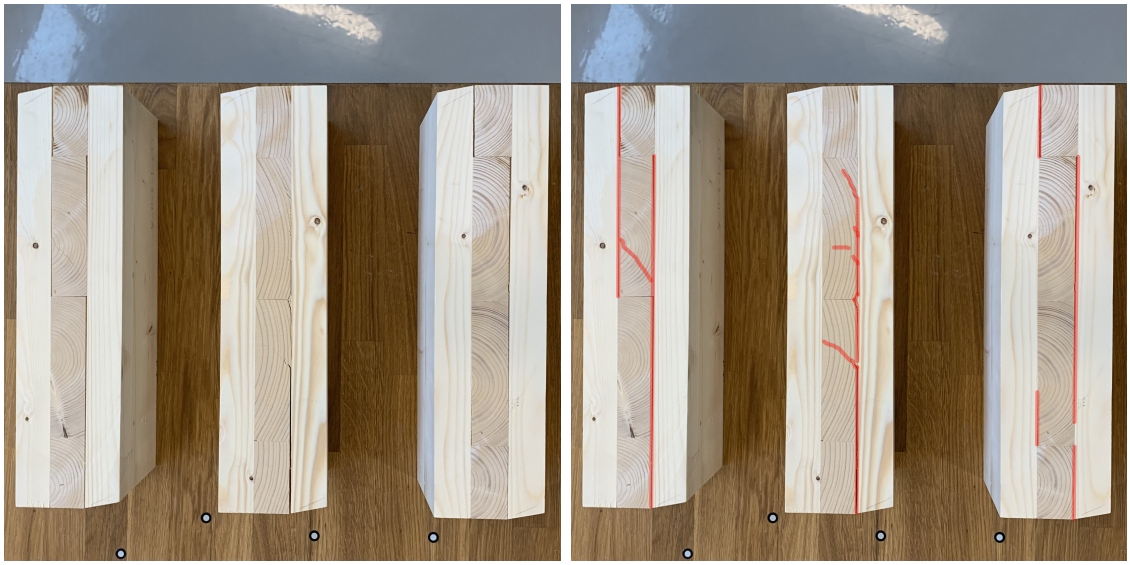

Figure 4.27: Results from the test of Configuration I, in the order; average, low, and high strength. (April 6th 2022)

It can be observed in Figure 4.27, where all the remaining visible cracks are highlighted in red, that all three specimens failed in the bondlines or in panel shear close to the bondlines. Some shear cracks can also be observed in the radial direction of the cross-layers in the specimens of average and low strength. However, the specimen of high strength shows no visible shear cracks in the cross-layer. The specimen of low strength is the only specimen with visible shear cracks in the tangential direction.

The test results for Configuration I are presented in Table 4.26.

Specimen	**Failure load [kN]**	**Deformation [mm]**	**Time [s]**	**Loading rate [mm/min]**
Average strength	44.50	1.79	123	0.8
Low strength	28.14	2.35	121	0.8
High strength	34.98	1.47	156	0.5

Table 4.26: Test results from the testing of Configuration I.

For the average and low strength specimens of Configuration I, the loading rate was a deformation of 0.8 mm per minute. As can be seen in Table 4.26, the loading time for these specimens were below the minimum recommended loading time and therefore, the loading rate was adjusted to a deformation of 0.5 mm per minute for the high strength specimen. However, it can be observed that the loading time for the high strength specimen was also below the recommended value of 300 ± 120 s.

The load-deformation curves for the testing of Configuration I are illustrated in Figure 4.28.

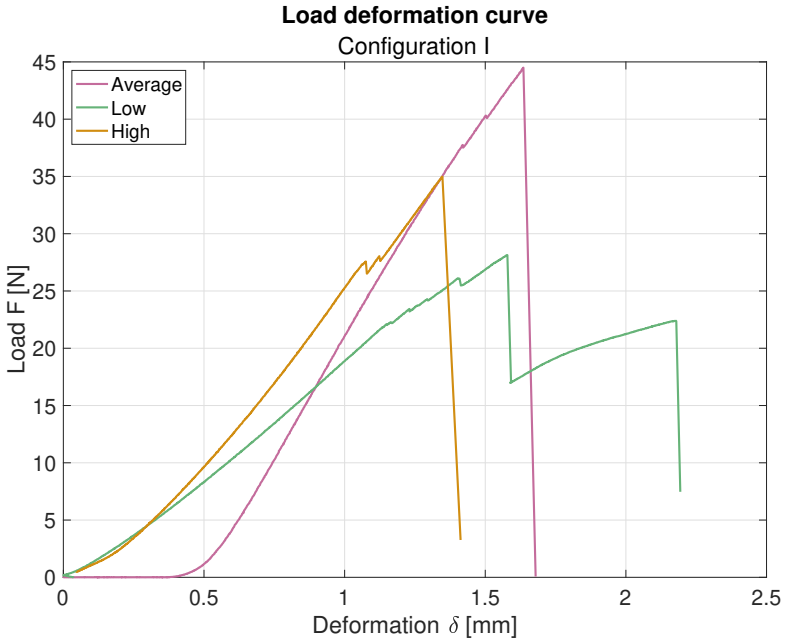

Figure 4.28: Load-deformation curves for Configuration I.

It can be observed in Figure 4.28 that the curve of the average strength specimen has the largest inclination, indicating that the specimen had the highest stiffness, followed by the specimen of high and low strength, respectively. Furthermore, it can be observed that the average strength specimen also had the highest failure load, followed by the specimen of high and low strength.

The failure modes and shear strengths of each specimen of Configuration I are presented in Table 4.27. The shear strengths are calculated according to Equation 3.9.

Specimen	Failure mode	Shear strength [MPa]
Average strength	Bondline failure	1.12
Low strength	Bondline failure	0.71
High strength	Bondline failure	0.88

Table 4.27: Failure modes and calculated shear strengths of Configuration I.

It can be observed in Table 4.27 that all three specimens failed in the bondlines and that the average strength specimen had the highest shear strength, followed by the high and low strength specimens.

The strain distribution in the average strength specimen of Configuration I just before and directly after failure, as obtained using ARAMIS, is shown in Figure 4.29.

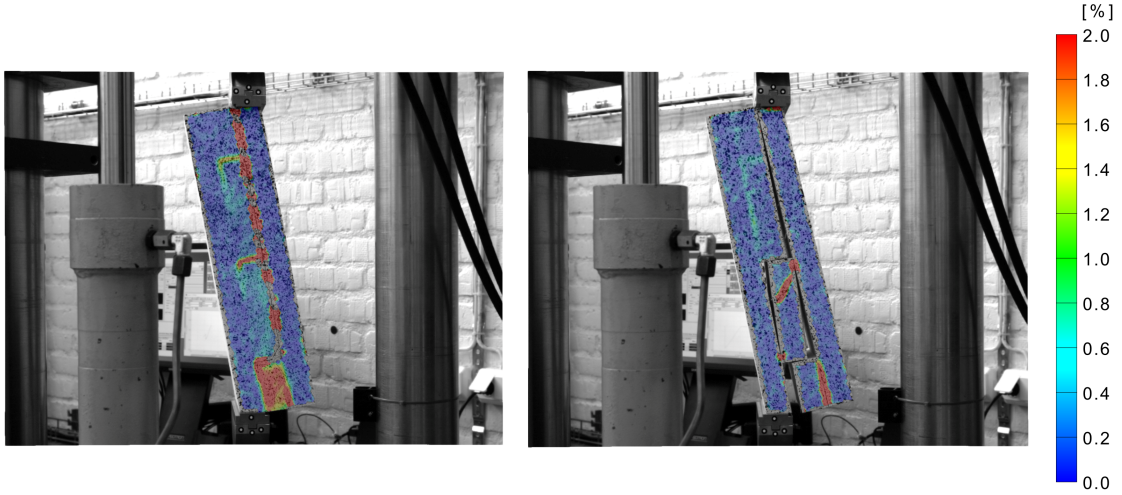

Figure 4.29: Strain distribution observed using ARAMIS right before and after failure for the average strength specimen of Configuration I.

It can be observed in Figure 4.29 that, before failure, the largest deformations occurred in the bondlines and between the lamellas in the cross-layer. Large deformations can also be observed in the bottom edge lamella of the cross-layer, as well as some smaller deformations in the tangential direction of the cross-layer. It is clear that the specimen experienced bondline failure.

The strain distribution in the low strength specimen of Configuration I just before and directly after failure, as obtained using ARAMIS, is shown in Figure 4.30.

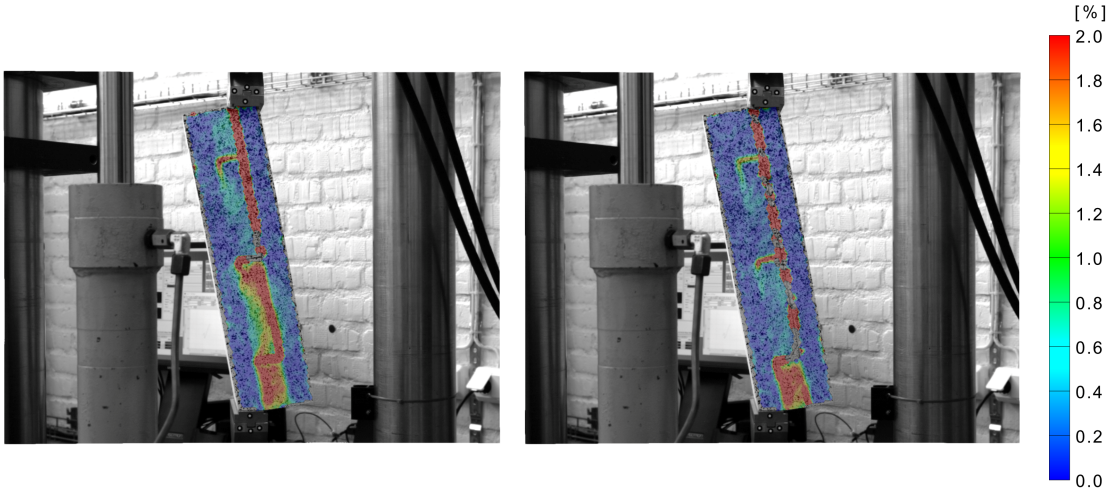

Figure 4.30: Strain distribution observed using ARAMIS right before and after failure for the low strength specimen of Configuration I

It can be observed in Figure 4.30 that, before failure, the largest deformations occurred in the bondlines and in the cross-layer. However, after failure, the cracking appears to have mainly occurred in the bondline.

The strain distribution in the high strength specimen of Configuration I just before and directly after failure, as obtained using ARAMIS, is shown in Figure 4.31.

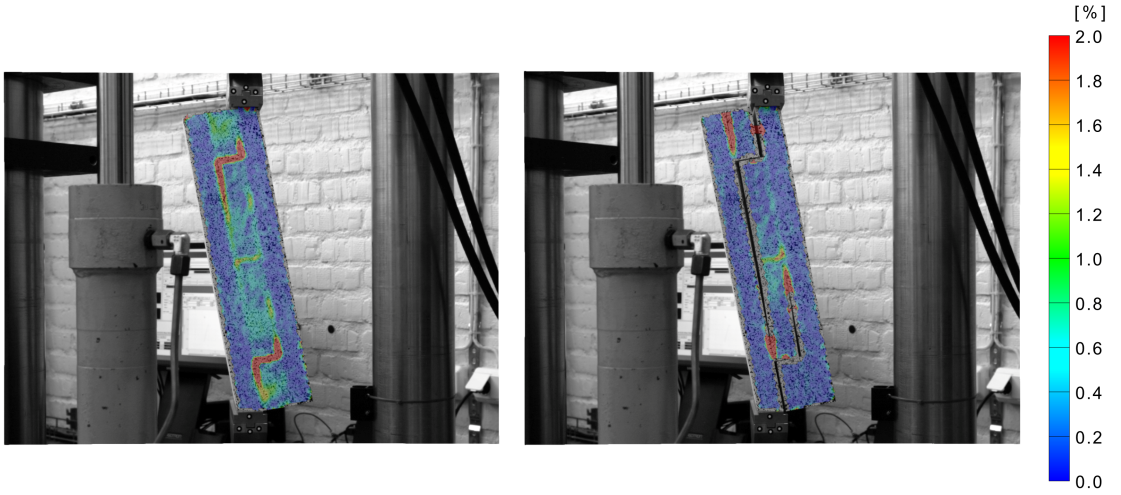

Figure 4.31: Strain distribution observed using ARAMIS right before and after failure for the high strength specimen of Configuration I

It can be observed in Figure 4.31 that, before failure, the largest deformations occurred in the bondlines and between the lamellas in the cross-layer. Smaller deformations can also be observed in the lamellas of the cross-layer. It is clear that the specimen experienced bondline failure.

4.5.4 Configuration II

The results of the testing of Configuration II are shown in Figure 4.32.

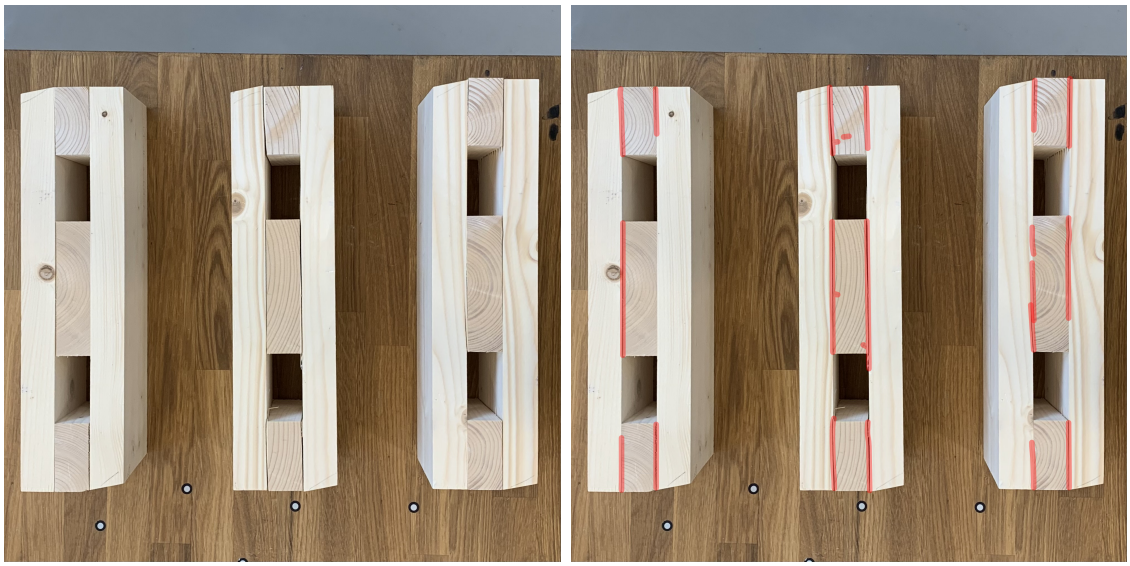

Figure 4.32: Results from the test of Configuration II, in the order; average, low, and high strength. (April 6th 2022)

It can be observed in Figure 4.32, where all the remaining visible cracks are highlighted in red, that all three specimens failed in the bondlines or in panel shear close to the bondlines. Only the specimen of low strength displays a few visible shear cracks in the radial direction of the cross-layers.

The test results for Configuration II are presented in Table 4.28.

Specimen	**Failure load [kN]**	**Deformation [mm]**	**Time [s]**	**Loading rate [mm/min]**
Average strength	20.24	1.59	134	0.5
Low strength	19.97	1.87	216	0.5
High strength	24.98	1.49	170	0.5

Table 4.28: Test results from the testing of Configuration II.

The loading rate for all the specimens of Configuration II was a deformation of 0.5 mm per minute. As can be seen in Table 4.28, both the average and the high strength specimen reached their respective failure load too rapidly, while the low strength specimen reached the failure load within the recommended loading time.

The load-deformation curves for the testing of Configuration II are illustrated in Figure 4.33.

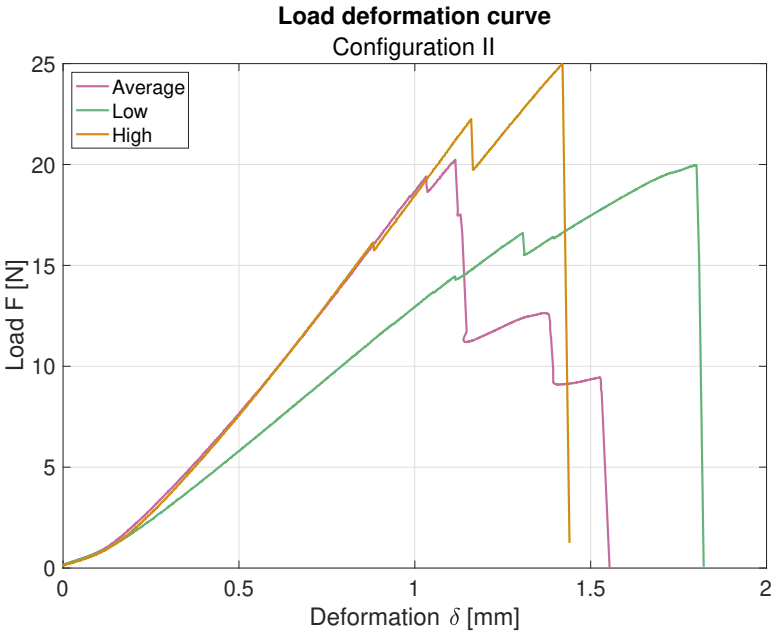

Figure 4.33: Load-deformation curves for Configuration II.

It can be observed in Figure 4.33 that the curves of the average and high strength specimens have the same inclination, indicating that the two specimens had the same stiffness and that it was higher than the stiffness of the low strength specimen. However, the failure load of the high strength specimen was higher than that of the average strength specimen, followed by the low strength specimen.

The failure modes and shear strengths of each specimen of Configuration II are presented in Table 4.29. The shear strengths are calculated according to Equations 3.8 – 3.9.

Specimen	Failure mode	Shear strength [MPa]
Average strength	Bondline failure	0.77
Low strength	Panel shear failure	0.50
High strength	Panel shear failure	0.63

Table 4.29: Failure modes and calculated shear strengths of Configuration II.

It can be observed in Table 4.29 that the average strength specimen experienced bondline failure, whereas the low and the high strength specimens failed in panel shear. Furthermore, the shear strength of the average strength specimen was the highest, followed by the high and low strength specimens.

The strain distribution in the average strength specimen of Configuration II, just before and directly after failure, as obtained using ARAMIS, is shown in Figure 4.34.

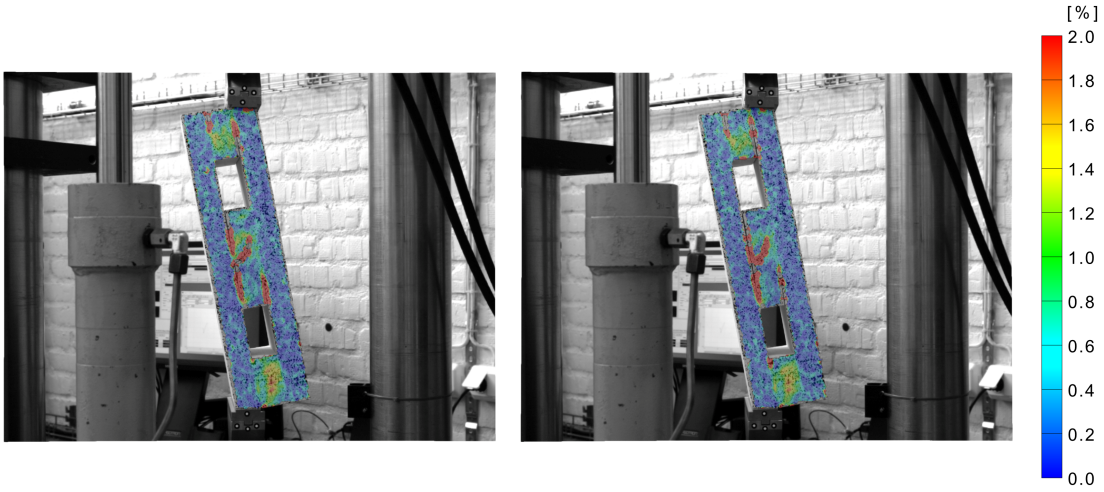

Figure 4.34: Strain distribution observed using ARAMIS right before and after failure for the average strength specimen of Configuration II.

It can be observed in Figure 4.34 that, both before and after failure, the largest deformations occurred in the bondlines and in the cross-layer. The main reason for failure appears to be cracking of the bondlines.

The strain distribution in the low strength specimen of Configuration II, just before and directly after failure, as obtained using ARAMIS, is shown in Figure 4.35.

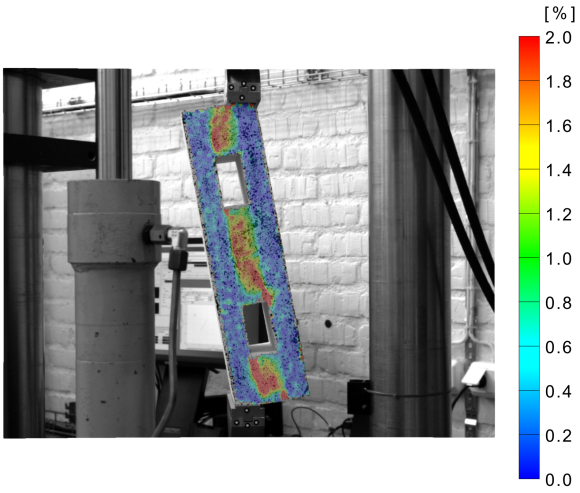

Figure 4.35: Strain distribution observed using ARAMIS right before failure for the low strength specimen of Configuration II.

For the low strength specimen, there is no image to be shown of the specimen after failure due to the specimen splitting in half and falling down. However, it can be observed in Figure 4.35 that, before failure, the largest deformations occurred in the tangential direction of the lamellas in the cross-layer.

The strain distribution in the high strength specimen of Configuration II, just before and directly after failure, as obtained using ARAMIS, is shown in Figure 4.36.

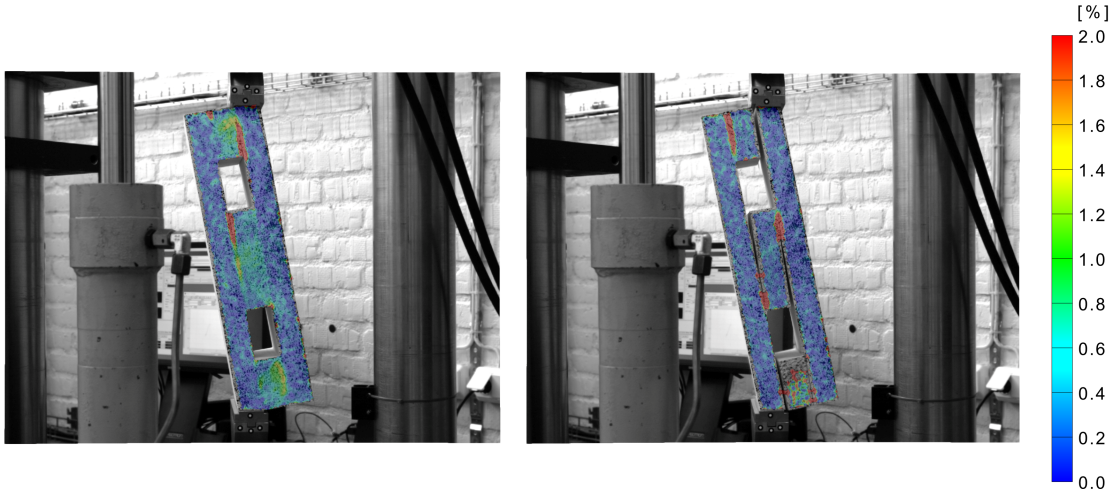

Figure 4.36: Strain distribution observed using ARAMIS right before and after failure for the high strength specimen of Configuration II.

It can be observed in Figure 4.36 that, before failure, the largest deformations occur in the bondlines, whereas smaller deformations can be observed in the lamellas of the cross-layer. After failure, the largest cracks appear in the bondline.

4.5.5 Configuration III

The results of the testing of Configuration III are shown in Figure 4.37.



Figure 4.37: Results from the test of Configuration III, in the order; average, low, and high strength. (April 6th 2022)

It can be observed in Figure 4.37, where all the remaining visible cracks are highlighted in red, that all three specimens failed in the bondlines or in panel shear close to the bondlines. Some shear cracks in the radial direction of the cross-layer lamellas can be observed in all three specimens, as well as a few panel shear cracks in the average and high strength specimen.

The test results for Configuration III are presented in Table 4.30.

Specimen	**Failure load [kN]**	**Deformation [mm]**	**Time [s]**	**Loading rate [mm/min]**
Average strength	30.10	1.82	374	0.5
Low strength	19.35	2.05	225	0.5
High strength	30.38	1.81	181	0.5

Table 4.30: Test results from the testing of Configuration III.

The loading rate for all the specimens of Configuration III was a deformation of 0.5 mm per minute. As can be seen in Table 4.30, the failure load was reached within the recommended loading time for all three specimens.

The load-deformation curves for the testing of Configuration III are illustrated in Figure 4.38.

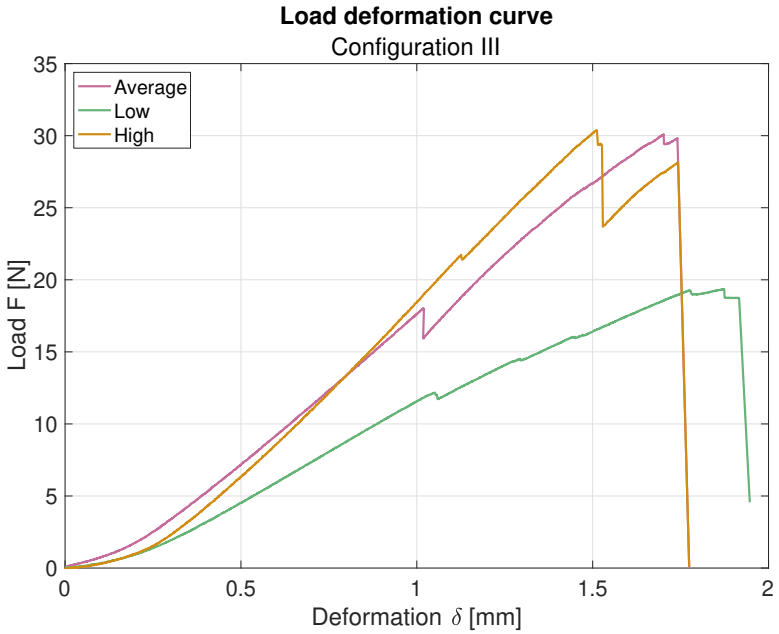

Figure 4.38: Load-deformation curves for Configuration III.

It can be observed in Figure 4.38 that the curves of the average and high strength specimens have a similar inclination, indicating that the two specimens had roughly the same stiffness and that it was higher than the stiffness of the low strength specimen. Furthermore, the failure loads of the average and high strength specimens were almost equal, whereas the failure load of the low strength specimen was considerably lower.

The failure modes and shear strengths of each specimen of Configuration III are presented in Table 4.31. The shear strengths are calculated according to Equations 3.8 – 3.9.

Specimen	Failure mode	Shear strength [MPa]
Average strength	Bondline failure	1.14
Low strength	Bondline failure	0.73
High strength	Panel shear failure	0.58

Table 4.31: Failure modes and calculated shear strengths of Configuration III.

In Table 4.31, it can be observed that both the average and low strength specimens experienced bondline failure, whereas the high strength specimen failed in panel shear. Furthermore, the average strength specimen had the highest shear strength, followed by the low and high strength specimen.

The strain distribution in the average strength specimen of Configuration III just before and directly after failure, as obtained using ARAMIS, is shown in Figure 4.39.

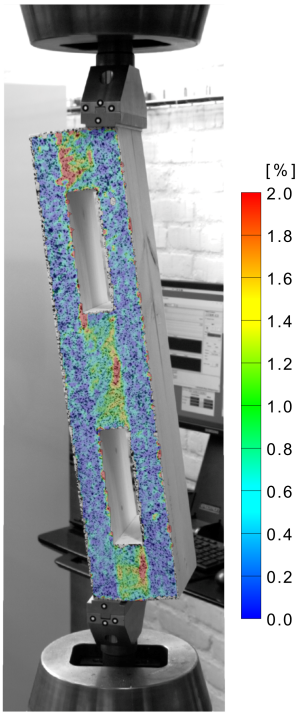

Figure 4.39: Strain distribution observed using ARAMIS right before and after failure for the average strength specimen of Configuration III.

For the average strength specimen, there is no image to be shown of the specimen after failure due to the specimen splitting in half and falling down. However, it can be observed in Figure 4.39 that, before failure, the largest deformations occurred in the bondlines and in the cross-layer.

The strain distribution in the low strength specimen of Configuration III just before and directly after failure, as obtained using ARAMIS, is shown in Figure 4.40.

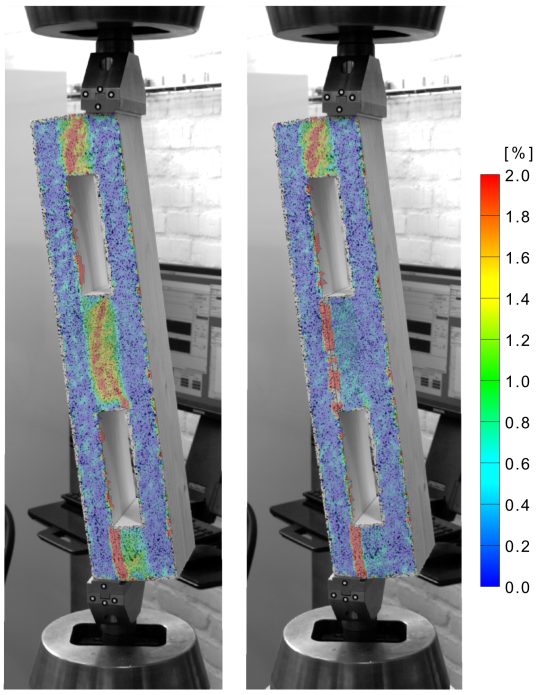

Figure 4.40: Strain distribution observed using ARAMIS right before and after failure for the low strength specimen of Configuration III.

It can be observed in Figure 4.40 that, before failure, the main deformations occurred in the tangential direction of the cross-layer, as well as in the bondline at the bottom of the specimen. After failure, the main deformations are present in the bondlines.

The strain distribution in the high strength specimen of Configuration III just before and directly after failure, as obtained using ARAMIS, is shown in Figure 4.41.

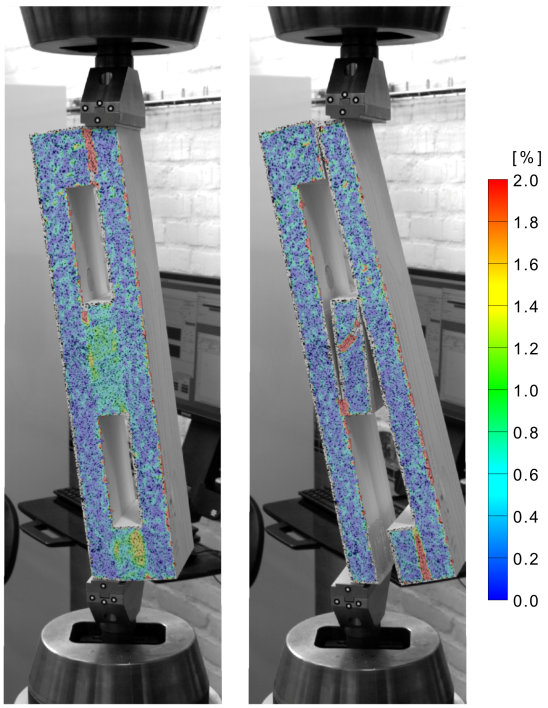

Figure 4.41: Strain distribution observed using ARAMIS right before and after failure for the high strength specimen of Configuration III.

It can be observed in Figure 4.41 that, before failure, the main deformations occurred in the bondline at the top of the specimen. Smaller deformations can also be observed in the cross-layer. After failure, the main deformations are present in the bondlines.

4.5.6 Configuration IV

The results of the testing of Configuration IV are shown in Figure 4.42.



Figure 4.42: Results from the test of Configuration IV, in the order; average, low, and high strength. (May 6th 2022)

It can be observed in Figure 4.42, where all the remaining visible cracks are highlighted in red, that the low and high strength specimens mainly failed in the bondlines or in panel shear close to the bondlines. The low strength specimen also displays significant shear cracking in the radial direction of one cross-layer, as well as some minor cracks in the tangential direction. The average strength specimen shows almost no sign of failure apart from some minor shear cracks in the radial direction.

The test results for Configuration IV are presented in Table 4.32.

Specimen	**Failure load [kN]**	**Deformation [mm]**	**Time [s]**	**Loading rate [mm/min]**
Average strength	62.66	5.07	431	0.5
Low strength	56.46	2.95	214	0.8
High strength	76.79	4.07	296	0.8

Table 4.32: Test results from the testing of Configuration IV.

The loading rate for the average strength specimen of Configuration IV was set to a deformation of 0.5 mm per minute. However, as can be seen in Table 4.32, the loading time exceeded the recommended time limit. Therefore, the loading rate was adjusted to a deformation of 0.8 mm per minute for the low and high strength specimen and it can be observed that the failure load was reached within the recommended time limit for both specimens.

The load-deformation curves for the testing of Configuration IV are illustrated in Figure 4.43.

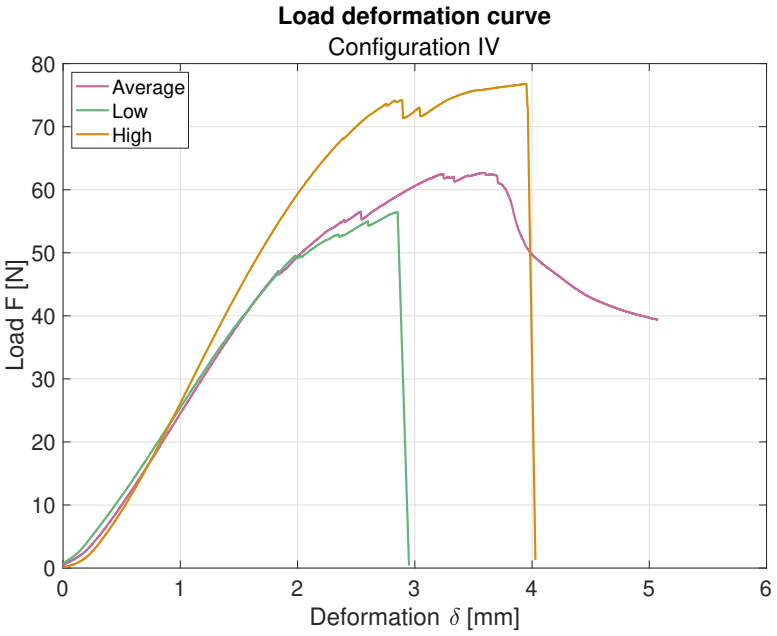

Figure 4.43: Load-deformation curves for Configuration IV.

It can be observed in Figure 4.43 that the failure of the average specimen was ductile, whereas the failure of the low and high strength specimens were of a more brittle character. Furthermore, the failure load of the high strength specimen was the highest, followed by the failure load of the average and low strength specimens.

The failure modes and shear strengths of each specimen of Configuration IV are presented in Table 4.33. The shear strengths are calculated according to Equations 3.8 – 3.10.

Specimen	**Failure mode**	**Shear strength [MPa]**
Average strength	Panel shear failure	1.58
Low strength	Rolling shear failure	1.43
High strength	Bondline failure	1.94

Table 4.33: Failure modes and calculated shear strengths of Configuration IV.

In Table 4.33, it can be observed that both the average and low strength specimens failed in panel shear, whereas the high strength specimen experienced bondline failure. Furthermore, the shear strength of the high strength specimen was the highest, followed by the average and low strength specimens.

4.5.7 Configuration V

The results of the testing of Configuration V are shown in Figure 4.44.



Figure 4.44: Results from the test of Configuration V, in the order; average, low, and high strength. (May 6th 2022)

It can be observed in Figure 4.44, where all the remaining visible cracks are highlighted in red, that all three specimens failed in the cross-layer, i.e. due to rolling shear.

The test results for Configuration V are presented in Table 4.34.

Specimen	**Failure load [kN]**	**Deformation [mm]**	**Time [s]**	**Loading rate [mm/min]**
Average strength	58.83	3.80	309	0.7
Low strength	55.89	4.10	339	0.7
High strength	63.86	4.76	397	0.7

Table 4.34: Test results from the testing of Configuration V.

The loading rate for all the specimens of Configuration V was a deformation of 0.7 mm per minute. As can be seen in Table 4.34, all the specimens reached their respective failure load within the recommended time limit.

The load-deformation curves for the testing of Configuration V are illustrated in Figure 4.45.

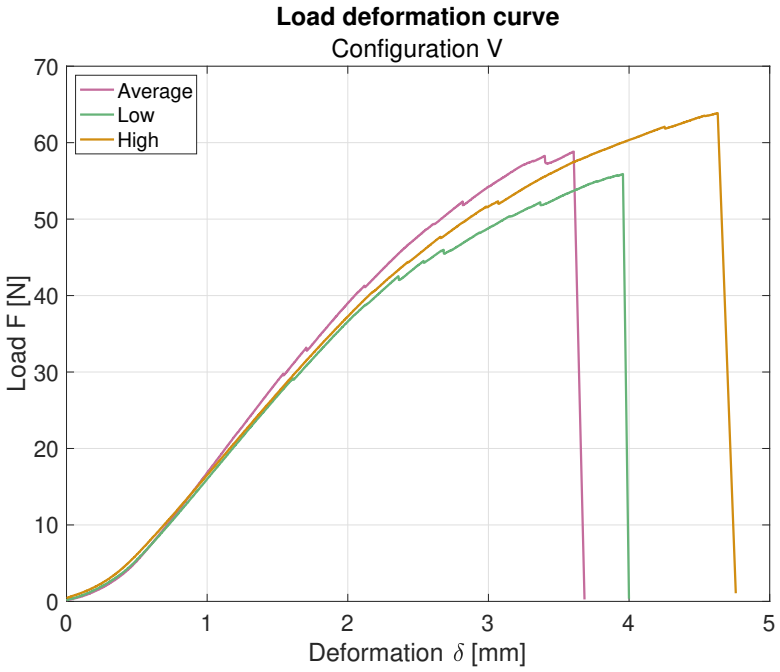

Figure 4.45: Load-deformation curves for Configuration V.

As can be seen in Figure 4.45, all three specimens displayed a similar behaviour and the failure was brittle for all the specimens. The failure load of the high strength specimen was the highest, followed by the average and low strength specimen.

The failure modes and shear strengths of each specimen of Configuration V are presented in Table 4.35. The rolling shear strengths are calculated according to Equation 3.10.

Specimen	**Failure mode**	**Shear strength [MPa]**
Average strength	Rolling shear failure	1.49
Low strength	Rolling shear failure	1.41
High strength	Rolling shear failure	1.61

Table 4.35: Failure modes and calculated shear strengths of Configuration V.

In Table 4.35, it can be observed that all three specimens failed due to rolling shear. Furthermore, the high strength specimen had the highest shear strength, followed by the average and the low strength specimens.

4.5.8 Configuration VI

The results of the testing of Configuration VI are shown in Figure 4.46.

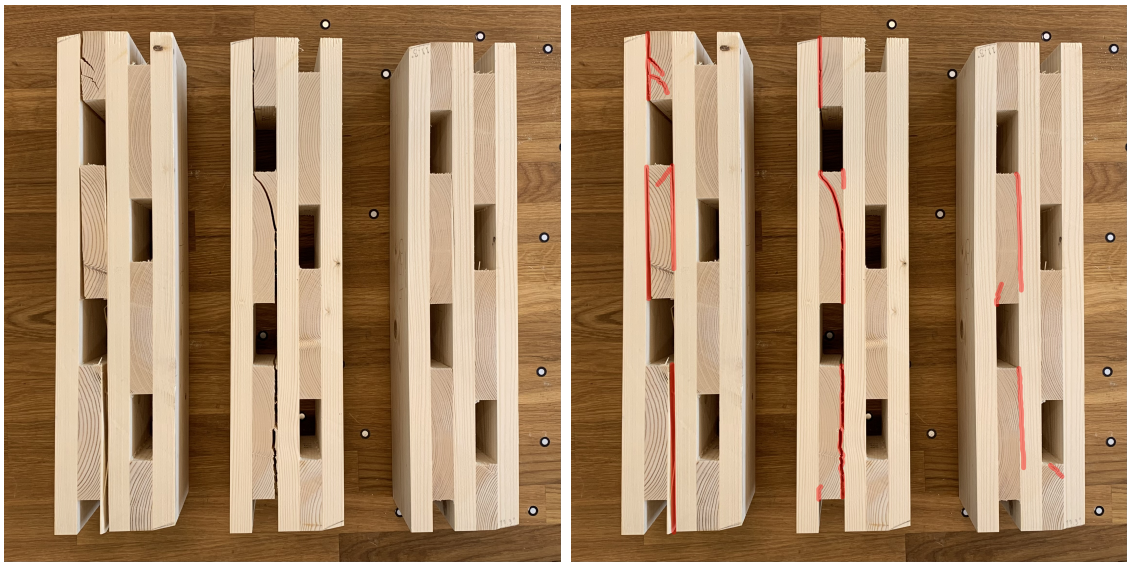

Figure 4.46: Results from the test of Configuration VI, in the order; average, low, and high strength. (May 6th 2022)

It can be observed in Figure 4.46, where all the remaining visible cracks are highlighted in red, that the low strength specimen failed due to rolling shear and the high strength specimen failed due to panel shear. However, it is difficult to determine the ultimate cause of failure in the average strength specimen for it displays significant cracking both due to rolling shear and panel shear, although the most probable cause of failure is rolling shear.

The test results for Configuration VI are presented in Table 4.36.

Specimen	**Failure load [kN]**	**Deformation [mm]**	**Time [s]**	**Loading rate [mm/min]**
Average strength	45.28	3.31	292	0.5
Low strength	46.48	2.85	323	0.5
High strength	42.59	4.17	367	0.5

Table 4.36: Test results from the testing of Configuration VI.

The loading rate for all the specimens of Configuration VI was a deformation of 0.5 mm per minute. As can be observed in Table 4.36, all the specimens reached their respective failure load within the recommended time limit.

The load-deformation curves for the testing of Configuration VI are illustrated in Figure 4.47.

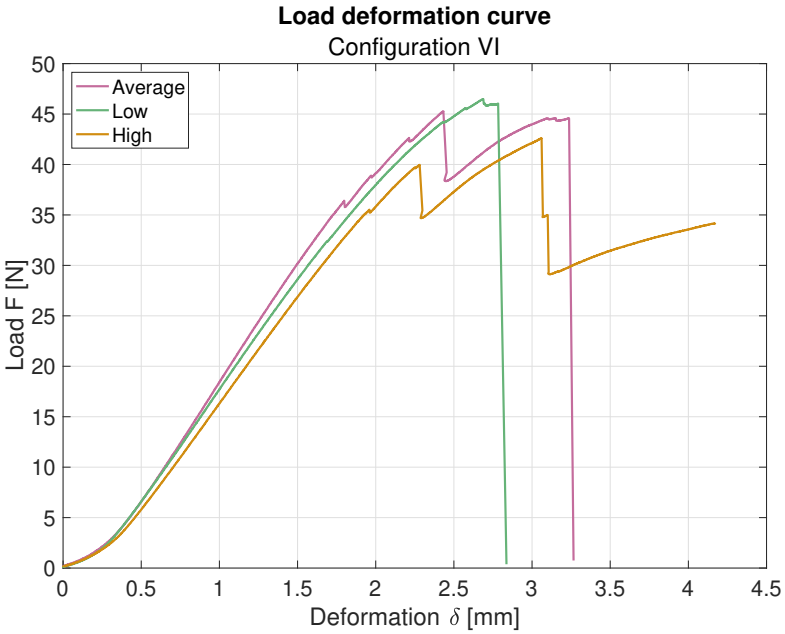

Figure 4.47: Load-deformation curves for Configuration VI.

It can be observed in Figure 4.47 that all the specimens displayed a similar behaviour and that the inclination of the curve for the average strength specimen is the largest, indicating that it had the highest stiffness, followed by the low and high strength specimens, respectively. However, the low strength specimen had the highest failure load, followed by the average and high specimens. Furthermore, it can also be observed that the behaviour of the low strength specimen was brittle in comparison to the behaviour of the average and high strength specimens.

The failure modes and shear strengths of each specimen of Configuration VI are presented in Table 4.37. The shear strengths are calculated according to Equations 3.8 and 3.10.

Specimen	**Failure mode**	**Shear strength [MPa]**
Average strength	Rolling shear failure	1.37
Low strength	Rolling shear failure	1.41
High strength	Panel shear failure	0.86

Table 4.37: Failure modes and calculated shear strengths of Configuration VI.

In Table 4.37, it can be observed that the average and the low strength specimens experienced rolling shear failure, whereas the high strength specimen failed in panel shear. It can also be observed that the low strength specimen had the highest shear strength, followed by the average and the high strength specimens.

4.5.9 Configuration VII

The results of the testing of Configuration VII are shown in Figure 4.48.

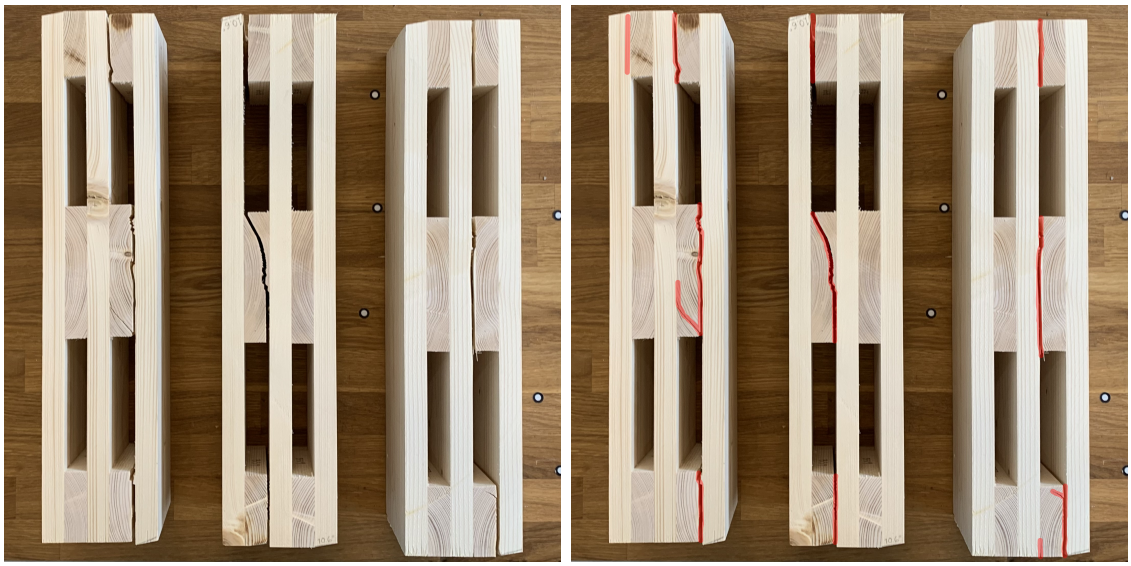

Figure 4.48: Results from the test of Configuration VII, in the order; average, low, and high strength. (May 6th 2022)

It can be observed in Figure 4.48, where all the remaining visible cracks are highlighted in red, that rolling shear failure occurred in the average and the low strength specimens, whereas the high strength specimen mainly failed in the bondline.

The test results for Configuration VII are presented in Table 4.38.

Specimen	**Failure load [kN]**	**Deformation [mm]**	**Time [s]**	**Loading rate [mm/min]**
Average strength	42.50	3.90	458	0.5
Low strength	38.74	3.41	284	0.7
High strength	45.58	3.59	294	0.7

Table 4.38: Test results from the testing of Configuration VII.

For the average strength specimen of Configuration VII, the loading rate was a deformation of 0.5 mm per minute. However, as can be seen in Table 4.38, the loading time exceeded the recommended time limit. Therefore, the loading rate was adjusted to a deformation of 0.7 mm per minute for the low and high strength specimen and it can be observed that the failure load was reached within the recommended time limit for both specimens.

The load-deformation curves for the testing of Configuration VII are illustrated in Figure 4.49.

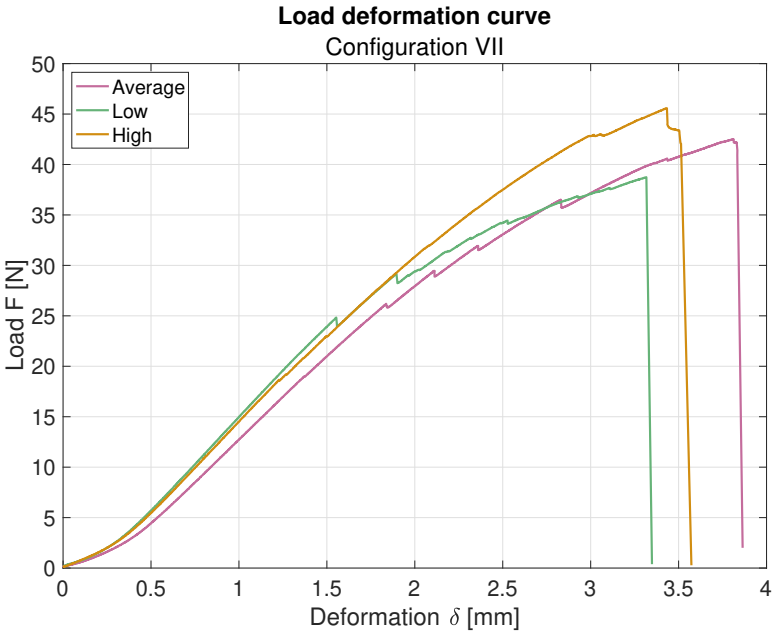

Figure 4.49: Load-deformation curves for Configuration VII.

As can be seen in Figure 4.49, all the specimens showed a similar behaviour. It can be observed that the failure of all three specimens were brittle and that the failure load of the high strength specimen was the highest, followed by the average and low strength specimens.

The failure modes and shear strengths of each specimen of Configuration VII are presented in Table 4.39. The shear strengths are calculated according to Equations 3.9 and 3.10.

Specimen	**Failure mode**	**Shear strength [MPa]**
Average strength	Rolling shear failure	1.61
Low strength	Rolling shear failure	1.47
High strength	Bondline failure	1.73

Table 4.39: Failure modes and calculated shear strengths of Configuration VII.

It can be observed in Table 4.39 that the average and low strength specimens failed due to rolling shear, whereas the high strength specimen experienced bondline failure. Furthermore, the high strength specimen had the highest shear strength, followed by the average and low strength specimen.

4.5.10 Configuration VIII

The results of the testing of Configuration VIII are shown in Figure 4.50.



Figure 4.50: Results from the test of Configuration VIII, in the order; average, low, and high strength. (May 6th 2022)

It can be observed in Figure 4.50, where all the remaining visible cracks are highlighted in red, that the average and high strength specimens failed due to panel shear, whereas the low strength specimen failed in the bondline. It can also be observed that the low and high strength specimens display some minor rolling shear cracks in the cross-layers.

The test results for Configuration VIII are presented in Table 4.40.

Specimen	**Failure load [kN]**	**Deformation [mm]**	**Time [s]**	**Loading rate [mm/min]**
Average strength	43.19	3.03	242	0.7
Low strength	38.07	2.62	213	0.7
High strength	48.53	3.63	297	0.7

Table 4.40: Test results from the testing of Configuration VIII.

The loading rate for all the specimens of Configuration VIII was a deformation of 0.7 mm per minute. As can be observed in Table 4.40, all the specimens reached their respective failure load within the recommended time limit.

The load-deformation curves for the testing of Configuration VIII are illustrated in Figure 4.51.

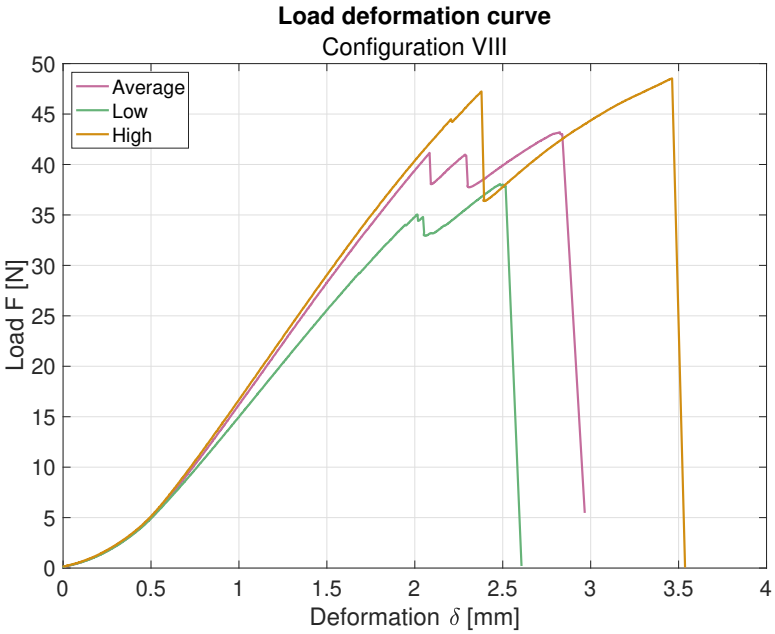

Figure 4.51: Load-deformation curves for Configuration VIII.

As can be seen in Figure 4.51, the curves of the average and high strength specimens have the largest inclination, indicating that they had highest stiffness, followed by the low strength specimen. Furthermore, the high strength specimen had the highest failure load, followed by the average and low strength specimen.

The failure modes and shear strengths of each specimen of Configuration VIII are presented in Table 4.41. The shear strengths are calculated according to Equations 3.8 and 3.9.

Specimen	**Failure mode**	**Shear strength [MPa]**
Average strength	Panel shear failure	0.65
Low strength	Bondline failure	1.15
High strength	Panel shear failure	0.74

Table 4.41: Failure modes and calculated shear strengths of Configuration VIII.

In Table 4.41, it can be observed that both the average and high strength specimen failed in panel shear, whereas the low strength specimen failed in the bondlines. Furthermore, it can also be observed that the shear strength of the low strength specimen was the highest, followed by the high and average strength specimens.

4.5.11 Configuration IX

The results of the testing of Configuration IX are shown in Figure 4.52.

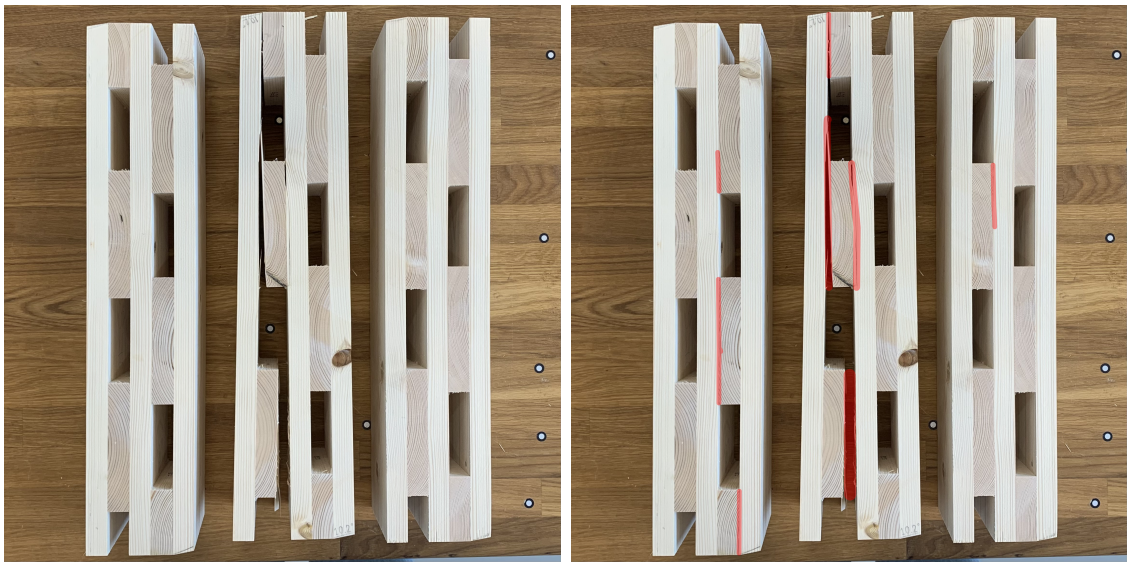

Figure 4.52: Results from the test of Configuration IX, in the order; average, low, and high strength. (May 6th 2022)

It can be observed in Figure 4.52, where all the remaining visible cracks are highlighted in red, that all three specimens failed due to panel shear, although the cracking of both the average and high strength specimens is very subtle.

The test results for Configuration IX are presented in Table 4.42.

Specimen	**Failure load [kN]**	**Deformation [mm]**	**Time [s]**	**Loading rate [mm/min]**
Average strength	41.95	2.51	208	0.7
Low strength	40.74	2.55	210	0.7
High strength	73.31	3.60	287	0.7

Table 4.42: Test results from the testing of Configuration IX.

The loading rate for all the specimens of Configuration IX was a deformation of 0.7 mm per minute. As can be seen in Table 4.42, all the specimens reached their respective failure load within the recommended time limit.

The load-deformation curves for the testing of Configuration IX are illustrated in Figure 4.53.

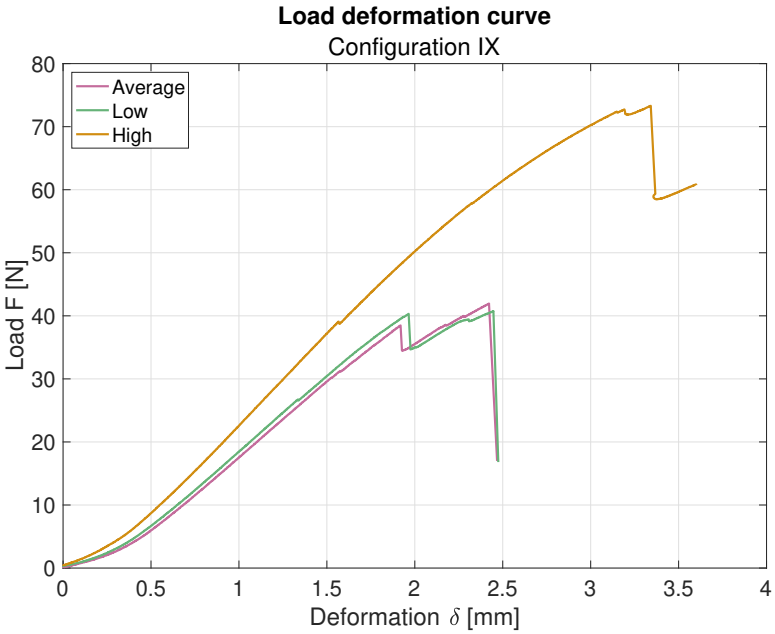

Figure 4.53: Load-deformation curves for Configuration IX.

As can be seen in Figure 4.53, the curve of the high strength specimen has a larger inclination than that of the average and low strength specimens. It can also be observed that the behaviour and the failure load of the average and low strength specimens were close to equal, whereas the failure load of the high strength specimen was considerably higher.

The failure modes and shear strengths of each specimen of Configuration IX are presented in Table 4.43. The shear strengths are calculated according to Equation 3.8.

Specimen	Failure mode	Shear strength [MPa]
Average strength	Panel shear failure	0.76
Low strength	Panel shear failure	0.74
High strength	Panel shear failure	1.33

Table 4.43: Failure modes and calculated shear strengths of Configuration IX.

In Table 4.43, it can be observed that all three specimens failed due to panel shear and that the shear strength of the high strength specimen was the highest, followed by the average and low strength specimens.

4.5.12 Compilation of results

For a better comparison between the results of the various configurations, the results are summarised with regard to failure mode and shear strength, as well as geometrical properties and failure load ratios.

4.5.12.1 Shear strengths and failure modes

The observed failure modes and calculated shear strengths of all the specimens of all configurations are summarised in Table 4.44.

Specimen	Failure mode	Shear strength [MPa]
Configuration I		
Average strength	Bondline failure	1.12
Low strength	Bondline failure	0.71
High strength	Bondline failure	0.88
Configuration II		
Average strength	Bondline failure	0.77
Low strength	Panel shear failure	0.50
High strength	Panel shear failure	0.63
Configuration III		
Average strength	Bondline failure	1.14
Low strength	Bondline failure	0.73
High strength	Panel shear failure	0.58
Configuration IV		
Average strength	Panel shear failure	1.58
Low strength	Rolling shear failure	1.43
High strength	Bondline failure	1.94
Configuration V		
Average strength	Rolling shear failure	1.49
Low strength	Rolling shear failure	1.41
High strength	Rolling shear failure	1.61
Configuration VI		
Average strength	Rolling shear failure	1.37
Low strength	Rolling shear failure	1.41
High strength	Panel shear failure	0.86
Configuration VII		
Average strength	Rolling shear failure	1.61
Low strength	Rolling shear failure	1.47
High strength	Bondline failure	1.73
Configuration VIII		
Average strength	Panel shear failure	0.65
Low strength	Bondline failure	1.15
High strength	Panel shear failure	0.74
Configuration IX		
Average strength	Panel shear failure	0.76
Low strength	Panel shear failure	0.74
High strength	Panel shear failure	1.33

Table 4.44: Summary of the failure modes and calculated shear strengths of all the specimens.

In Table 4.44, it can be observed that nine specimens failed in the bondlines, ten specimens failed due to panel shear, and eight specimens failed due to rolling shear. It can also be observed that the shear strengths vary between 0.50 MPa to 1.94

MPa, from the weakest to the strongest specimen.

4.5.12.2 Geometrical properties and failure load ratios

For the determination of the failure load ratios of the three-layer specimens, Configuration I was used as reference for the length and failure load. The geometrical properties and the results of the calculation of the failure load ratios for the three-layer specimens are presented in Table 4.45.

Configuration	**I**	**II**	**II**
Geometrical properties			
Air gap width b_{airgap} [mm]	0	60	120
Length ratio η_{L} [−]	1.00	1.00	1.33
Volume ratio η_{V} [−]	1.00	0.89	0.83
Material reduction μ_{M} [%]	0.00	11.12	16.67
Failure loads F_{max} [kN]			
Average strength	44.50	20.24	30.10
Low strength	28.14	19.97	19.35
High strength	34.98	24.98	30.38
Adjusted failure loads F_{adjusted} [kN]			
Average strength	44.50	20.24	22.58
Low strength	28.14	19.97	14.51
High strength	34.98	24.98	22.79
Failure load ratio η_{F} [−]			
Average strength	1.00	0.45	0.51
Low strength	1.00	0.71	0.52
High strength	1.00	0.71	0.65

Table 4.45: The geometrical properties and results of the calculation of the failure load ratios for the three-layer specimens.

It can be observed in Table 4.45 that the adjusted failure loads of the specimens vary between 14.51 kN and 44.50 kN, from the weakest to the strongest. It can also be seen that the failure load ratio varies between 0.45 and 1.00 for the average strength specimens and 0.52 and 1.00 for the low strength specimens, whereas for the high strength specimens, the ratio varies between 0.65 and 1.00. Furthermore, it can be observed that the reduction in strength in general correlates to the reduction of material.

For the determination of the failure load ratios of the five-layer specimens, Configuration IV was used as reference for the length and the failure load. The geometrical properties and the results of the calculation of the failure load ratios for the five-layer specimens are presented in Table 4.46.

Configuration	**IV**	**V**	**VI**	**VII**	**VIII**	**IX**
Geometrical properties						
Air gap width b_{airgap} [mm]	0	60	60	120	120	80
Length ratio η_{L} [−]	1.00	1.50	1.25	1.33	1.67	1.39
Volume ratio η_{V} [−]	1.00	0.87	0.87	0.80	0.80	0.84
Material reduction μ_{M} [%]	0.00	13.33	13.33	20.00	20.00	16.00
Failure loads F_{max} [kN]						
Average strength	62.66	58.83	45.28	42.50	43.19	41.95
Low strength	56.46	55.89	46.48	38.74	38.07	40.74
High strength	76.69	63.86	42.59	45.58	48.53	73.31
Adjusted failure loads F_{adjusted} [kN]						
Average strength	62.66	39.22	36.22	31.88	25.91	30.20
Low strength	56.46	37.26	37.18	29.06	22.84	29.33
High strength	76.69	42.57	34.07	34.19	29.12	52.78
Failure load ratio η_{F} [−]						
Average strength	1.00	0.63	0.58	0.51	0.41	0.48
Low strength	1.00	0.66	0.66	0.51	0.40	0.52
High strength	1.00	0.56	0.44	0.45	0.38	0.69

Table 4.46: The geometrical properties and results of the calculation of the failure load ratio for the five-layer specimens.

It can be observed in Table 4.46 that the adjusted failure loads of the specimens vary between 29.06 kN to 76.69 kN, from the weakest to the strongest. It can also be seen that the failure load ratio varies between 0.41 and 1.00 for the average strength specimens and 0.40 and 1.00 for the low strength specimens, whereas for the high strength specimens, the ratio varies between 0.38 and 1.00.

Furthermore, it can be observed that for the configurations with the same reduction in material, i.e. Configuration V and VI, as well as Configuration VII and VIII, the configurations with a centered air gap layout perform better in general than those with a shifted air gap layout. It can also be observed that for the configurations with different air gap widths in a shifted layout, i.e. Configuration VI, VIII, and IX, the capacity is the lowest for Configuration VIII, with the largest air gap width of 120 mm, whereas the highest capacity varies between specimens of Configuration VI and IX, with smaller air gaps.

4.6 Finite element modelling in Abaqus

For the results of the finite element modelling, the shear stress distribution in the LR- and RT-plane, as well as the normal stress distribution in the RR-direction, are presented for each configuration. The stress distribution along the paths of the respective configuration, as discussed in Section 3.6.6.1, are also presented and compared. Furthermore, the utilisation ratio of the interaction between the shear stresses and the normal stresses perpendicular to the grain are calculated and plotted for comparison. Note that the scale of the legend vary between the different contour plots.

For the plotting and utilisation ratio calculations of two example configurations, Configuration I and IV, see Appendix B and C, respectively. All the figures that are presented for all the configurations can be found in higher resolution in Appendix H.

4.6.1 Load scale factor

To calculate the load scale factor for the three-layer configurations, the pressure area of Configuration I was used as the reference area, whereas for the five-layer configurations, Configuration IV was used as reference. The properties used to calculate the various ratios and the results of the calculation of the load scale factor are presented in Table 4.47.

Configuration	**Length** L [m]	**Length ratio** η_L [–]	**Pressure area** A_p [m^2]	**Area ratio** η_A [–]	**LSF** [–]
Three-layer					
I	0.360	1.00	0.007	1.00	1.00
II	0.360	1.00	0.007	1.00	1.00
III	0.480	1.33	0.006	0.81	1.08
Five-layer					
IV	0.360	1.00	0.002	1.00	1.00
V	0.540	1.50	0.002	0.984	1.48
VI	0.450	1.25	0.002	0.989	1.24
VII	0.480	1.33	0.002	0.987	1.32
VIII	0.600	1.67	0.002	0.981	1.63
IX	0.500	1.39	0.002	0.986	1.37

Table 4.47: Input data and results of the calculation of the load scale factor.

4.6.2 Calculation of design strength properties

The calculated design strength properties that are used for the determination of the utilisation ratio of the interaction between stresses for each configuration are presented in Table 4.48.

Design strength property	**Denotation**	**Value [MPa]**
Compression perpendicular to grain	$f_{c,90,z,d}$	1.60
Tension perpendicular to grain	$f_{t,90,x,d}$	0.256
	$f_{t,90,y,d}$	0.256
Panel shear	$f_{v,090,xlay,d}$	2.56
	$f_{v,090,xlay,d}$	2.56
Rolling shear (three-layer)	$f_{v,9090,xlay,3,d}$	0.448
	$f_{v,9090,ylay,3,d}$	0.448
Rolling shear (five-layer)	$f_{v,9090,xlay,5,d}$	0.704
	$f_{v,9090,xlay,5,d}$	0.704

Table 4.48: Design strength properties used for the determination of the utilisation ratio.

4.6.3 Configuration I

The shear stress distribution of Configuration I in the LR-plane, i.e. the panel shear stress distribution, is illustrated in Figure 4.54.

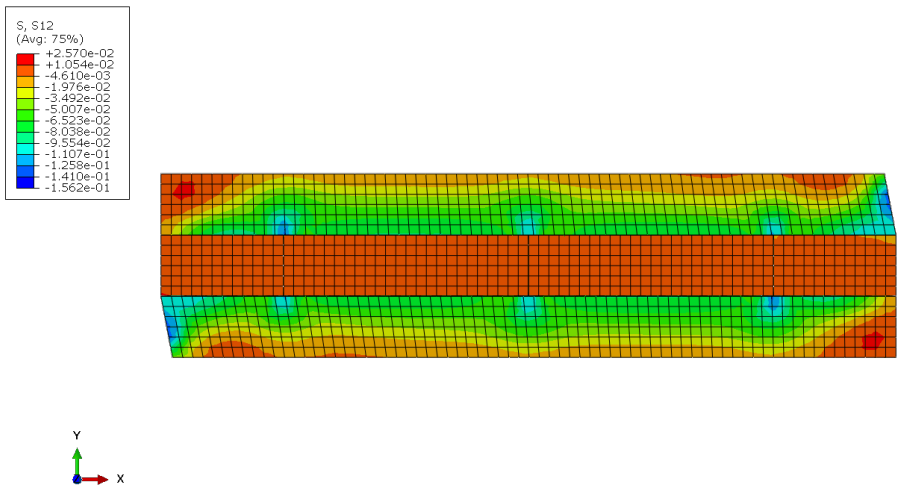

Figure 4.54: Shear stress distribution of Configuration I in the LR-plane.

It can be observed in Figure 4.54 that the inclined surfaces, on which the uniform pressure is applied, are subjected to compression, while the opposite corners are subjected to tension. Furthermore, the longitudinal layers are subjected to high concentrations of compression stresses at the positions where the edges of the cross-layer lamellas and the longitudinal layers intersect.

The shear stress distribution of Configuration I in the RT-plane, i.e. the rolling shear stress distribution, is illustrated in Figure 4.55.

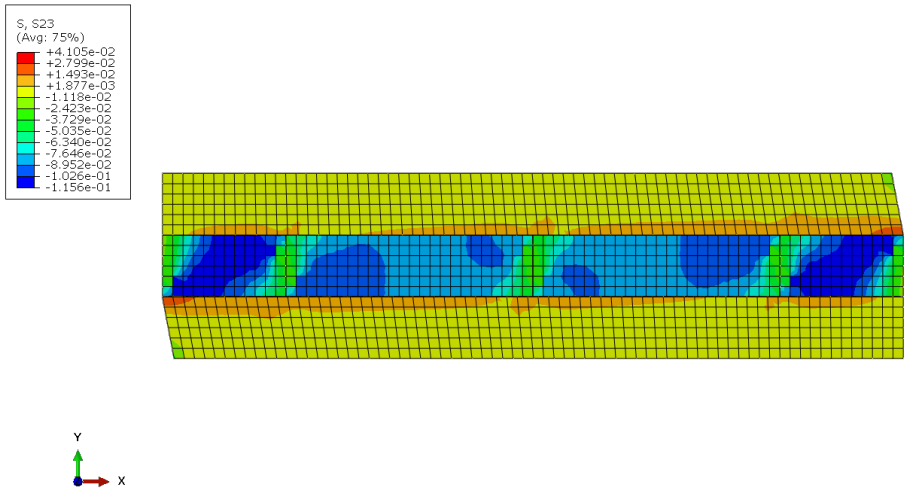

Figure 4.55: Shear stress distribution of Configuration I in the RT-plane.

It can be observed in Figure 4.55 that the cross-layer lamellas are subjected to compression stresses, with the highest concentrations closest to the load application positions. Furthermore, it can be observed that the inner edges of the longitudinal lamellas are subjected to tensile stresses, with the highest concentrations located closest to the load application positions.

The normal stress distribution of Configuration I in the RR-direction, i.e. the stress distribution perpendicular to the grain, is illustrated in Figure 4.56.

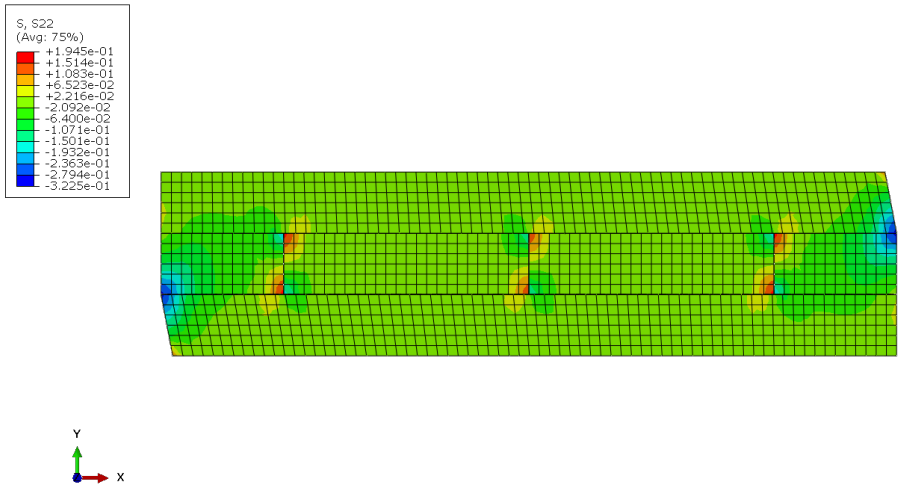

Figure 4.56: Normal stress distribution of Configuration I in the RR-direction.

It can be observed in Figure 4.56 that the opposite corners of the cross-layer lamellas are subjected to high tensile stresses perpendicular to the grain, while the outermost edges, which are closest to the areas of the application of load, are subjected to compression stresses perpendicular to the grain.

The stress distribution along paths in the LR- and RT-plane of the upper longitudinal layer and the cross-layer of Configuration I are shown in Figure 4.57.

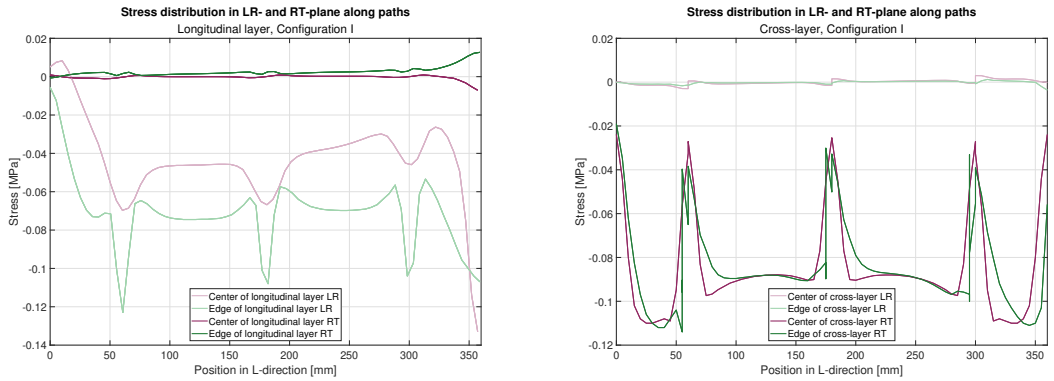

Figure 4.57: Stress distribution along paths in the longitudinal layer and in the cross-layer of Configuration I.

It can be observed in the left graph of Figure 4.57 that the dominant shear stress in the longitudinal layer is the panel shear stress, i.e. the shear stress in the LR-plane. The longitudinal layer is mostly subjected to compression, with distinct stress concentrations by the edges of the cross-layer lamellas. The maximum compression occurs by the position where the pressure is applied, i.e. on the right end of the layer.

For the cross-layer, as can be seen in the right graph of Figure 4.57, the rolling shear stress is the dominant shear stress, i.e. the shear stress in the RT-plane. The cross-layer is only subjected to compression, with high compression stresses along the edges of the cross-layer lamellas. However, the stress concentrations are significantly lower by the intersection between the cross-layer lamellas.

The dominant shear stress and the normal stress distribution in the RR-direction, i.e. the stress distribution perpendicular to the grain, in each layer of Configuration I are shown in Figure 4.58.

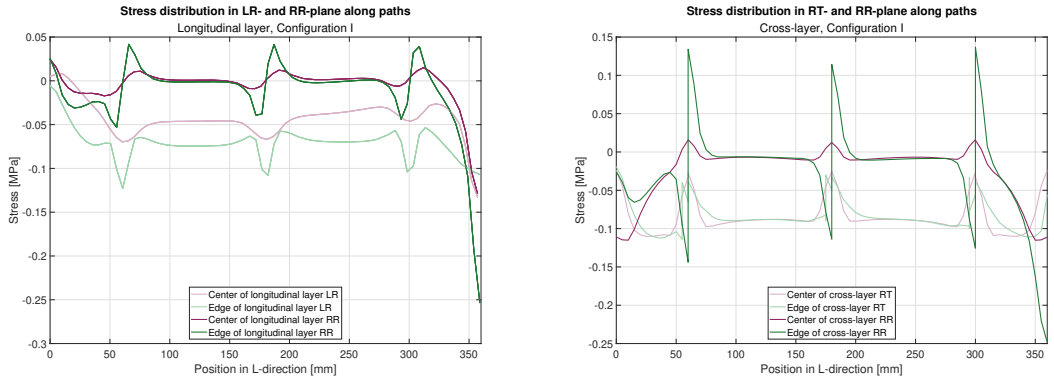

Figure 4.58: The dominant shear stress and stress perpendicular to the grain in the longitudinal layer and in the cross-layer of Configuration I.

It can be observed in the left graph of Figure 4.58 that the dominant stresses in both the LR-plane and the RR-direction of the longitudinal layer occur along the edge paths. It can also be observed that the stresses perpendicular to the grain, i.e in the RR-direction, alternate between tension and compression at the positions of the edges of the cross-layer lamellas, whereas the longitudinal layer is mainly subjected to compression stresses in the LR-plane.

In the right graph of Figure 4.58, it can be observed that the dominant stresses in the RR-direction of the cross-layer occur along the edge path, whereas the stresses in the RT-plane show a similar behaviour and magnitude for both the centre and edge path. It can also be observed that the stresses in the RR-direction alternate between tension and compression at the positions of the edges of the cross-layer lamellas, whereas the cross-layer is only subjected to compression stresses in the RT-plane.

The utilisation ratio of the interaction of Configuration I is presented in Figure 4.59.

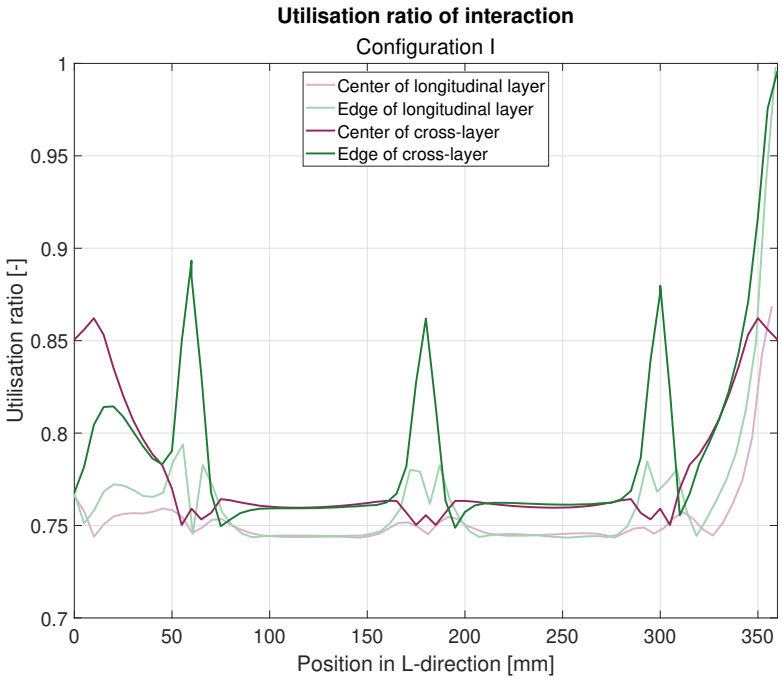

Figure 4.59: Utilisation ratio of interaction in Configuration I.

As can be observed in Figure 4.59, the utilisation ratio is the highest by the right end of the specimen, where the load is applied. The overall utilisation ratio is the highest in the edge path of the cross-layer, with distinct stress concentrations by the edges of the cross-layer lamellas.

4.6.4 Configuration II

The shear stress distribution of Configuration II in the LR-plane, i.e. the panel shear stress distribution, is illustrated in Figure 4.60.

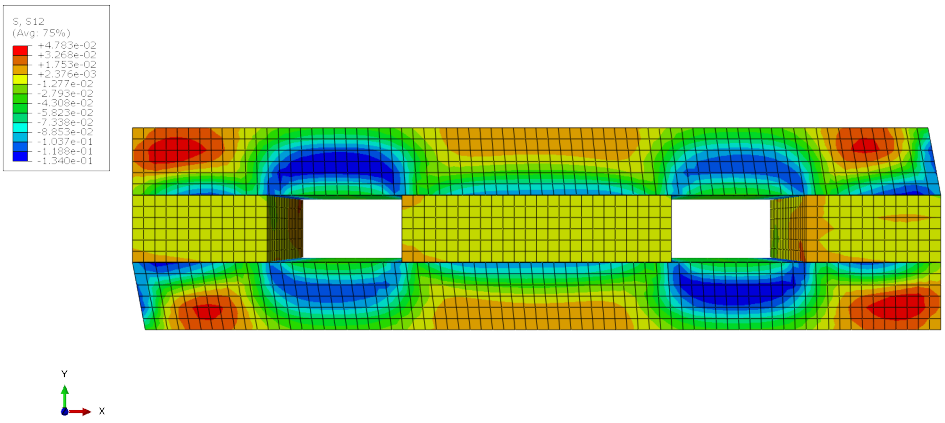

Figure 4.60: Shear stress distribution of Configuration II in the LR-plane.

It can be observed in Figure 4.60 that the inclined surfaces, on which the uniform pressure is applied, are subjected to compression, while the opposite corners of the longitudinal lamellas are subjected to tension. It can also be observed that the areas above and below the air gaps, as well as the inner edges of the longitudinal layers, are subjected to high concentrations of compression stresses, whereas the areas above and below the cross-layer lamellas are subjected to tensile stresses.

The shear stress distribution of Configuration II in the RT-plane, i.e. the rolling shear stress distribution, is illustrated in Figure 4.61.

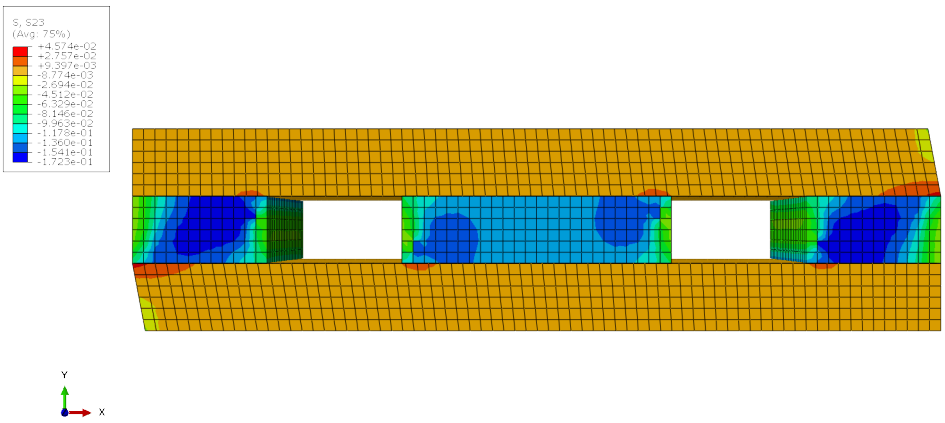

Figure 4.61: Shear stress distribution of Configuration II in the RT-plane.

It can be observed in Figure 4.61 that the cross-layer lamellas are only subjected to compression stresses, with the highest concentrations closest to the load application positions. It can also be observed that the inner edges of the longitudinal lamellas

are mainly subjected to tensile stresses, with the highest concentration at the positions close to the edges of the cross-layers.

The normal stress distribution of Configuration II in the RR-direction, i.e. the stress distribution perpendicular to the grain, is illustrated in Figure 4.62.

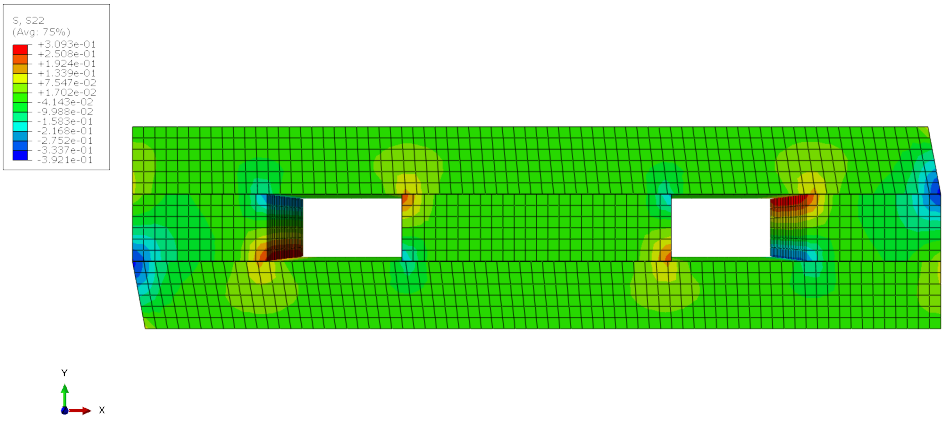

Figure 4.62: Normal stress distribution of Configuration II in the RR-direction.

It can be observed in Figure 4.62 that the corners of the cross-layer lamellas, on opposite sides of the air gaps, are subjected to high tensile stresses perpendicular to the grain, while the opposed corners are subjected to compression stresses perpendicular to the grain. Furthermore, high compression stresses perpendicular to the grain also occur at the positions of the load application.

The stress distribution along paths in the LR- and RT-plane of the upper longitudinal layer and the cross-layer of Configuration II are shown in Figure 4.63.

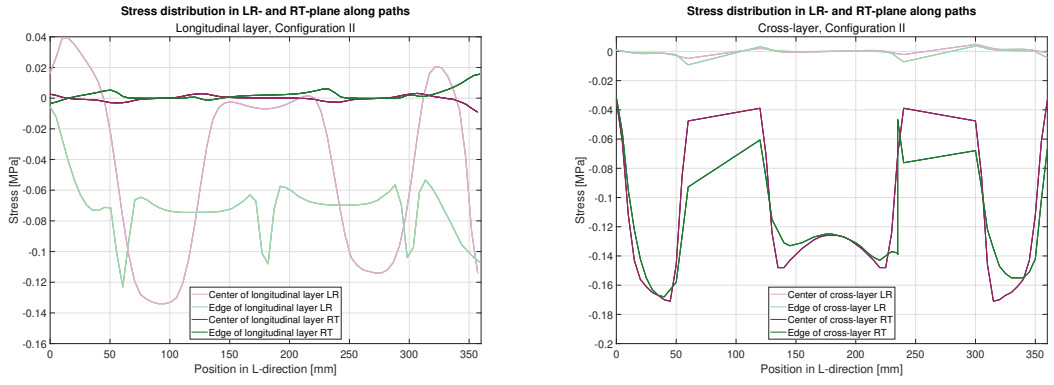

Figure 4.63: Stress distribution along paths in the longitudinal layer and in the cross-layer of Configuration II.

It can be observed in the left graph of Figure 4.63 that the dominant shear stress in the longitudinal layer is the panel shear stress, i.e. the shear stress in the LR-plane. The longitudinal layer is mostly subjected to compression stresses, with distinct

stress concentrations by the positions of the air gaps in the centre path of the layer. Furthermore, the maximum compression stress occurs by the position of the left airgap, whereas the maximum tensile stress occurs on the opposite edge of where the pressure is applied, i.e. on the left edge of the specimen.

For the cross-layer, as can be seen in the right graph of Figure 4.63, the rolling shear stress, i.e. the shear stress in the RT-plane, is the dominant shear stress of the cross-layer. Significant peaks in compression stresses can be observed by the edges of the cross-layer lamellas, i.e. at the locations of the air gaps.

The dominant shear stress and the normal stress distribution in RR-direction, i.e. the stress distribution perpendicular to the grain, in each layer of Configuration II are shown in Figure 4.64.

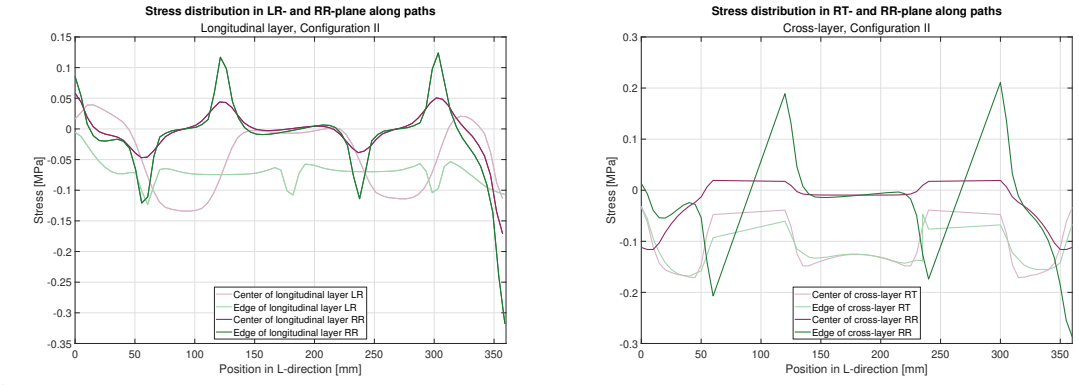

Figure 4.64: The dominant shear stress and stress perpendicular to the grain in the longitudinal layer and in the cross-layer of Configuration II.

It can be observed in the left graph of Figure 4.64 that the dominant stresses in the LR-plane of the longitudinal layer occur along the centre path, whereas the dominant stresses in the RR-direction occur along the edge path. It can also be observed that the stresses perpendicular to the grain, i.e in the RR-direction, alternate between tension and compression by the edges of the cross-layer lamellas, i.e by the corners of the air gaps, whereas the longitudinal layer is mainly subjected to compression stresses in the LR-plane. The highest compression stress occurs perpendicular to the grain in the edge path of the longitudinal layer at the position where the pressure is applied, i.e by the right end of the specimen.

In the right graph of Figure 4.64, it can be observed that the dominant stresses in the RR-direction of the cross-layer occur along the edge path, whereas the stresses in the RT-plane show a similar behaviour and magnitude for both the centre and edge path. It can also be observed that the stresses in the RR-direction alternate between tension and compression by the edges of the cross-layer lamellas, i.e by the corners of the air gaps, whereas the cross-layer is only subjected to compression stresses in the RT-plane.

The utilisation ratio of the interaction of Configuration II is presented in Figure 4.65.

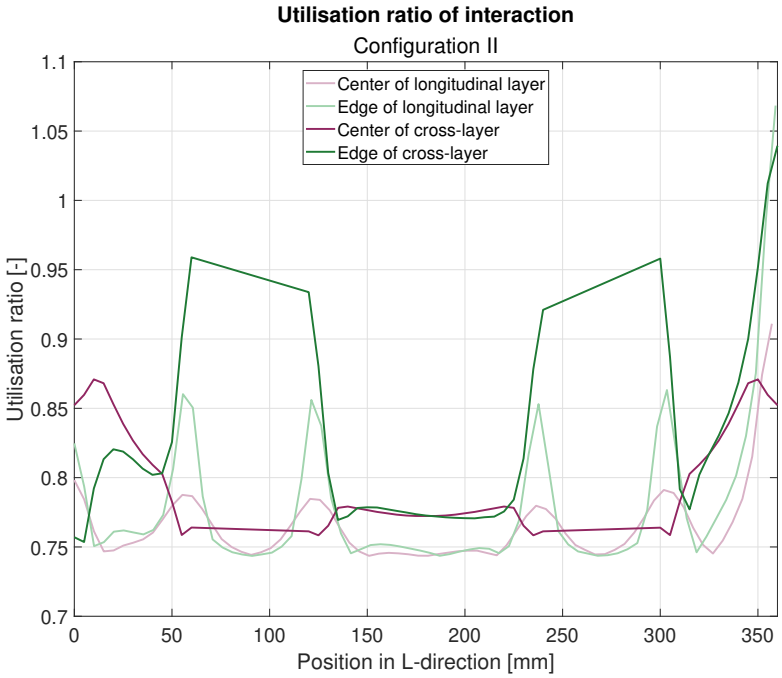

Figure 4.65: Utilisation ratio of interaction in Configuration II.

As can be observed in Figure 4.65, the utilisation ratio is the highest by the right end of the specimen, where the load is applied. However, the overall utilisation ratio is the highest in the edge path of the cross-layer, with distinct stress concentrations by the edges of the cross-layer lamellas, i.e by the corners of the air gaps. Significant peaks in utilisation ratio can also be observed in the edge path of the longitudinal layers at the same positions.

4.6.5 Configuration III

The shear stress distribution of Configuration III in the LR-plane, i.e. the panel shear stress distribution, is illustrated in Figure 4.66.

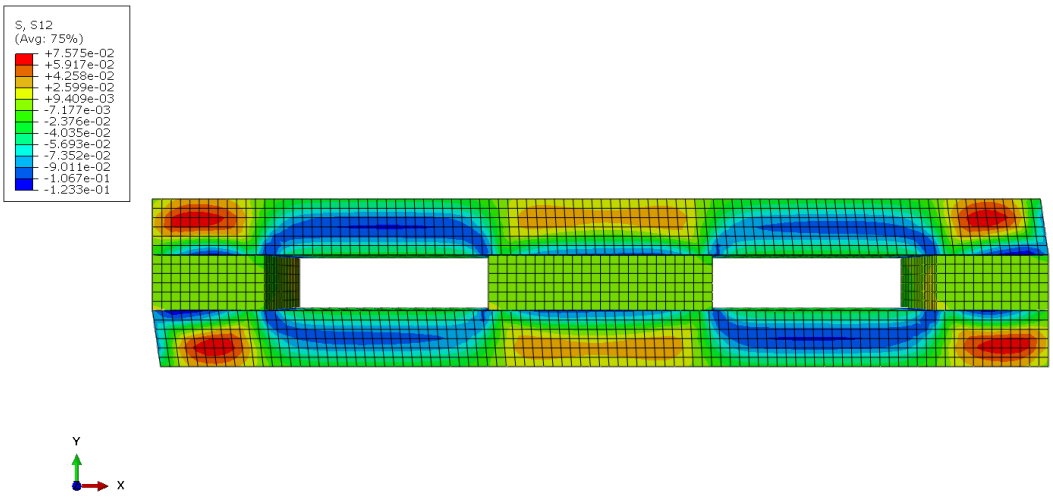

Figure 4.66: Shear stress distribution of Configuration III in the LR-plane.

It can be observed in Figure 4.66 that the inclined surfaces, on which the uniform pressure is applied, are subjected to compression stresses. It can also be observed that the areas above and below the air gaps, as well as the inner edges of the longitudinal layers, are subjected to high concentrations of compression stresses, whereas the areas above and below the cross-layer lamellas are subjected to tension.

The shear stress distribution of Configuration III in the RT-plane, i.e. the rolling shear stress distribution, is illustrated in Figure 4.67.

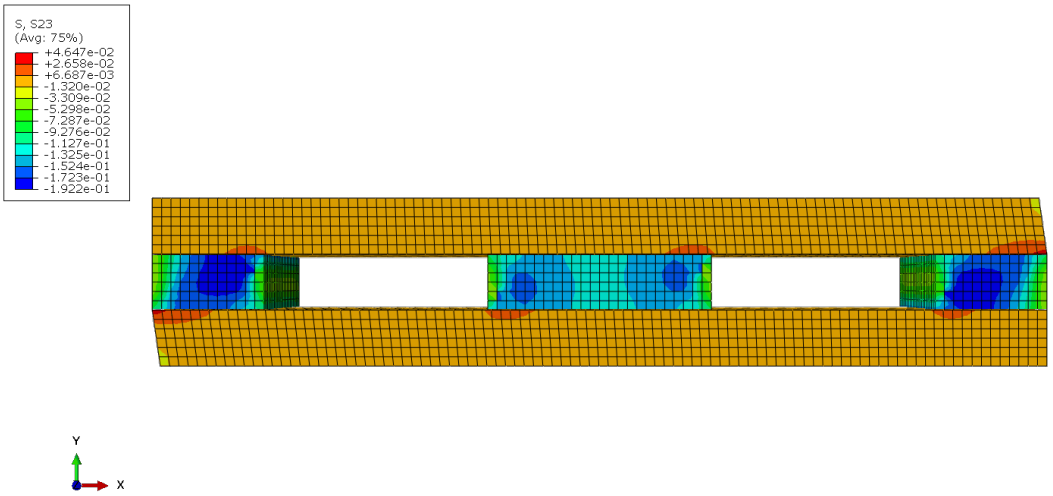

Figure 4.67: Shear stress distribution of Configuration III in the RT-plane.

It can be observed in Figure 4.67 that the cross-layer lamellas are only subjected to compression stresses, with the highest concentrations closest to the load application positions. It can also be observed that the inner edges of the longitudinal layers are mainly subjected to tensile stresses, with the highest concentration at the positions closest to the load application positions.

The normal stress distribution of Configuration III in the RR-direction, i.e. the stress distribution perpendicular to the grain, is illustrated in Figure 4.68.

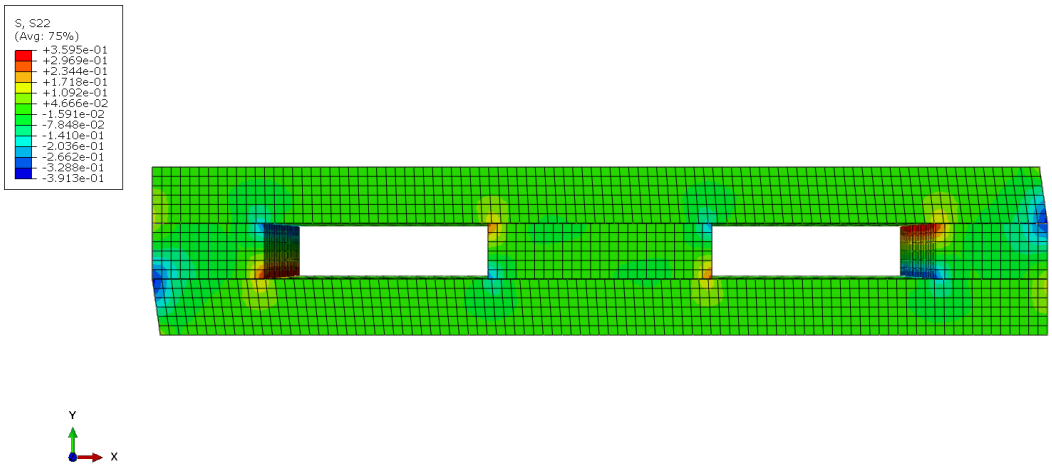

Figure 4.68: Normal stress distribution of Configuration III in the RR-direction.

It can be observed in Figure 4.68 that the corners of the cross-layer lamellas, on opposite sides of the air gaps, are subjected to high tensile stresses perpendicular to the grain, while the opposed corners are subjected to compression stresses perpendicular to the grain. Furthermore, high compression stresses perpendicular to the grain also occur at the load application positions.

The stress distribution along paths in the LR- and RT-plane of the upper longitudinal layer and the cross-layer of Configuration III are shown in Figure 4.69.

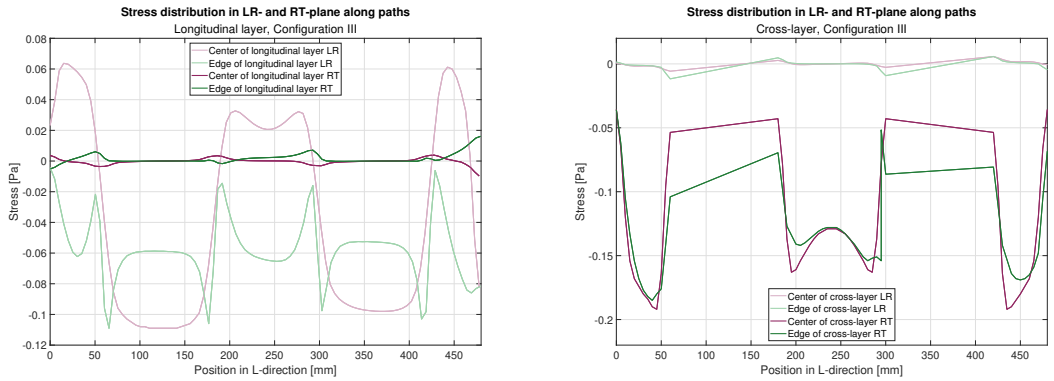

Figure 4.69: Stress distribution along paths in the longitudinal layer and in the cross-layer of Configuration III.

It can be observed in the left graph of Figure 4.69 that the dominant shear stress in the longitudinal layer is the panel shear stress, i.e. the shear stress in the LR-plane. The centre path of the longitudinal layer is mainly subjected to tensile stresses above the cross-layer lamellas and to compression stresses above the air gaps, whereas the edge path of the longitudinal layer is subjected to compression stresses along the entire length. Furthermore, the maximum compression stresses occur by the positions of the air gaps, whereas the maximum tensile stresses occur on the opposite edge of where the pressure is applied, i.e. on the left end of the specimen.

For the cross-layer, as can be seen in the right graph of Figure 4.69, the rolling shear stress, i.e. the shear stress in the RT-plane, is the dominant shear stress. It can be observed that the cross-layer is only subjected to compression stresses in the RT-plane, with significant stresses by the edges of the cross-layer lamellas, i.e. at the locations of the air gaps.

The dominant shear stress and the normal stress distribution in the RR-direction, i.e. the stress distribution perpendicular to the grain, in each layer of Configuration III are shown in Figure 4.70.

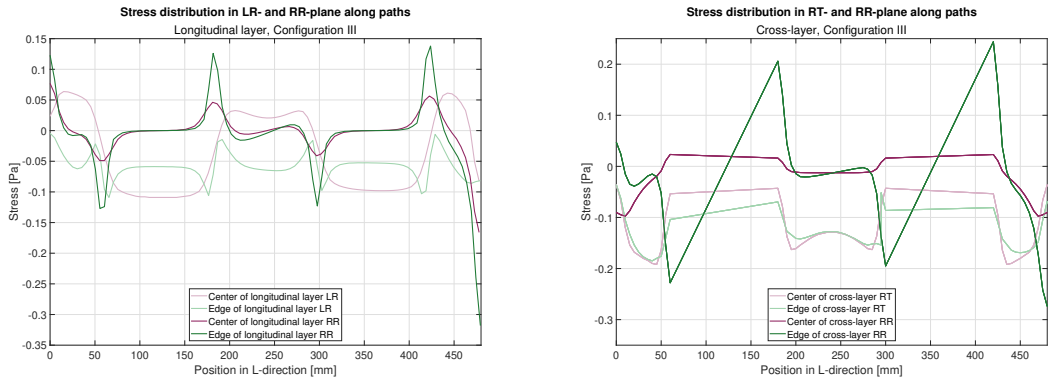

Figure 4.70: The dominant shear stress and stress perpendicular to the grain in the longitudinal layer and in the cross-layer of Configuration III.

It can be observed in the left graph of Figure 4.70 that the dominant stresses in the LR-plane of the longitudinal layer occur along the centre path, whereas the dominant stresses in the RR-direction occur along the edge path. Furthermore, the stresses perpendicular to the grain, i.e in the RR-direction, alternate between tension and compression by the edges of the cross-layer lamellas, i.e by the corners of the air gaps. It can also be observed that the stresses in the LR-plane alternate between tension and compression for the centre path, whereas the edge path of the longitudinal layer is only subjected to compression stresses. The highest compression stresses occur perpendicular to the grain in the edge path of the longitudinal layer at the position where the pressure is applied, i.e by the right end of the specimen, whereas the highest tensile stresses occur perpendicular to the grain in the same path, but at the left edges of the cross-layer lamellas.

In the right graph of Figure 4.70, it can be observed that the dominant stresses in the RR-direction of the cross-layer occur along the edge path, whereas the stresses in the RT-plane show a similar behaviour and magnitude for both the centre and edge path. It can also be observed that the stresses in the RR-direction alternate between tension and compression by the edges of the cross-layer lamellas, i.e by the corners of the air gaps, whereas the cross-layer is only subjected to compression stresses in the RT-plane.

The utilisation ratio of the interaction of Configuration III is presented in Figure 4.71

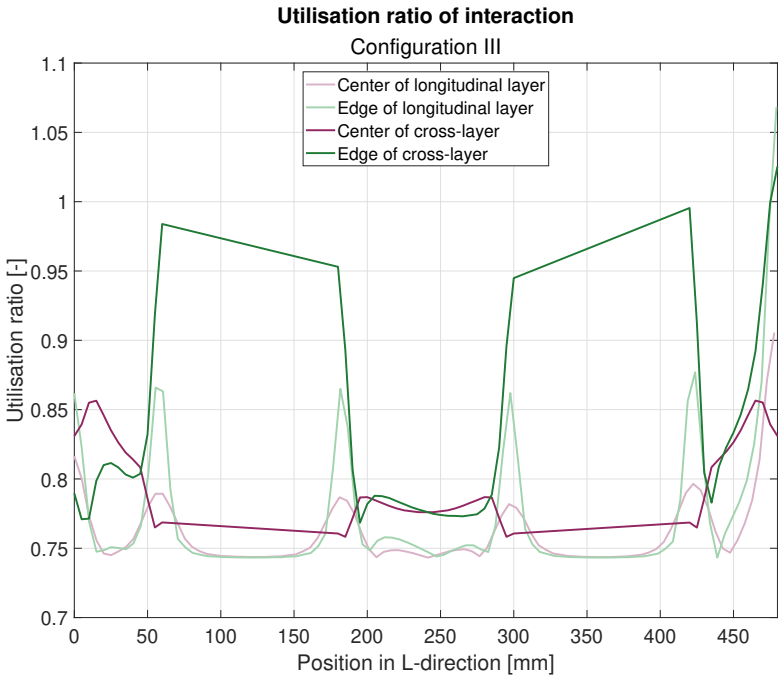

Figure 4.71: Utilisation ratio of interaction in Configuration III.

As can be observed in Figure 4.71, the utilisation ratio is the highest by the right end of the specimen, where the load is applied. However, the overall utilisation ratio is the highest in the edge path of the cross-layer, with distinct stress concentrations by the edges of the cross-layer lamellas, i.e by the corners of the air gaps. Significant peaks in utilisation ratio can also be observed in the edge path of the longitudinal layers at the same positions.

4.6.6 Configuration IV

The shear stress distribution of Configuration IV in the LR-plane, i.e. the panel shear stress distribution, is illustrated in Figure 4.72.

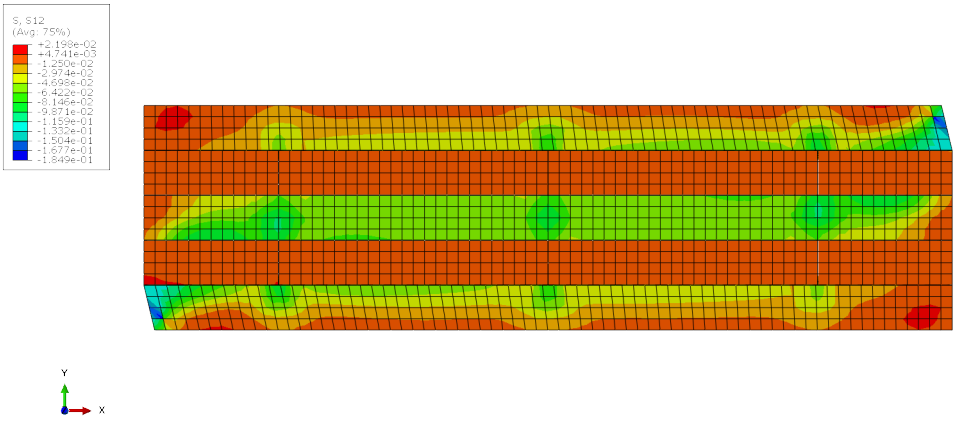

Figure 4.72: Shear stress distribution of Configuration IV in the LR-plane.

It can be observed in Figure 4.72 that the inclined surfaces, on which the uniform pressure is applied, are subjected to compression, while the opposite corners of the lamellas are subjected to tension. Furthermore, the outer longitudinal layers display concentrations of compression stresses at the positions where the edges of the cross-layer lamellas and the longitudinal layers intersect, whereas the mid longitudinal layer is subjected to compression stresses all along the entire length, with the exception of the ends, which are subjected to tension.

The shear stress distribution of Configuration IV in the RT-plane, i.e. the rolling shear stress distribution, is illustrated in Figure 4.73.

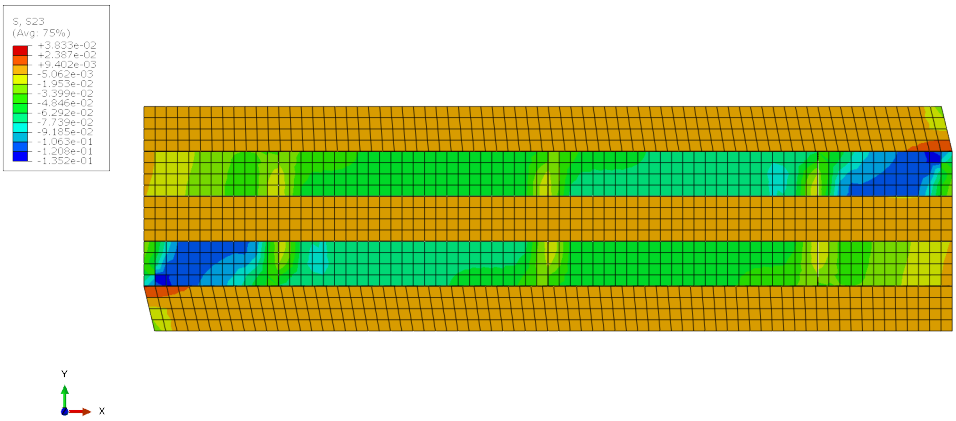

Figure 4.73: Shear stress distribution of Configuration IV in the RT-plane.

It can be observed in Figure 4.73 that the cross-layer lamellas are subjected to compression stresses, with the highest concentrations closest to the load application positions. Furthermore, it can be observed that the inner edges of the longitudinal lamellas are subjected to tensile stresses close to the positions of the load application.

The normal stress distribution of Configuration IV in the RR-direction, i.e. the stress distribution perpendicular to the grain, is illustrated in Figure 4.74.

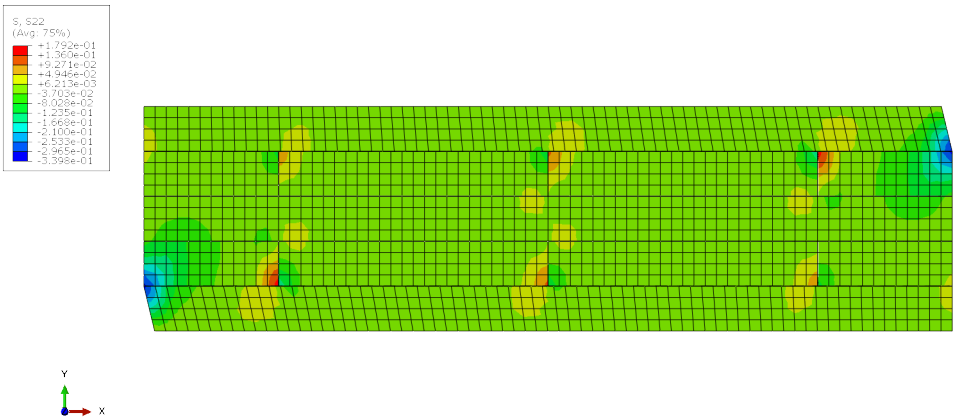

Figure 4.74: Normal stress distribution of Configuration IV in the RR-direction.

It can be observed in Figure 4.74 that the opposite corners of the inner cross-layer lamellas are subjected to tensile stresses perpendicular to the grain, while the outermost corners, which are closest to the areas of the application of load, are subjected to compression stresses perpendicular to the grain. Furthermore, the longitudinal layers display similar stress concentrations in the corresponding positions.

The stress distribution along paths in the LR- and RT-plane of the upper longitudinal layer, the cross-layer, and the mid longitudinal layer of Configuration IV are shown in Figure 4.75.

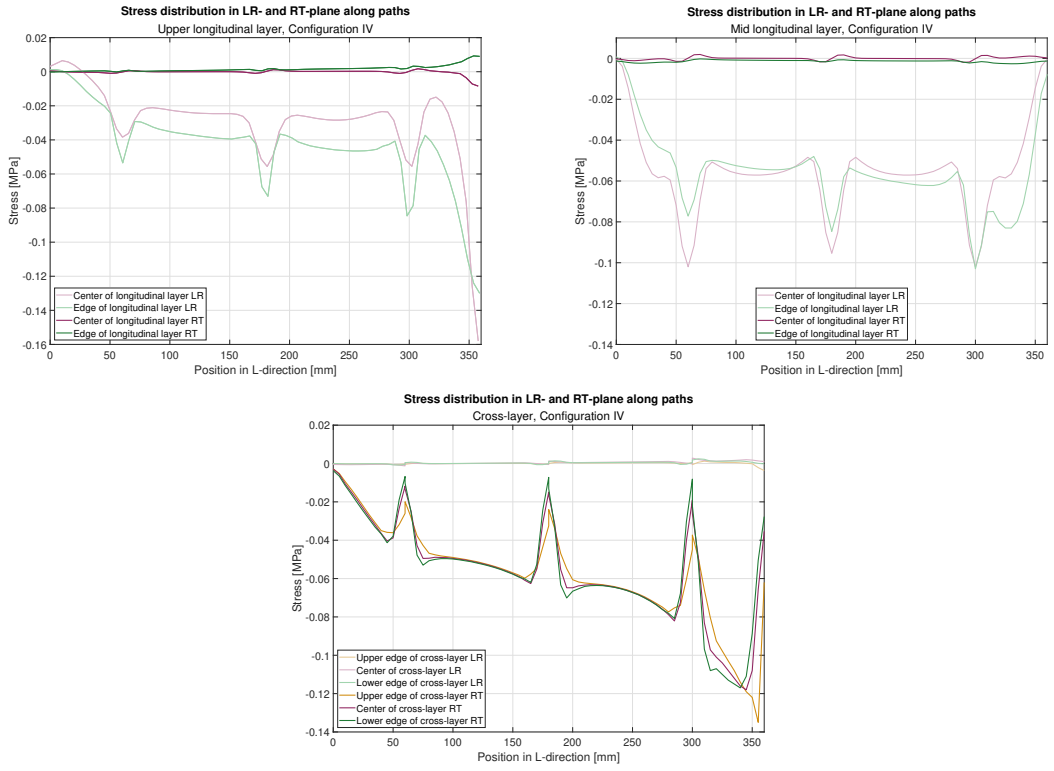

Figure 4.75: Stress distribution along paths in the upper longitudinal layer, the mid longitudinal layer, and the cross-layer of Configuration IV.

It can be observed in the top left graph and the top right graph of Figure 4.75 that the dominant shear stress in the upper longitudinal layer and the mid longitudinal layer is the panel shear stress, i.e. the shear stress in the LR-plane. For the upper longitudinal layer, there is a significant increase in compression stress by the right end of the layer, i.e. at the position of the load application, whereas for the mid longitudinal layer, the stress distribution is more or less symmetrical along the length. As can be seen in both graphs of the longitudinal layers, there are significant peaks in compression stress by the edges of the cross-layer lamellas.

For the cross-layer, as can be seen in the bottom graph of Figure 4.75, the rolling shear stress is the dominant shear stress, i.e. the shear stress in the RT-plane. Similar to the upper longitudinal layer, an increase in compression stress can be observed by the right end of the specimen, i.e. at the position of the load application. It can also be observed that there is a significant decrease in stress by the edges of the cross-layer lamellas.

The dominant shear stress and the normal stress distribution in the RR-direction, i.e. the stress distribution perpendicular to the grain, in each layer of Configuration IV are shown in Figure 4.76.

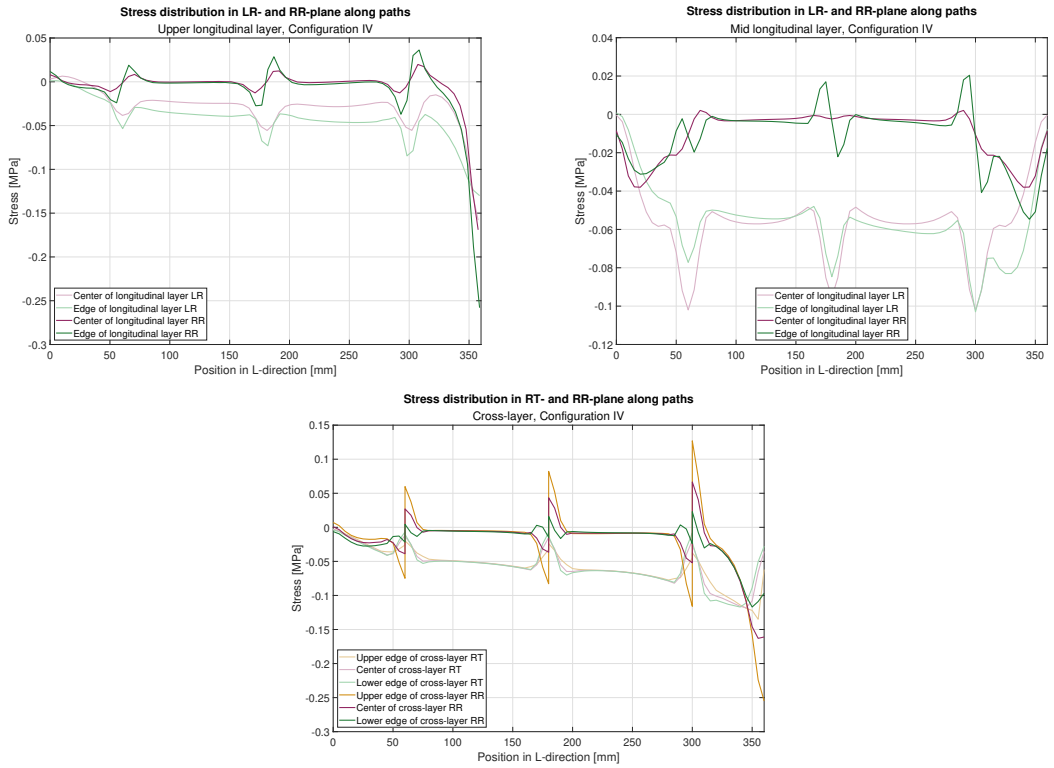

Figure 4.76: The dominant shear stress and stress perpendicular to the grain in the upper longitudinal layer, the mid longitudinal layer, and the cross-layer of Configuration IV.

It can be observed in the top left graph of Figure 4.76 that the stress distribution in the upper longitudinal layer display a similar behaviour in both the LR-plane and the RR-direction, with a significant increase in compression stress by the right end of the layer, i.e. at the position of the load application. It can also be observed that the stresses perpendicular to the grain, i.e. in the RR-direction, alternate between tension and compression, whereas the upper longitudinal layer is mainly subjected to compression stresses in the LR-plane.

In the top right graph of Figure 4.76, it can be observed that the dominant stress of the mid longitudinal layer is the panel shear stress, i.e. the shear stress in the LR-plane. Both the stresses in the LR-plane and in the RR-direction are more or less symmetrical and display significant stress concentrations by the edges of the cross-layer lamellas.

In the bottom graph of Figure 4.76, it can be observed that the dominant stress of the cross-layer is the stress perpendicular to the grain, i.e. the stress in the RR-direction. Both the stresses in the RT-plane and in the RR-direction display a similar behaviour with stress concentrations by the edges of the cross-layer lamellas,

as well as a significant increase in compression stress by the right end of the specimen, i.e. at the position closest to the load application. It can also be observed that the stresses in the RR-direction alternate between tension and compression by the edges of the cross-layer lamellas, whereas the cross-layer is only subjected to compression stresses in the RT-plane.

The utilisation ratio of the interaction of Configuration IV is presented in Figure 4.77.

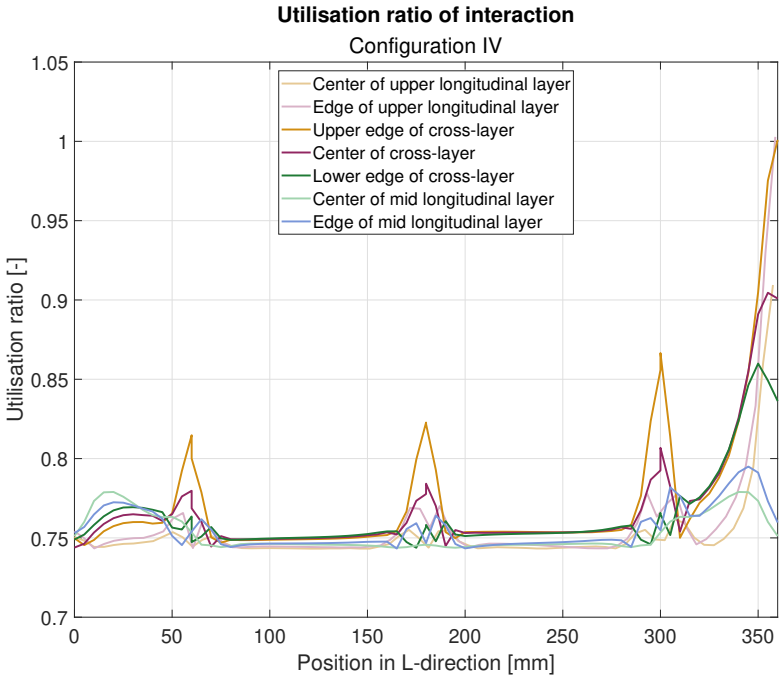

Figure 4.77: Utilisation ratio of interaction in Configuration IV.

As can be observed in Figure 4.77, the utilisation ratio is the highest for the upper edge of the cross-layer, with a significant increase in utilisation ratio close the right of the specimen, end where the pressure is applied. It can also be observed that all paths display a peak in the utilisation ratio by the edges of the cross-layer lamellas.

4.6.7 Configuration V

The shear stress distribution of Configuration V in the LR-plane, i.e. the panel shear stress distribution, is illustrated in Figure 4.78.

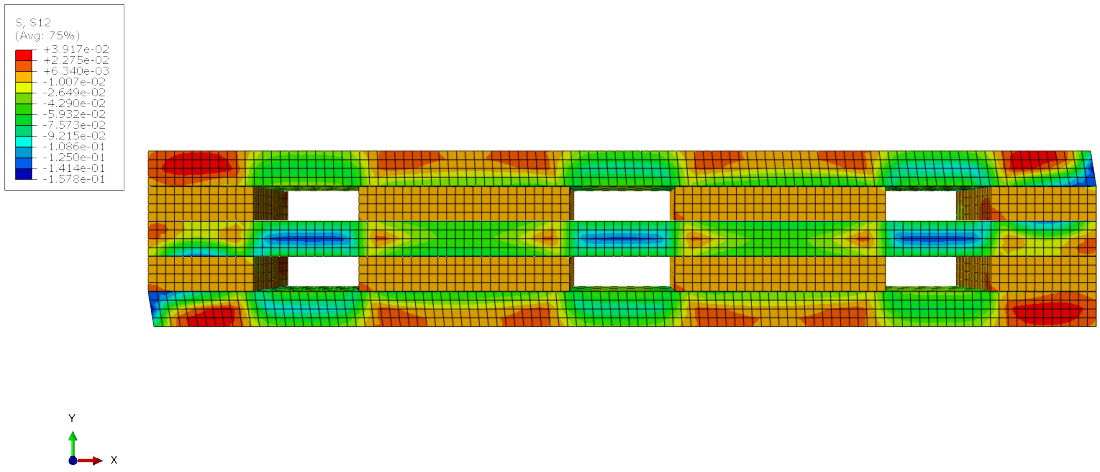

Figure 4.78: Shear stress distribution of Configuration V in the LR-plane.

It can be observed in Figure 4.78 that the inclined surfaces, on which the uniform pressure is applied, are subjected to compression, while the opposite corners of the lamellas are subjected to tension. Furthermore, all the longitudinal layers display concentrations of compression stresses in the areas above and below the air gaps and concentrations of tensile stresses above and below the cross-layer lamellas. However, the compression stresses are more noticeable in the mid longitudinal layer, whereas the tensile stresses are more noticeable in the outer longitudinal layers.

The shear stress distribution of Configuration V in the RT-plane, i.e. the rolling shear stress distribution, is illustrated in Figure 4.79.

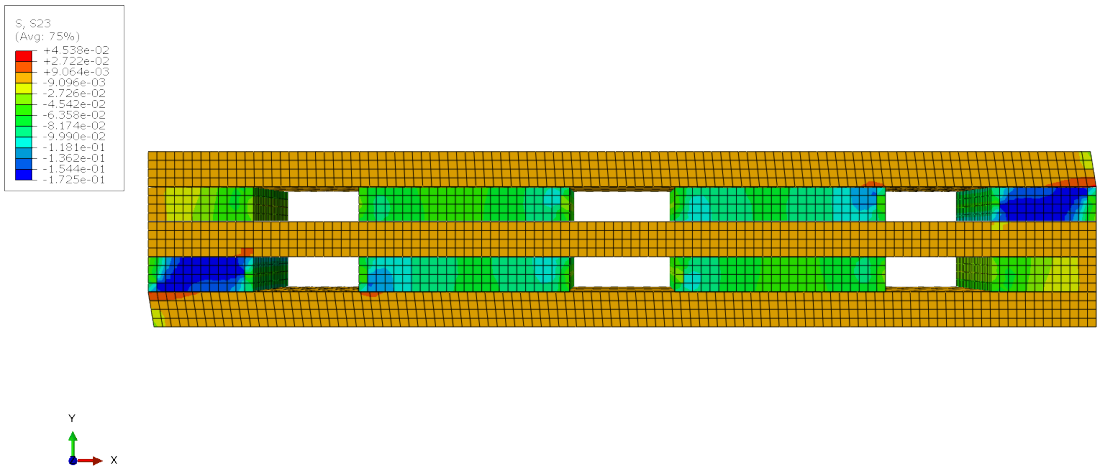

Figure 4.79: Shear stress distribution of Configuration V in the RT-plane.

It can be observed in Figure 4.79 that the cross-layer lamellas are subjected to compression stresses, with the highest concentrations closest to the load application positions. It can also be observed that the inner edges of the longitudinal lamellas are subjected to tensile stresses close to the positions of the load application.

The normal stress distribution of Configuration V in the RR-direction, i.e. the stress distribution perpendicular to the grain, is illustrated in Figure 4.80.

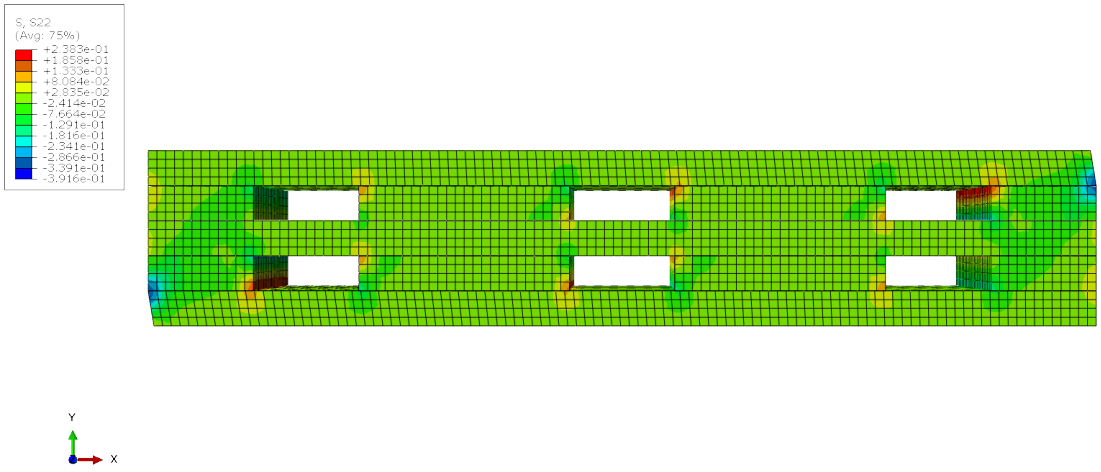

Figure 4.80: Normal stress distribution of Configuration V in the RR-direction.

It can be observed in Figure 4.80 that the corners of the cross-layer lamellas, on opposite sides of the air gaps, are subjected to tensile stresses perpendicular to the grain, while the outermost corners, which are closest to the areas of the application of load, are subjected to compression stresses perpendicular to the grain. Furthermore, the longitudinal layers display similar stress concentrations in the corresponding positions.

The stress distribution along paths in the LR- and RT-plane of the upper longitudinal layer, the mid longitudinal layer, and the cross-layer of Configuration V are shown in Figure 4.81.

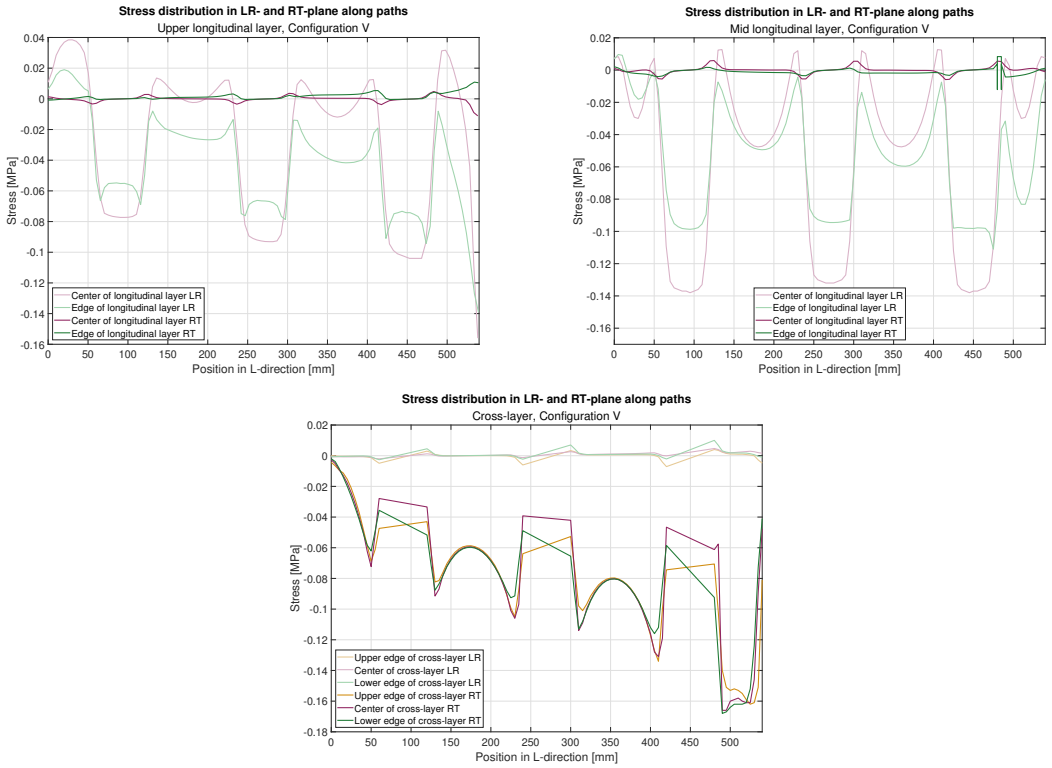

Figure 4.81: Stress distribution along paths in the upper longitudinal layer, the mid longitudinal layer, and the cross-layer of Configuration V.

It can be observed in the top left graph and the top right graph of Figure 4.81 that the dominant shear stress in the upper longitudinal layer and the mid longitudinal layer is the panel shear stress, i.e. the shear stress in the LR-plane. For the upper longitudinal layer, there is a considerable increase in compression stress by the right end of the layer, i.e. at the position closest to the load application, whereas for the mid longitudinal layer, the stress distribution is more or less symmetrical. As can be seen in both graphs for the longitudinal layers, the areas above and below the air gaps are subjected to significant compression stresses, with the highest stress concentrations in the centre of the longitudinal layers. It can also be observed that the mid longitudinal layer is subjected to higher stresses than the upper longitudinal layer, apart from the stress concentration closest to the load application.

For the cross-layer, as can be seen in the bottom graph of Figure 4.81, the rolling shear stress is the dominant shear stress, i.e. the shear stress in the RT-plane. Similar to the upper longitudinal layer, an increase in compression stress can be observed towards the right end of the layer. It can also be observed that the cross-layer is only subjected to compression stresses in the RT-plane and that the magnitude of the stresses in the upper edge path, in comparison to the lower edge path, alternates along the length of the air gaps.

The dominant shear stress and the normal stress distribution in the RR-direction, i.e. the stress distribution perpendicular to the grain, in each layer of Configuration V are shown in Figure 4.82.

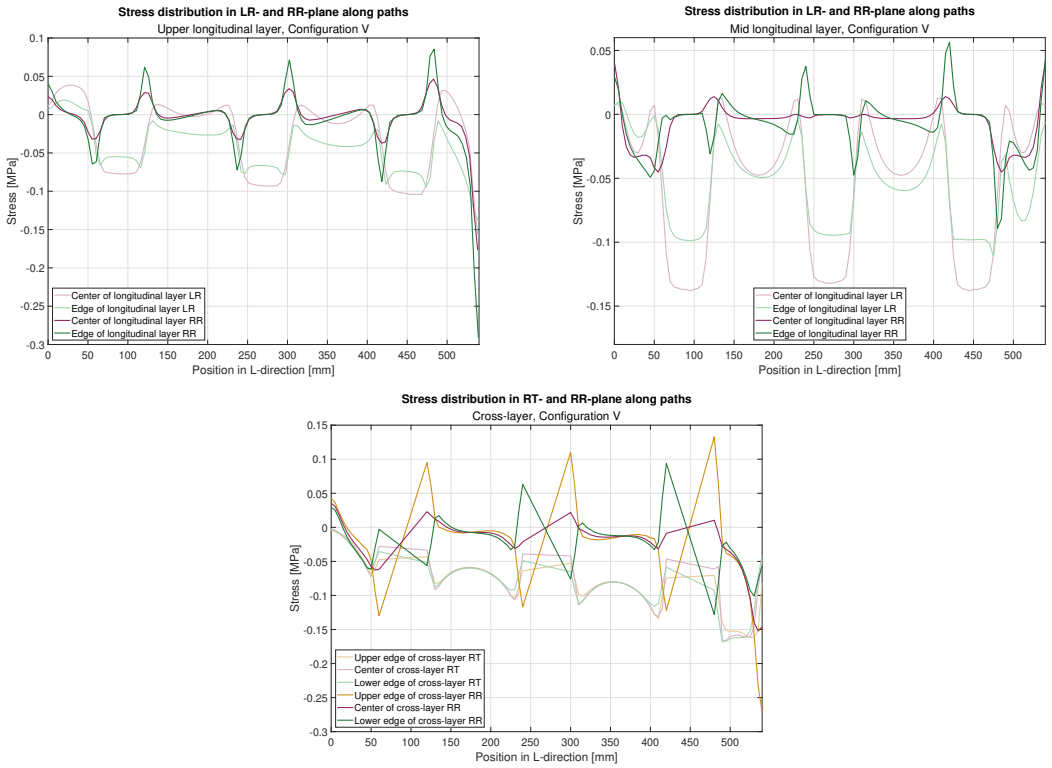

Figure 4.82: The dominant shear stress and stress perpendicular to the grain in the upper longitudinal layer, the mid longitudinal layer, and the cross-layer of Configuration V.

It can be observed in the top left graph of Figure 4.82 that the stress distribution of the upper longitudinal layer in the LR-plane displays high compression stresses along the lengths of the air gaps, whereas the stress distribution in the RR-direction shows high stress concentrations by the edges of the cross-layer lamellas, i.e. by the edges of the air gaps. It can also be observed that the stresses perpendicular to the grain, i.e. in the RR-direction, alternate between tension and compression, whereas the upper longitudinal layer is mainly subjected to compression stresses in the LR-plane. The highest stresses in all four paths are located by the right end of the layer, i.e. at the position of the load application.

In the top right graph of Figure 4.82, it can be observed that the dominant stress of the mid longitudinal layer is the panel shear stress, i.e. the shear stress in the LR-plane. Both the stresses in the LR-plane and in the RR-direction are more or less symmetrical. However, the stress distribution in the LR-plane displays high compression stresses along the lengths of the air gaps, whereas the stress distribution in the RR-direction shows high stress concentrations by the edges of the cross-layer lamellas. Similar to the upper longitudinal layer, it can be observed that the stresses perpendicular to the grain alternate between tension and compression.

In the bottom graph of Figure 4.82, it can be observed that the dominant stress of the cross-layer is the stress perpendicular to the grain, i.e. the stress in the RR-direction. Both the stresses in the RT-plane and in the RR-direction display a similar behaviour, with stress concentrations by the edges of the cross-layer lamellas, as well as a significant increase in compression stress by the right end of the specimen, i.e. at the position closest to the load application. It can also be observed that the stresses in the RR-direction alternate between tension and compression by the edges of the cross-layer lamellas, whereas the cross-layer is only subjected to compression stresses in the RT-plane.

The utilisation ratio of the interaction of Configuration V is presented in Figure 4.83.

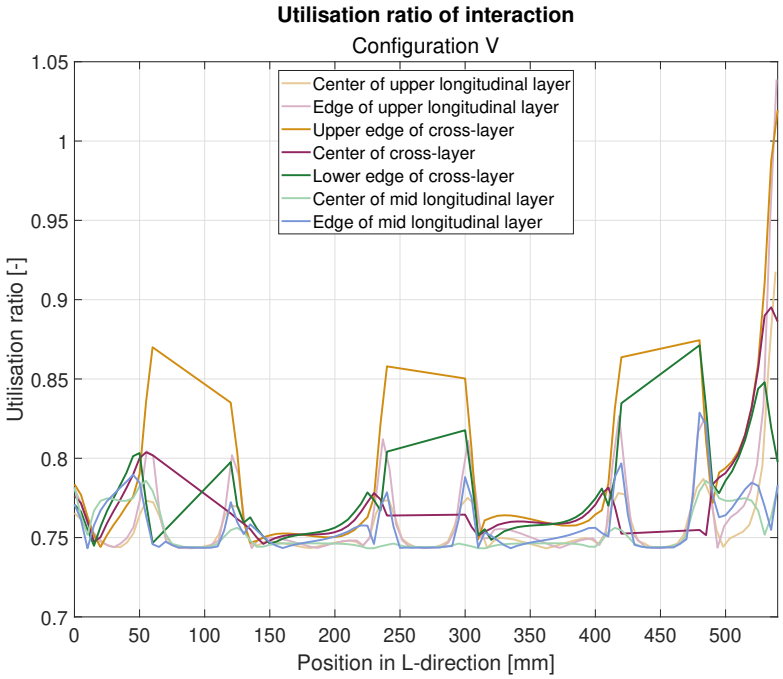

Figure 4.83: Utilisation ratio of interaction in Configuration V.

As can be observed in Figure 4.83, the utilisation ratio is the highest for the upper edge of the cross-layer, with a significant increase in utilisation ratio by the right end of the specimen. Furthermore, local peaks in the utilisation ratio can be observed for all paths by the edges of the cross-layer lamellas, i.e. by the position of the air gaps.

4.6.8 Configuration VI

The shear stress distribution of Configuration VI in the LR-plane, i.e. the panel shear stress distribution, is illustrated in Figure 4.84.

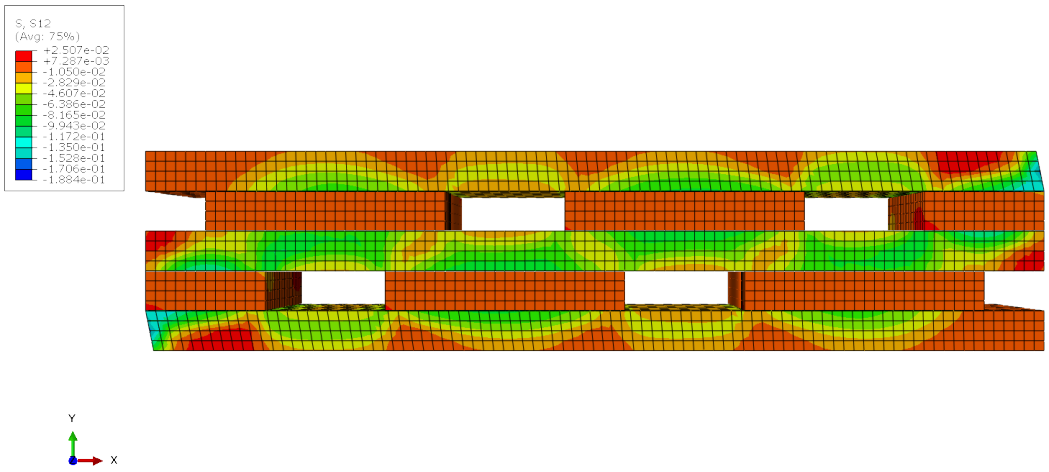

Figure 4.84: Shear stress distribution of Configuration VI in the LR-plane.

It can be observed in Figure 4.84 that the inclined surfaces, on which the uniform pressure is applied, are subjected to compression, while the opposite corners of the lamellas are subjected to minor tensile stresses. It can also be observed that all the longitudinal layers display concentrations of compression stresses in the areas above and below the cross-layer lamellas and that the magnitude of the stresses alternates along with the shift of the air gaps. Furthermore, significant concentrations of compression stresses can be observed in the mid longitudinal layer by the edges of the outermost cross-layer lamellas, as well as by the intersections of the air gaps and the cross-layer lamellas.

The shear stress distribution of Configuration VI in the RT-plane, i.e. the rolling shear stress distribution, is illustrated in Figure 4.85.

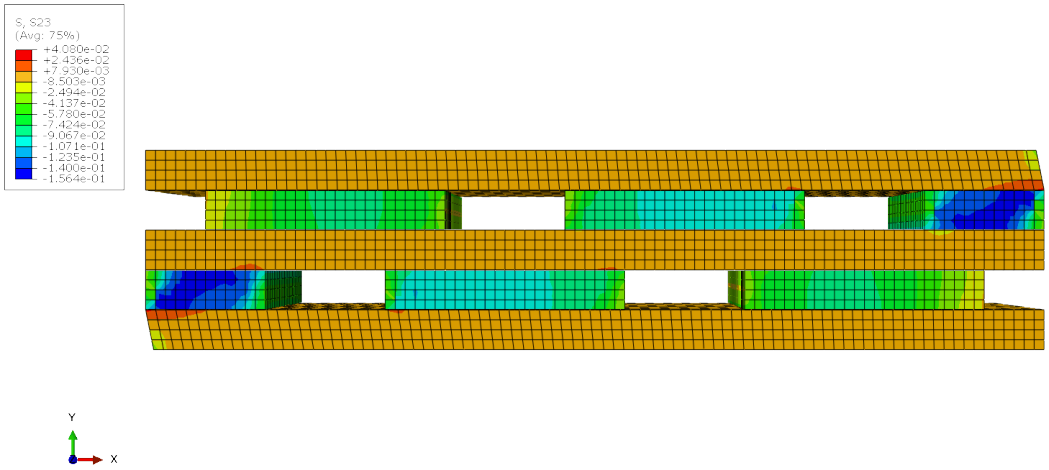

Figure 4.85: Shear stress distribution of Configuration VI in the RT-plane.

It can be observed in Figure 4.85 that the cross-layer lamellas are subjected to compression stresses, with the highest concentrations closest to the load application positions. It can also be observed that the inner edges of the outer longitudinal lamellas are subjected to tensile stresses close to the positions of the load application, as well as by the corners where the longitudinal layers and the cross-layer lamellas intersect.

The normal stress distribution of Configuration VI in the RR-direction, i.e. the stress distribution perpendicular to the grain, is illustrated in Figure 4.86.

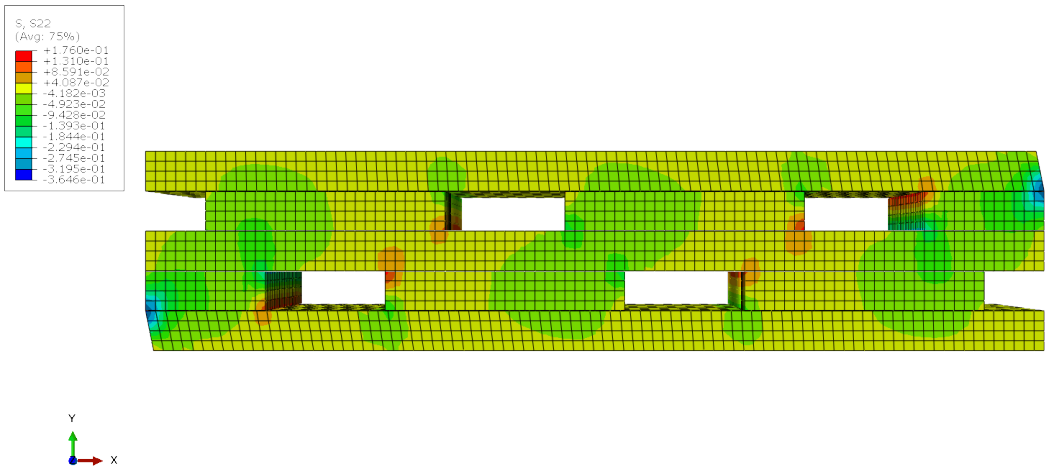

Figure 4.86: Normal stress distribution of Configuration VI in the RR-direction.

It can be observed in Figure 4.86 that the corners of the cross-layer lamellas, on opposite sides of the air gaps, are subjected to tensile stresses perpendicular to the grain, while the outermost edges, which are closest to the areas of the application of load, are subjected to compression stresses perpendicular to the grain. Furthermore, the longitudinal layers display similar stress concentrations in the corresponding positions.

The stress distribution along paths in the LR- and RT-plane of the upper longitudinal layer, the mid longitudinal layer, and the cross-layer of Configuration VI are shown in Figure 4.87.

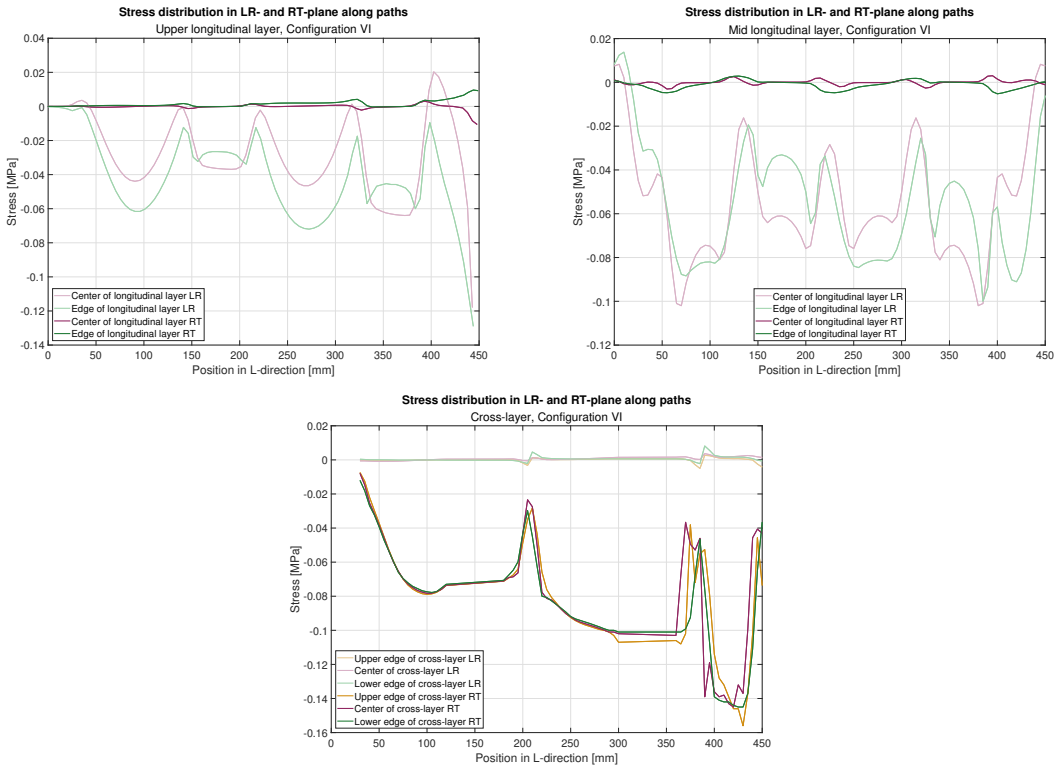

Figure 4.87: Stress distribution along paths in the upper longitudinal layer, the mid longitudinal layer, and the cross-layer of Configuration VI.

It can be observed in the top left graph and the top right graph of Figure 4.87 that the dominant shear stress in the upper longitudinal layer and the mid longitudinal layer is the panel shear stress, i.e. the shear stress in the LR-plane. A significant increase in compression stresses can be observed by the right end of the upper longitudinal layer, where the pressure is applied. For the mid longitudinal layer, the stress distribution is more or less symmetrical, with distinct stress concentrations by the edges of the cross-layer lamellas.

For the cross-layer, as can be seen in the bottom graph of Figure 4.87, the rolling shear stress is the dominant shear stress, i.e. the shear stress in the RT-plane. Similar to the upper longitudinal layer, an increase in compression stresses can be observed towards the right end of the specimen. It can also be observed that there

is a significant decrease in stress by the edges of the cross-layer lamellas. Note that the curves begin at 30 mm since the upper cross-layer, from which the stress distributions are retrieved, begins with an air gap on the left end of the specimen. The dominant shear stress and the normal stress distribution in the RR-direction, i.e. the stress distribution perpendicular to the grain, in each layer of Configuration VI are shown in Figure 4.88.

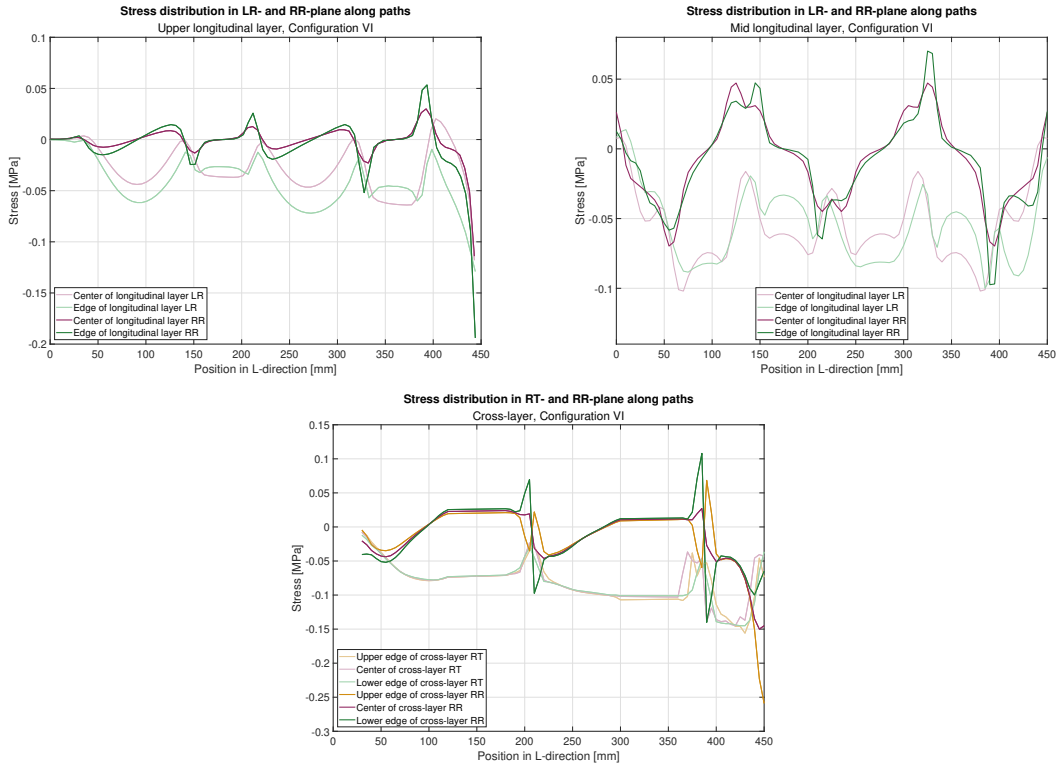

Figure 4.88: The dominant shear stress and stress perpendicular to the grain in the upper longitudinal layer, the mid longitudinal layer, and the cross-layer of Configuration VI.

It can be observed in the top left graph of Figure 4.88 that the stress distribution in the upper longitudinal layer in the LR-plane displays high compression stresses along the lengths of the air gaps, whereas the stress distribution in the RR-direction shows high stress concentrations by the edges of the cross-layer lamellas, i.e. by the edges of the air gaps. It can also be observed that the stresses perpendicular to the grain, i.e. in the RR-direction, alternate between tension and compression, whereas the upper longitudinal layer is mainly subjected to compression stresses in the LR-plane. The highest stresses in all four paths are located by the right end of the layer, i.e. at the position of the load application.

In the top right graph of Figure 4.88, it can be observed that both the stresses in the RT-plane and in the RR-direction display a somewhat similar behaviour, with stress concentrations of the similar magnitude by the edges of the cross-layer lamellas and the air gaps. However, the stresses perpendicular to the grain, i.e. in the RR-direction, alternate between tension and compression, whereas the mid

longitudinal layer is mainly subjected to compression stresses in the LR-plane.

In the bottom graph of Figure 4.88, it can be observed that the dominant stress of the cross-layer is the stress perpendicular to the grain, i.e. the stress in the RR-direction. Both the stresses in the RT-plane and in the RR-direction display a similar behaviour with stress concentrations by the edges of the cross-layer lamellas, as well as an increase in compression stress by the right end of the specimen. However, the stresses in the RR-direction alternate between tension and compression by the edges of the cross-layer lamellas, whereas the cross-layer is only subjected to compression stresses in the RT-plane. Note that the curves begin at 30 mm since the upper cross-layer, from which the stress distributions are retrieved, begins with an air gap on the left end of the specimen.

The utilisation ratio of the interaction of Configuration VI is presented in Figure 4.89

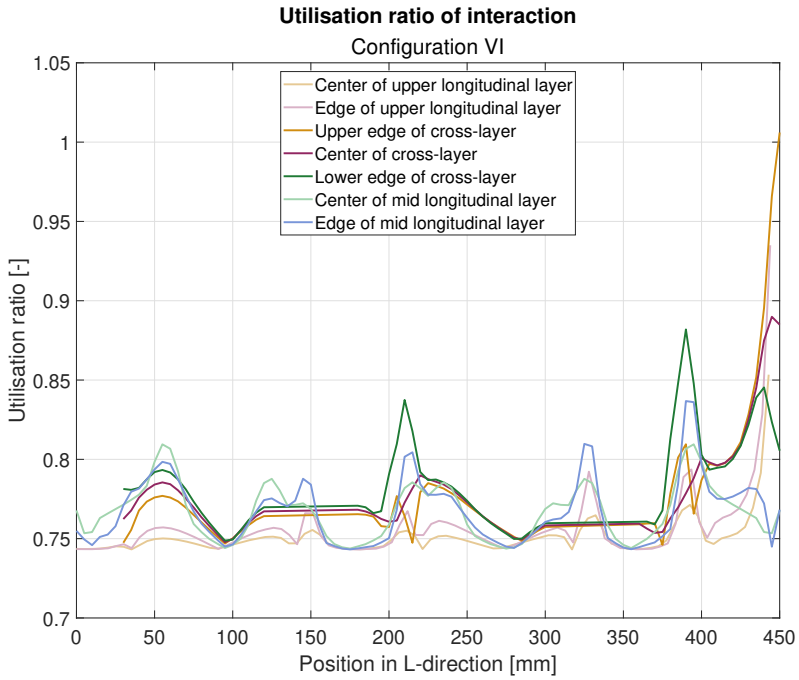

Figure 4.89: Utilisation ratio of interaction in Configuration VI.

As can be observed in Figure 4.89, the upper edge path of the cross-layer has the highest utilisation ratio, whereas all the paths display a rather consistent utilisation ratio, with smaller peaks by the edges of the cross-layer lamellas and the air gaps.

4.6.9 Configuration VII

The shear stress distribution of Configuration VII in the LR-plane is illustrated in Figure 4.90.

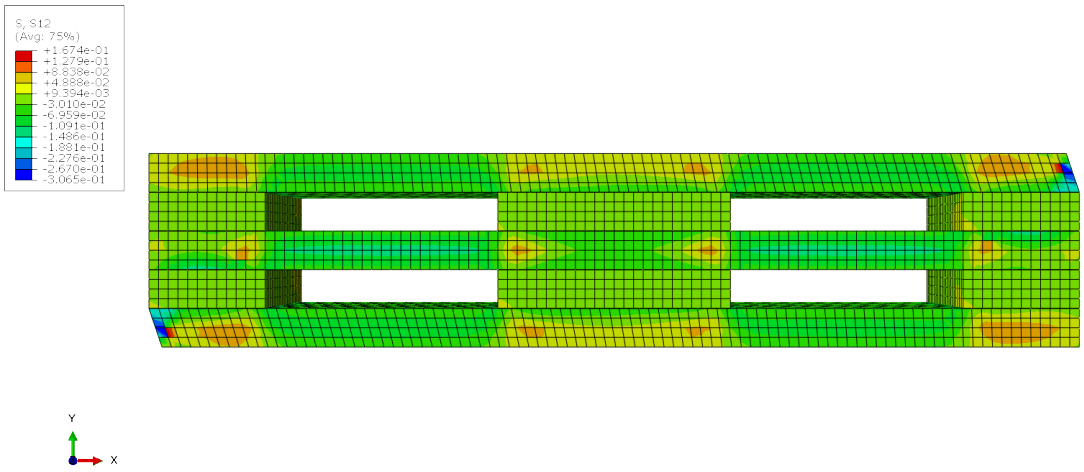

Figure 4.90: Shear stress distribution of Configuration VII in the LR-plane.

It can be observed in Figure 4.90 that the inclined surfaces, on which the uniform pressure is applied, are subjected to compression, while the opposite corners of the lamellas are subjected to tension. It can also be observed that the outer longitudinal layers are subjected to minor compression stresses above and below the air gaps and that larger compression stresses occur in the mid longitudinal layer between the air gaps. Furthermore, all the longitudinal layers display concentrations of tensile stresses by the edges of the air gaps in the areas above and below the cross-layer lamellas.

The shear stress distribution of Configuration VII in the RT-plane, i.e. the rolling shear stress distribution, is illustrated in Figure 4.91.

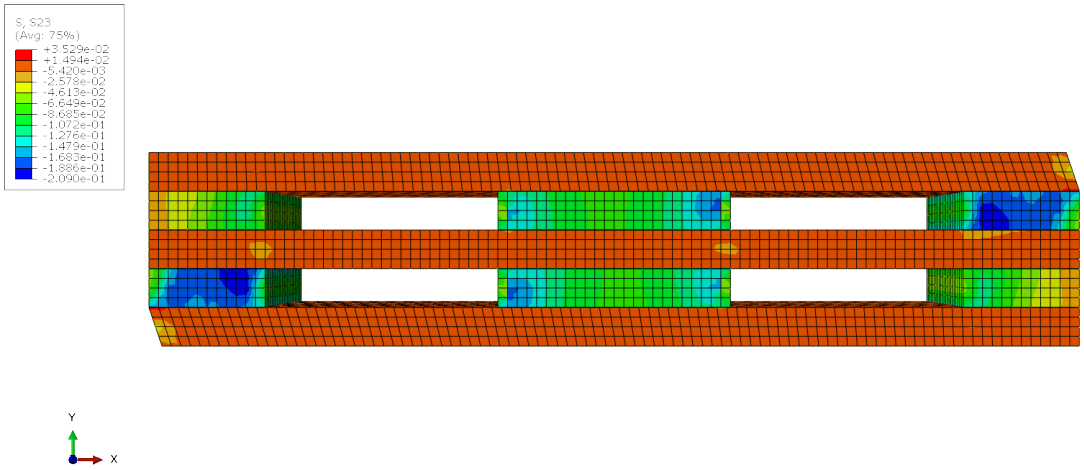

Figure 4.91: Shear stress distribution of Configuration VII in the RT-plane.

It can be observed in Figure 4.91 that the cross-layer lamellas are subjected to compression stresses, with the highest concentrations closest to the load application.

The normal stress distribution of Configuration VII in the RR-direction, i.e. the stress distribution perpendicular to the grain, is illustrated in Figure 4.92.

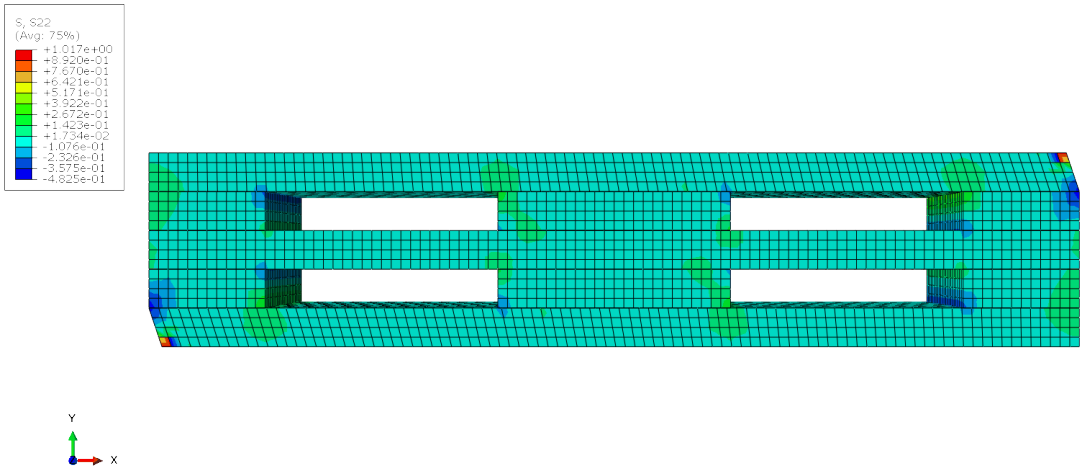

Figure 4.92: Normal stress distribution of Configuration VII in the RR-direction.

It can be observed in Figure 4.92 that the corners of the cross-layer lamellas, on opposite sides of the air gaps, are subjected to tensile stresses perpendicular to the grain, while the opposed corners are subjected to compression stresses perpendicular to the grain. Furthermore, both high compression and tensile stresses occur by the inclined surfaces on which the pressure is applied.

The stress distribution along paths in the LR- and RT-plane of the upper longitudinal layer, the mid longitudinal layer, and the cross-layer of Configuration VII are shown in Figure 4.93.

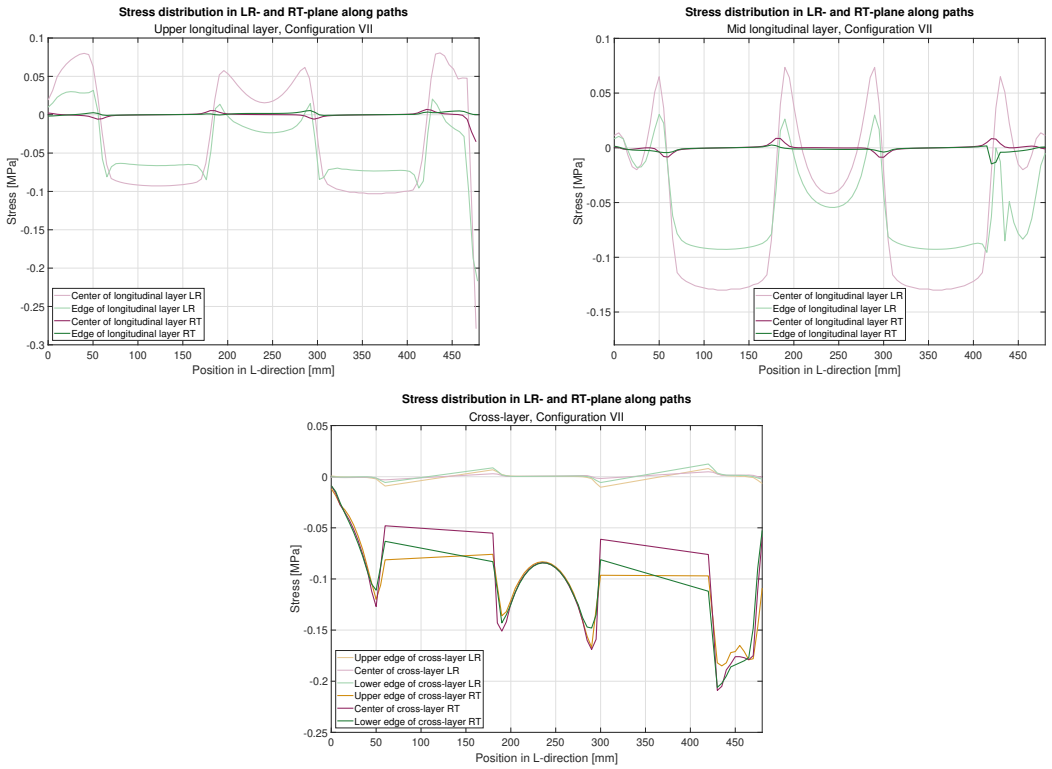

Figure 4.93: Stress distribution along paths in the upper longitudinal layer, the mid longitudinal layer, and the cross-layer of Configuration VII.

It can be observed in the top left graph and the top right graph of Figure 4.93 that the dominant shear stress in the upper longitudinal layer and the mid longitudinal layer is the panel shear stress, i.e. the shear stress in the LR-plane. Both the upper and mid longitudinal layer are subjected to tension above the cross-layer lamellas and compression above the air gaps in the LR-plane. A significant increase in compression stress by the right end of upper longitudinal layer can also be observed.

For the cross-layer, as can be seen in the bottom graph of Figure 4.93, the rolling shear stress is the dominant shear stress, i.e. the shear stress in the RT-plane. Similar to the upper longitudinal layer, an increase in the compression stresses can be observed towards the right end of the layer. It can also be observed that the cross-layer is only subjected to compression stresses in the RT-plane and that the magnitude of the stresses in the upper edge path, in comparison to the lower edge path, alternates along the length of the air gaps.

The dominant shear stress and the normal stress distribution in the RR-direction, i.e. the stress distribution perpendicular to the grain, in each layer of Configuration VII are shown in 4.94.

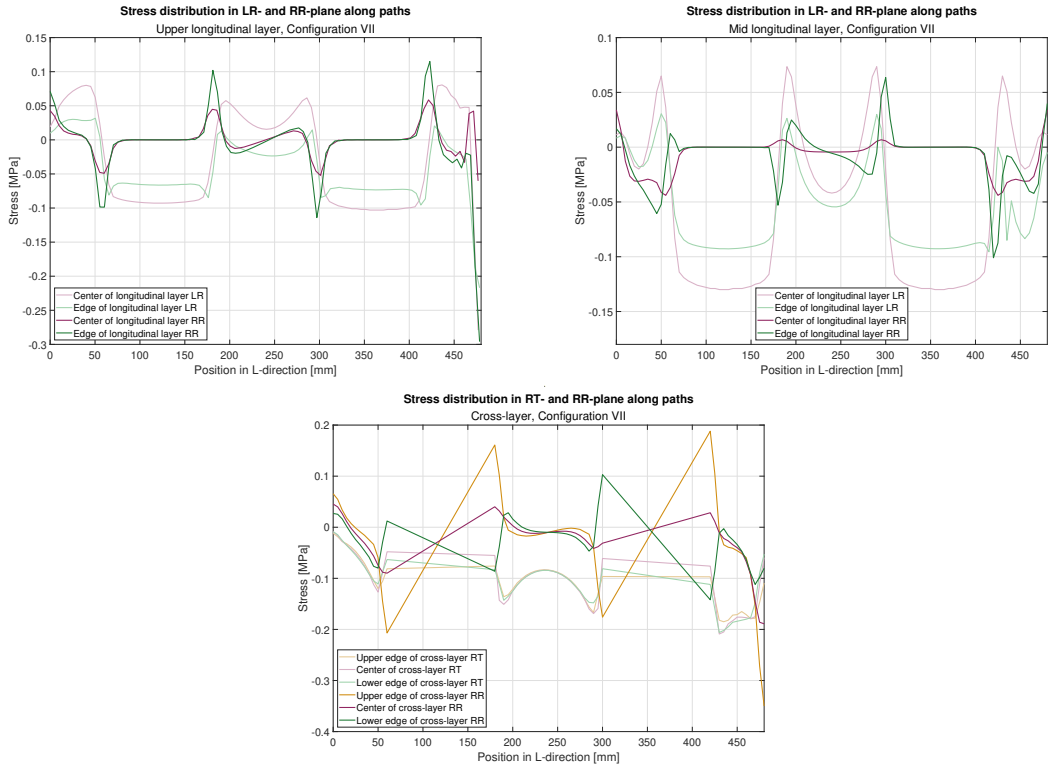

Figure 4.94: The dominant shear stress and stress perpendicular to the grain in the upper longitudinal layer, the mid longitudinal layer, and the cross-layer of Configuration VII.

It can be observed in the top left graph of Figure 4.94 that the stress distribution in the upper longitudinal layer in the LR-plane displays high compression stresses along the lengths of the air gaps, whereas the stress distribution in the RR-direction shows high stress concentrations by the edges of the cross-layer lamellas, i.e. by the edges of the air gaps. It can also be observed that the stresses in both the LR-plane and the RR-direction alternate between tension and compression, although the alternations are more noticeable in the RR-direction. The highest stresses in all four paths are located by the right end of the layer, i.e. at the position of the load application.

In the top right graph of Figure 4.94, it can be observed that the dominant stress of the mid longitudinal layer is the panel shear stress, i.e. the shear stress in the LR-plane. Both the stresses in the LR-plane and in the RR-direction are more or less symmetrical. However, the stress distribution in the LR-plane displays high compression stresses along the lengths of the air gaps, whereas the stress distribution in the RR-direction shows high stress concentrations by the edges of the cross-layer lamellas. Similar to the upper longitudinal layer, it can be observed that the stresses perpendicular to the grain alternate between tension and compression.

In the bottom graph of Figure 4.94, it can be observed that the dominant stress of the cross-layer is the stress perpendicular to the grain, i.e. the stress in the RR-direction. Both the stresses in the RT-plane and in the RR-direction display a similar behaviour with stress concentrations by the edges of the cross-layer lamellas, as well as a significant increase in compression stress by the right end of the specimen. It can also be observed that the stresses in the RR-direction alternate between tension and compression by the edges of the cross-layer lamellas, whereas the cross-layer is only subjected to compression stresses in the RT-plane.

The utilisation ratio of the interaction of Configuration VI is presented in Figure 4.95.

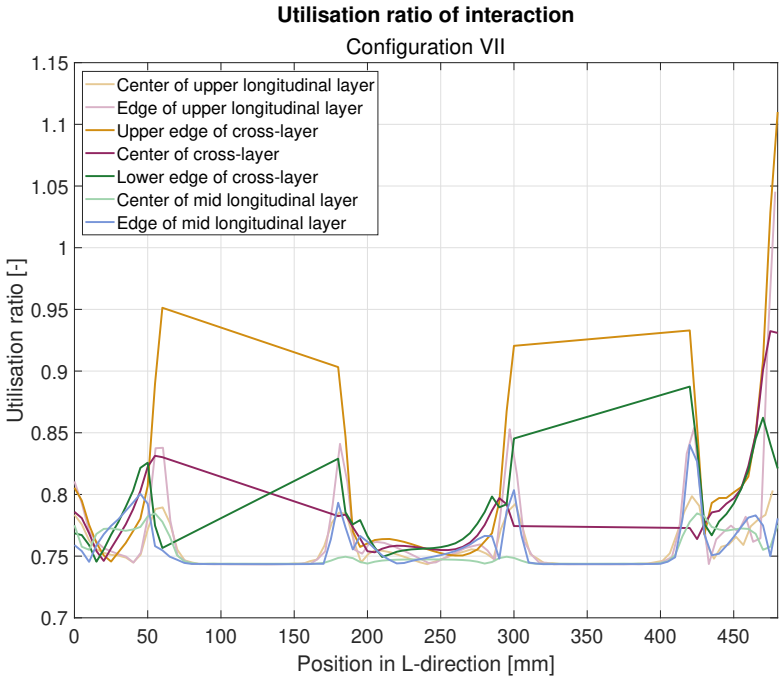

Figure 4.95: Utilisation ratio of interaction in Configuration VII.

As can be observed in Figure 4.95, the utilisation ratio is the highest for the upper edge of the cross-layer, with a significant increase in utilisation ratio by the right end of the specimen. Furthermore, local peaks in the utilisation ratio can be observed for all paths by the edges of the cross-layer lamellas, i.e. by the edges of the air gaps.

4.6.10 Configuration VIII

The shear stress distribution of Configuration VIII in the LR-plane is illustrated in Figure 4.96.

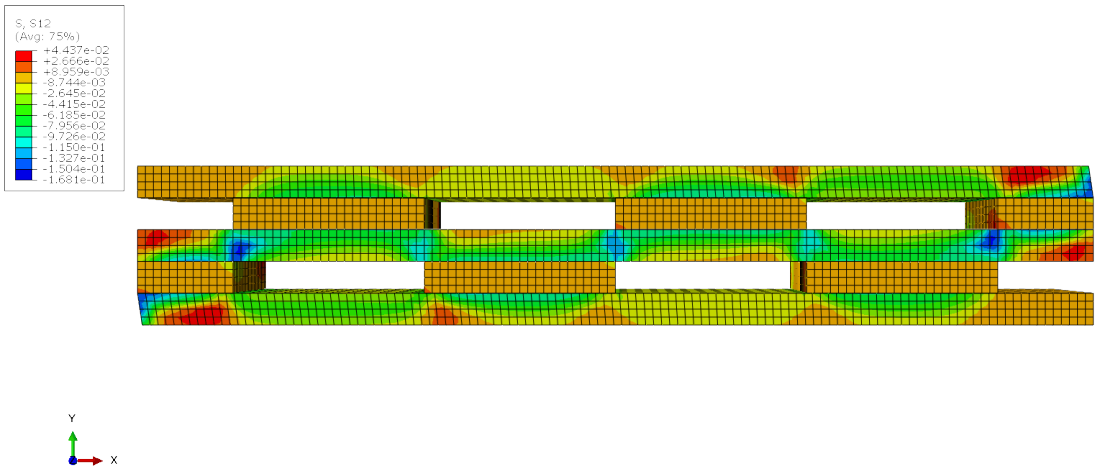

Figure 4.96: Shear stress distribution of Configuration VIII in the LR-plane.

It can be observed in Figure 4.96 that the inclined surfaces, on which the uniform pressure is applied, are subjected to compression, while the opposite corners of the lamellas are subjected to minor tensile stresses. It can also be observed that all the longitudinal layers display concentrations of compression stresses in the areas above and below the cross-layer lamellas and that the magnitude of the stresses alternates along with the shift of the air gaps. Furthermore, significant concentrations of compression stresses can be observed in the mid longitudinal layer by the edges of the outermost cross-layer lamellas, as well as by the intersection of the air gaps and cross-layer lamellas.

The shear stress distribution of Configuration VIII in the RT-plane, i.e. the rolling shear stress distribution, is illustrated in Figure 4.97.

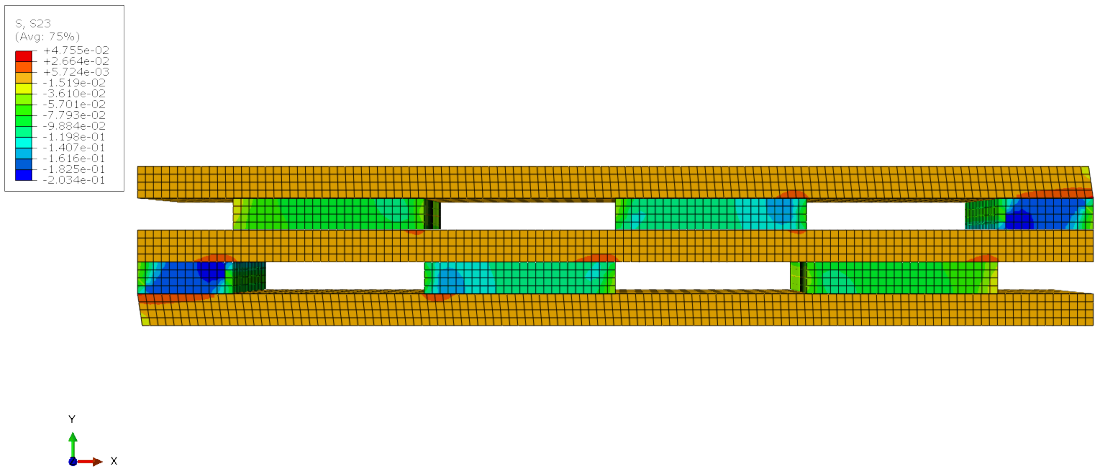

Figure 4.97: Shear stress distribution of Configuration VIII in the RT-plane.

It can be observed in Figure 4.97 that the cross-layer lamellas are subjected to compression stresses, with the highest concentrations closest to the load application positions. It can also be observed that the inner edges of the outer longitudinal lamellas are subjected to tensile stresses close to the positions of the load application, as well as by the corners where the longitudinal layers and the cross-layer lamellas intersect.

The normal stress distribution of Configuration VIII in the RR-direction, i.e. the stress distribution perpendicular to the grain, is illustrated in Figure 4.98.

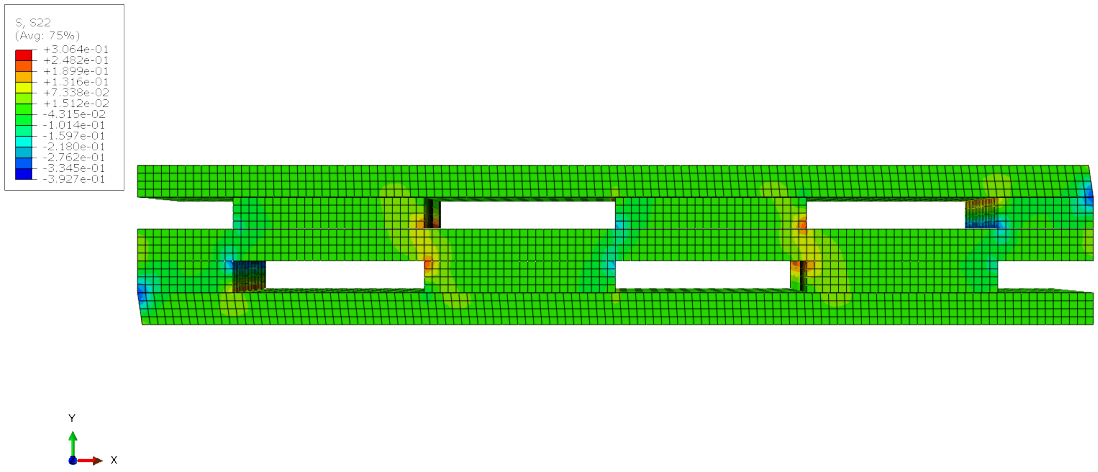

Figure 4.98: Normal stress distribution of Configuration VIII in the RR-direction.

It can be observed in Figure 4.98 that the corners of the cross-layer lamellas, on opposite sides of the air gaps, are subjected to tensile stresses perpendicular to the

grain, while the outermost edges, which are closest to the areas of the application of load, are subjected to compression stresses perpendicular to the grain. Furthermore, the longitudinal layers display similar stress concentrations in the corresponding positions.

The stress distribution along paths in the LR- and RT-plane of the upper longitudinal layer, the mid longitudinal layer, and the cross-layer of Configuration VIII are shown in Figure 4.99.

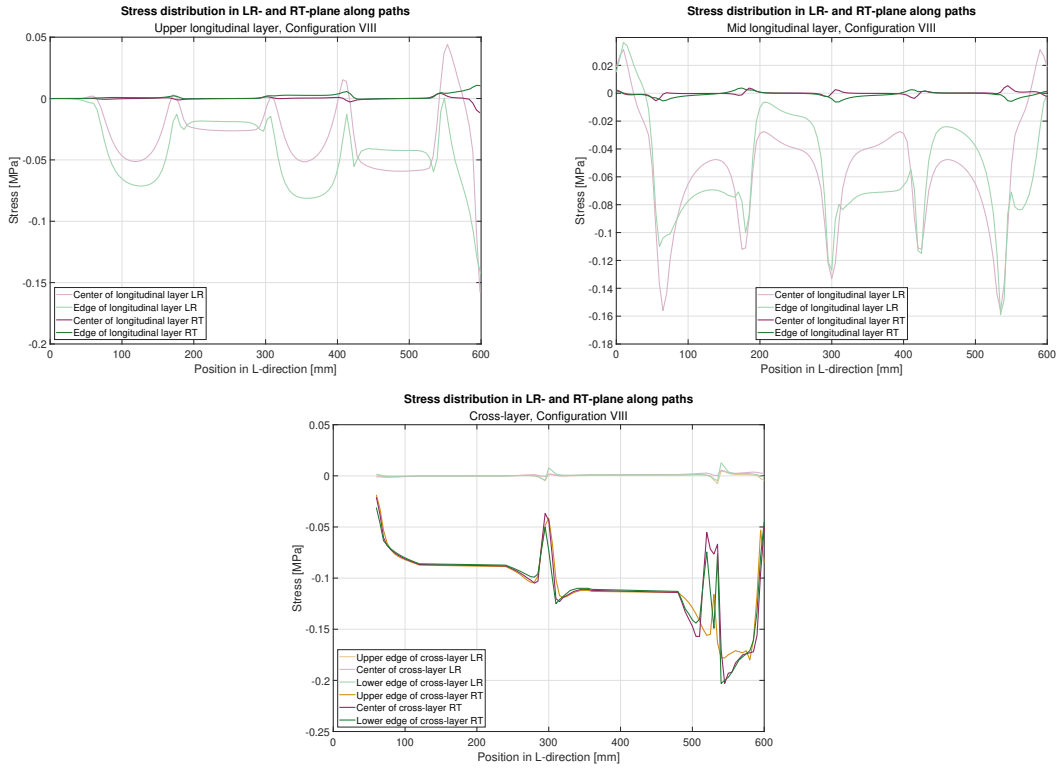

Figure 4.99: Stress distribution along paths in the upper longitudinal layer, the mid longitudinal layer, and the cross-layer of Configuration VIII.

It can be observed in the top left graph and the top right graph of Figure 4.99 that the dominant shear stress in the upper longitudinal layer and the mid longitudinal layer is the panel shear stress, i.e. the shear stress in the LR-plane. A significant increase in compression stresses can be observed by the right end of the upper longitudinal layer, where the pressure is applied. For the mid longitudinal layer, the stress distribution is more or less symmetrical, with distinct stress concentrations by the edges of the cross-layer lamellas.

For the cross-layer, as can be seen in the bottom graph of Figure 4.99, the rolling shear stress is the dominant shear stress, i.e. the shear stress in the RT-plane. Similar to the upper longitudinal layer, an increase in compression stresses can be observed towards the right end of the specimen. It can also be observed that there is a significant decrease in stress by the edges of the cross-layer lamellas. Note that the curves begin at 60 mm since the upper cross-layer, from which the stress distri-

butions are retrieved, begins with an air gap on the left end of the specimen.

The dominant shear stress and the normal stress distribution in the RR-direction, i.e. the stress distribution perpendicular to the grain, in each layer of Configuration VIII are shown in Figure 4.100.

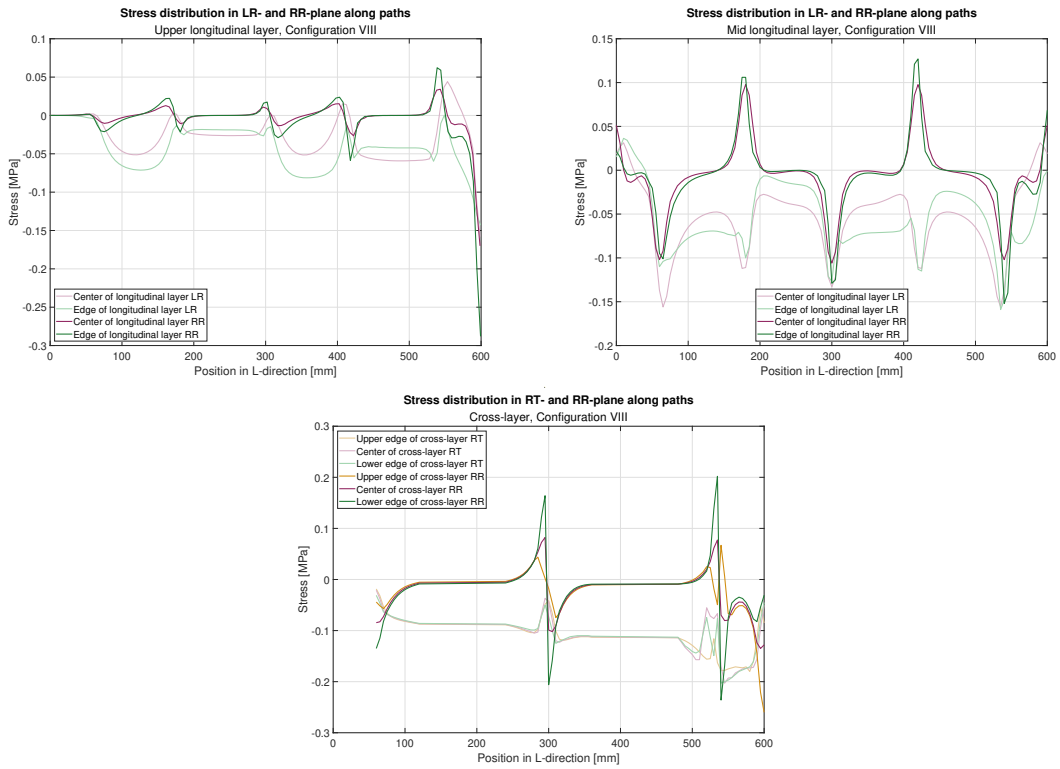

Figure 4.100: The dominant shear stress and stress perpendicular to the grain in the upper longitudinal layer, the mid longitudinal layer, and the cross-layer of Configuration VIII.

It can be observed in the top left graph of Figure 4.100 that the stress distribution in the upper longitudinal layer in the LR-plane displays high compression stresses along the lengths of the air gaps, whereas the stress distribution in the RR-direction displays high stress concentrations by the edges of the cross-layer lamellas, i.e. by the edges of the air gaps. It can also be observed that the stresses perpendicular to the grain, i.e. in the RR-direction, alternate between tension and compression, whereas the upper longitudinal layer is mainly subjected to compression stresses in the LR-plane. The highest stresses in all four paths are located by the right end of the layer, i.e. at the position of the load application.

In the top right graph of Figure 4.100, it can be observed that both the stresses in the RT-plane and in the RR-direction display a somewhat similar behaviour, with stress concentrations by the edges of the cross-layer lamellas and the air gaps. However, the stresses perpendicular to the grain, i.e. in the RR-direction, alternate between tension and compression, whereas the mid longitudinal layer is mainly subjected to compression stresses in the LR-plane.

In the bottom graph of Figure 4.100, it can be observed that the dominant stress of the cross-layer is the stress perpendicular to the grain, i.e. the stress in the RR-direction. Both the stresses in the RT-plane and in the RR-direction display a similar behaviour with stress concentrations by the edges of the cross-layer lamellas, as well as an increase in compression stress by the right end of the specimen. However, the stresses perpendicular to the grain, i.e. in the RR-direction, alternate between tension and compression by the edges of the cross-layer lamellas, whereas the cross-layer is only subjected to compression stresses in the RT-plane. Note that the curves begin at 60 mm since the upper cross-layer, from which the stress distributions are retrieved, begins with an air gap on the left end of the specimen.

The utilisation ratio of the interaction of Configuration VI is presented in Figure 4.101.

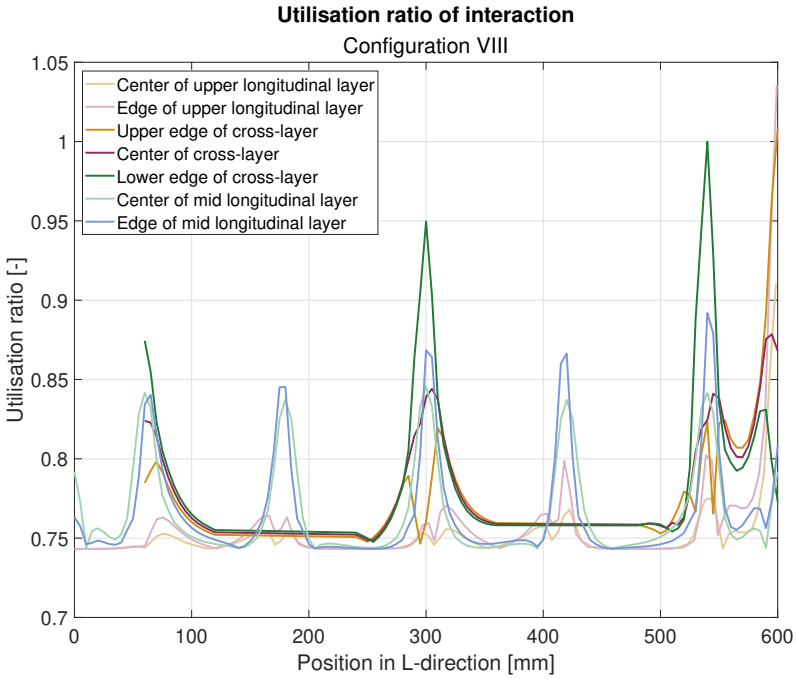

Figure 4.101: Utilisation ratio of interaction in Configuration VIII.

As can be observed in Figure 4.101, the utilisation ratio is the highest for the edges of the cross-layer, followed by the mid longitudinal layer, with significant peaks in the utilisation ratio by the edges of the cross-layer lamellas.

4.6.11 Configuration IX

The shear stress distribution of Configuration IX in the LR-plane, i.e. the panel shear stress distribution, is illustrated in Figure 4.102.

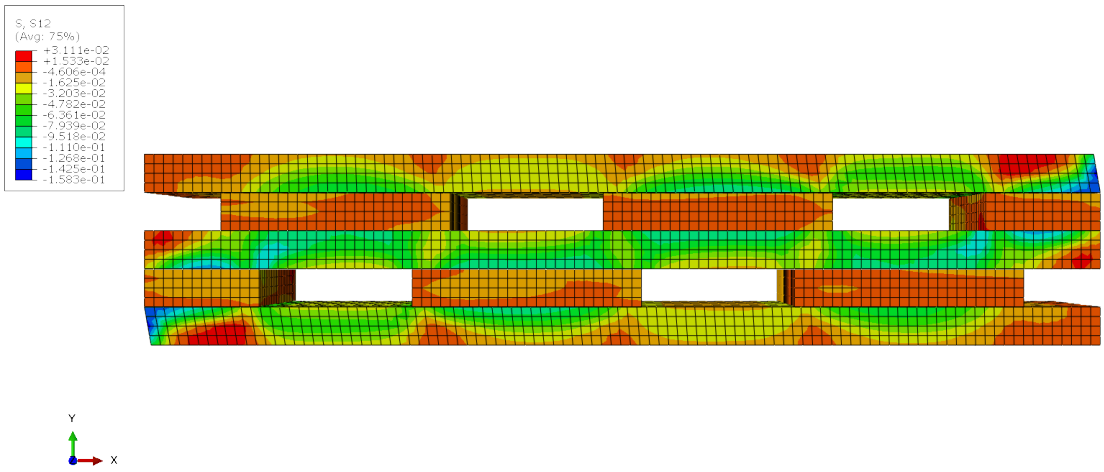

Figure 4.102: Shear stress distribution of Configuration IX in the LR-plane.

It can be observed in Figure 4.102 that the inclined surfaces, on which the uniform pressure is applied, are subjected to compression, while the opposite corners of the lamellas are subjected to minor tensile stresses. It can also be observed that all the longitudinal layers display concentrations of compression stresses in the areas above and below the cross-layer lamellas and that the magnitude of the stresses alternates along with the shift of the air gaps. Furthermore, significant concentrations of compression stresses can be observed in the mid longitudinal layer by the edges of the outermost cross-layer lamellas, as well as by the intersection of the air gaps and the cross-layer lamellas.

The shear stress distribution of Configuration IX in the RT-plane, i.e. the rolling shear stress distribution, is illustrated in Figure 4.103.

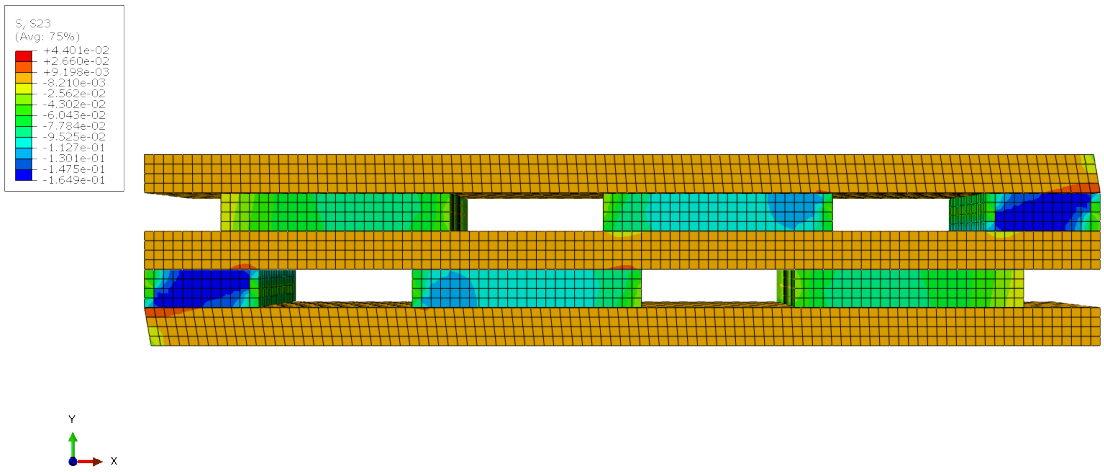

Figure 4.103: Shear stress distribution of Configuration IX in the RT-plane.

It can be observed in Figure 4.102 that the cross-layer lamellas are subjected to compression stresses, with the highest concentrations closest to the load application positions. It can also be observed that the inner edges of the outer longitudinal lamellas are subjected to tensile stresses close to the positions of the load application, as well as by the corners where the longitudinal layers and the cross-layer lamellas intersect.

The normal stress distribution of Configuration IX in the RR-direction, i.e. the stress distribution perpendicular to the grain, is illustrated in Figure 4.104.

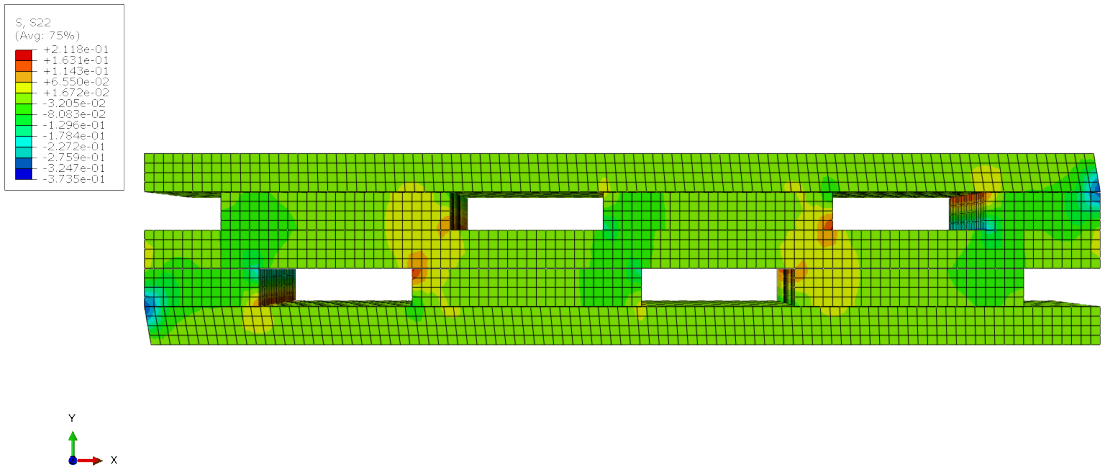

Figure 4.104: Normal stress distribution of Configuration IX in the RR-direction.

It can be observed in Figure 4.104 that the corners of the cross-layer lamellas, on opposite sides of the air gaps, are subjected to tensile stresses perpendicular to the

grain, while the outermost edges, which are closest to the areas of the application of load, are subjected to compression stresses perpendicular to the grain.

The stress distribution along paths in the LR- and RT-plane of the upper longitudinal layer, the mid longitudinal layer, and the cross-layer of Configuration IX are shown in Figure 4.105.

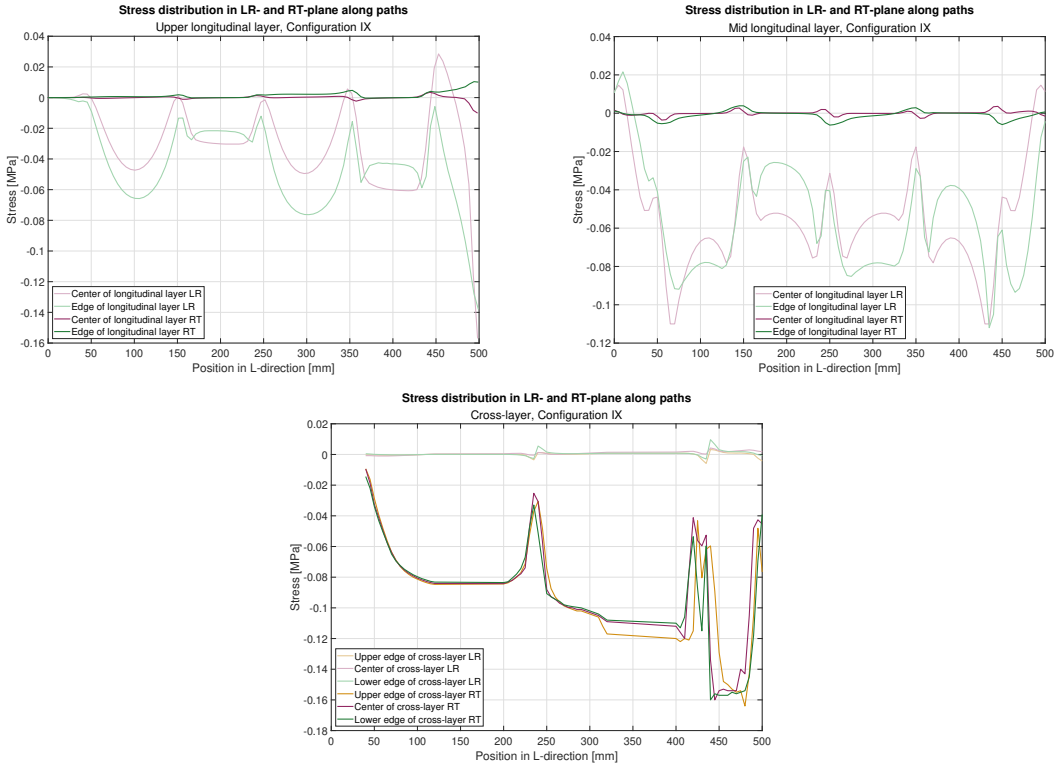

Figure 4.105: Stress distribution along paths in the upper longitudinal layer, the mid longitudinal layer, and the cross-layer of Configuration IX.

It can be observed in the top left graph and the top right graph of Figure 4.105 that the dominant shear stress in the upper longitudinal layer and the mid longitudinal layer is the panel shear stress, i.e. the shear stress in the LR-plane. A significant increase in compression stresses can be observed by the right end of the upper longitudinal layer, where the pressure is applied. For the mid longitudinal layer, the stress distribution is more or less symmetrical, with distinct stress concentrations by the edges of the cross-layer lamellas.

For the cross-layer, as can be seen in the bottom graph of Figure 4.105, the rolling shear stress is the dominant shear stress, i.e. the shear stress in the RT-plane. Similar to the upper longitudinal layer, an increase in compression stresses can be observed towards the right end of the specimen. It can also be observed that there is a significant decrease in stress by the edges of the cross-layer lamellas. Note that the curves begin at 40 mm since the upper cross-layer, from which the stress distributions are retrieved, begins with an air gap on the left end of the specimen.

The dominant shear stress and the normal stress distribution in the RR-direction, i.e. the stress distribution perpendicular to the grain, in each layer of Configuration IX are shown in Figure 4.106.

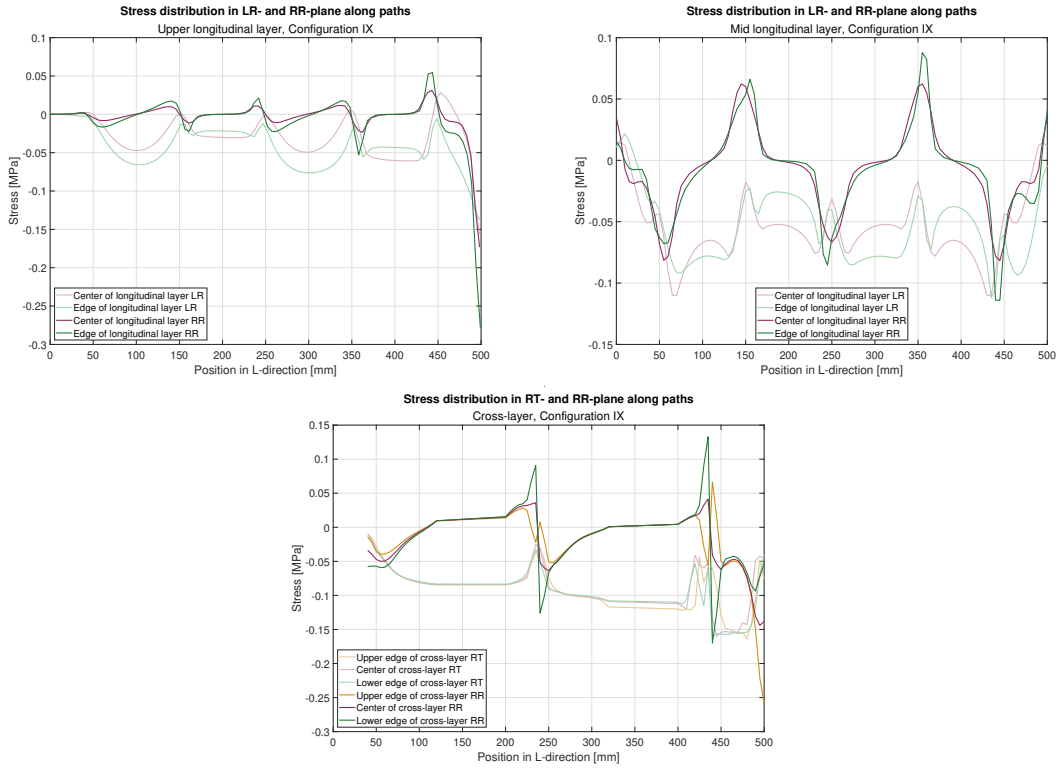

Figure 4.106: The dominant shear stress and stress perpendicular to the grain in the upper longitudinal layer, the mid longitudinal layer, and the cross-layer of Configuration IX.

It can be observed in the top left graph of Figure 4.106 that the stress distribution in the upper longitudinal layer in the LR-plane displays high compression stresses along the lengths of the air gaps, whereas the stress distribution in the RR-direction displays high stress concentrations by the edges of the cross-layer lamellas, i.e. by the edges of the air gaps. A minor alternation between tension and compression can be observed for the stresses perpendicular to the grain, i.e. in the RR-direction, whereas the upper longitudinal layer is mainly subjected to compression stresses in the LR-plane. The highest stresses in all four paths are located by the right end of the layer, i.e. at the position of the load application.

In the top right graph of Figure 4.106, it can be observed that both the stresses in the RT-plane and in the RR-direction display a similar behaviour, with stress concentrations by the edges of the cross-layer lamellas and the air gaps. However, the stresses perpendicular to the grain, i.e. in the RR-direction, alternate between tension and compression, whereas the mid longitudinal layer is mainly subjected to compression stresses in the LR-plane.

In the bottom graph of Figure 4.106, it can be observed that both the stresses in the RT-plane and in the RR-direction display a similar behaviour with stress concentrations by the edges of the cross-layer lamellas, as well as an increase in compression stress by the right end of the specimen. However, the stresses perpendicular to the grain, i.e. in the RR-direction, alternate between tension and compression by the edges of the cross-layer lamellas, whereas the cross-layer is only subjected to compression stresses in the RT-plane. Note that the curves begin at 40 mm since the upper cross-layer, from which the stress distributions are retrieved, begins with an air gap on the left end of the specimen.

The utilisation ratio of the interaction of Configuration VI is presented in Figure 4.107.

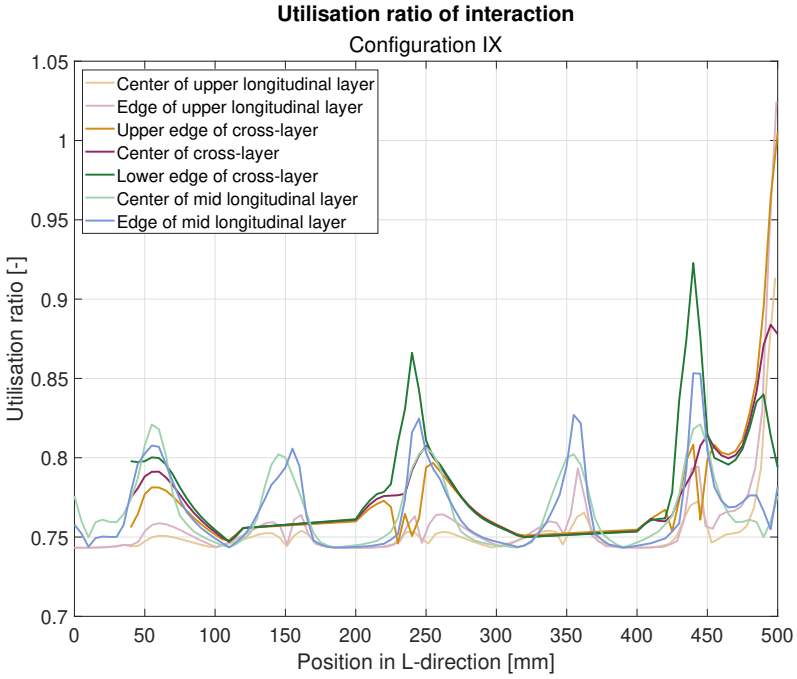

Figure 4.107: Utilisation ratio of interaction in Configuration IX.

As can be observed in Figure 4.107, the utilisation ratio is the highest for the edges of the cross-layer, followed by the mid longitudinal layer, with significant peaks in the utilisation ratio by the edges of the cross-layer lamellas.

5

Discussion

In this section, the method that has been applied to obtain the results will be evaluated and the detected sources of error that might have influenced the final outcome will be discussed and analysed. Furthermore, the results of the physical testing of the specimens, as well as the finite element modelling, will be explained and discussed.

5.1 Preparation and manufacturing

During the preparation and the manufacturing phase of the project, several decisions regarding the method, as well as sources of error, might have influenced the final results to varying degrees.

5.1.1 Conditioning

As stated in Section 4.1, the observed moisture content at equilibrium was around 10 % for the boards of type A and around 11 % for the boards of type B. The conditioning procedure according to Eurocode, as presented in Section 2.5.1, suggests an environment with a relative humidity of 65 $\pm$ 5 % in order to obtain a equilibrium moisture content of 12 %. The relative humidity in the climate chamber, in which the boards were stored for the conditioning procedure, was 60 % and therefore, a slightly lower equilibrium moisture content than 12 % was obtained for both board types.

Furthermore, the measured moisture content for the boards of type A was 1 % lower at equilibrium than the moisture content for the boards of type B, indicating that the boards had in fact not reached true moisture equilibrium. One reason that could explain the difference is that the average density of the boards of type A was approximately $50 - 60$ kg/m^3 lower than that of the boards of type B, see Tables 4.4 and 4.2 in Section 4.2, indicating that the density and moisture content is highly dependent on each other. Another reason could be that the structure of the boards vary and, therefore, the moisture resistance varies, resulting in different moisture equilibriums. Although this might have influenced the performance of the specimens, mainly with regard to internal stresses caused by the variations in moisture content, the effect of the relatively small differences has most likely not affected the outcome of the strength tests to a significant extent.

5.1.2 Manufacturing

For the manufacturing of the final specimens, several steps in the method were altered based on the results of the test specimens. Furthermore, the choice of adhesive and the adhesive application method had a large impact on the results.

5.1.2.1 General method

Based on the results of the trial test round, in particular the observed excessive strength of the solid test specimen during the initial test in comparison to the second test with the shortened specimen, all the designed configurations were reviewed and shortened to a length including at most three lamellas in the cross-layers.

Furthermore, there was an attempt to remove all major visible defects in the boards during the manufacturing, in particular in the boards that were used for the lamellas in the cross-layer, as well as in the areas of the boards that would be located close to the load application. However, the strength grading was conducted before the removal of defects and, as discussed in Section 2.1.2, these natural characteristics highly influence the properties of the material. Therefore, the actual strengths of the specimens are most likely higher than the assumed strengths, with regard to density and longitudinal MOE.

In particular, the boards that were used for the cross-layer lamellas were modified to a greater extent than the boards that were used for the longitudinal layers, indicating that the difference in strength between the average, low, and high strength specimens is probably more substantial than accounted for. This could be one explanation why some of the low or average strength specimens, in fact, performed better than some of the high strength specimens.

5.1.2.2 Adhesive

All the specimens of the three-layer configurations either failed in the bondlines or displayed noticeable bondline cracking and due to this, no conclusions can be drawn regarding the actual strength of the specimen, since the failure load corresponds to the strength of the adhesive, rather than the strength of the panel. This led to an alteration of the method with regard to the application of the adhesive and vacuum pressing procedure for the manufacturing of the five-layer specimens.

For the manufacturing of the three-layer configurations, the adhesive was applied using the notched edge of the applicator, which was noticeable when observing the specimens after failure and it was assumed that the amount of adhesive was inadequate. Furthermore, as stated in Section 3.4.1.3, all three specimens of one configuration were glued and assembled before placing all of them in the vacuum press. The adhesive that was used was fast-drying, with an open time of around five minutes, and hence, the adhesive most likely began to harden before the specimens were placed in the vacuum press. Therefore, the manufacturing method of the five-layer configurations was altered; the adhesive was applied with a uniform layer

and only one specimen was glued and assembled at the time before placing it in the vacuum press. This resulted in a smaller proportion of specimens of the five-layer configurations failing in the bondlines. However, as can be observed in Table 4.44, there were still a few specimens that experienced bondline failure.

The original plan was to use a polyurethane adhesive, also known as PUR, which is the most commonly used adhesive for engineered wood products, such as CLT and glulam. However, due to delivery delay, Cascol Indoor wood adhesive was used as a substitute, which is a PVAC-based adhesive.

As can be observed in Table 4.44, in total, nine out of 27 specimens failed in the bondlines rather than in the wood. Furthermore, the vacuum press that was used had a pressing power of approximately 0.09 N/mm^2, whereas a minimum pressure of 0.6 MPa is recommended for the lamination of spruce, according to Raknes (1986). This suggests that the replacement of the adhesive, in combination with the inadequate vacuum pressing, have influenced the results of the testing to a considerable extent.

5.2 Testing of specimens

The discussion of the results from the testing of the specimens is divided between the three-layer configurations and the five-layer configurations. The comparison between the specimens of the configurations are performed by analysing the relation between the material reduction and the failure load ratio, which corresponds to the reduction of strength in comparison to the reference configurations, as presented in Section 4.5.12.2.

5.2.1 Three-layer configurations

As discussed in Section 5.1.2.2, a large portion of the three-layer specimens failed in the bondlines, more specifically six out of nine specimens experienced bondline failure, as can be seen in Table 4.44. Therefore, it is difficult to draw conclusions regarding the actual strength of the specimens, since the failure presumably occurred due to the inadequate adhesive and method of adhesive application.

The failure load ratio in relation to the material reduction for all the specimens of the three-layer configurations is compared in Figure 5.1.

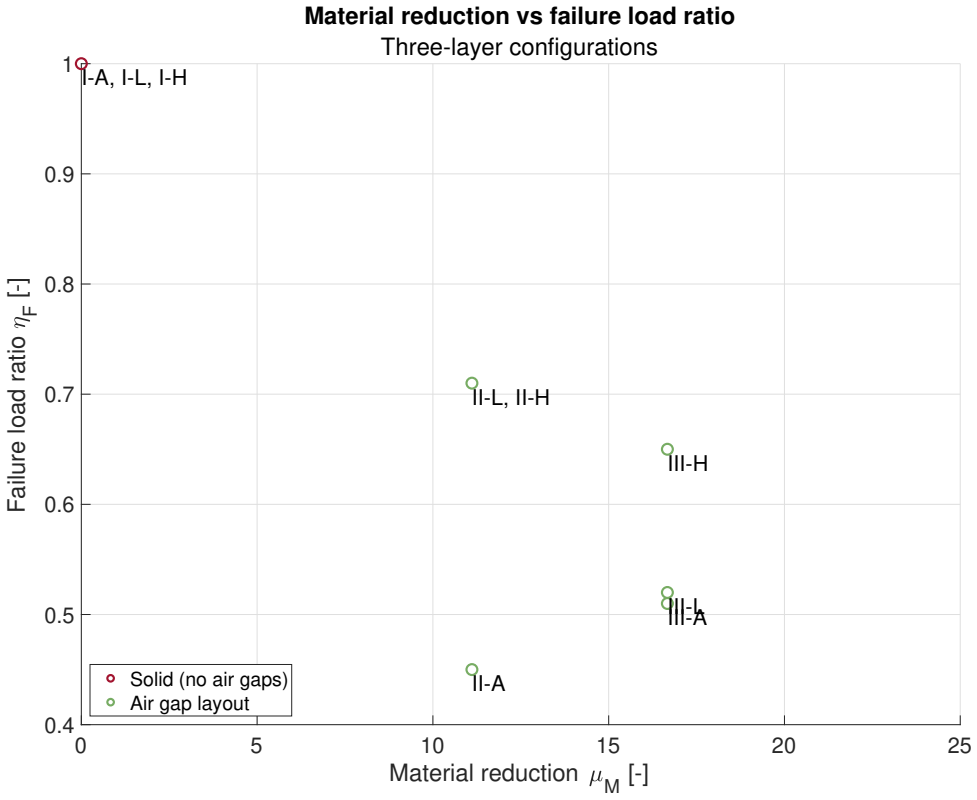

Figure 5.1: Comparison of failure load ratio and material reduction for three-layer configurations.

It can be seen in Figure 5.1 that a reduction in strength, i.e. the failure load ratio, correlates to the reduction of material. The average strength specimen of Configuration II appears to be deviating, with a high reduction in strength in relation to the material reduction.

Due to the small amount of specimens, it is difficult to determine a clear relation between the strength reduction and the material reduction, especially since the most of the three-layer specimens experienced failure in the bondlines and not in the wood material itself.

5.2.2 Five-layer configurations

The results for the five-layer specimens show a greater variety in the observed failure modes, with seven specimens failing in panel shear, three specimens failing in the bondlines, and eight specimens failing in the cross-layers due to rolling shear, as shown in Table 4.44. This indicates that the alterations of the manufacturing method were beneficial.

The failure load ratio in relation to the material reduction for all the specimens of the five-layer configurations is compared in Figure 5.2.

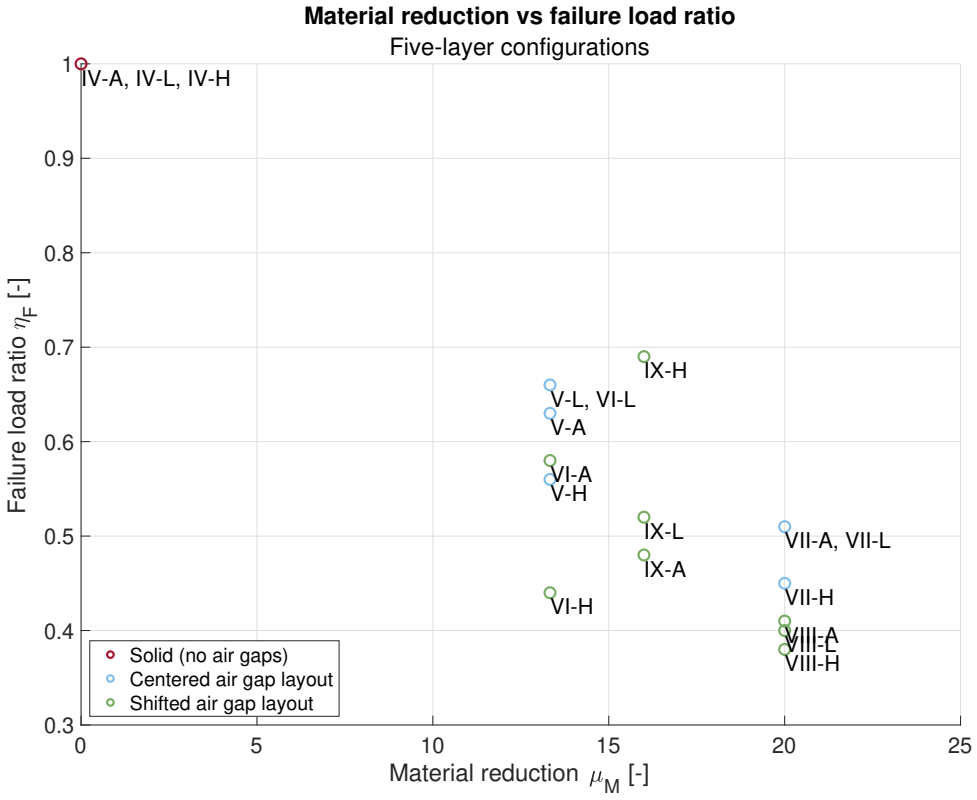

Figure 5.2: Comparison of failure load ratio and material reduction for five-layer configurations.

In Figure 5.2, the specimens with centred air gap layout and shifted air gap layout are plotted, respectively, using different colours in order to be able to compare their performance. For Configuration V, with 60 mm wide air gaps in a centred layout, it can be seen that the specimens generally have a higher capacity than the specimens of Configuration VI, with 60 mm air gaps in a shifted layout. Furthermore, it can be observed that for Configuration VII, with 120 mm wide air gaps in a centred layout, the specimens generally have a higher capacity than the specimens of Configuration VIII, with 120 mm wide air gaps in a shifted layout, and that the difference is even more noticeable than for Configurations V and VI. This indicates that a centred air gap layout is more effective than a shifted air gap layout.

There are several possible explanations why the specimens with a centred air gap layout perform better than the specimens with a shifted air gap layout. One reason could be that all the specimens with a shifted air gap layout have cross-layers that end with an air gap. This might cause a reduction in the stiffness of the specimen, in comparison to the specimens with solid ends of the cross-layers. Furthermore, the specimens with centred air gaps are fully symmetrical with cross-layer lamellas in the centre of the layout, meaning that the specimens have solid wood in the centre of the ideal force path, which is not always the case for the specimens with shifted air gaps. In general, the force path might be subjected to less disturbances in the specimens with centred air gaps, in comparison to the specimens with shifted air

gaps. However, the effect of these differences might be less noticeable if the test specimens were significantly longer.

Regarding the results of the failure load ratio with respect to the air gap width, it is evident that there is a direct correlation between an increase in air gap width and a decrease in shear capacity, as can be seen in Table 4.46. It can be observed that all the specimens with 60 mm air gaps have a higher failure load ratio than the specimens with 80 mm air gaps, followed by the specimens with 120 mm air gaps. This is true for both the specimens with centred and with shifted air gaps, indicating that the width of the air gaps, and thereby the reduction of material, has a higher influence on the performance of the panel in comparison to the layout of the air gaps.

5.3 Finite element modelling in Abaqus

The discussion of the results from the finite element modelling in Abaqus is divided between the three-layer configurations and the five-layer configurations. The comparison between the configurations are performed by analysing the stress distributions in the LR- and RT-plane, as well as in the RR-direction, and the utilisation ratio of the interaction of the various stresses.

Furthermore, the maximum utilisation ratio can be observed by the right end of the models for all the configurations, i.e. at the position of the load application, and due to this, the discussion will be focused on the utilisation ratio along the lengths.

5.3.1 Three-layer configurations

For all the three-layer configurations, the stress distribution in the LR-plane of the longitudinal layer displays distinct stress concentrations by the edges of the cross-layer lamellas. Furthermore, the compression stresses in the longitudinal lamellas were magnified above and below the air gaps for the configurations with air gaps, i.e. Configurations II and III, than those of the solid configuration, i.e. Configuration I, indicating that the air gaps decrease the capacity of the configuration.

All the three-layer configurations display a similar behaviour in the cross-layer with regard to the stress distribution in the RT-plane, with high compression stresses by the edges of the cross-layer lamellas and the magnitude of the stresses appears to be increasing with increasing air gap width. Furthermore, the configurations display a similar behaviour in the R-direction of the longitudinal layer and the cross-layer, respectively, but with varying magnitudes depending on the width of the air gaps. The magnitude of the alternating stresses seemingly increases with increasing air gap width, indicating that the capacity of the configurations decreases with increasing air gap width.

The utilisation ratio for all the configurations appears to be the highest in the edge of the cross-layer by the edges of the cross-layer lamellas, i.e. by the air gaps in

the configurations with air gaps. Furthermore, the introduction of air gaps with a larger width yields a higher utilisation ratio, where the highest magnitude of almost 1.0 can be observed for Configuration III, with 120 mm air gaps.

5.3.2 Five-layer configurations

For the five-layer configurations, the configurations with the same material reduction, but with different air gap layouts, as well as the configurations with the same air gap layouts, but with different air gap widths, are compared in more detail.

5.3.2.1 Air gap layout

For Configurations V and VI, with 60 mm wide air gaps in a centred and shifted layout, respectively, several differences can be observed in the stress distribution in all the analysed layers. For Configuration V, with the centred air gap layout, high concentrations of compression stresses can be observed in the longitudinal layers of the LR-plane by the position of the air gaps, with the maximum magnitude varying between approximately 0.07 and 0.1 MPa in the upper longitudinal layer and a maximum magnitude almost reaching 0.14 MPa in the mid longitudinal layer. For Configuration VI, with the shifted air gap layout, the maximum compression stresses in the upper longitudinal layer can be observed above the cross-layer lamellas, with a maximum magnitude of 0.07 MPa, whereas the maximum compression stresses in the mid longitudinal layer reach a magnitude of 0.1 MPa.

Furthermore, the behaviour of the stresses perpendicular to the grain vary between the configurations and the magnitude is slightly higher for the shifted layout in comparison to the centred layout. A similar behaviour can be observed for the cross-layer, where it can be seen that the magnitude of the alternating tensile and compression stresses perpendicular to the grain are significantly higher for the centred layout than for the shifted layout.

The observed differences in magnitude of the stresses are reflected in the utilisation ratios of the configurations. For Configuration V, the utilisation ratio is the highest for the edges of the cross-layer, whereas for Configuration VI, the most distinct peaks in the utilisation ratio can be observed for the lower edge of the cross-layer, as well as a few minor peaks for the paths in the mid longitudinal layer. When comparing the two configurations, the maximum utilisation ratio is observed in the cross-layer of Configuration VI, indicating that the general performance is slightly better for Configuration V, with the centred layout, than for Configuration VI, with the shifted air gap layout.

For Configurations VII and VIII, with 120 mm wide air gaps in a centred and shifted layout, respectively, the similar differences can be observed as for Configurations V and VI. Configuration VII, with the centred air gap layout, is subjected to stresses of a greater magnitude in the LR-plane of the upper longitudinal layer, as well as in the RT-plane of the cross-layer, than Configuration VIII, with the shifted air gap layout. However, the maximum compression stresses in the LR-plane of the

mid longitudinal layer are slightly higher for Configuration VIII and furthermore, the stresses perpendicular to the grain by the edges of the air gaps are significantly higher than those for Configuration VII.

Moreover, a similar comparison can be made for the utilisation ratios of Configurations VII and VIII as for Configurations V and VI. When comparing the two configurations, the maximum utilisation ratio is observed in the cross-layer of Configuration VIII, reaching almost 1.0 by the edge of one cross-layer lamella, indicating that the general performance is slightly better for Configuration VII, with the centred layout, than for Configuration VIII, with the shifted air gap layout.

5.3.2.2 Air gap width

Configurations VI, VIII, and IX have a shifted air gap layout and air gap widths of 60 mm, 120 mm, and 80 mm, respectively. All configurations display more or less the same behaviour, but the stresses are of varying magnitude. It is evident that the magnitude of the dominant stresses in all the layers increase with increasing air gap width, and the reduction in capacity appears to be proportional to the air gap width.

Furthermore, it can be observed that the utilisation ratio along the length of all three configurations are similar, with peaks of varying magnitudes at the same positions. The general utilisation ratio is the lowest for Configuration VI, with 60 mm air gaps, indicating that the capacity is the highest for this configuration, whereas for Configuration VIII, with 120 mm air gaps, the peaks of the utilisation ratio are considerably higher than for both Configurations VI and IX. This further emphasises that the capacity of the configuration is highly dependant on the material reduction.

6

Conclusion

The aim of this thesis was to design a material-optimised CLT panel by introducing air gaps in the cross-layers. By designing and manufacturing a variety of configurations, with different air gap layouts and widths, and conducting strength tests on small scale test specimens, the shear capacity was determined and compared with the material reduction of the specimens. The conclusions that were drawn based on the results, as well as a proposal for further work, are presented.

6.1 Conditioning

The moisture content of the boards that were used for the manufacturing of the specimens was measured on three different occasions; two times before manufacturing and one time directly after testing. It was concluded that the specimens never reached the ideal moisture content of 12 % and that there were minor variations in the moisture content before and after testing, suggesting that the boards never truly reached equilibrium. Although this might have influenced the performance of the specimens, mainly with regard to internal stresses caused by the variations in moisture content, the effect was concluded to be insignificant in the context.

6.2 Manufacturing

For the manufacturing of the specimens, two test specimens were produced for the purpose of verifying the manufacturing method. Furthermore, the manufacturing and testing of the three-layer specimens were conducted before the manufacturing of the five-layer specimens, and based on the test results, the manufacturing method was refined.

From the results of the testing of the three-layer specimens, it was evident that the amount of adhesive was inadequate and that the production process was too slow in relation to the hardening time of the adhesive. The method for the application of adhesive was altered for the five-layer specimens. However, the bondlines still proved to be inadequate and it was concluded that the pressure of the vacuum press that was used for assembly was insufficient, in combination with the choice of adhesive.

6.3 Strength of cross-layer lamellas

Due to the modification of the boards that were used for the manufacturing of the specimens, by the removal of most major visible defects, no valid conclusions could be drawn regarding how the shear capacity of the specimen is affected by an increase or a decrease of the strength of the cross-layer lamellas, since the strength properties of the refined lamellas are unknown.

6.4 Material reduction

For both the three-layer and five-layer specimens, a significant reduction in strength was noticed for the specimens with air gaps in comparison to the solid specimens. Furthermore, the correlation between the reduction of material and the reduction of structural capacity was concluded to be linear to some extent, since the general performance of the specimens directly corresponded to the width of the air gaps, where an increase in air gap width resulted in a reduction of capacity.

6.5 Air gap layout

From the test results of the five-layer specimens, it was observed that for the specimens with the same air gap widths, the specimens with a centred air gap layout generally performed better than the specimens with a shifted air gap layout. However, it was concluded that the reduction of material influences the performance of the panel to a greater extent than the layout of the air gaps.

6.6 Finite element modelling

For both the three-layer and five-layer configurations from the finite element modelling, a reduction in strength could be observed for the configurations with air gaps, where the capacity of the configuration decreased with increasing air gap widths.

Furthermore, for the five-layer configurations, the configurations with a centred air gap layout displayed, in general, stress concentrations of a larger magnitude than the configurations with a shifted air gap layout. However, the interaction of the dominant stresses reaches the maximum magnitude in the configurations with a shifted air gap layout and it was concluded that the centred air gap layout provides a higher capacity in general, although the material reduction had a more significant influence on the structural performance.

6.7 Further work

As stated in the limitations, the scope of this thesis only includes the strength testing of the specimens on a small scale. For future research, the results from this thesis might be used for the prediction of the behaviour of a large scale panel. Furthermore, the obtained results might be utilised to conduct a parametric study in order to optimise the panels. However, full scale testing is essential to conduct in order to obtain more comprehensive results.

Moreover, due to the loss of test data, it is necessary to conduct new strength tests and analyse the local deformations using ARAMIS, or similar equipment, in order to obtain a better understanding of the behaviour and to obtain more extensive results regarding the shear capacity of the specimens.

Bibliography

Andersen, J. H., Rasmussen, N. L., and Ryberg, M. W. (2021). Comparative life cycle assessment of cross laminated timber building and concrete building with special focus on biogenic carbon. *Energy & Buildings*.

Blaß, H. J. and Sandhaas, C. (2017). *Timber Engineering Principles for Design*. KIT Scientific Publishing.

Brandt, K. (2015). CLT – the future has historic roots. *Wood Magazine*.

Casco® (2019). Casco® Cascol Indoor Product Data Sheet.

CBI (2017). *Exporting cross laminated timber (CLT) to Western Europe*. Retrieved from https://www.cbi.eu/market-information/timber-products/cross-laminated-timber/europe (March 8th 2022).

Dahl, K. B. (2009). *Mechanical properties of clear wood from Norway spruce*. PhD thesis, Norweigan University of Science and Technology, Trondheim.

Dassault Systèmes (2020). *Defining orthotropic elasticity in plane stress*. Retrieved from https://help.3ds.com/2020/english/dssimulia_established/SIMACAEMATRefMap/simamat-c-linearelastic.htm?contextscope=all&id=67c55a2a7a4b46f494ee31c93c5fba13#simamat-c-linearelastic-planestress (February 23th 2022).

EN 14081-1 (2016). *Timber structures - Strength graded structural timber with rectangular cross section - Part 1: General requirements*. European Committee for Standardization.

EN 16351 (2015). *Timber structures - Cross laminated timber - Requirements*. European Committee for Standardization.

EN 408 (2010). *Timber structures - Structural timber and glued laminated timber - Determination of some physical and mechanical properties*. European Committee for Standardization.

EN 789 (2004). *Timber structures - Test methods - Determination of mechanical properties of wood based panels*. European Committee for Standardization.

Eurocode EN 1995-1-1 (2004). *Eurocode 5: Design of timber structures - Part 1-1: General - Common rules and rules for buildings*. European Committee for Standardization.

Gustafsson, A. (2019). *The CLT Handbook*. Svenskt Trä.

Holmberg, H. and Sandberg, D. (1997). *Structure and Properties of Scandinavian Timber*. HoS Grenarna HB, Stockholm.

Johansson, M. (2016). *Design of timber structures - Structural aspects of timber construction*, volume 1. Swedish Forest Industries Federation, 2:2016 edition.

Kohlhauser, C. and Hellmich, C. (2012). Determination of Poisson's ratios in isotropic, transversely isotropic, and orthotropic materials by means of combined ultrasonic-mechanical testing of normal stiffnesses: Application to metals and wood. *European Journal of Mechanics, A/Solids*.

Mayencourt, P., Rasid, I. M., and Mueller, C. (2018). Structural Optimization of Cross-Laminated Timber Panels. Technical report, Massachusetts Institute of Technology.

Muszynski, L., Larasatie, P., Guerrero, J. E. M., Albee, R., and Hansen, E. N. (2020). Global CLT industry in 2020: Growth beyond the Alpine Region. Technical report, Oregon State University.

Niemz, P. and Caduff, D. (2007). Untersuchungen zur Bestimmung der Poissonschen Konstanten an Fichtenholz. *Holz als Roh- und Werkstoff*.

Raknes, E. (1986). *Trälimning*. Universitetsforlaget AS, Oslo, 2nd edition.

Steiger, R. and Gehri, E. (2011). Interaction of shear stresses and stresses perpendicular to the grain. Technical report.

United Nations Environment Programme (2021). *2021 Global Status Report for Buildings and Construction*. Global Alliance for Buildings and Construction.

A

FFT Analyser manual

FFT Analyser - Manual

Determination of the modulus of elasticity of prismatic bars by longitudinal vibration

Principle
Dynamic longitudinal modulus of elasticity (MOE) of homogenous prismatic bars is given by the following term:

$$MOE_{dyn,long} = \rho V^2$$

where: ρ is the density and V is the velocity of sound. A precise sound velocity determination is given by longitudinal vibration:

$$V = 2Lf$$

where L is the length of the beams, f is the longitudinal vibration frequency.

Material and dimensions
Material is basically any solid material. Recommended length minimum 0,5m and minimum 5 times of the width of the bar. We can test shorter beams, but high frequency respond microphone is required, like dynamic microphone. This case the minimum length goes down to 0,3m.

Setup
Using the following setup determination of the longitudinal vibration frequency is easy:

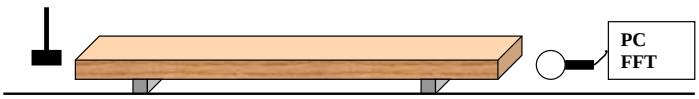

The test bar is supported by two rubber strips. End of the bar is hit by hammer. There is a microphone at the opposite end.

Test procedure
Please hit the end of the bar. Direction of hit is longitudinal. Material of the hammer head is steel or hard wood (hard type). A perfect hit is speedy and the hammer spring back from the bar.
Settings of the FFT software: Frequency range: 11025 (or 5512) Hz, Trigger level 5% but in noisy environment higher trigger level is recommended.
Typically more than one peak is observed. Selecting of the longitudinal vibration frequency please predict the longitudinal frequency of dry wood samples by the following term:

$$f = 2500 / L$$

where the L is the length in m and the predicted frequency is given in Hz. The actual frequency will be in the range of predicted frequency +/-20%. For wet wood samples please use 1600 instead of 2500.

Equipment list

Balance	Measuring tape and/or caliper
Rubber strips	Soft and hard hammers
Samples	PC with sound card, microphone and FFT software

FFT Analyser - Manual

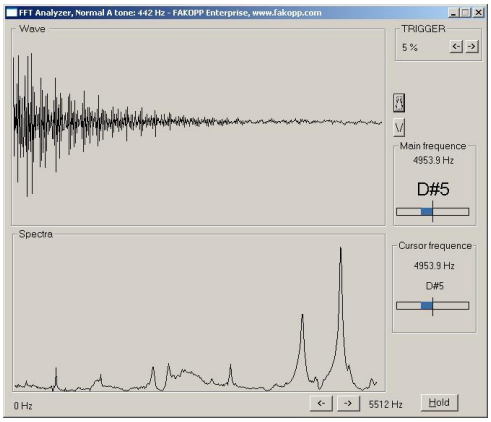

Example spectra: Length=0,5m, longitudinal vibration frequency = 4954Hz. Velocity = 4954m/s. Material: Robinia pseudoacacia, dimensions: 13 x 70 x 500mm

2

FFT Analyser - Manual

Determination of the modulus of elasticity of prismatic bars by bending vibration

Principle
Dynamic bending modulus of elasticity (MOE) of homogenius prismatic bars is given by the following term, where the effect of the shear is neglected:

$$MOE_{dyn,bending} = \left(\frac{2 f_n}{\gamma_n \pi}\right)^2 \frac{mL^3}{I}$$

where f_n is bending vibration frequency, n is the mode number, support condition is free
$\gamma_n = (n+0.5)^2$, n is mode number, but $\gamma_1 = 2.267$
m is the mass of the bar
L is the length of the bar
I is the inertia, $I = \frac{ab^3}{12}$ where a is the width and b is the thickness of the bar

Effect of shear is minor if the length of the bar is higher than 30 times of the thickness.
When the length is shorter, the obtained result is lower than the correct one.
Perfect solution provided by Timoshenko equation. Another practice deals with this problem.

Material and dimensions
Material is basically any solid material. Recommended length is at least 30 times of the thickness of the bar. Slender beam is recommended.

Setup
Using the following setup determination of the bending vibration frequency is easy:

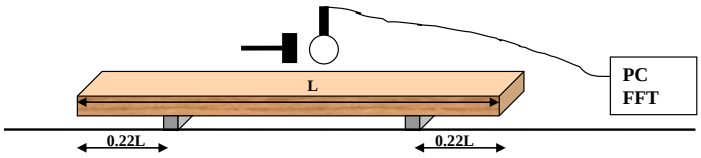

The test bar is supported by two rubber strips at 0,223L locations from the end. Center of the bar is hit by hammer, where a microphone picks up the vibration signal.

Test procedure
Please hit the center of the bar. Material of the hammer head is rubber (soft type). Settings of the FFT software: Frequency range: 1102 Hz, Trigger level 5% but in noisy environment higher level is recommended.
The tallest peak is belongs to the bending vibration, mode number 1.
For testing higher modes please place rubber supports at nodal points and the maximum amplitude locations are the hit and microphone locations. The following figure shows the nodal locations at the first 4 modes:

FFT Analyser - Manual

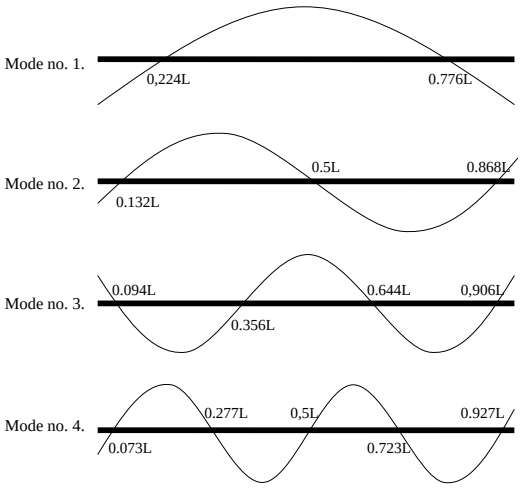

The nodal locations, bending of uniform cross-section bar, free support condition.

Equipment list

Balance	Measuring tape and/or caliper
Rubber strips	Soft and hard hammers
Samples	PC with sound card, microphone and FFT software

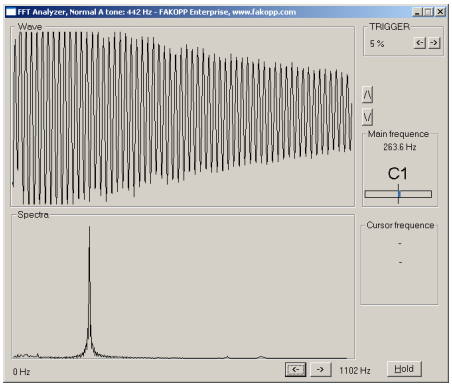

Example spectra: Bending vibration, mode no. 1. Frequency=263,6Hz
Material: Robinia pseudoacacia, dimensions: 13 x 70 x 500mm

4

B

Matlab code (three-layer configuration example)

Configuration I

```
clear; clc; clf;
```

Load-deformation curve

Dimensions

```
l = 0.36;       % Length [m]
b = 0.11;       % Width  [m]
```

Average strength

Loading test data

```
A = load('CLT_3_0_A.mat');
A = cell2mat(struct2cell(A));
```

Plotting of load deformation curve

```
u_A = abs(A(:,1));
F_A = abs(A(:,2));
t_A = A(:,3);

figure(1)
plot(u_A(1:984),F_A(1:984),'color','#C46C9C','linewidth',2)
hold on
```

Failure load

```
[F_max_A,i_A] = max(F_A(:));
F_max_A
F_max_A =

   44.4970
```

Deformation at failure

```
u_max_A = max(u_A(:))
```

```
u_max_A =

    1.7895
```

Time at failure

```
T_A = t_A(i_A)
```

```
T_A =

  122.8828
```

Low strength

Loading test data

```
L = load('CLT_3_0_L.mat');
L = cell2mat(struct2cell(L));
```

Plotting load deformation curve

```
u_L = abs(L(:,1));
F_L = abs(L(:,2));
t_L = L(:,3);

plot(u_L(1:1331),F_L(1:1331),'color','#66B378','linewidth',2)
hold on
```

Failure load

```
[F_max_L,i_L] = max(F_L(:));
F_max_L
```

```
F_max_L =

   28.1378
```

Deformation at failure

```
u_max_L = max(u_L(:))
```

```
u_max_L =

    2.3485
```

Time at failure

```
T_L = t_L(i_L)
```

```
T_L =

  121.1328
```

High strength

Loading test data

```
H = load('CLT_3_0_H.mat');
H = cell2mat(struct2cell(H));
```

Plotting load deformation curve

```
u_H = abs(H(:,1));
F_H = abs(H(:,2));
t_H = H(:,3);

plot(u_H(1:1251),F_H(1:1251),'color','#D18D11','linewidth',2)
```

Plot settings

```
title('Load deformation curve', 'FontSize', 24)
subtitle('Configuration I', 'FontSize', 20)
xlabel('Deformation \delta [mm]')
ylabel('Load F [N]')
set(gca,'FontSize',20)
legend('Average', 'Low', 'High', 'Location', 'northwest')
grid on
```

Failure load

```
[F_max_H,i_H] = max(F_H(:));
F_max_H
F_max_H =

   34.9771
```

Deformation at failure

```
u_max_H = max(u_H(:))
u_max_H =

    1.4706
```

Time at failure

```
T_H = t_H(i_H)
T_H =

  156.1328
```

Abaqus stress paths

Loading test data

Stress in LR-plane

Upper longitudinal center

```
UC_12 = load('1_12_UC.mat');
UC_12 = cell2mat(struct2cell(UC_12));
```

Upper longitudinal edge

```
UE_12 = load('1_12_UE.mat');
UE_12 = cell2mat(struct2cell(UE_12));
```

Cross-layer center

```
CC_12 = load('1_12_CC.mat');
CC_12 = cell2mat(struct2cell(CC_12));
```

Cross-layer edge

```
CE_12 = load('1_12_CE.mat');
CE_12 = cell2mat(struct2cell(CE_12));
```

Stress in RT-plane

Upper longitudinal center

```
UC_23 = load('1_23_UC.mat');
UC_23 = cell2mat(struct2cell(UC_23));
```

Upper longitudinal edge

```
UE_23 = load('1_23_UE.mat');
UE_23 = cell2mat(struct2cell(UE_23));
```

Cross-layer center

```
CC_23 = load('1_23_CC.mat');
CC_23 = cell2mat(struct2cell(CC_23));
```

Cross-layer edge

```
CE_23 = load('1_23_CE.mat');
CE_23 = cell2mat(struct2cell(CE_23));
```

Stress in R-direction

Upper longitudinal center

```
UC_22 = load('1_22_UC.mat');
UC_22 = cell2mat(struct2cell(UC_22));
```

Upper longitudinal edge

```
UE_22 = load('1_22_UE.mat');
UE_22 = cell2mat(struct2cell(UE_22));
```

Cross-layer center

```
CC_22 = load('1_22_CC.mat');
CC_22 = cell2mat(struct2cell(CC_22));
```

Cross-layer edge

```
CE_22 = load('1_22_CE.mat');
CE_22 = cell2mat(struct2cell(CE_22));
```

Plotting (longitudinal layer, LR+RT)

```
figure(2)
plot(UC_12(:,1),UC_12(:,2),'color','#d9b2c7','linewidth',2)
hold on
plot(UE_12(:,1),UE_12(:,2),'color','#a1d4ae','linewidth',2)
hold on
plot(UC_23(:,1),UC_23(:,2),'color','#912661','linewidth',2)
hold on
plot(UE_23(:,1),UE_23(:,2),'color','#1f7a35','linewidth',2)
```

Plot settings

```
title('Stress distribution in LR- and RT-plane along paths', 'FontSize', 24)
subtitle('Longitudinal layer, Configuration I', 'FontSize', 20)
xlabel('Position in L-direction [mm]')
ylabel('Stress [Pa]')
set(gca,'FontSize',20)
legend('Center of longitudinal layer LR', 'Edge of longitudinal layer LR', ...
       'Center of longitudinal layer RT', 'Edge of longitudinal layer RT', ...
       'Location', 'south')
xlim([0 l*1000])
grid on
```

Plotting (cross-layer, LR+RT)

```
figure(3)
plot(CC_12(:,1),CC_12(:,2),'color','#d9b2c7','linewidth',2)
hold on
plot(CE_12(:,1),CE_12(:,2),'color','#a1d4ae','linewidth',2)
hold on
plot(CC_23(:,1),CC_23(:,2),'color','#912661','linewidth',2)
hold on
plot(CE_23(:,1),CE_23(:,2),'color','#1f7a35','linewidth',2)
```

Plot settings

```
title('Stress distribution in LR- and RT-plane along paths', 'FontSize', 24)
subtitle('Cross-layer, Configuration I', 'FontSize', 20)
xlabel('Position in L-direction [mm]')
ylabel('Stress [Pa]')
set(gca,'FontSize',20)
legend('Center of cross-layer LR', 'Edge of cross-layer LR', ...
       'Center of cross-layer RT', 'Edge of cross-layer RT', ...
       'Location', 'south')
xlim([0 l*1000])
grid on
```

Plotting (longitudinal layer, LR+RR)

```
figure(4)
plot(UC_12(:,1),UC_12(:,2),'color','#d9b2c7','linewidth',2)
hold on
plot(UE_12(:,1),UE_12(:,2),'color','#a1d4ae','linewidth',2)
hold on
plot(UC_22(:,1),UC_22(:,2),'color','#912661','linewidth',2)
hold on
plot(UE_22(:,1),UE_22(:,2),'color','#1f7a35','linewidth',2)
```

Plot settings

```
title('Stress distribution in LR- and RR-plane along paths', 'FontSize', 24)
subtitle('Longitudinal layer, Configuration I', 'FontSize', 20)
xlabel('Position in L-direction [mm]')
ylabel('Stress [Pa]')
set(gca,'FontSize',20)
legend('Center of longitudinal layer LR', 'Edge of longitudinal layer LR', ...
       'Center of longitudinal layer RR', 'Edge of longitudinal layer RR', ...
       'Location', 'south')
xlim([0 l*1000])
grid on
```

Plotting (cross-layer, RT+RR)

```
figure(5)
plot(CC_23(:,1),CC_23(:,2),'color','#d9b2c7','linewidth',2)
hold on
plot(CE_23(:,1),CE_23(:,2),'color','#a1d4ae','linewidth',2)
hold on
plot(CC_22(:,1),CC_22(:,2),'color','#912661','linewidth',2)
hold on
plot(CE_22(:,1),CE_22(:,2),'color','#1f7a35','linewidth',2)
```

Plot settings

```
title('Stress distribution in RT- and RR-plane along paths', 'FontSize', 24)
subtitle('Cross-layer, Configuration I', 'FontSize', 20)
xlabel('Position in L-direction [mm]')
ylabel('Stress [Pa]')
set(gca,'FontSize',20)
legend('Center of cross-layer RT', 'Edge of cross-layer RT', ...
       'Center of cross-layer RR', 'Edge of cross-layer RR', ...
       'Location', 'south')
xlim([0 l*1000])
grid on
```

Interaction

Indata

```
f_c90k = 2.5;
f_t90k = 0.4;
f_vk = 4.0;
f_rk = 0.7;
k_mod = 0.80;
gamma_M = 1.25;
```

Design values

```
f_c90d = k_mod * f_c90k / gamma_M;
f_t90d = k_mod * f_t90k / gamma_M;
f_vd = k_mod * f_vk / gamma_M;
f_rd = k_mod * f_rk / gamma_M;
```

Upper longitudinal center

```
int_UC = (f_c90d + abs(UC_22(:,2))).^2 ./ (f_c90d + f_t90d)^2 + ...
          UC_12(:,2).^2 ./ f_vd^2 .* (1 - (f_c90d / (f_c90d + f_t90d))^2);
```

Upper longitudinal edge

```
int_UE = (f_c90d + abs(UE_22(:,2))).^2 ./ (f_c90d + f_t90d)^2 + ...
          UE_12(:,2).^2 ./ f_vd^2 .* (1 - (f_c90d / (f_c90d + f_t90d))^2);
```

Cross-layer center

```
int_CC = (f_c90d + abs(CC_22(:,2))).^2 ./ (f_c90d + f_t90d)^2 + ...
          CC_23(:,2).^2 ./ f_rd^2 .* (1 - (f_c90d / (f_c90d + f_t90d))^2);
```

Cross-layer edge

```
int_CE = (f_c90d + abs(CE_22(:,2))).^2 ./ (f_c90d + f_t90d)^2 + ...
          CE_23(:,2).^2 ./ f_rd^2 .* (1 - (f_c90d / (f_c90d + f_t90d))^2);
```

Plotting utilisation ratio of interaction

```
figure(6)
plot(UC_12(:,1),int_UC,'color','#d9b2c7','linewidth',2)
hold on
plot(UE_12(:,1),int_UE,'color','#a1d4ae','linewidth',2)
hold on
plot(CC_12(:,1),int_CC,'color','#912661','linewidth',2)
hold on
plot(CE_12(:,1),int_CE,'color','#1f7a35','linewidth',2)
```

Plot settings

```
title('Utilisation ratio of interaction', 'FontSize', 24)
subtitle('Configuration I', 'FontSize', 20)
xlabel('Position in L-direction [mm]')
ylabel('Utilisation ratio [-]')
set(gca,'FontSize',20)
legend('Center of longitudinal layer', 'Edge of longitudinal layer', ...
       'Center of cross-layer', 'Edge of cross-layer', ...
       'Location', 'north')
xlim([0 l*1000])
grid on
```

C

Matlab code (five-layer configuration example)

Configuration IV

```
clear; clc; clf;
```

Load-deformation curve

Dimensions

```
l = 0.36;       % Length [m]
b = 0.11;       % Width  [m]
```

Average strength

Loading test data

```
A = load('CLT_5_0_A.mat');
A = cell2mat(struct2cell(A));
```

Plotting load deformation curve

```
u_A = abs(A(:,1));
F_A = abs(A(:,2));
t_A = A(:,3);

figure(1)
plot(u_A,F_A,'color','#C46C9C','linewidth',2)
hold on
```

Failure load

```
[F_max_A,i_A] = max(F_A(:));
F_max_A
F_max_A =

   62.6597
```

Deformation at failure
```
u_max_A = max(u_A(:))
u_max_A =

    5.0697
```

Time at failure
```
T_A = t_A(i_A)
T_A =

  431.3848
```

Low strength

Loading test data
```
L = load('CLT_5_0_L.mat');
L = cell2mat(struct2cell(L));
```

Plotting load deformation curve
```
u_L = abs(L(:,1));
F_L = abs(L(:,2));
t_L = L(:,3);

plot(u_L(1:1713),F_L(1:1713),'color','#66B378','linewidth',2)
hold on
```

Failure load
```
[F_max_L,i_L] = max(F_L(:));
F_max_L
F_max_L =

   56.4575
```

Deformation at failure
```
u_max_L = max(u_L(:))
u_max_L =

    2.9504
```

Time at failure
```
T_L = t_L(i_L)
T_L =

  214.0078
```

High strength

Loading test data

```
H = load('CLT_5_0_H.mat');
H = cell2mat(struct2cell(H));
```

Plotting load deformation curve

```
u_H = abs(H(:,1));
F_H = abs(H(:,2));
t_H = H(:,3);

plot(u_H(1:2378),F_H(1:2378),'color','#D18D11','linewidth',2)
```

Plot settings

```
title('Load deformation curve', 'FontSize', 24)
subtitle('Configuration IV', 'FontSize', 20)
xlabel('Deformation \delta [mm]')
ylabel('Load F [N]')
set(gca,'FontSize',20)
legend('Average', 'Low', 'High', 'Location', 'northwest')
grid on
```

Failure load

```
[F_max_H,i_H] = max(F_H(:));
F_max_H
F_max_H =

   76.7888
```

Deformation at failure

```
u_max_H = max(u_H(:))
u_max_H =

    4.0693
```

Time at failure

```
T_H = t_H(i_H)
T_H =

  296.3828
```

Abaqus stress paths

Loading test data

Stress in LR-plane

Upper longitudinal center

```
UC_12 = load('4_12_UC.mat');
UC_12 = cell2mat(struct2cell(UC_12));
```

Upper longitudinal edge

```
UE_12 = load('4_12_UE.mat');
UE_12 = cell2mat(struct2cell(UE_12));
```

Cross-layer upper edge

```
C_UE_12 = load('4_12_C_UE.mat');
C_UE_12 = cell2mat(struct2cell(C_UE_12));
```

Cross-layer center

```
CC_12 = load('4_12_CC.mat');
CC_12 = cell2mat(struct2cell(CC_12));
```

Cross-layer lower edge

```
C_LE_12 = load('4_12_C_LE.mat');
C_LE_12 = cell2mat(struct2cell(C_LE_12));
```

Mid longitudinal edge

```
ME_12 = load('4_12_ME.mat');
ME_12 = cell2mat(struct2cell(ME_12));
```

Mid longitudinal center

```
MC_12 = load('4_12_MC.mat');
MC_12 = cell2mat(struct2cell(MC_12));
```

Stress in RT-plane

Upper longitudinal center

```
UC_23 = load('4_23_UC.mat');
UC_23 = cell2mat(struct2cell(UC_23));
```

Upper longitudinal edge

```
UE_23 = load('4_23_UE.mat');
UE_23 = cell2mat(struct2cell(UE_23));
```

Cross-layer upper edge

```
C_UE_23 = load('4_23_C_UE.mat');
C_UE_23 = cell2mat(struct2cell(C_UE_23));
```

Cross-layer center
```
CC_23 = load('4_23_CC.mat');
CC_23 = cell2mat(struct2cell(CC_23));
```

Cross-layer lower edge
```
C_LE_23 = load('4_23_C_LE.mat');
C_LE_23 = cell2mat(struct2cell(C_LE_23));
```

Mid longitudinal edge
```
ME_23 = load('4_23_ME.mat');
ME_23 = cell2mat(struct2cell(ME_23));
```

Mid longitudinal center
```
MC_23 = load('4_23_MC.mat');
MC_23 = cell2mat(struct2cell(MC_23));
```

Stress in R-direction

Upper longitudinal center
```
UC_22 = load('4_22_UC.mat');
UC_22 = cell2mat(struct2cell(UC_22));
```

Upper longitudinal edge
```
UE_22 = load('4_22_UE.mat');
UE_22 = cell2mat(struct2cell(UE_22));
```

Cross-layer upper edge
```
C_UE_22 = load('4_22_C_UE.mat');
C_UE_22 = cell2mat(struct2cell(C_UE_22));
```

Cross-layer center
```
CC_22 = load('4_22_CC.mat');
CC_22 = cell2mat(struct2cell(CC_22));
```

Cross-layer lower edge
```
C_LE_22 = load('4_22_C_LE.mat');
C_LE_22 = cell2mat(struct2cell(C_LE_22));
```

Mid longitudinal edge
```
ME_22 = load('4_22_ME.mat');
ME_22 = cell2mat(struct2cell(ME_22));
```

Mid longitudinal center
```
MC_22 = load('4_22_MC.mat');
MC_22 = cell2mat(struct2cell(MC_22));
```

Plotting (upper longitudinal layer, LR+RT)

```
figure(2)
plot(UC_12(:,1),UC_12(:,2),'color','#d9b2c7','linewidth',2)
hold on
plot(UE_12(:,1),UE_12(:,2),'color','#a1d4ae','linewidth',2)
hold on
plot(UC_23(:,1),UC_23(:,2),'color','#912661','linewidth',2)
hold on
plot(UE_23(:,1),UE_23(:,2),'color','#1f7a35','linewidth',2)
```

Plot settings

```
title('Stress distribution in LR- and RT-plane along paths', 'FontSize', 24)
subtitle('Upper longitudinal layer, Configuration IV', 'FontSize', 20)
xlabel('Position in L-direction [mm]')
ylabel('Stress [MPa]')
set(gca,'FontSize',20)
legend('Center of longitudinal layer LR', 'Edge of longitudinal layer LR', ...
       'Center of longitudinal layer RT', 'Edge of longitudinal layer RT', ...
       'Location', 'southwest')
xlim([0 l*1000])
grid on
```

Plotting (cross-layer, LR+RT)

```
figure(3)
plot(C_UE_12(:,1),C_UE_12(:,2),'color','#e6c995','linewidth',2)
hold on
plot(CC_12(:,1),CC_12(:,2),'color','#d9b2c7','linewidth',2)
hold on
plot(C_LE_12(:,1),C_LE_12(:,2),'color','#a1d4ae','linewidth',2)
hold on
plot(C_UE_23(:,1),C_UE_23(:,2),'color','#D18D11','linewidth',2)
hold on
plot(CC_23(:,1),CC_23(:,2),'color','#912661','linewidth',2)
hold on
plot(C_LE_23(:,1),C_LE_23(:,2),'color','#1f7a35','linewidth',2)
```

Plot settings

```
title('Stress distribution in LR- and RT-plane along paths', 'FontSize', 24)
subtitle('Cross-layer, Configuration IV', 'FontSize', 20)
xlabel('Position in L-direction [mm]')
ylabel('Stress [MPa]')
set(gca,'FontSize',20)
legend('Upper edge of cross-layer LR', 'Center of cross-layer LR', ...
       'Lower edge of cross-layer LR', 'Upper edge of cross-layer RT', ...
       'Center of cross-layer RT', 'Lower edge of cross-layer RT', ...
       'Location', 'southwest')
xlim([0 l*1000])
```

```
grid on
```
Plotting (mid longitudinal layer, LR+RT)
```
figure(4)
plot(MC_12(:,1),MC_12(:,2),'color','#d9b2c7','linewidth',2)
hold on
plot(ME_12(:,1),ME_12(:,2),'color','#a1d4ae','linewidth',2)
hold on
plot(MC_23(:,1),MC_23(:,2),'color','#912661','linewidth',2)
hold on
plot(ME_23(:,1),ME_23(:,2),'color','#1f7a35','linewidth',2)
```

Plot settings
```
title('Stress distribution in LR- and RT-plane along paths', 'FontSize', 24)
subtitle('Mid longitudinal layer, Configuration IV', 'FontSize', 20)
xlabel('Position in L-direction [mm]')
ylabel('Stress [MPa]')
set(gca,'FontSize',20)
legend('Center of longitudinal layer LR', 'Edge of longitudinal layer LR', ...
       'Center of longitudinal layer RT', 'Edge of longitudinal layer RT', ...
       'Location', 'south')
xlim([0 l*1000])
ylim([-0.14 0.01])
grid on
```

Plotting (upper longitudinal layer, LR+RR)
```
figure(5)
plot(UC_12(:,1),UC_12(:,2),'color','#d9b2c7','linewidth',2)
hold on
plot(UE_12(:,1),UE_12(:,2),'color','#a1d4ae','linewidth',2)
hold on
plot(UC_22(:,1),UC_22(:,2),'color','#912661','linewidth',2)
hold on
plot(UE_22(:,1),UE_22(:,2),'color','#1f7a35','linewidth',2)
```

Plot settings
```
title('Stress distribution in LR- and RR-plane along paths', 'FontSize', 24)
subtitle('Upper longitudinal layer, Configuration IV', 'FontSize', 20)
xlabel('Position in L-direction [mm]')
ylabel('Stress [MPa]')
set(gca,'FontSize',20)
legend('Center of longitudinal layer LR', 'Edge of longitudinal layer LR', ...
       'Center of longitudinal layer RR', 'Edge of longitudinal layer RR', ...
       'Location', 'southwest')
xlim([0 l*1000])
grid on
```

Plotting (cross-layer, RT+RR)

```
figure(6)
plot(C_UE_23(:,1),C_UE_23(:,2),'color','#e6c995','linewidth',2)
hold on
plot(CC_23(:,1),CC_23(:,2),'color','#d9b2c7','linewidth',2)
hold on
plot(C_LE_23(:,1),C_LE_23(:,2),'color','#a1d4ae','linewidth',2)
hold on
plot(C_UE_22(:,1),C_UE_22(:,2),'color','#D18D11','linewidth',2)
hold on
plot(CC_22(:,1),CC_22(:,2),'color','#912661','linewidth',2)
hold on
plot(C_LE_22(:,1),C_LE_22(:,2),'color','#1f7a35','linewidth',2)
```

Plot settings

```
title('Stress distribution in RT- and RR-plane along paths', 'FontSize', 24)
subtitle('Cross-layer, Configuration IV', 'FontSize', 20)
xlabel('Position in L-direction [mm]')
ylabel('Stress [MPa]')
set(gca,'FontSize',20)
legend('Upper edge of cross-layer RT', 'Center of cross-layer RT', ...
       'Lower edge of cross-layer RT', 'Upper edge of cross-layer RR', ...
       'Center of cross-layer RR', 'Lower edge of cross-layer RR', ...
       'Location', 'southwest')
xlim([0 l*1000])
grid on
```

Plotting (mid longitudinal layer, LR+RR)

```
figure(7)
plot(MC_12(:,1),MC_12(:,2),'color','#d9b2c7','linewidth',2)
hold on
plot(ME_12(:,1),ME_12(:,2),'color','#a1d4ae','linewidth',2)
hold on
plot(MC_22(:,1),MC_22(:,2),'color','#912661','linewidth',2)
hold on
plot(ME_22(:,1),ME_22(:,2),'color','#1f7a35','linewidth',2)
```

Plot settings

```
title('Stress distribution in LR- and RR-plane along paths', 'FontSize', 24)
subtitle('Mid longitudinal layer, Configuration IV', 'FontSize', 20)
xlabel('Position in L-direction [mm]')
ylabel('Stress [MPa]')
set(gca,'FontSize',20)
legend('Center of longitudinal layer LR', 'Edge of longitudinal layer LR', ...
       'Center of longitudinal layer RR', 'Edge of longitudinal layer RR', ...
       'Location', 'south')
xlim([0 l*1000])
```

```
grid on
```
Interaction

Indata
```
f_c90k = 2.5;
f_t90k = 0.4;
f_vk = 4.0;
f_rk = 1.1;
k_mod = 0.80;
gamma_M = 1.25;
```

Design values
```
f_c90d = k_mod * f_c90k / gamma_M;
f_t90d = k_mod * f_t90k / gamma_M;
f_vd = k_mod * f_vk / gamma_M;
f_rd = k_mod * f_rk / gamma_M;
```

Upper longitudinal center
```
int_UC = (f_c90d + abs(UC_22(:,2))).^2 ./ (f_c90d + f_t90d)^2 + ...
          UC_12(:,2).^2 ./ f_vd^2 .* (1 - (f_c90d / (f_c90d + f_t90d))^2);
```

Upper longitudinal edge
```
int_UE = (f_c90d + abs(UE_22(:,2))).^2 ./ (f_c90d + f_t90d)^2 + ...
          UE_12(:,2).^2 ./ f_vd^2 .* (1 - (f_c90d / (f_c90d + f_t90d))^2);
```

Cross-layer upper edge
```
int_C_UE = (f_c90d + abs(C_UE_22(:,2))).^2 ./ (f_c90d + f_t90d)^2 + ...
            C_UE_23(:,2).^2 ./ f_rd^2 .* (1 - (f_c90d / (f_c90d + f_t90d))^2);
```

Cross-layer center
```
int_CC = (f_c90d + abs(CC_22(:,2))).^2 ./ (f_c90d + f_t90d)^2 + ...
          CC_23(:,2).^2 ./ f_rd^2 .* (1 - (f_c90d / (f_c90d + f_t90d))^2);
```

Cross-layer lower edge
```
int_C_LE = (f_c90d + abs(C_LE_22(:,2))).^2 ./ (f_c90d + f_t90d)^2 + ...
            C_LE_23(:,2).^2 ./ f_rd^2 .* (1 - (f_c90d / (f_c90d + f_t90d))^2);
```

Mid longitudinal center
```
int_MC = (f_c90d + abs(MC_22(:,2))).^2 ./ (f_c90d + f_t90d)^2 + ...
          MC_12(:,2).^2 ./ f_vd^2 .* (1 - (f_c90d / (f_c90d + f_t90d))^2);
```

Mid longitudinal edge
```
int_ME = (f_c90d + abs(ME_22(:,2))).^2 ./ (f_c90d + f_t90d)^2 + ...
          ME_12(:,2).^2 ./ f_vd^2 .* (1 - (f_c90d / (f_c90d + f_t90d))^2);
```

Plotting utilisation ratio of interaction

```
figure(8)
plot(UC_12(:,1),int_UC,'color','#e6c995','linewidth',2)
hold on
plot(UE_12(:,1),int_UE,'color','#d9b2c7','linewidth',2)
hold on
plot(C_UE_12(:,1),int_C_UE,'color','#D18D11','linewidth',2)
hold on
plot(CC_12(:,1),int_CC,'color','#912661','linewidth',2)
hold on
plot(C_LE_12(:,1),int_C_LE,'color','#1f7a35','linewidth',2)
hold on
plot(MC_12(:,1),int_MC,'color','#a1d4ae','linewidth',2)
hold on
plot(ME_12(:,1),int_ME,'color','#7996d9','linewidth',2)
```

Plot settings

```
title('Utilisation ratio of interaction', 'FontSize', 24)
subtitle('Configuration IV', 'FontSize', 20)
xlabel('Position in L-direction [mm]')
ylabel('Utilisation ratio [-]')
set(gca,'FontSize',20)
legend('Center of upper longitudinal layer', ...
       'Edge of upper longitudinal layer', ...
       'Upper edge of cross-layer', 'Center of cross-layer', ...
       'Lower edge of cross-layer', 'Center of mid longitudinal layer', ...
       'Edge of mid longitudinal layer', 'Location', 'north')
xlim([0 l*1000])
grid on
```

D

Configurations data

Configuration I			
Average strength specimen	**Board no.**	**Density [kg/m3]**	**MOE [Pa]**
Longitudinal layers	A1	426,70	11 185,60
Cross-layer	A1	426,70	11 185,60
Low strength specimen	**Board no.**	**Density [kg/m3]**	**MOE [Pa]**
Longitudinal layers	A38	424,67	11 624,96
Cross-layer	A12	363,63	9 787,13
High strength specimen	**Board no.**	**Density [kg/m3]**	**MOE [Pa]**
Longitudinal layers	A38	424,67	11 624,96
Cross-layer	A37	470,75	14 116,06
Difference in strength		**Density [kg/m3]**	**MOE [Pa]**
Average		425,69	11 405,28
Decrease (low strength)		14,58%	14,19%
Increase (high strength)		10,59%	23,77%

Configuration II			
Average strength specimen	**Board no.**	**Density [kg/m3]**	**MOE [Pa]**
Longitudinal layers	A3	403,46	11 939,76
Cross-layer	A3	403,46	11 939,76
Low strength specimen	**Board no.**	**Density [kg/m3]**	**MOE [Pa]**
Longitudinal layers	A6	405,77	12 043,52
Cross-layer	A12	363,63	9 787,13
High strength specimen	**Board no.**	**Density [kg/m3]**	**MOE [Pa]**
Longitudinal layers	A6	405,77	12 043,52
Cross-layer	A37	470,75	14 116,06
Difference in strength		**Density [kg/m3]**	**MOE [Pa]**
Average		404,62	11 991,64
Decrease (low strength)		10,13%	18,38%
Increase (high strength)		16,35%	17,72%

Configuration III			
Average strength specimen	**Board no.**	**Density [kg/m3]**	**MOE [Pa]**
Longitudinal layers	A39	417,83	11 090,42
Cross-layer	A39	417,83	11 090,42
Low strength specimen	**Board no.**	**Density [kg/m3]**	**MOE [Pa]**
Longitudinal layers	A10	406,81	11 000,09
Cross-layer	A12	363,63	9 787,13
High strength specimen	**Board no.**	**Density [kg/m3]**	**MOE [Pa]**
Longitudinal layers	A26	400,26	10 906,51
Cross-layer	A37	470,75	14 116,06
Difference in strength		**Density [kg/m3]**	**MOE [Pa]**
Average		408,30	10 999,01
Decrease (low strength)		10,94%	11,02%
Increase (high strength)		15,30%	28,34%

Configuration IV			
Average strength specimen	**Board no.**	**Density [kg/m3]**	**MOE [Pa]**
Longitudinal layers	B54	488,02	14 273,00
Cross-layers	B54	488,02	14 273,00
	B2	495,49	14 214,07
Low strength specimen	**Board no.**	**Density [kg/m3]**	**MOE [Pa]**
Longitudinal layers	B2	495,49	14 214,07
Cross-layers	B30	456,72	12 771,20
High strength specimen	**Board no.**	**Density [kg/m3]**	**MOE [Pa]**
Longitudinal layers	B41	497,75	14 172,28
Cross-layers	B8	557,08	16 316,78
Difference in strength		**Density [kg/m3]**	**MOE [Pa]**
Average		493,75	14 219,78
Decrease (low strength)		7,50%	10,19%
Increase (high strength)		12,83%	14,75%

Configuration V			
Average strength specimen	**Board no.**	**Density [kg/m3]**	**MOE [Pa]**
Longitudinal layers	B63	485,31	15 569,24
Cross-layers	B46	480,16	15 775,97
Low strength specimen	**Board no.**	**Density [kg/m3]**	**MOE [Pa]**
Longitudinal layers	B37	492,38	15 751,43
Cross-layers	B51	426,98	13 833,80
High strength specimen	**Board no.**	**Density [kg/m3]**	**MOE [Pa]**
Longitudinal layers	B52	493,33	15 470,93
Cross-layers	B58	520,83	17 184,13
Difference in strength		**Density [kg/m3]**	**MOE [Pa]**
Average		487,80	15 641,89
Decrease (low strength)		12,47%	11,56%
Increase (high strength)		6,77%	9,86%

Configuration VI			
Average strength specimen	**Board no.**	**Density [kg/m3]**	**MOE [Pa]**
Longitudinal layers	B1	472,74	15 381,01
Cross-layers	B1	472,74	15 381,01
	B45	477,64	15 540,24
	B76	477,89	15 180,00
Low strength specimen	**Board no.**	**Density [kg/m3]**	**MOE [Pa]**
Longitudinal layers	B45	477,64	15 540,24
Cross-layers	B51	426,98	13 833,80
High strength specimen	**Board no.**	**Density [kg/m3]**	**MOE [Pa]**
Longitudinal layers	B76	477,89	15 180,00
Cross-layers	B58	520,83	17 184,13
Difference in strength		**Density [kg/m3]**	**MOE [Pa]**
Average		476,09	15 367,08
Decrease (low strength)		10,32%	9,98%
Increase (high strength)		9,40%	11,82%

Configuration VII			
Average strength specimen	**Board no.**	**Density [kg/m3]**	**MOE [Pa]**
Longitudinal layers	B17	466,50	13 342,31
Cross-layers	B17	466,50	13 342,31
	B69	468,60	13 543,18
Low strength specimen	**Board no.**	**Density [kg/m3]**	**MOE [Pa]**
Longitudinal layers	B69	468,60	13 543,18
Cross-layers	B39	435,31	11 626,42
High strength specimen	**Board no.**	**Density [kg/m3]**	**MOE [Pa]**
Longitudinal layers	B74	455,12	13 747,30
Cross-layers	B70	503,31	15 402,72
Difference in strength		**Density [kg/m3]**	**MOE [Pa]**
Average		463,41	13 544,26
Decrease (low strength)		6,06%	14,16%
Increase (high strength)		8,61%	13,72%

Configuration VIII			
Average strength specimen	**Board no.**	**Density [kg/m3]**	**MOE [Pa]**
Longitudinal layers	B23	477,01	13 765,68
	B65	470,63	13 764,12
Cross-layers	B65	470,63	13 764,12
Low strength specimen	**Board no.**	**Density [kg/m3]**	**MOE [Pa]**
Longitudinal layers	B82	480,47	13 618,98
	B29	482,22	13 281,13
Cross-layers	B39	435,31	11 626,42
High strength specimen	**Board no.**	**Density [kg/m3]**	**MOE [Pa]**
Longitudinal layers	B19	485,35	13 387,77
	B29	482,22	13 281,13
Cross-layers	B70	503,31	15 402,72
Difference in strength		**Density [kg/m3]**	**MOE [Pa]**
Average		479,14	13 563,54
Decrease (low strength)		9,15%	14,28%
Increase (high strength)		5,05%	13,56%

Configuration IX			
Average strength specimen	**Board no.**	**Density [kg/m3]**	**MOE [Pa]**
Longitudinal layers	B12	500,94	15 153,58
Cross-layers	B12	500,94	15 153,58
	B18	501,43	15 212,37
	B7	502,70	15 251,08
Low strength specimen	**Board no.**	**Density [kg/m3]**	**MOE [Pa]**
Longitudinal layers	B18	501,43	15 212,37
Cross-layers	B55	451,44	13 415,26
High strength specimen	**Board no.**	**Density [kg/m3]**	**MOE [Pa]**
Longitudinal layers	B7	502,70	15 251,08
Cross-layers	B8	557,08	16 316,78
Difference in strength		**Density [kg/m3]**	**MOE [Pa]**
Average		501,69	15 205,68
Decrease (low strength)		10,02%	11,77%
Increase (high strength)		11,04%	7,31%

E

Calculation of shear strength

Configuration I	**Average**	**Low**	**High**	
Failure mode	Bondline	Bondline	Bondline	
Input				**Unit**
Specimen width *b*	0,110	0,110	0,110	[m]
Specimen length *L*	0,360	0,360	0,360	[m]
Failure load *F_max*	44,50	28,14	34,98	[kN]
Shear strength				
Bondline shear strength *f_b*	1123737	710606	883333	[Pa]
	1,12	**0,71**	**0,88**	[MPa]

Configuration II	**Average**	**Low**	**High**	
Failure mode	Bondline	Panel	Panel	
Input				**Unit**
Specimen width *b*	0,110	0,110	0,110	[m]
Specimen length *L*	0,360	0,360	0,360	[m]
Cross-layer interface length *L_c*	0,240	0,240	0,240	[m]
Failure load *F_max*	20,24	19,97	24,98	[kN]
Shear strength				
Panel shear strength *f_v*		504293	630808	[Pa]
		0,50	**0,63**	[MPa]
Bondline shear strength *f_b*	766667			[Pa]
	0,77			[MPa]

Configuration III	**Average**	**Low**	**High**	
Failure mode	Bondline	Bondline	Panel	
Input				**Unit**
Specimen width *b*	0,110	0,110	0,110	[m]
Specimen length *L*	0,480	0,480	0,480	[m]
Cross-layer interface length *L_c*	0,240	0,240	0,240	[m]
Failure load *F_max*	30,10	19,35	30,38	[kN]
Shear strength				
Panel shear strength *f_v*			575379	[Pa]
			0,58	[MPa]
Bondline shear strength *f_b*	1140152	732955		[Pa]
	1,14	**0,73**		[MPa]

Configuration IV	**Average**	**Low**	**High**	
Failure mode	Panel	Rolling	Bondline	
Input				**Unit**
Specimen width *b*	0,110	0,110	0,110	[m]
Specimen length *L*	0,360	0,360	0,360	[m]
Failure load *F_max*	62,66	56,46	76,69	[kN]
Shear strength				
Panel shear strength *f_v*	1582323			[Pa]
	1,58			[MPa]
Bondline shear strength *f_b*			1936616	[Pa]
			1,94	[MPa]
Rolling shear strength *f_r*		1425758		[Pa]
		1,43		[MPa]

Configuration V	**Average**	**Low**	**High**	
Failure mode	Rolling	Rolling	Rolling	
Input				**Unit**
Specimen width *b*	0,110	0,110	0,110	[m]
Specimen length *L*	0,540	0,540	0,540	[m]
Cross-layer interface length *L_c*	0,360	0,360	0,360	[m]
Failure load *F_max*	58,83	55,89	63,86	[kN]
Shear strength				
Rolling shear strength *f_r*	1485606	1411364	1612626	Pa
	1,49	**1,41**	**1,61**	MPa

Configuration VI	**Average**	**Low**	**High**	
Failure mode	Rolling	Rolling	Panel	
Input				**Unit**
Specimen width *b*	0,110	0,110	0,110	[m]
Specimen length *L*	0,450	0,450	0,450	[m]
Cross-layer interface length *L_c*	0,300	0,300	0,300	[m]
Failure load *F_max*	45,28	46,48	42,59	[kN]
Shear strength				
Panel shear strength *f_v*			860404	[Pa]
			0,86	[MPa]
Rolling shear strength *f_r*	1372121	1408485		[Pa]
	1,37	**1,41**		[MPa]

Configuration VII	**Average**	**Low**	**High**	
Failure mode	Rolling	Rolling	Bondline	
Input				**Unit**
Specimen width *b*	0,110	0,110	0,110	[m]
Specimen length *L*	0,480	0,480	0,480	[m]
Cross-layer interface length *L_c*	0,240	0,240	0,240	[m]
Failure load *F_max*	42,50	38,74	45,58	[kN]
Shear strength				
Bondline shear strength *f_b*			1726515	[Pa]
			1,73	[MPa]
Rolling shear strength *f_r*	1609848	1467424		[Pa]
	1,61	**1,47**		[MPa]

Configuration VIII	**Average**	**Low**	**High**	
Failure mode	Panel	Bondline	Panel	
Input				**Unit**
Specimen width *b*	0,110	0,110	0,110	[m]
Specimen length *L*	0,600	0,600	0,600	[m]
Cross-layer interface length *L_c*	0,300	0,300	0,300	[m]
Failure load *F_max*	43,19	38,07	48,53	[kN]
Shear strength				
Panel shear strength *f_v*	654394		735303	[Pa]
	0,65		**0,74**	[MPa]
Bondline shear strength *f_b*		1153636		[Pa]
		1,15		[MPa]

Configuration IX	**Average**	**Low**	**High**	
Failure mode	Panel	Panel	Panel	
Input				**Unit**
Specimen width *b*	0,110	0,110	0,110	[m]
Specimen length *L*	0,500	0,500	0,500	[m]
Cross-layer interface length *L_c*	0,300	0,300	0,300	[m]
Failure load *F_max*	41,95	40,74	73,31	[kN]
Shear strength				
Panel shear strength *f_v*	762727	740727	1332909	[Pa]
	0,76	**0,74**	**1,33**	[MPa]

F

Calculation of failure load ratio

Configuration I		
Reference configuration for three-layer configurations		
Geometry	**Value**	**Unit**
Specimen length *L*	0,36	[m]
Specimen width *b*	0,11	[m]
Total thickness of specimen *h*	0,90	[m]
Lamella thickness *t*	0,30	[m]
Air gap width *b_airgap*	0,00	[m]
Wood volume *V_wood*	0,036	[m3]
Maximum volume *V_max*	0,036	[m3]
Geometrical ratios		
Length ratio *η_L*	1,00	[-]
Volume ratio *η_V*	1,00	[-]
Material reduction μ_M	0,00	[%]
Failure loads *F_max*		
Average strength specimen	44,50	[kN]
Low strength specimen	28,14	[kN]
High strength specimen	34,98	[kN]
Adjusted failure loads *F_adjusted*		
Average strength specimen	44,50	[kN]
Low strength specimen	28,14	[kN]
High strength specimen	34,98	[kN]
Failure load ratio *η_F*		
Average strength specimen	1,00	[-]
Low strength specimen	1,00	[-]
High strength specimen	1,00	[-]

Configuration II		
Three-layer configuration		
Geometry		
Specimen length *L*	0,360	[m]
Cross-layer interface length *L_c*	0,240	[m]
Specimen width *b*	0,110	[m]
Total thickness of specimen *h*	0,900	[m]
Lamella thickness *t*	0,300	[m]
Air gap width *b_airgap*	0,600	[m]
Wood volume *V_wood*	0,032	[m3]
Maximum volume *V_max*	0,036	[m3]
Geometrical ratios		
Length ratio *η_L*	1,00	[-]
Volume ratio *η_V*	0,89	[-]
Material reduction μ_M	11,11	[%]
Failure loads *F_max*		
Average strength specimen	20,24	[kN]
Low strength specimen	19,97	[kN]
High strength specimen	24,98	[kN]

Adjusted failure loads *F_adjusted*		
Average strength specimen	20,24	[kN]
Low strength specimen	19,97	[kN]
High strength specimen	24,98	[kN]
Failure load ratio *η_F*		
Average strength specimen	0,45	[-]
Low strength specimen	0,71	[-]
High strength specimen	0,71	[-]

Configuration III		
Three-layer configuration		
Geometry		
Specimen length *L*	0,480	[m]
Cross-layer interface length *L_c*	0,240	[m]
Specimen width *b*	0,110	[m]
Total thickness of specimen *h*	0,900	[m]
Lamella thickness *t*	0,300	[m]
Air gap width *b_airgap*	0,120	[m]
Wood volume *V_wood*	0,040	[m3]
Maximum volume *V_max*	0,048	[m3]
Geometrical ratios		
Length ratio *η_L*	1,33	[-]
Volume ratio *η_V*	0,83	[-]
Material reduction μ_M	16,67	[%]
Failure loads *F_max*		
Average strength specimen	30,10	[kN]
Low strength specimen	19,35	[kN]
High strength specimen	30,38	[kN]
Adjusted failure loads *F_adjusted*		
Average strength specimen	22,58	[kN]
Low strength specimen	14,51	[kN]
High strength specimen	22,79	[kN]
Failure load ratio *η_F*		
Average strength specimen	0,51	[-]
Low strength specimen	0,52	[-]
High strength specimen	0,65	[-]

Configuration IV		
Reference configuration for five-layer configurations		
Geometry	**Value**	**Unit**
Specimen length *L*	0,360	[m]
Specimen width *b*	0,110	[m]
Total thickness of specimen *h*	1,000	[m]
Lamella thickness *t*	0,200	[m]
Air gap width *b_airgap*	0,000	[m]
Wood volume *V_wood*	0,040	[m3]
Maximum volume *V_max*	0,040	[m3]
Geometrical ratios		
Length ratio *η_L*	1,00	[-]
Volume ratio *η_V*	1,00	[-]
Material reduction μ_M	0,00	[%]
Failure loads *F_max*		
Average strength specimen	62,66	[kN]
Low strength specimen	56,46	[kN]
High strength specimen	76,69	[kN]
Adjusted failure loads *F_adjusted*		
Average strength specimen	62,66	[kN]
Low strength specimen	56,46	[kN]
High strength specimen	76,69	[kN]
Failure load ratio *η_F*		
Average strength specimen	1,00	[-]
Low strength specimen	1,00	[-]
High strength specimen	1,00	[-]

Configuration V		
Five-layer configuration		
Geometry		
Specimen length *L*	0,540	[m]
Cross-layer interface length *L_c*	0,360	[m]
Specimen width *b*	0,110	[m]
Total thickness of specimen *h*	1,000	[m]
Lamella thickness *t*	0,200	[m]
Air gap width *b_airgap*	0,600	[m]
Wood volume *V_wood*	0,051	[m3]
Maximum volume *V_max*	0,059	[m3]
Geometrical ratios		
Length ratio *η_L*	1,50	[-]
Volume ratio *η_V*	0,87	[-]
Material reduction μ_M	13,33	[%]
Failure loads *F_max*		
Average strength specimen	58,83	[kN]
Low strength specimen	55,89	[kN]
High strength specimen	63,86	[kN]

Adjusted failure loads *F_adjusted*		
Average strength specimen	39,22	[kN]
Low strength specimen	37,26	[kN]
High strength specimen	42,57	[kN]
Failure load ratio *η_F*		
Average strength specimen	0,63	[-]
Low strength specimen	0,66	[-]
High strength specimen	0,56	[-]

Configuration VI		
Five-layer configuration		
Geometry		
Specimen length *L*	0,450	[m]
Cross-layer interface length *L_c*	0,300	[m]
Specimen width *b*	0,110	[m]
Total thickness of specimen *h*	1,000	[m]
Lamella thickness *t*	0,200	[m]
Air gap width *b_airgap*	0,600	[m]
Wood volume *V_wood*	0,043	[m3]
Maximum volume *V_max*	0,050	[m3]
Geometrical ratios		
Length ratio *η_L*	1,25	[-]
Volume ratio *η_V*	0,87	[-]
Material reduction μ_M	13,33	[%]
Failure loads *F_max*		
Average strength specimen	45,28	[kN]
Low strength specimen	46,48	[kN]
High strength specimen	42,59	[kN]
Adjusted failure loads *F_adjusted*		
Average strength specimen	36,22	[kN]
Low strength specimen	37,18	[kN]
High strength specimen	34,07	[kN]
Failure load ratio *η_F*		
Average strength specimen	0,58	[-]
Low strength specimen	0,66	[-]
High strength specimen	0,44	[-]

Configuration VII			
Five-layer configuration			
Geometry	**Value**		**Unit**
Specimen length *L*		0,480	[m]
Cross-layer interface length *L_c*		0,240	[m]
Specimen width *b*		0,110	[m]
Total thickness of specimen *h*		1,000	[m]
Lamella thickness *t*		0,200	[m]
Air gap width *b_airgap*		0,120	[m]
Wood volume *V_wood*		0,042	[m3]
Maximum volume *V_max*		0,053	[m3]
Geometrical ratios			
Length ratio *η_L*		1,33	[-]
Volume ratio *η_V*		0,80	[-]
Material reduction μ_M		20,00	[%]
Failure loads *F_max*			
Average strength specimen		42,50	[kN]
Low strength specimen		38,74	[kN]
High strength specimen		45,58	[kN]
Adjusted failure loads *F_adjusted*			
Average strength specimen		31,88	[kN]
Low strength specimen		29,06	[kN]
High strength specimen		34,19	[kN]
Failure load ratio *η_F*			
Average strength specimen		0,51	[-]
Low strength specimen		0,51	[-]
High strength specimen		0,45	[-]

Configuration VIII			
Five-layer configuration			
Geometry			
Specimen length *L*		0,600	[m]
Cross-layer interface length *L_c*		0,300	[m]
Specimen width *b*		0,110	[m]
Total thickness of specimen *h*		1,000	[m]
Lamella thickness *t*		0,200	[m]
Air gap width *b_airgap*		0,120	[m]
Wood volume *V_wood*		0,053	[m3]
Maximum volume *V_max*		0,066	[m3]
Geometrical ratios			
Length ratio *η_L*		1,67	[-]
Volume ratio *η_V*		0,80	[-]
Material reduction μ_M		20,00	[%]
Failure loads *F_max*			
Average strength specimen		43,19	[kN]
Low strength specimen		38,07	[kN]

High strength specimen	48,53	[kN]
Adjusted failure loads *F_adjusted*		
Average strength specimen	25,91	[kN]
Low strength specimen	22,84	[kN]
High strength specimen	29,12	[kN]
Failure load ratio *η_F*		
Average strength specimen	0,41	[-]
Low strength specimen	0,40	[-]
High strength specimen	0,38	[-]

Configuration IX		
Five-layer configuration		
Geometry		
Specimen length *L*	0,500	[m]
Cross-layer interface length *L_c*	0,300	[m]
Specimen width *b*	0,110	[m]
Total thickness of specimen *h*	1,000	[m]
Lamella thickness *t*	0,200	[m]
Air gap width *b_airgap*	0,800	[m]
Wood volume *V_wood*	0,046	[m3]
Maximum volume *V_max*	0,055	[m3]
Geometrical ratios		
Length ratio *η_L*	1,39	[-]
Volume ratio *η_V*	0,84	[-]
Material reduction μ_M	16,00	[%]
Failure loads *F_max*		
Average strength specimen	41,95	[kN]
Low strength specimen	40,74	[kN]
High strength specimen	73,31	[kN]
Adjusted failure loads *F_adjusted*		
Average strength specimen	30,20	[kN]
Low strength specimen	29,33	[kN]
High strength specimen	52,78	[kN]
Failure load ratio *η_F*		
Average strength specimen	0,48	[-]
Low strength specimen	0,52	[-]
High strength specimen	0,69	[-]

G

Calculation of load scale factor

Configuration I		
Reference configuration for three-layer configurations		
Input	**Value**	**Unit**
Lamella thickness *t*	0,030	[m]
Lamella width *b*	0,110	[m]
Lamella length *L*	0,360	[m]
Angle *α* in radians	0,192	[rad]
Angle *α* in degrees	11,0	[°]
Pressure area		
Pressure area width *b_p*	0,066	[m]
Pressure area length *l_p*	0,110	[m]
Pressure area *A_p*	0,007	[m2]
Load scale factor		
Ratio *η_A*	1,00	[-]
Ratio *η_L*	1,00	[-]
Load scale factor *LSF*	1,00	[-]

Configuration II		
Three-layer configuration		
Input	**Value**	**Unit**
Lamella thickness *t*	0,030	[m]
Lamella width *b*	0,110	[m]
Lamella length *L*	0,360	[m]
Angle *α* in radians	0,192	[rad]
Angle *α* in degrees	11,0	[°]
Pressure area		
Pressure area width *b_p*	0,066	[m]
Pressure area length *l_p*	0,110	[m]
Pressure area *A_p*	0,007	[m2]
Load scale factor		
Ratio *η_A*	1,00	[-]
Ratio *η_L*	1,00	[-]
Load scale factor *LSF*	1,00	[-]

Configuration III		
Three-layer configuration		
Input	**Value**	**Unit**
Lamella thickness *t*	0,030	[m]
Lamella width *b*	0,110	[m]
Lamella length *L*	0,480	[m]
Angle *α* in radians	0,145	[rad]
Angle *α* in degrees	8,30	[°]
Pressure area		
Pressure area width *b_p*	0,053	[m]
Pressure area length *l_p*	0,110	[m]
Pressure area *A_p*	0,006	[m2]
Load scale factor		
Ratio *η_A*	0,809	[-]
Ratio *η_L*	1,33	[-]
Load scale factor *LSF*	1,08	[-]

Configuration IV		
Reference configuration for five-layer configurations		
Input	**Value**	**Unit**
Lamella thickness *t*	0,020	[m]
Lamella width *b*	0,110	[m]
Lamella length *L*	0,360	[m]
Angle *α* in radians	0,245	[rad]
Angle *α* in degrees	14,0	[°]
Pressure area		
Pressure area width *b_p*	0,021	[m]
Pressure area length *l_p*	0,110	[m]
Pressure area *A_p*	0,002	[m2]
Load scale factor		
Ratio *η_A*	1,00	[-]
Ratio *η_L*	1,00	[-]
Load scale factor *LSF*	1,00	[-]

Configuration V		
Five-layer configuration		
Input	**Value**	**Unit**
Lamella thickness *t*	0,020	[m]
Lamella width *b*	0,110	[m]
Lamella length *L*	0,540	[m]
Angle *α* in radians	0,165	[rad]
Angle *α* in degrees	9,46	[°]
Pressure area		
Pressure area width *b_p*	0,020	[m]
Pressure area length *l_p*	0,110	[m]
Pressure area *A_p*	0,002	[m2]
Load scale factor		
Ratio *η_A*	0,984	[-]
Ratio *η_L*	1,50	[-]
Load scale factor *LSF*	1,48	[-]

Configuration VI		
Five-layer configuration		
Input	**Value**	**Unit**
Lamella thickness *t*	0,020	[m]
Lamella width *b*	0,110	[m]
Lamella length *L*	0,450	[m]
Angle *α* in radians	0,197	[rad]
Angle *α* in degrees	11,3	[°]
Pressure area		
Pressure area width *b_p*	0,020	[m]
Pressure area length *l_p*	0,110	[m]
Pressure area *A_p*	0,002	[m2]
Load scale factor		
Ratio *η_A*	0,989	[-]
Ratio *η_L*	1,25	[-]
Load scale factor *LSF*	1,24	[-]

Configuration VII		
Five-layer configuration		
Input	**Value**	**Unit**
Lamella thickness *t*	0,020	[m]
Lamella width *b*	0,110	[m]
Lamella length *L*	0,480	[m]
Angle *α* in radians	0,185	[rad]
Angle *α* in degrees	10,6	[°]
Pressure area		
Pressure area width *b_p*	0,020	[m]
Pressure area length *l_p*	0,110	[m]
Pressure area *A_p*	0,002	[m2]
Load scale factor		
Ratio *η_A*	0,987	[-]
Ratio *η_L*	1,33	[-]
Load scale factor *LSF*	1,32	[-]

Configuration VIII		
Five-layer configuration		
Input	**Value**	**Unit**
Lamella thickness *t*	0,020	[m]
Lamella width *b*	0,110	[m]
Lamella length *L*	0,600	[m]
Angle *α* in radians	0,149	[rad]
Angle *α* in degrees	8,53	[°]
Pressure area		
Pressure area width *b_p*	0,020	[m]
Pressure area length *l_p*	0,110	[m]
Pressure area *A_p*	0,002	[m2]
Load scale factor		
Ratio *η_A*	0,981	[-]
Ratio *η_L*	1,67	[-]
Load scale factor *LSF*	1,63	[-]

Configuration IX		
Five-layer configuration		
Input	**Value**	**Unit**
Lamella thickness *t*	0,020	[m]
Lamella width *b*	0,110	[m]
Lamella length *L*	0,500	[m]
Angle *α* in radians	0,178	[rad]
Angle *α* in degrees	10,2	[°]
Pressure area		
Pressure area width *b_p*	0,020	[m]
Pressure area length *l_p*	0,110	[m]
Pressure area *A_p*	0,002	[m2]
Load scale factor		
Ratio *η_A*	0,986	[-]
Ratio *η_L*	1,39	[-]
Load scale factor *LSF*	1,37	[-]

H

Figures from results

H.1 Configuration I

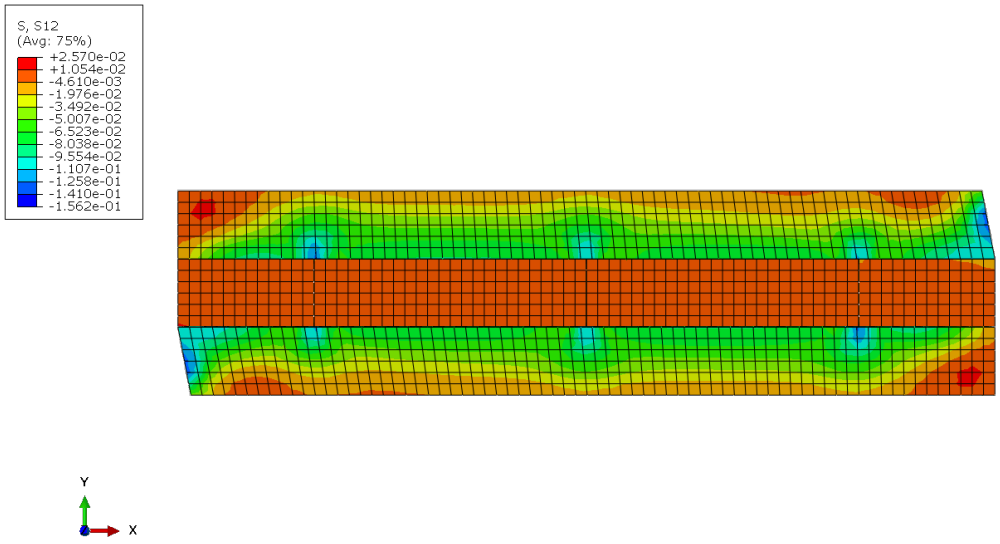

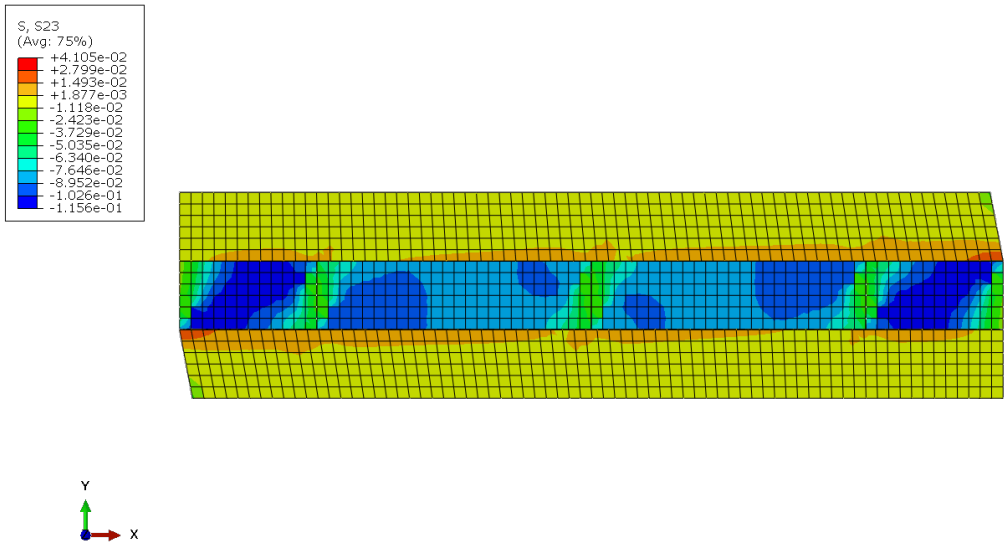

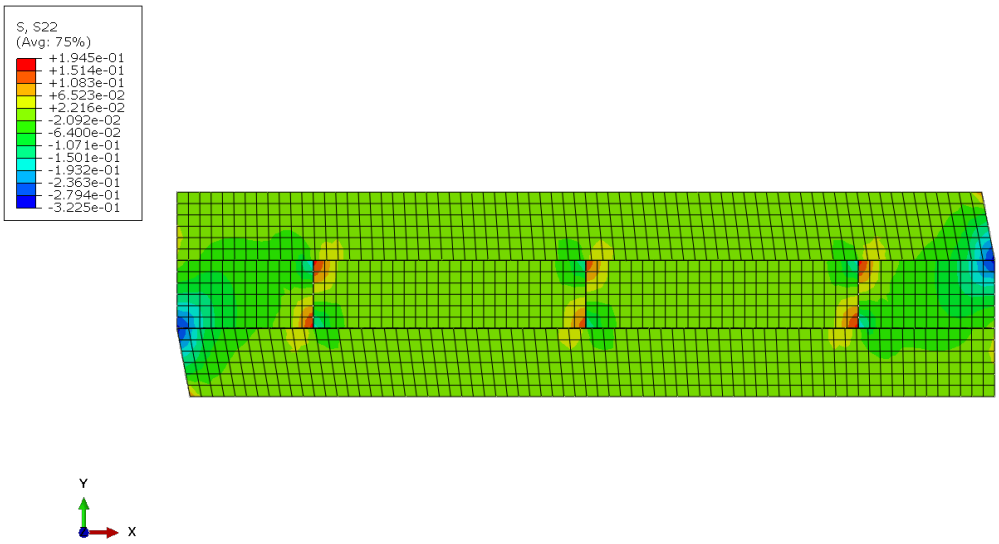
S, S22
(Avg: 75%)
+1.945e-01
+1.514e-01
+1.083e-01
+6.523e-02
+2.216e-02
-2.092e-02
-6.400e-02
-1.071e-01
-1.501e-01
-1.932e-01
-2.363e-01
-2.794e-01
-3.225e-01
Y
X

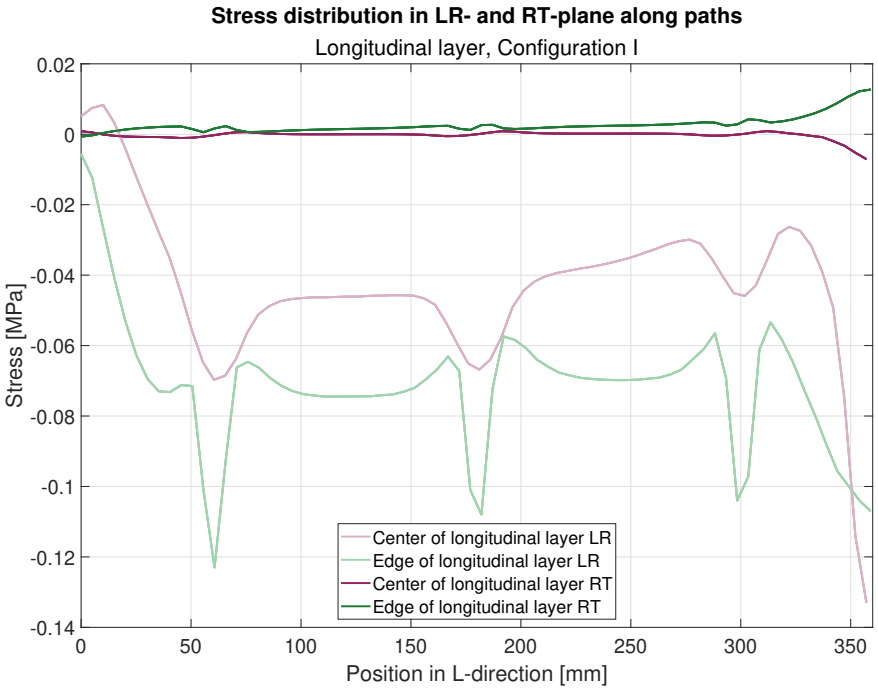
Stress distribution in LR- and RT-plane along paths
Longitudinal layer, Configuration I
Stress [MPa]
Position in L-direction [mm]
0.02
0
-0.02
-0.04
-0.06
-0.08
-0.1
-0.12
-0.14
0
50
100
150
200
250
300
350
Center of longitudinal layer LR
Edge of longitudinal layer LR
Center of longitudinal layer RT
Edge of longitudinal layer RT

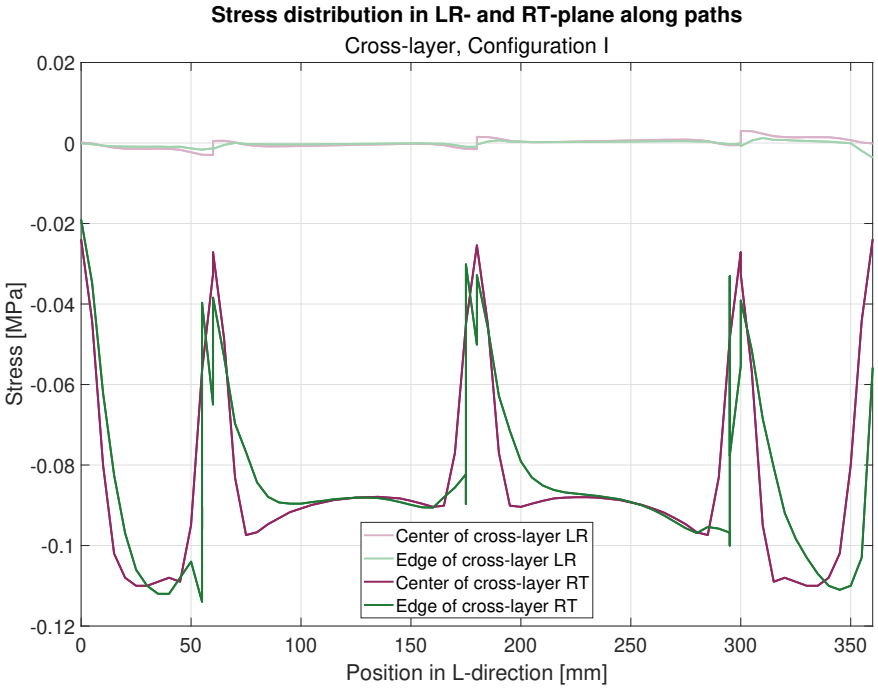
Stress distribution in LR- and RT-plane along paths
Cross-layer, Configuration I
Stress [MPa]
Position in L-direction [mm]
Center of cross-layer LR
Edge of cross-layer LR
Center of cross-layer RT
Edge of cross-layer RT

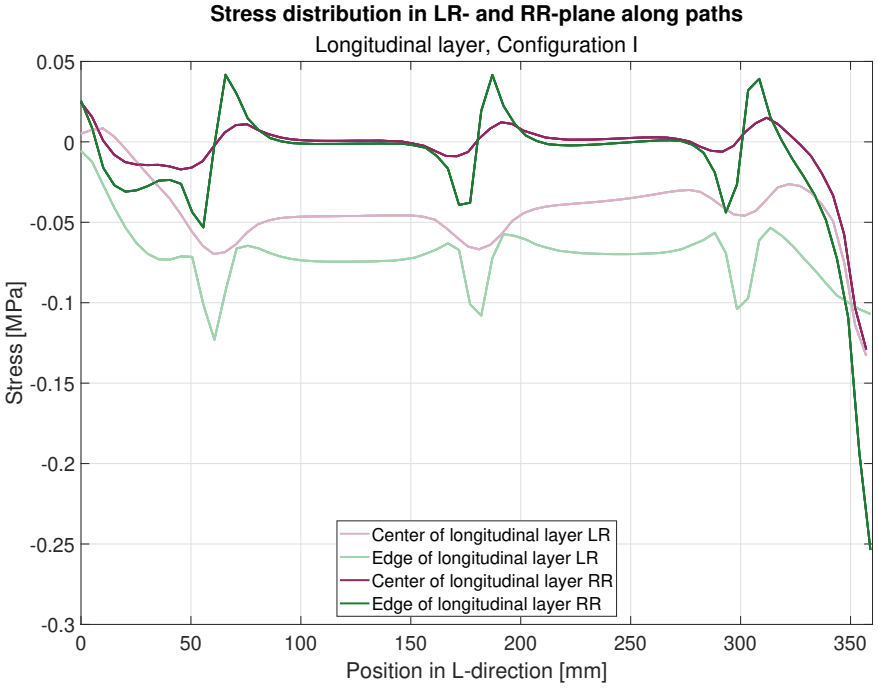
Stress distribution in LR- and RR-plane along paths
Longitudinal layer, Configuration I
Stress [MPa]
Position in L-direction [mm]
Center of longitudinal layer LR
Edge of longitudinal layer LR
Center of longitudinal layer RR
Edge of longitudinal layer RR

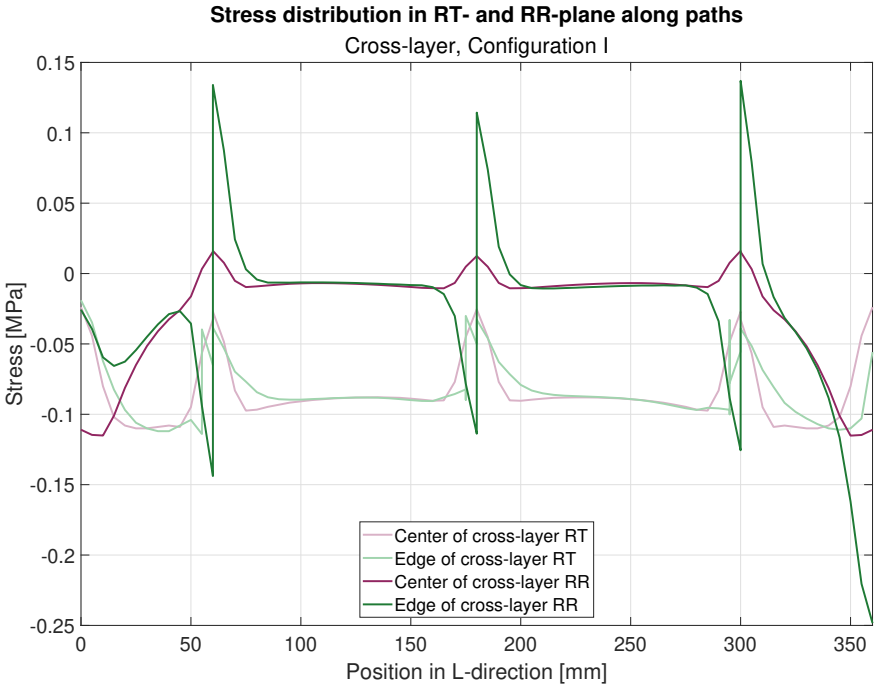
Stress distribution in RT- and RR-plane along paths
Cross-layer, Configuration I
Stress [MPa]
Position in L-direction [mm]
Center of cross-layer RT
Edge of cross-layer RT
Center of cross-layer RR
Edge of cross-layer RR

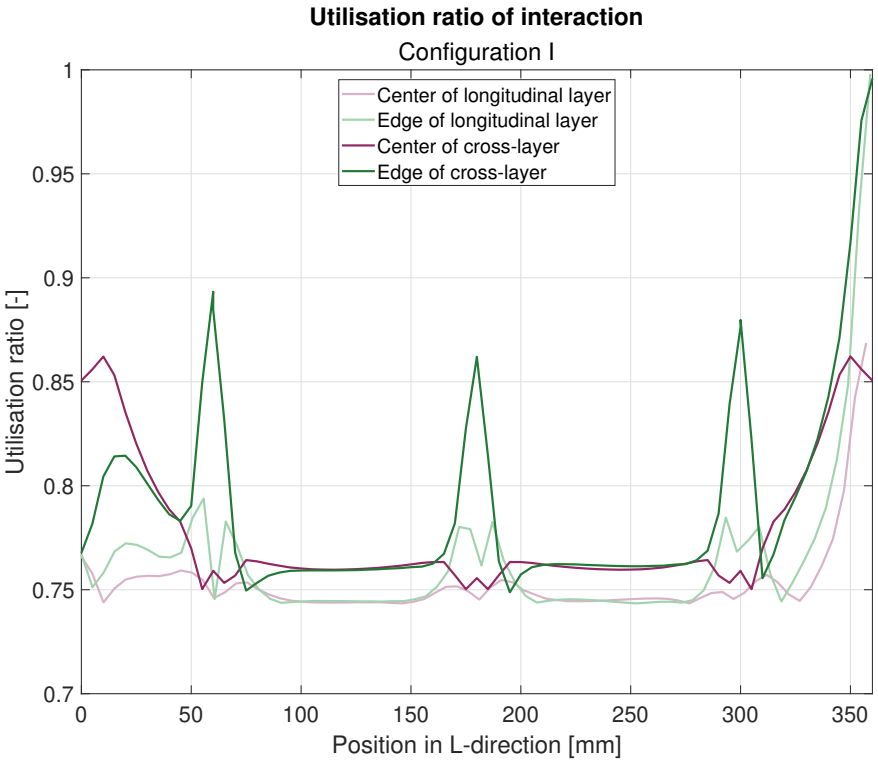
Utilisation ratio of interaction
Configuration I
Utilisation ratio [-]
Position in L-direction [mm]
Center of longitudinal layer
Edge of longitudinal layer
Center of cross-layer
Edge of cross-layer

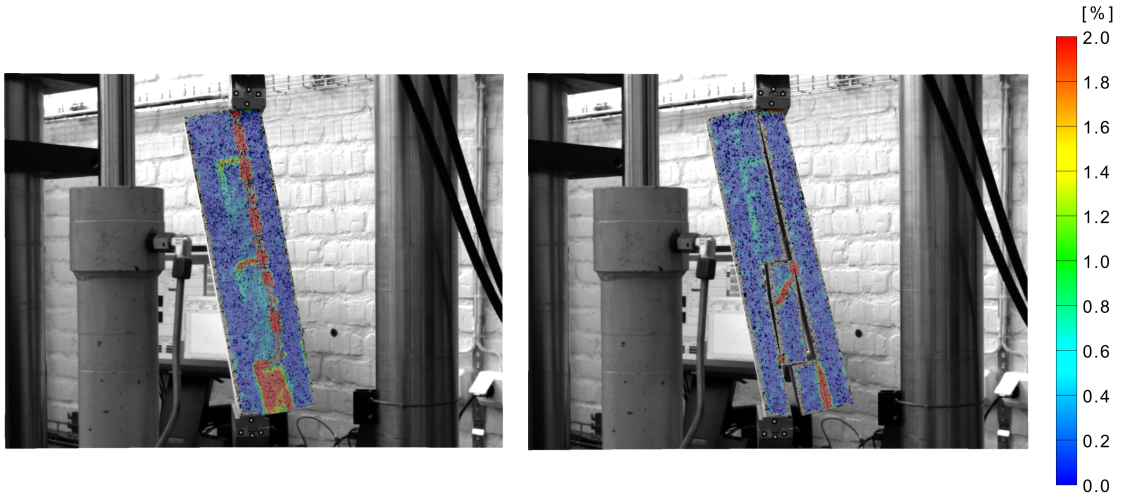
[%]
2.0
1.8
1.6
1.4
1.2
1.0
0.8
0.6
0.4
0.2
0.0

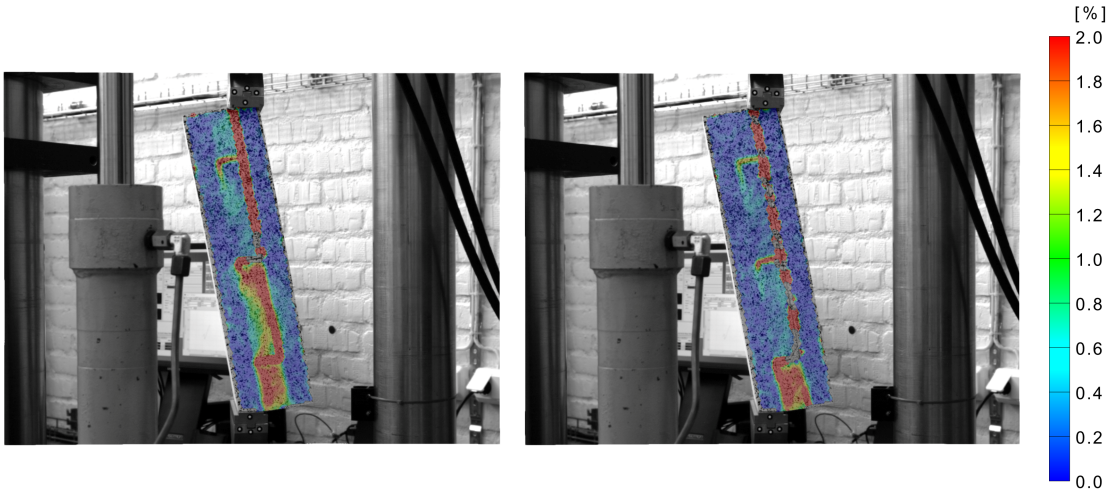
[%]
2.0
1.8
1.6
1.4
1.2
1.0
0.8
0.6
0.4
0.2
0.0

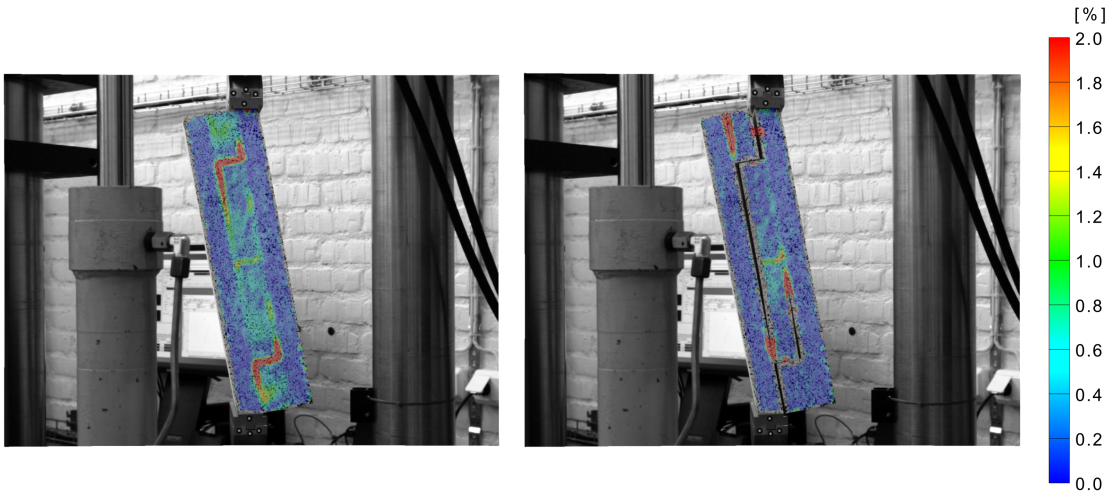
[%]
2.0
1.8
1.6
1.4
1.2
1.0
0.8
0.6
0.4
0.2
0.0

H.2 Configuration II

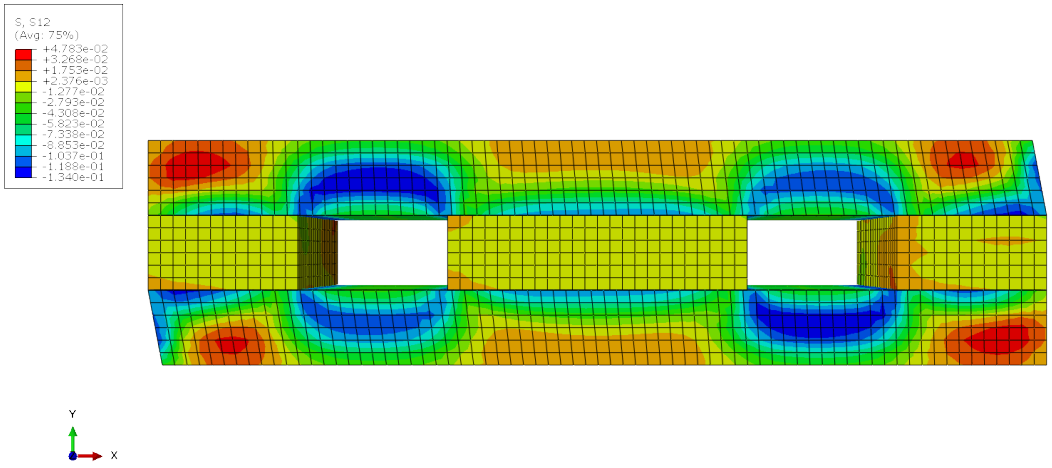

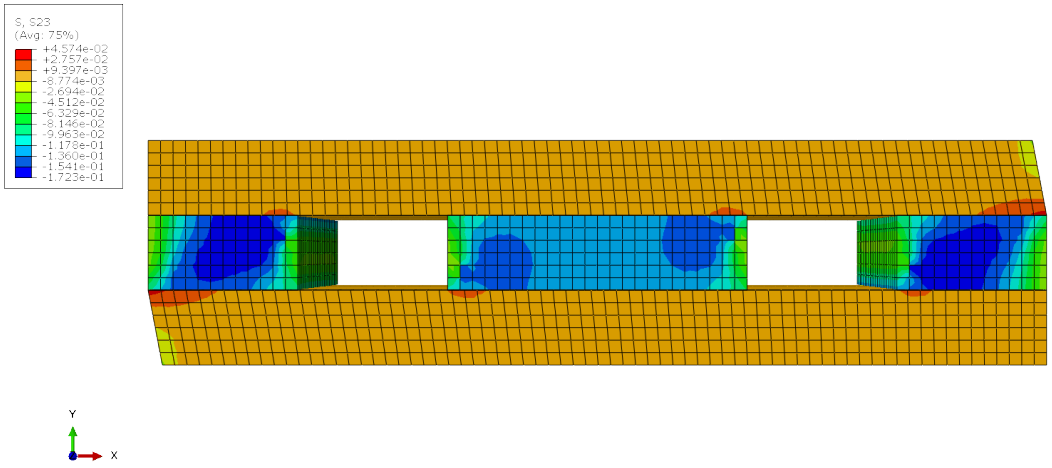

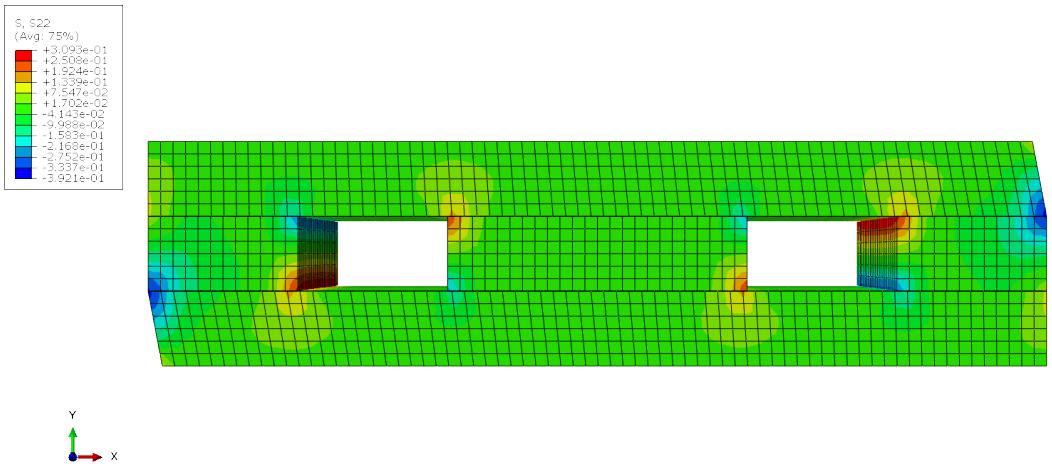

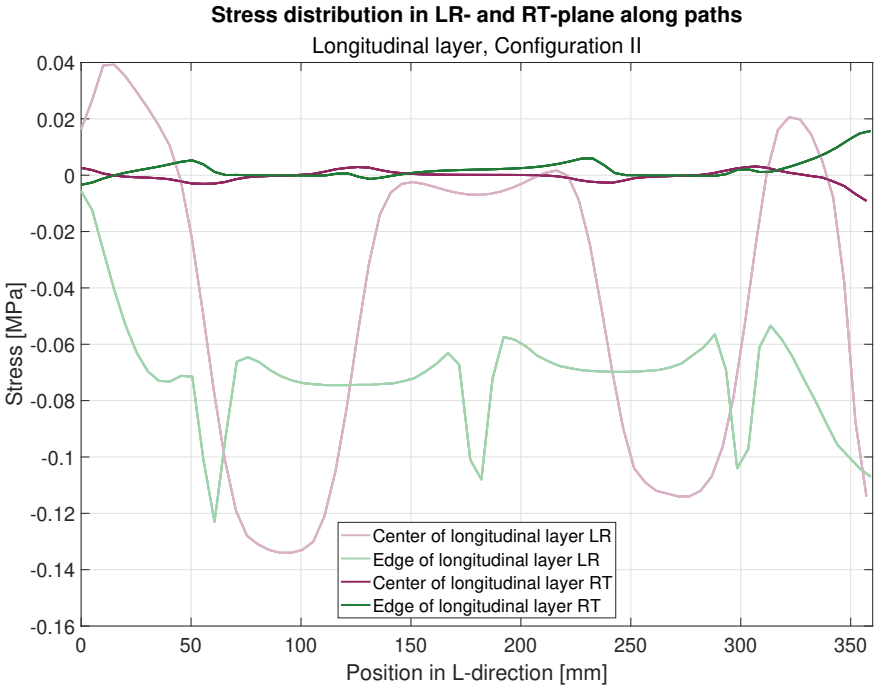
Stress distribution in LR- and RT-plane along paths
Longitudinal layer, Configuration II
Stress [MPa]
Position in L-direction [mm]
Center of longitudinal layer LR
Edge of longitudinal layer LR
Center of longitudinal layer RT
Edge of longitudinal layer RT

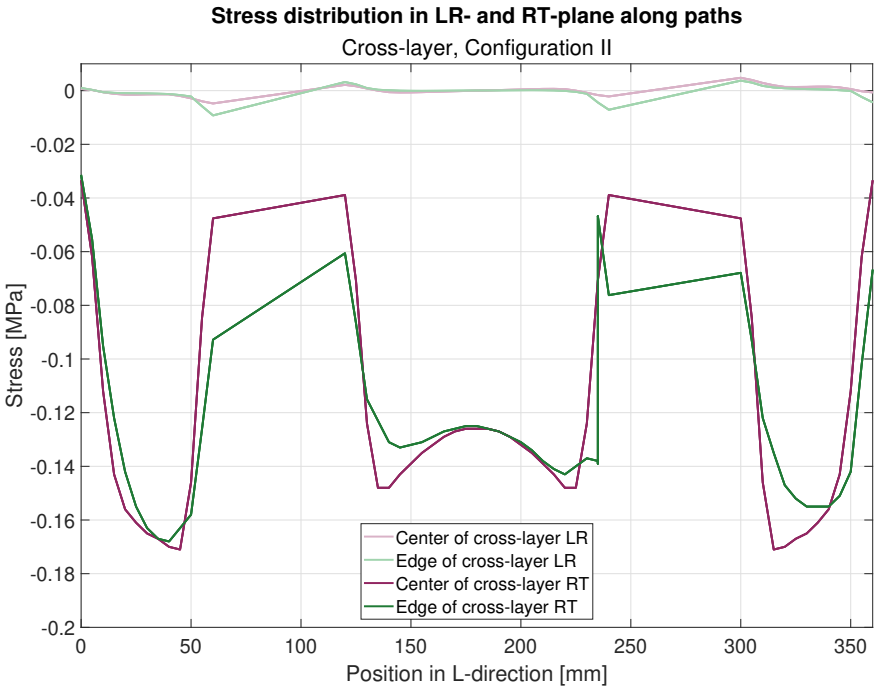
Stress distribution in LR- and RT-plane along paths
Cross-layer, Configuration II
Stress [MPa]
Position in L-direction [mm]
Center of cross-layer LR
Edge of cross-layer LR
Center of cross-layer RT
Edge of cross-layer RT

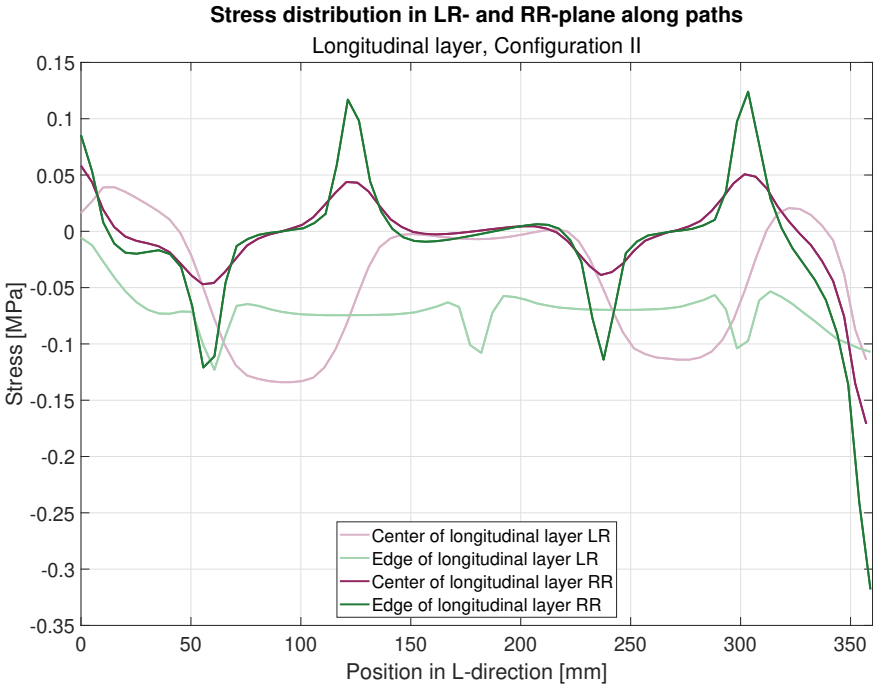
Stress distribution in LR- and RR-plane along paths
Longitudinal layer, Configuration II
Stress [MPa]
Position in L-direction [mm]
Center of longitudinal layer LR
Edge of longitudinal layer LR
Center of longitudinal layer RR
Edge of longitudinal layer RR

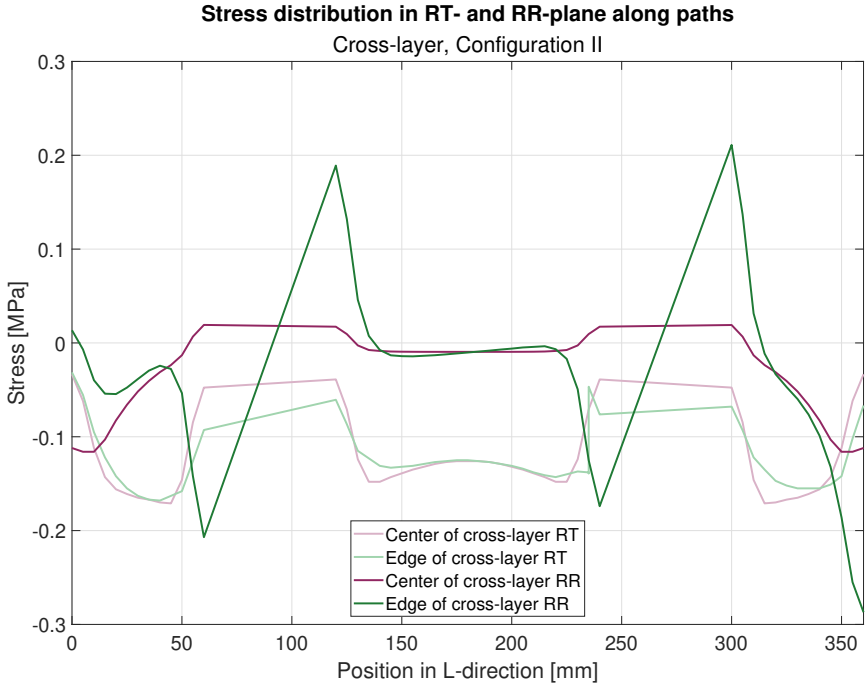
Stress distribution in RT- and RR-plane along paths
Cross-layer, Configuration II
Stress [MPa]
Position in L-direction [mm]
Center of cross-layer RT
Edge of cross-layer RT
Center of cross-layer RR
Edge of cross-layer RR

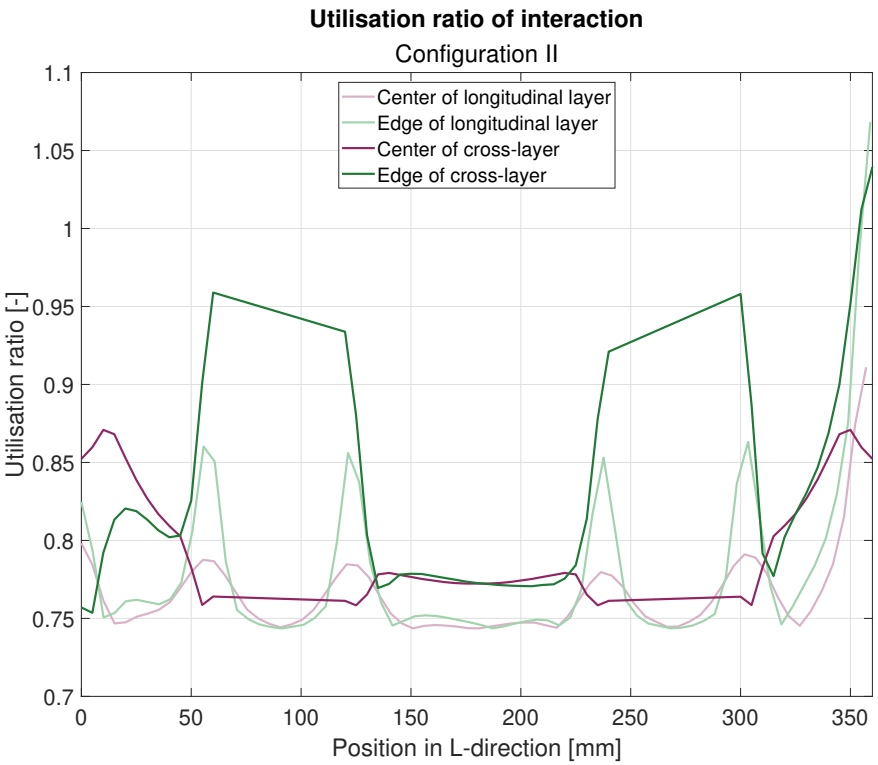
Utilisation ratio of interaction
Configuration II
Center of longitudinal layer
Edge of longitudinal layer
Center of cross-layer
Edge of cross-layer
Utilisation ratio [-]
Position in L-direction [mm]
1.1
1.05
1
0.95
0.9
0.85
0.8
0.75
0.7
0
50
100
150
200
250
300
350

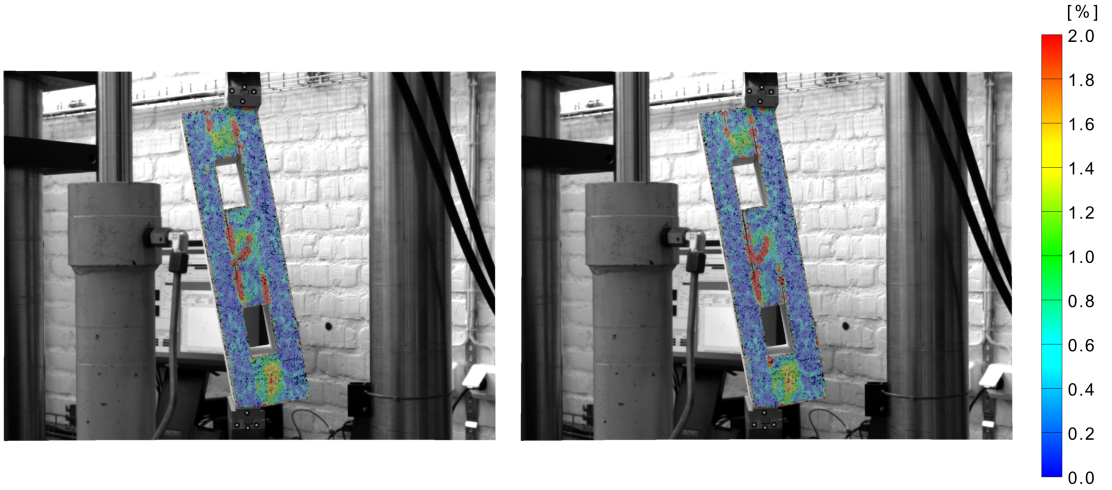
[%]
2.0
1.8
1.6
1.4
1.2
1.0
0.8
0.6
0.4
0.2
0.0

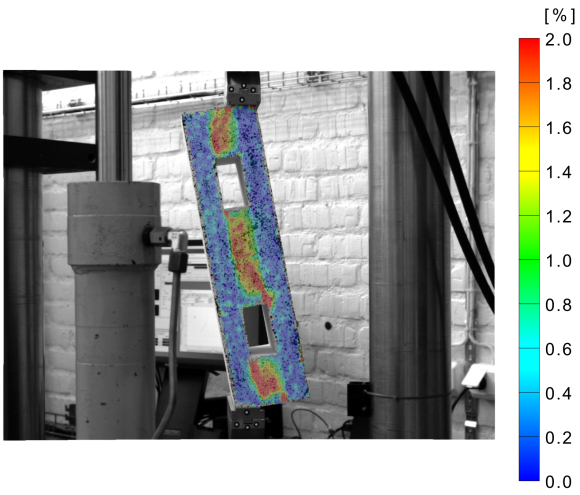
[%]
2.0
1.8
1.6
1.4
1.2
1.0
0.8
0.6
0.4
0.2
0.0

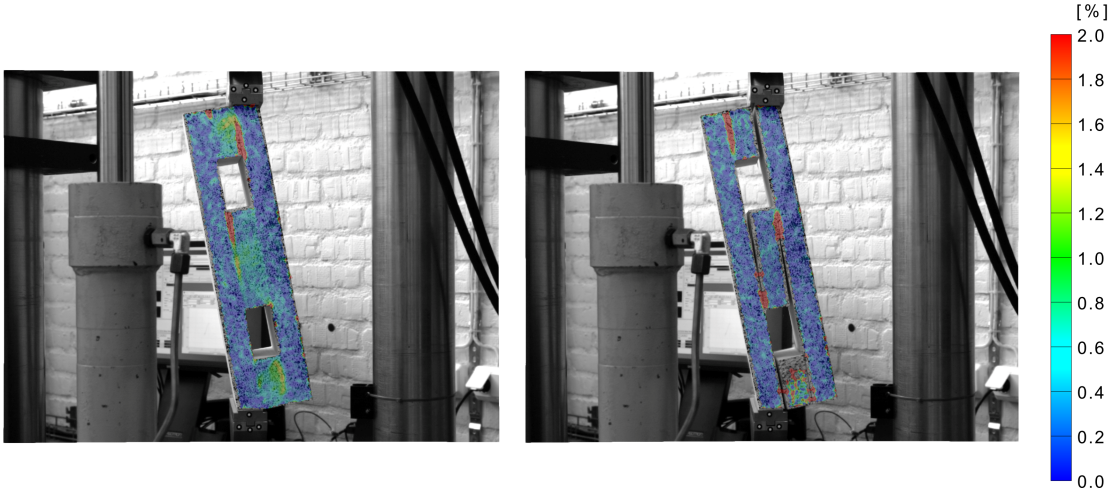
[%]
2.0
1.8
1.6
1.4
1.2
1.0
0.8
0.6
0.4
0.2
0.0

H.3 Configuration III

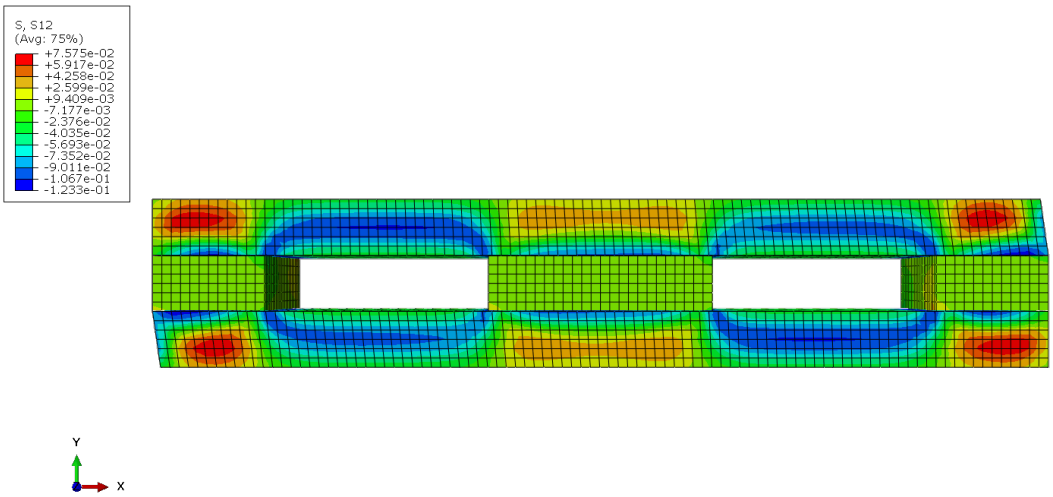

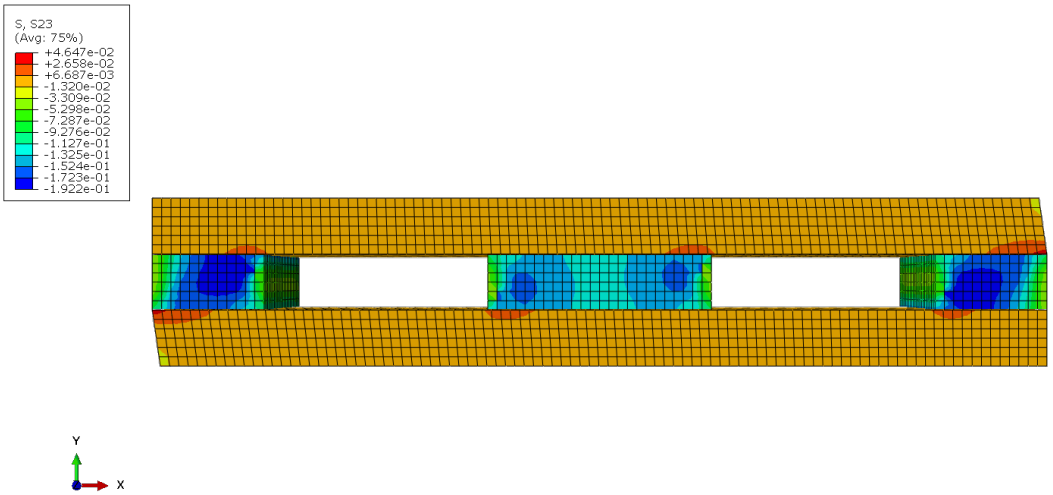

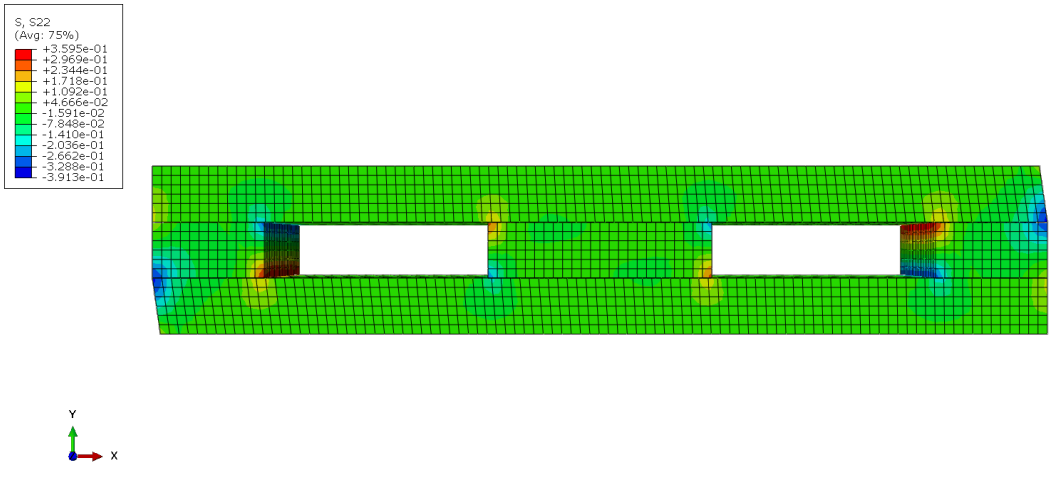

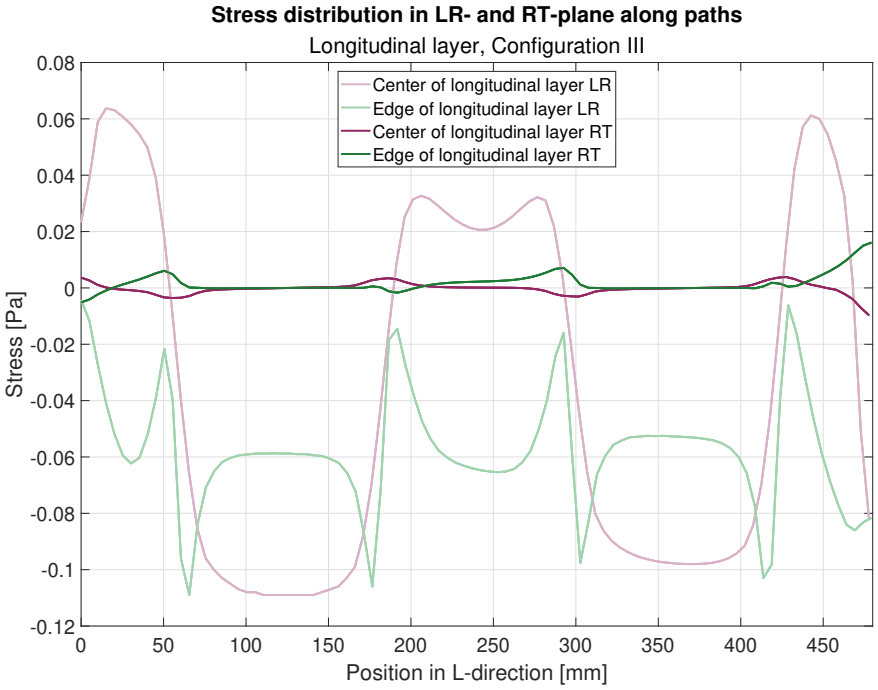
Stress distribution in LR- and RT-plane along paths
Longitudinal layer, Configuration III
Center of longitudinal layer LR
Edge of longitudinal layer LR
Center of longitudinal layer RT
Edge of longitudinal layer RT
Stress [Pa]
Position in L-direction [mm]

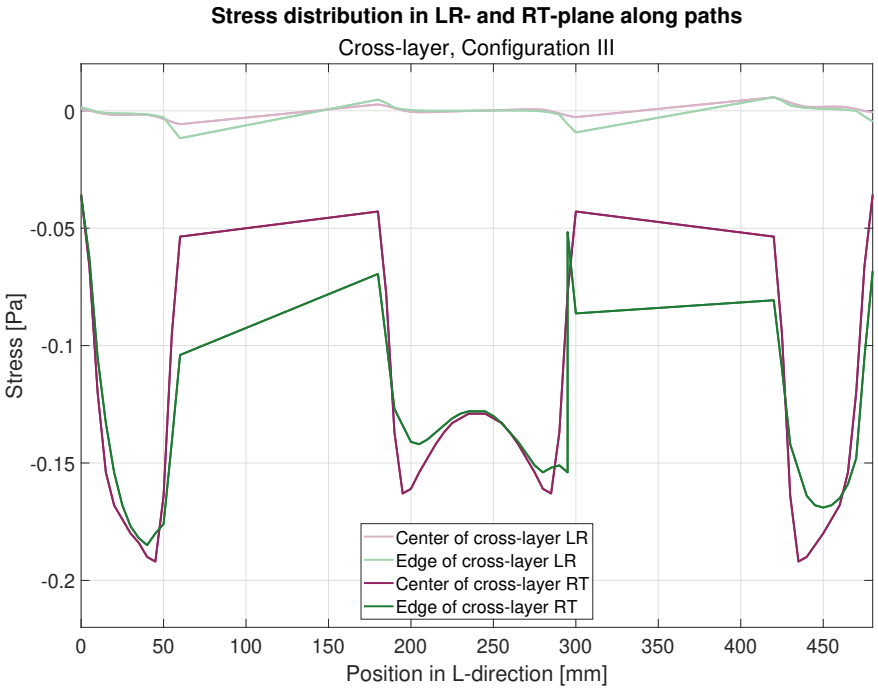
Stress distribution in LR- and RT-plane along paths
Cross-layer, Configuration III
Center of cross-layer LR
Edge of cross-layer LR
Center of cross-layer RT
Edge of cross-layer RT
Stress [Pa]
Position in L-direction [mm]

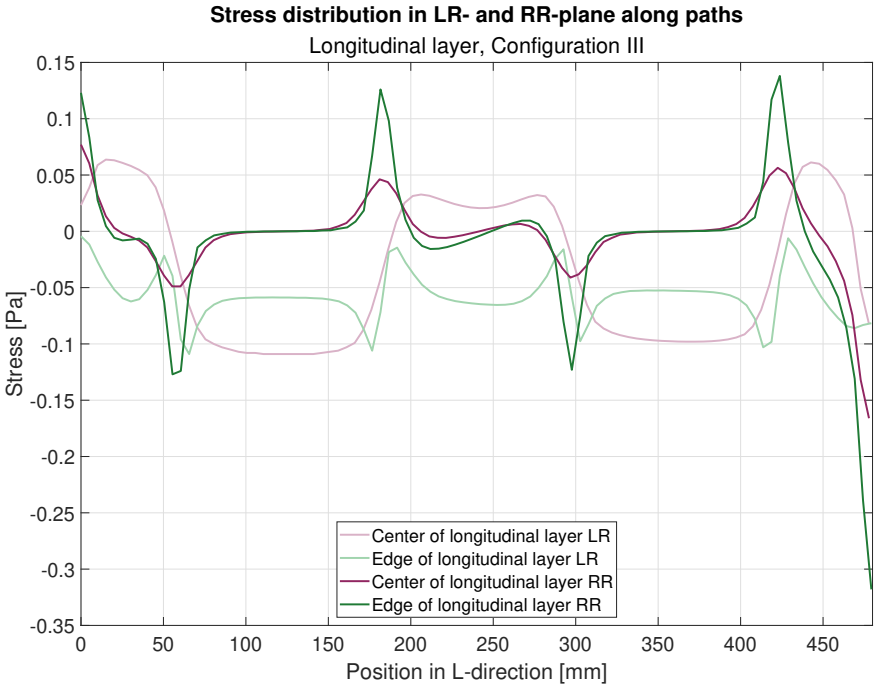
Stress distribution in LR- and RR-plane along paths
Longitudinal layer, Configuration III
Stress [Pa]
Position in L-direction [mm]
Center of longitudinal layer LR
Edge of longitudinal layer LR
Center of longitudinal layer RR
Edge of longitudinal layer RR

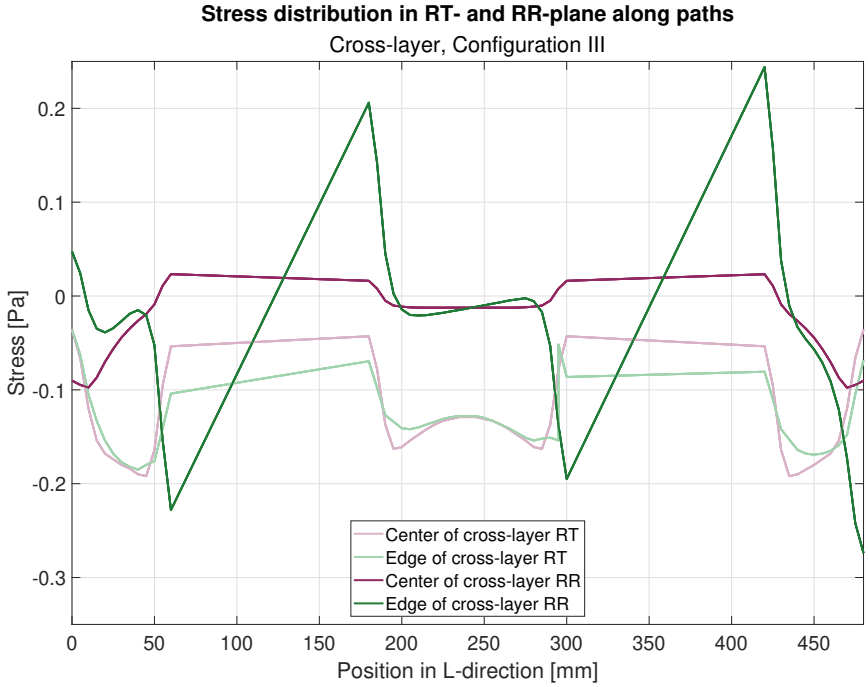
Stress distribution in RT- and RR-plane along paths
Cross-layer, Configuration III
Stress [Pa]
Position in L-direction [mm]
Center of cross-layer RT
Edge of cross-layer RT
Center of cross-layer RR
Edge of cross-layer RR

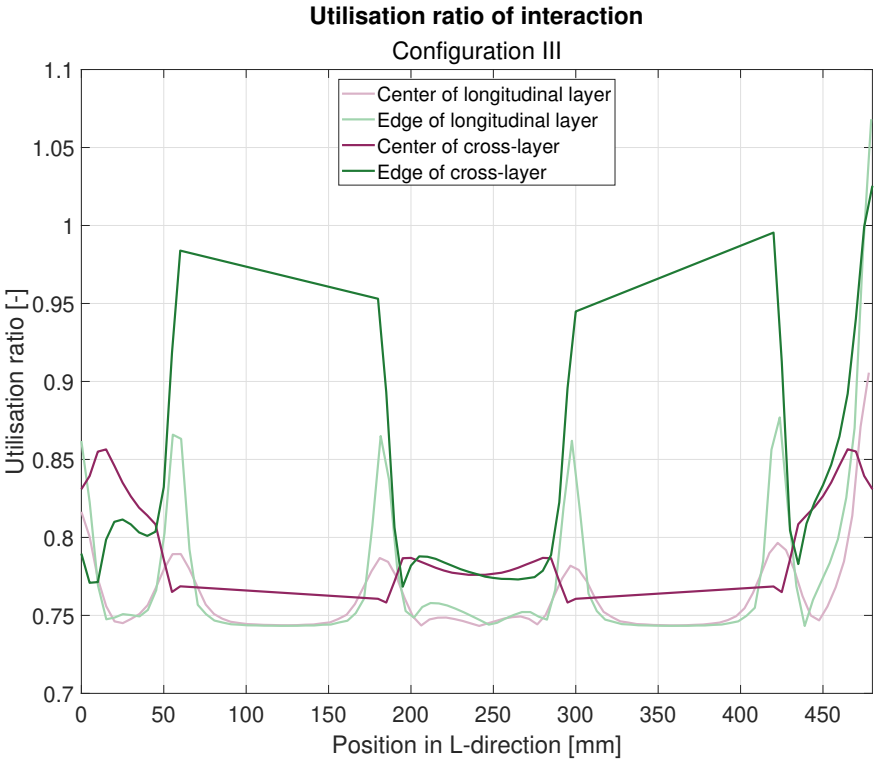
Utilisation ratio of interaction
Configuration III
Center of longitudinal layer
Edge of longitudinal layer
Center of cross-layer
Edge of cross-layer
Utilisation ratio [-]
1.1
1.05
1
0.95
0.9
0.85
0.8
0.75
0.7
0
50
100
150
200
250
300
350
400
450
Position in L-direction [mm]

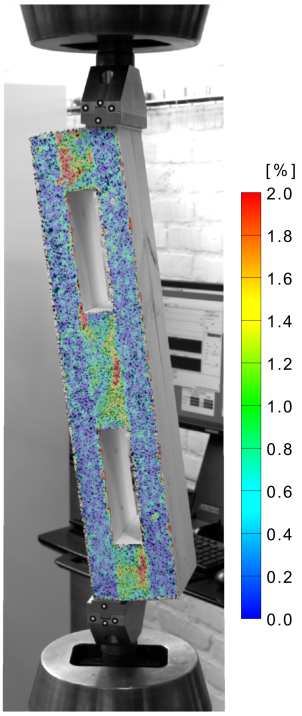
[%]
2.0
1.8
1.6
1.4
1.2
1.0
0.8
0.6
0.4
0.2
0.0

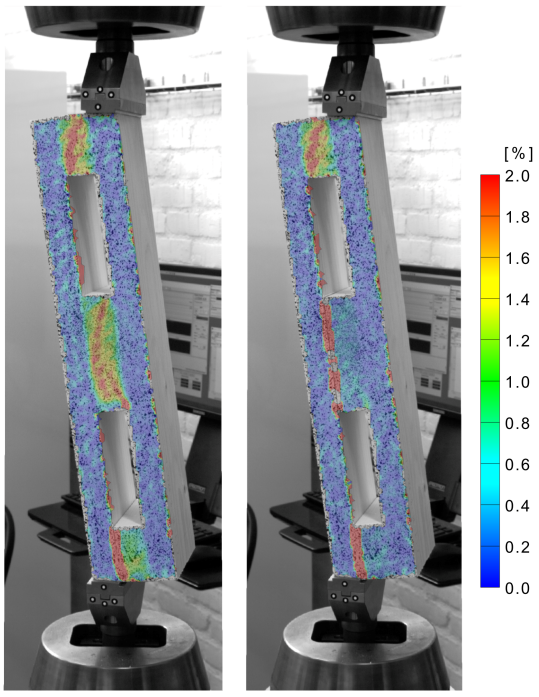
[%]
2.0
1.8
1.6
1.4
1.2
1.0
0.8
0.6
0.4
0.2
0.0

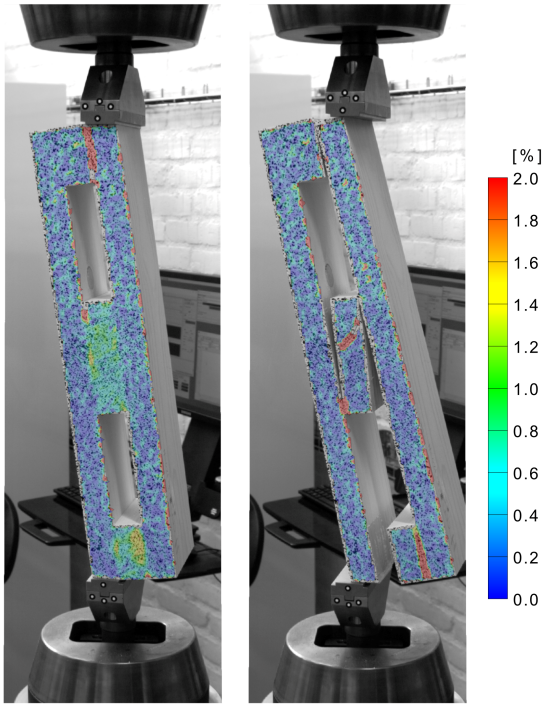
[%]
2.0
1.8
1.6
1.4
1.2
1.0
0.8
0.6
0.4
0.2
0.0

H.4 Configuration IV

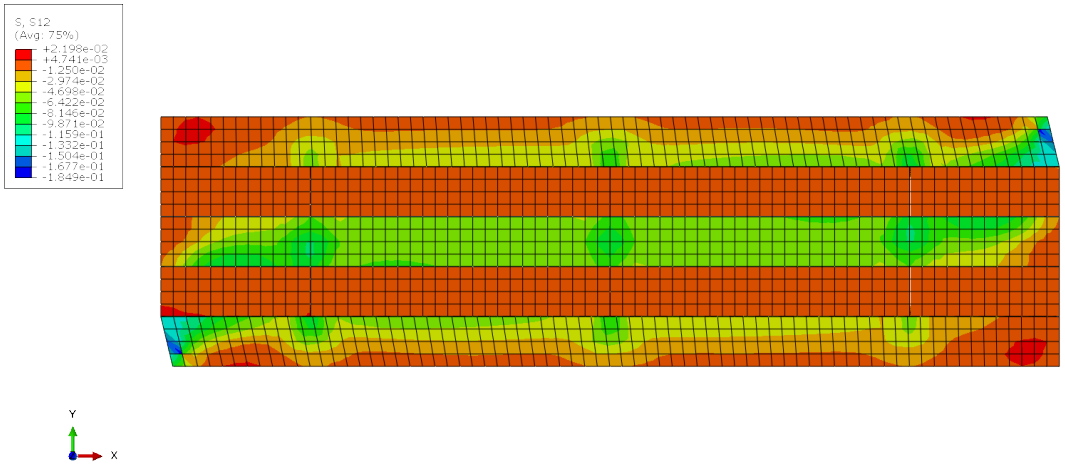

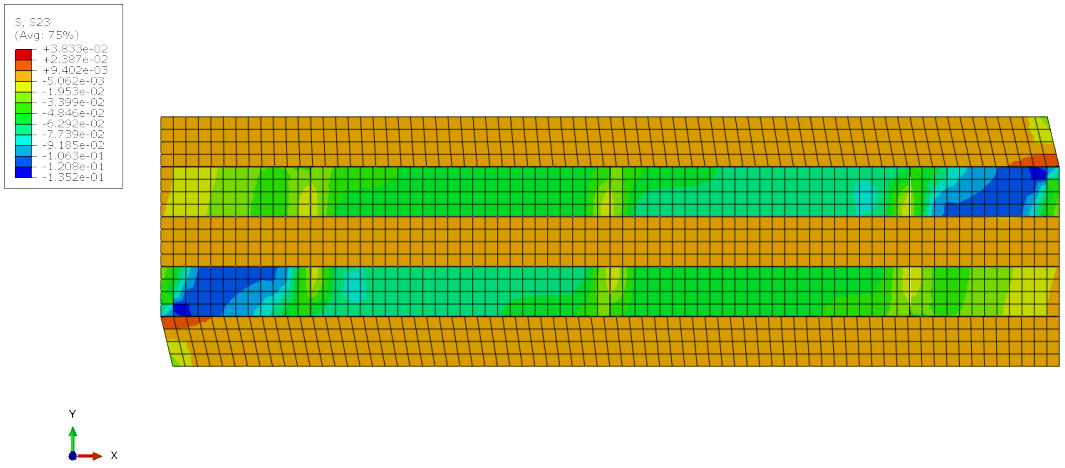

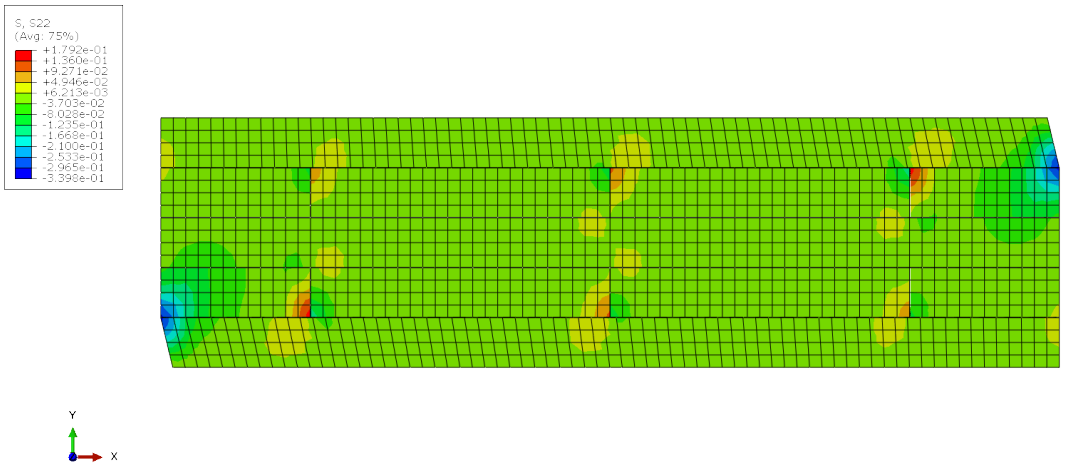

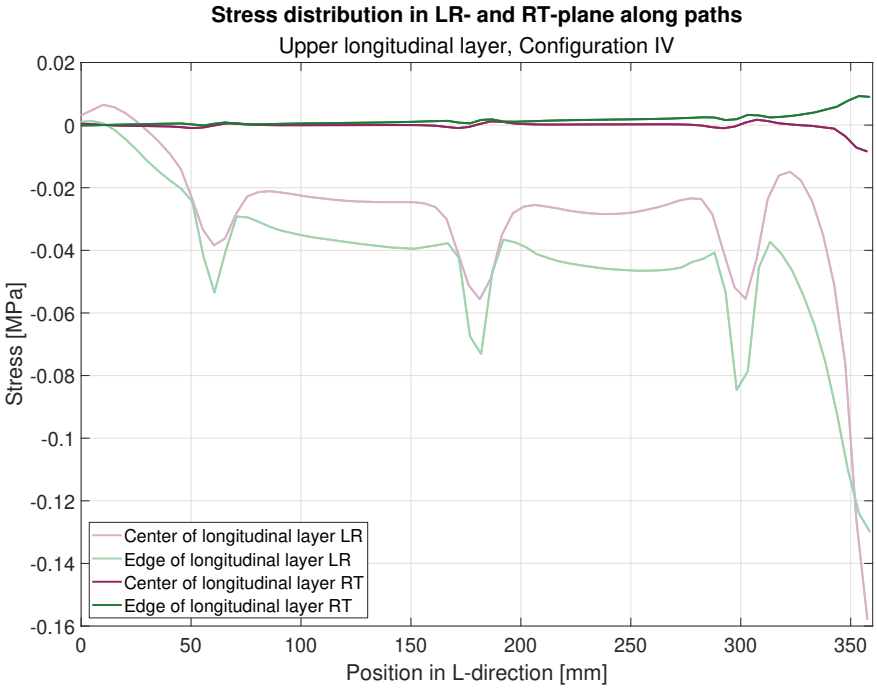
Stress distribution in LR- and RT-plane along paths
Upper longitudinal layer, Configuration IV
Stress [MPa]
Position in L-direction [mm]
Center of longitudinal layer LR
Edge of longitudinal layer LR
Center of longitudinal layer RT
Edge of longitudinal layer RT

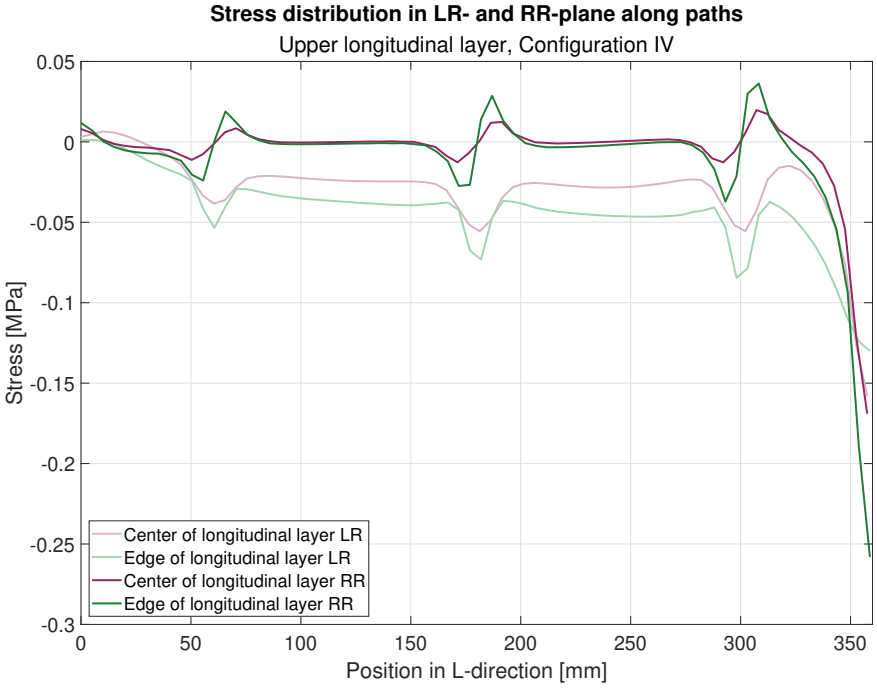
Stress distribution in LR- and RR-plane along paths
Upper longitudinal layer, Configuration IV
Stress [MPa]
Position in L-direction [mm]
Center of longitudinal layer LR
Edge of longitudinal layer LR
Center of longitudinal layer RR
Edge of longitudinal layer RR

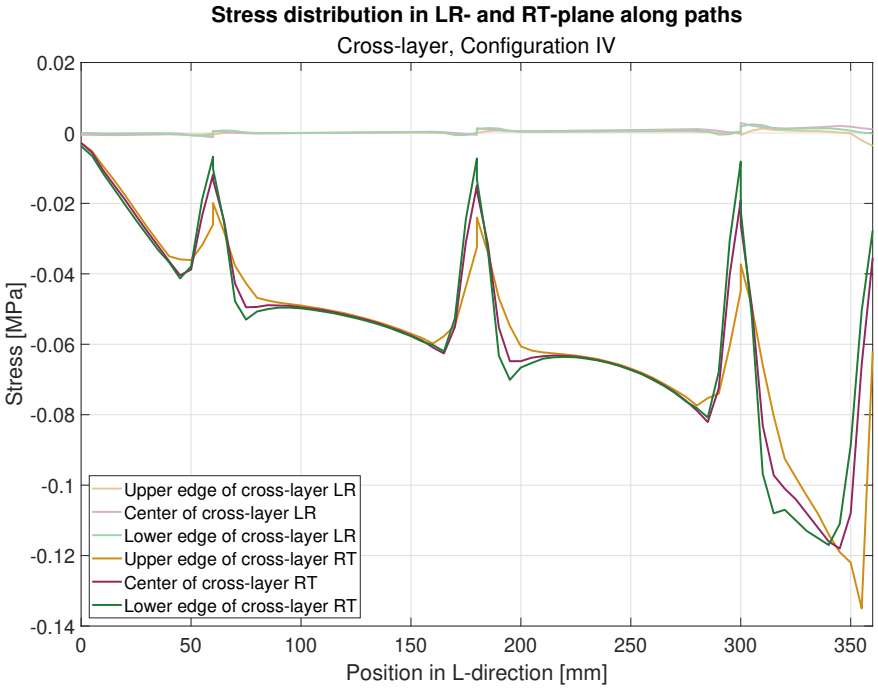
Stress distribution in LR- and RT-plane along paths
Cross-layer, Configuration IV
Stress [MPa]
Position in L-direction [mm]
Upper edge of cross-layer LR
Center of cross-layer LR
Lower edge of cross-layer LR
Upper edge of cross-layer RT
Center of cross-layer RT
Lower edge of cross-layer RT

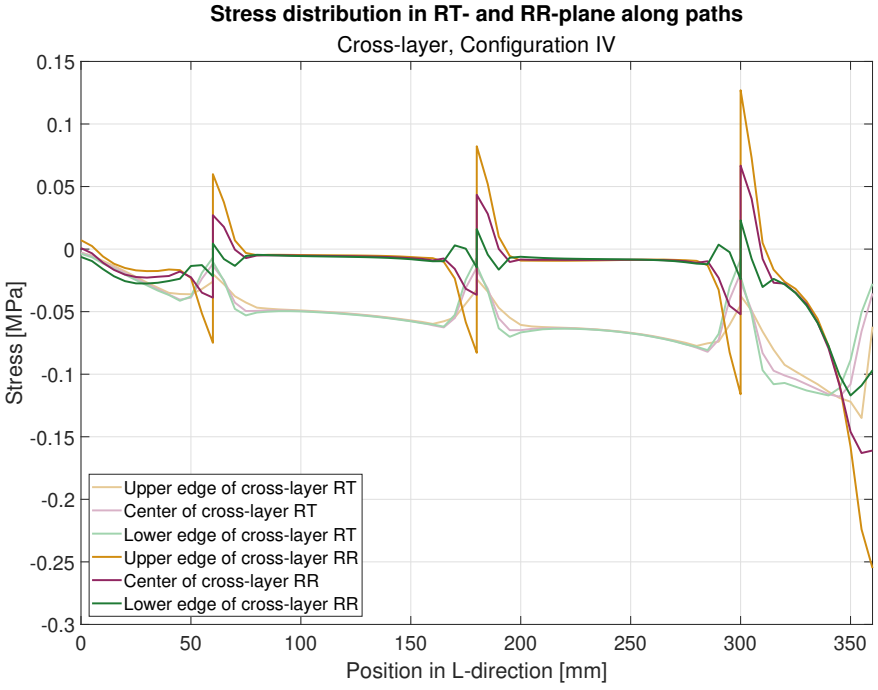
Stress distribution in RT- and RR-plane along paths
Cross-layer, Configuration IV
Stress [MPa]
Position in L-direction [mm]
Upper edge of cross-layer RT
Center of cross-layer RT
Lower edge of cross-layer RT
Upper edge of cross-layer RR
Center of cross-layer RR
Lower edge of cross-layer RR

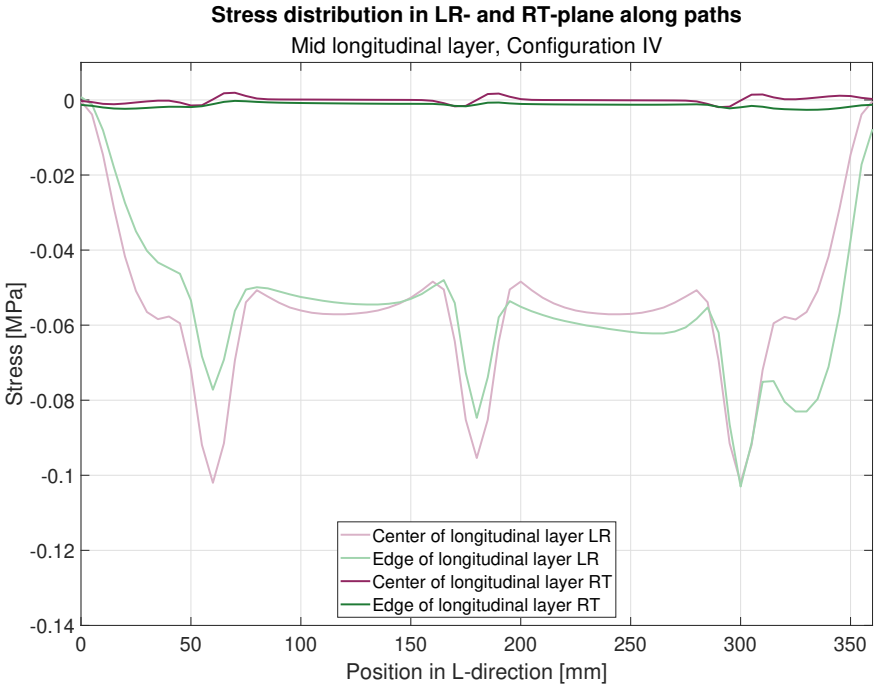
Stress distribution in LR- and RT-plane along paths
Mid longitudinal layer, Configuration IV
Stress [MPa]
Position in L-direction [mm]
Center of longitudinal layer LR
Edge of longitudinal layer LR
Center of longitudinal layer RT
Edge of longitudinal layer RT

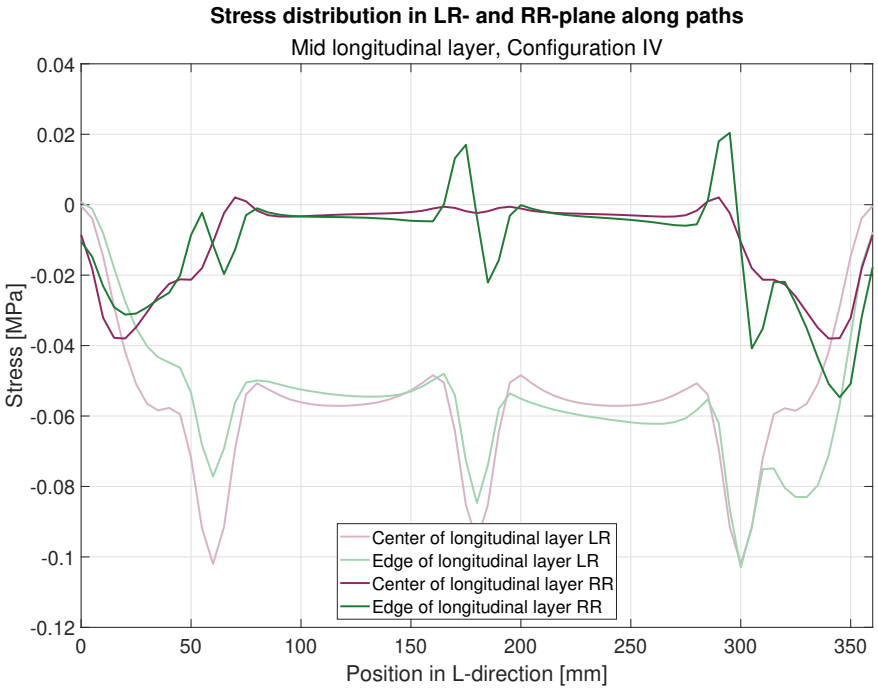
Stress distribution in LR- and RR-plane along paths
Mid longitudinal layer, Configuration IV
Stress [MPa]
Position in L-direction [mm]
Center of longitudinal layer LR
Edge of longitudinal layer LR
Center of longitudinal layer RR
Edge of longitudinal layer RR

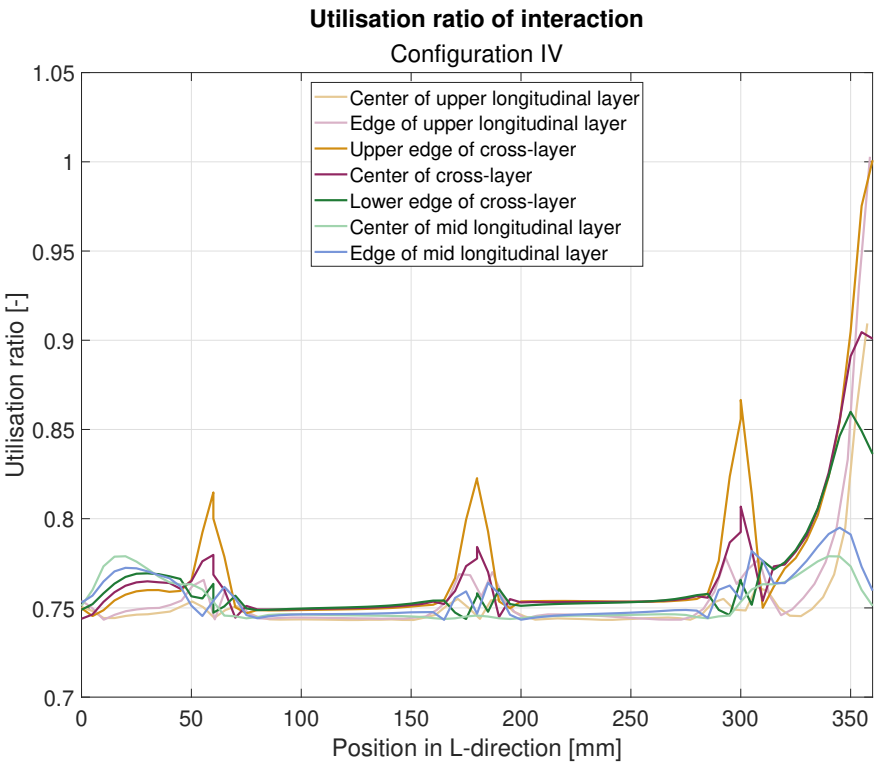
Utilisation ratio of interaction
Configuration IV
Center of upper longitudinal layer
Edge of upper longitudinal layer
Upper edge of cross-layer
Center of cross-layer
Lower edge of cross-layer
Center of mid longitudinal layer
Edge of mid longitudinal layer
Utilisation ratio [-]
Position in L-direction [mm]
1.05
1
0.95
0.9
0.85
0.8
0.75
0.7
0
50
100
150
200
250
300
350

H.5 Configuration V

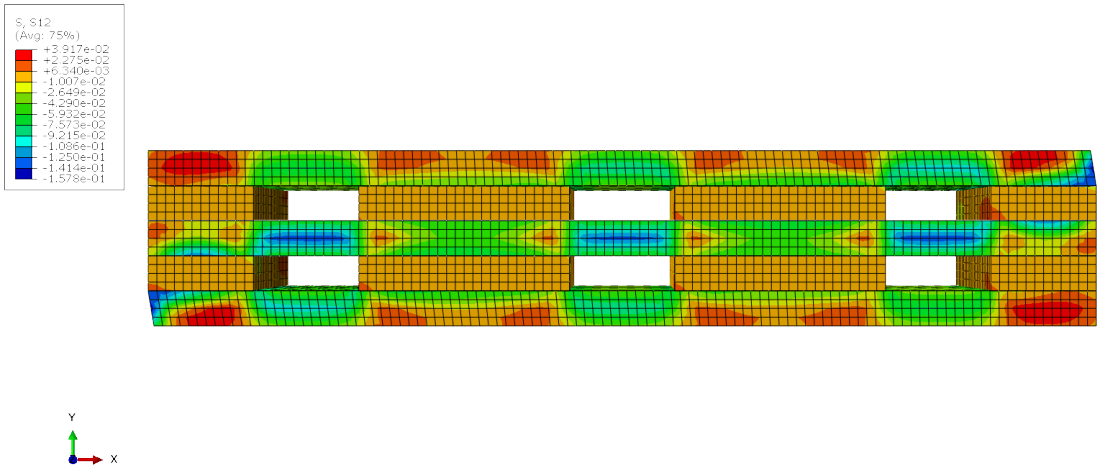

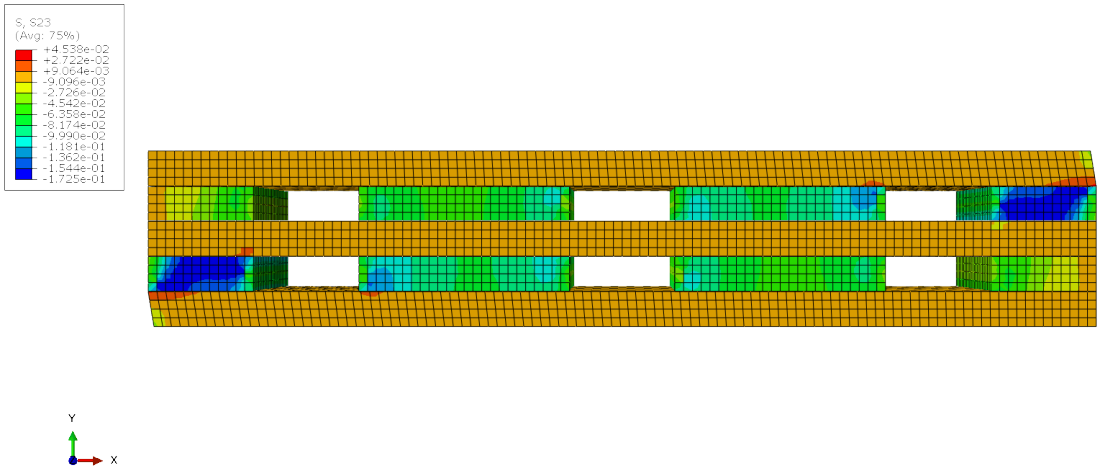

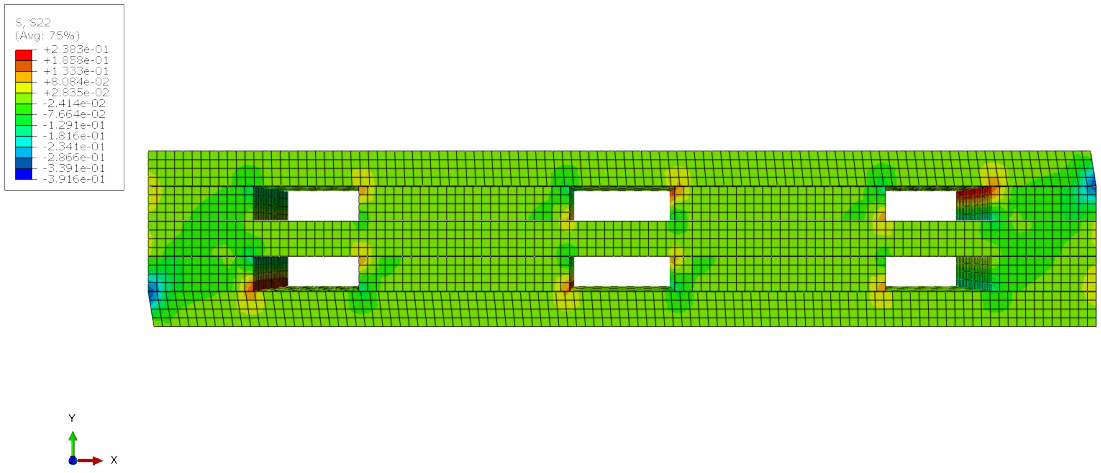

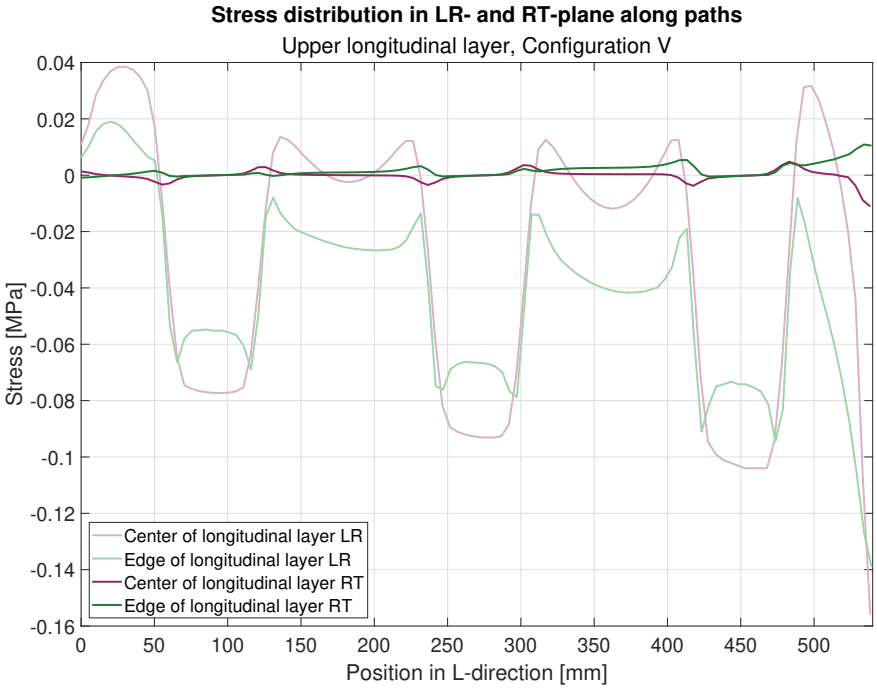
Stress distribution in LR- and RT-plane along paths
Upper longitudinal layer, Configuration V
Stress [MPa]
Position in L-direction [mm]
Center of longitudinal layer LR
Edge of longitudinal layer LR
Center of longitudinal layer RT
Edge of longitudinal layer RT

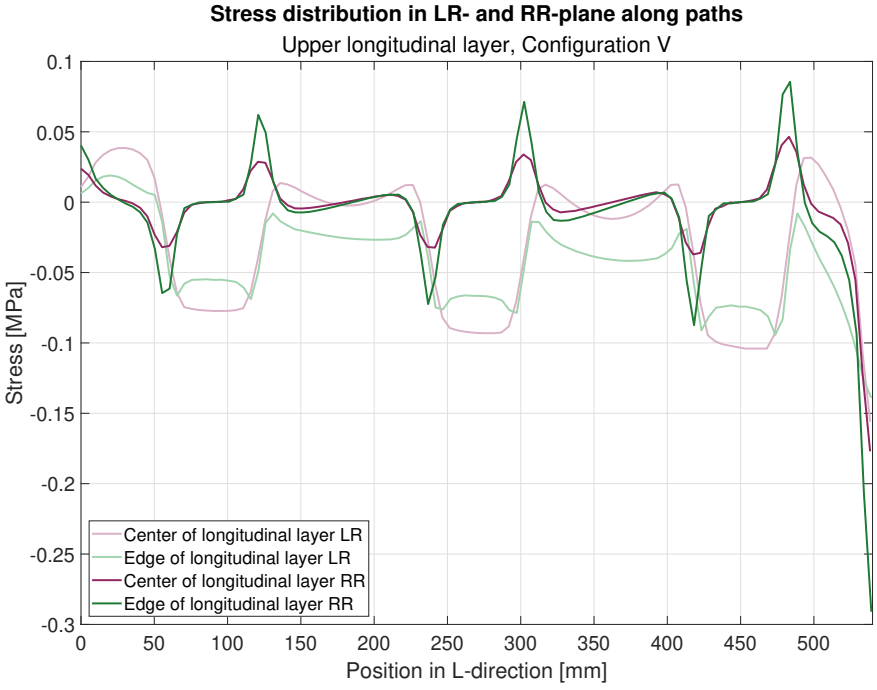
Stress distribution in LR- and RR-plane along paths
Upper longitudinal layer, Configuration V
Stress [MPa]
Position in L-direction [mm]
Center of longitudinal layer LR
Edge of longitudinal layer LR
Center of longitudinal layer RR
Edge of longitudinal layer RR

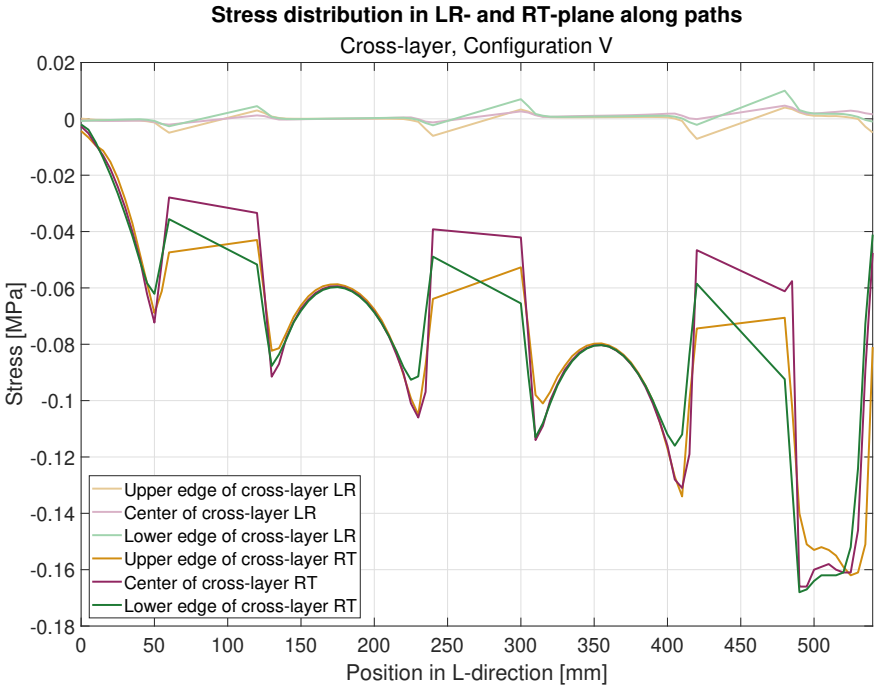
Stress distribution in LR- and RT-plane along paths
Cross-layer, Configuration V
Stress [MPa]
Position in L-direction [mm]
Upper edge of cross-layer LR
Center of cross-layer LR
Lower edge of cross-layer LR
Upper edge of cross-layer RT
Center of cross-layer RT
Lower edge of cross-layer RT

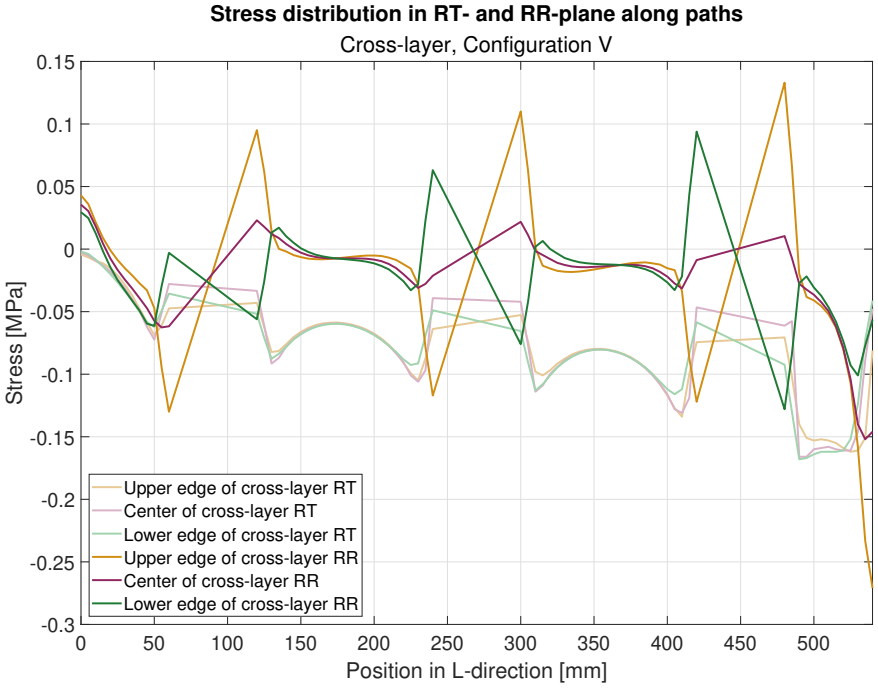
Stress distribution in RT- and RR-plane along paths
Cross-layer, Configuration V
Stress [MPa]
Position in L-direction [mm]
Upper edge of cross-layer RT
Center of cross-layer RT
Lower edge of cross-layer RT
Upper edge of cross-layer RR
Center of cross-layer RR
Lower edge of cross-layer RR

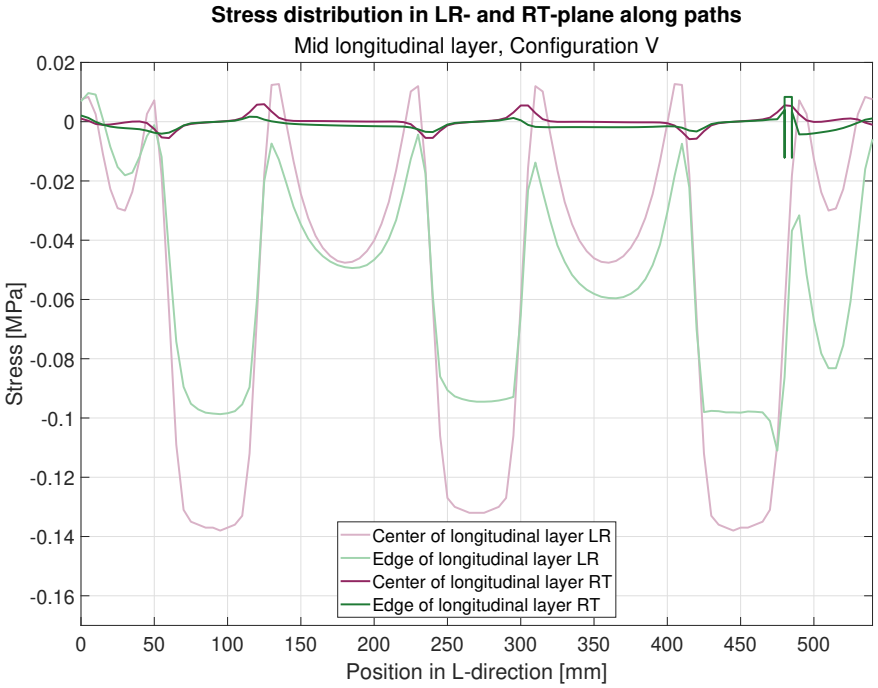
Stress distribution in LR- and RT-plane along paths
Mid longitudinal layer, Configuration V
Stress [MPa]
Position in L-direction [mm]
Center of longitudinal layer LR
Edge of longitudinal layer LR
Center of longitudinal layer RT
Edge of longitudinal layer RT

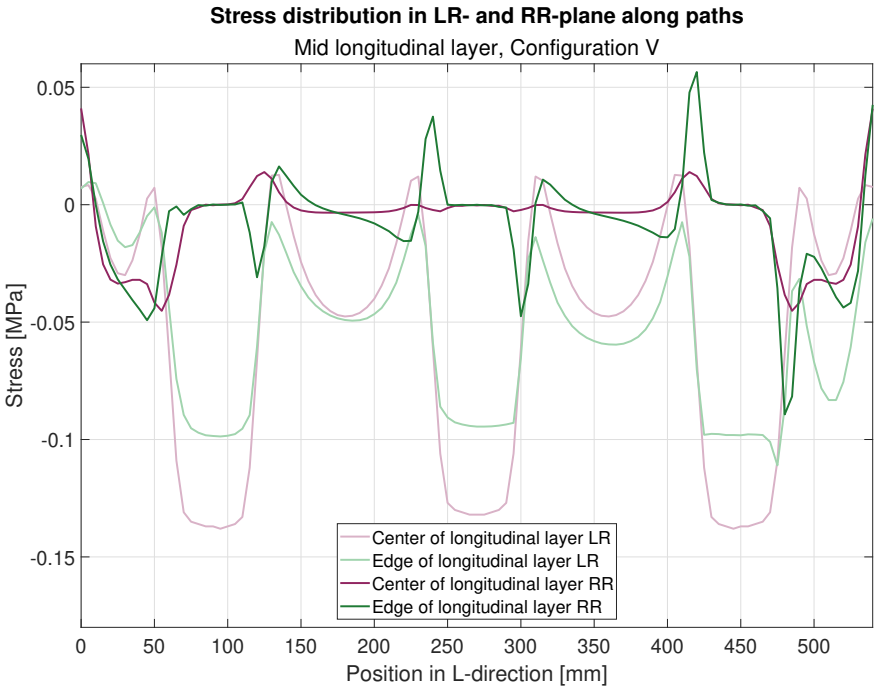
Stress distribution in LR- and RR-plane along paths
Mid longitudinal layer, Configuration V
Stress [MPa]
Position in L-direction [mm]
Center of longitudinal layer LR
Edge of longitudinal layer LR
Center of longitudinal layer RR
Edge of longitudinal layer RR

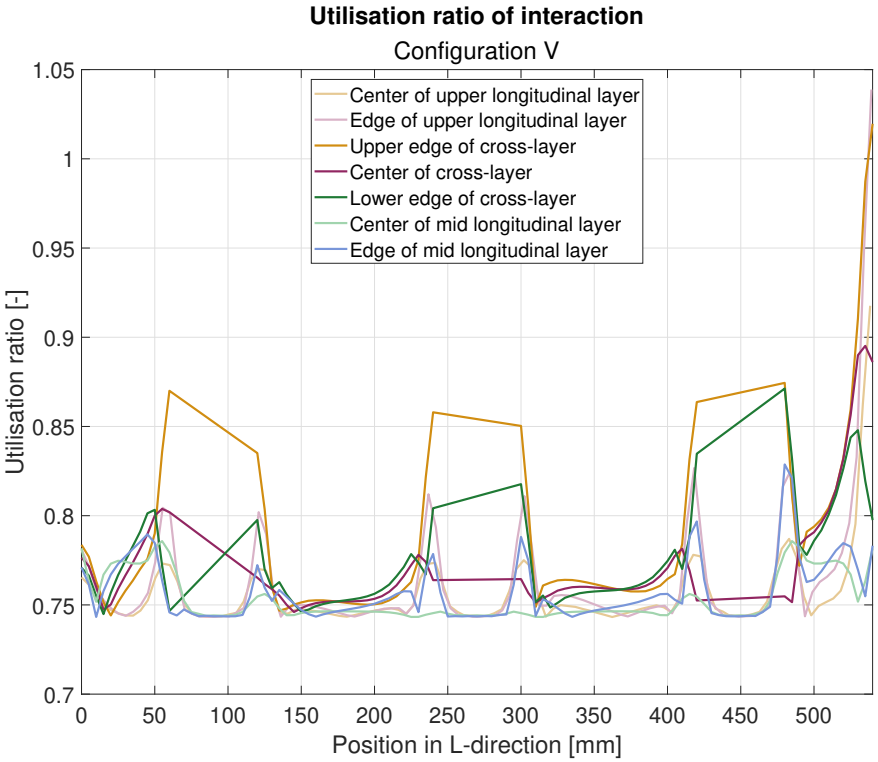
Utilisation ratio of interaction
Configuration V
Center of upper longitudinal layer
Edge of upper longitudinal layer
Upper edge of cross-layer
Center of cross-layer
Lower edge of cross-layer
Center of mid longitudinal layer
Edge of mid longitudinal layer
Utilisation ratio [-]
1.05
1
0.95
0.9
0.85
0.8
0.75
0.7
0
50
100
150
200
250
300
350
400
450
500
Position in L-direction [mm]

H.6 Configuration VI

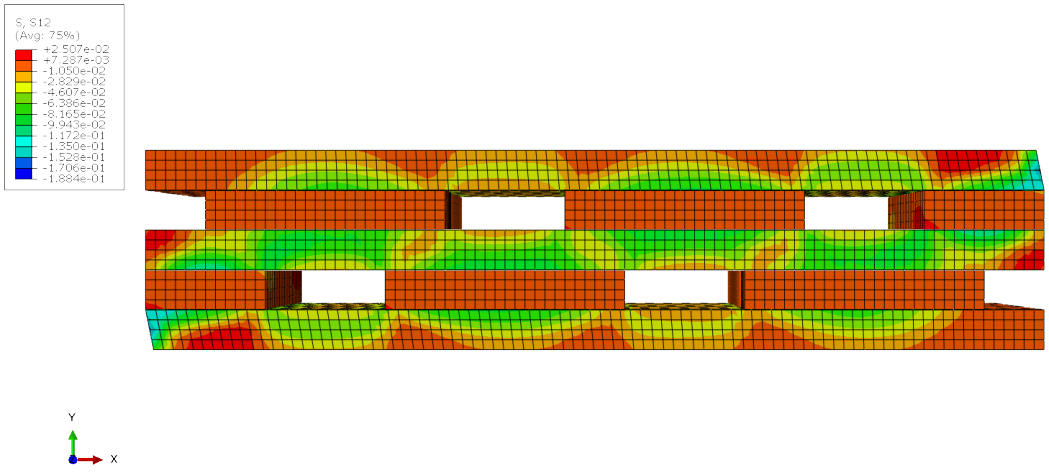

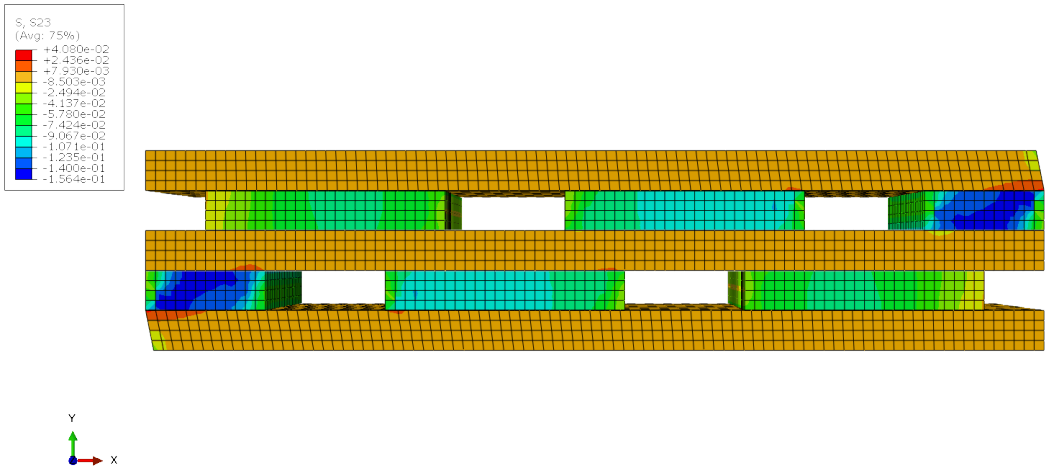

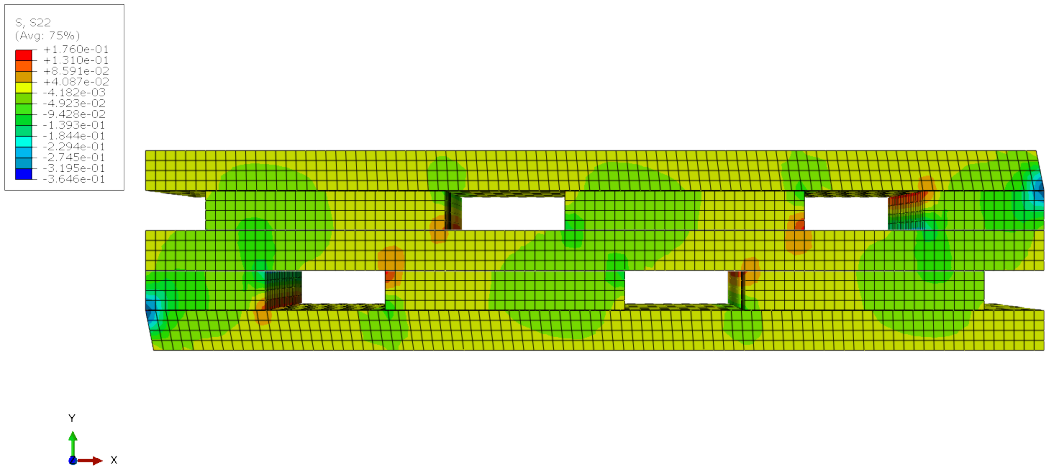

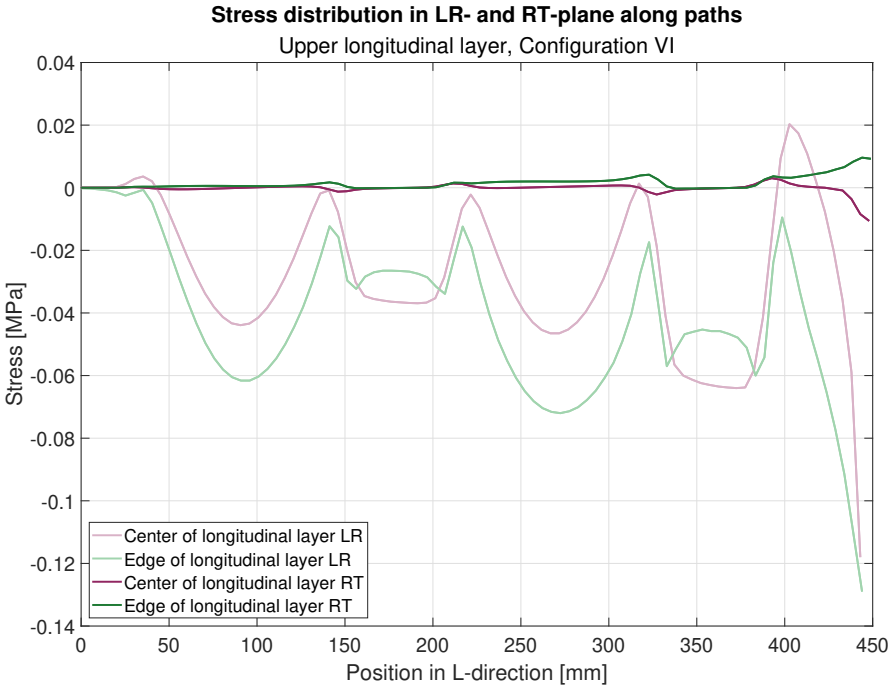
Stress distribution in LR- and RT-plane along paths
Upper longitudinal layer, Configuration VI
Stress [MPa]
Position in L-direction [mm]
Center of longitudinal layer LR
Edge of longitudinal layer LR
Center of longitudinal layer RT
Edge of longitudinal layer RT

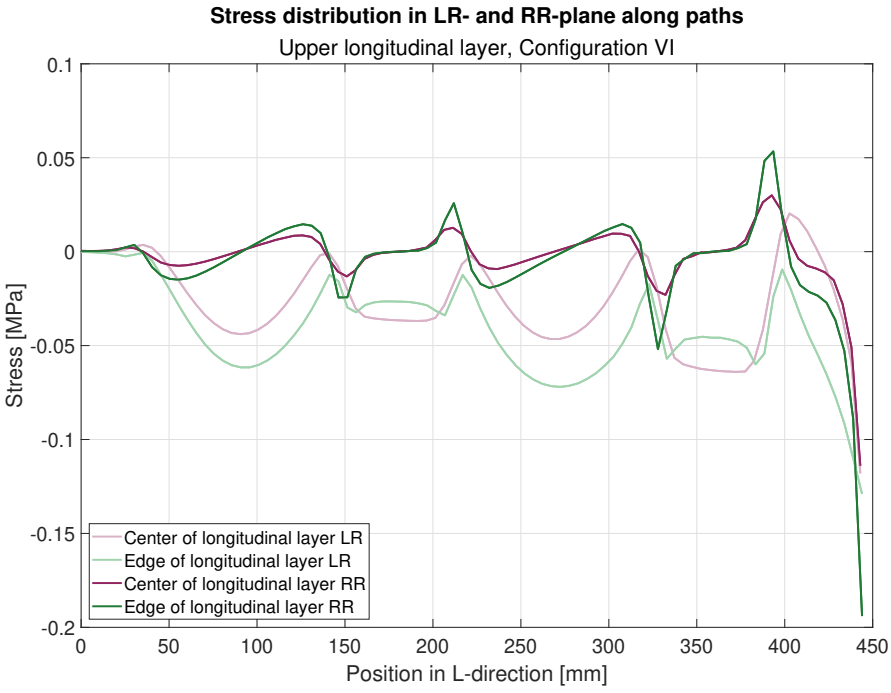
Stress distribution in LR- and RR-plane along paths
Upper longitudinal layer, Configuration VI
Stress [MPa]
Position in L-direction [mm]
Center of longitudinal layer LR
Edge of longitudinal layer LR
Center of longitudinal layer RR
Edge of longitudinal layer RR

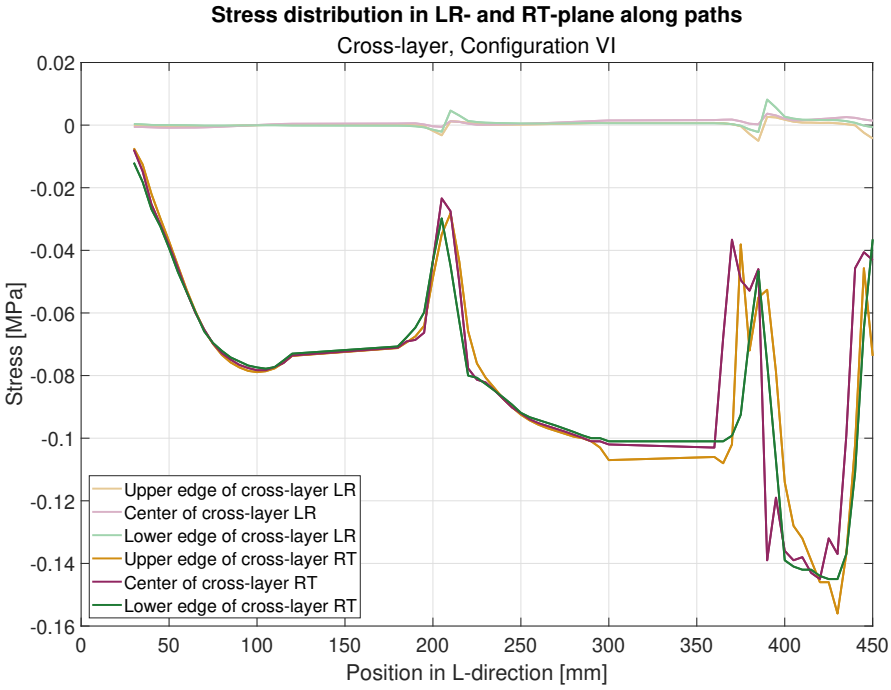
Stress distribution in LR- and RT-plane along paths
Cross-layer, Configuration VI
Stress [MPa]
Position in L-direction [mm]
Upper edge of cross-layer LR
Center of cross-layer LR
Lower edge of cross-layer LR
Upper edge of cross-layer RT
Center of cross-layer RT
Lower edge of cross-layer RT

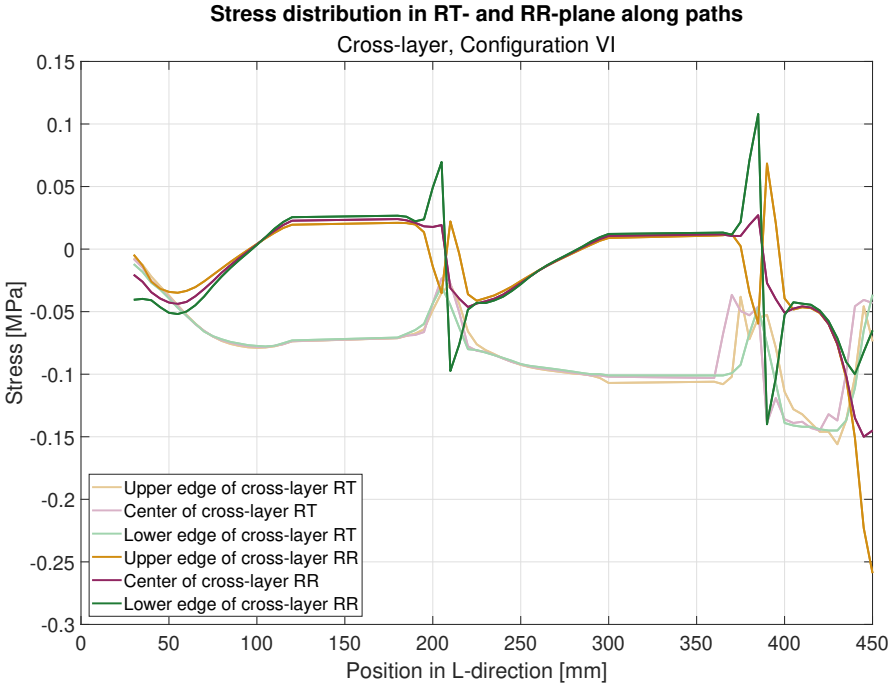
Stress distribution in RT- and RR-plane along paths
Cross-layer, Configuration VI
Stress [MPa]
Position in L-direction [mm]
Upper edge of cross-layer RT
Center of cross-layer RT
Lower edge of cross-layer RT
Upper edge of cross-layer RR
Center of cross-layer RR
Lower edge of cross-layer RR

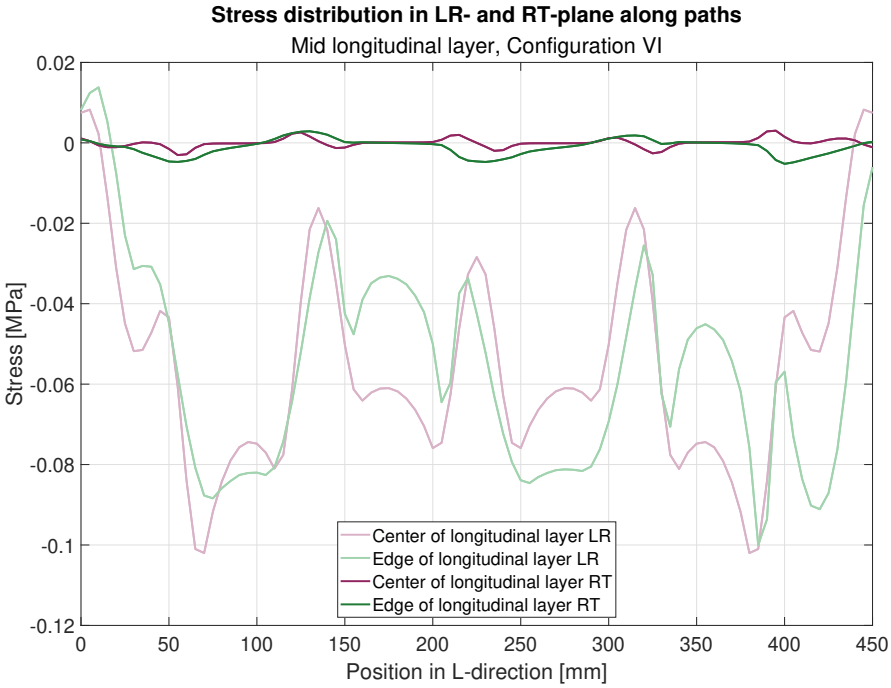
Stress distribution in LR- and RT-plane along paths
Mid longitudinal layer, Configuration VI
Stress [MPa]
Position in L-direction [mm]
Center of longitudinal layer LR
Edge of longitudinal layer LR
Center of longitudinal layer RT
Edge of longitudinal layer RT

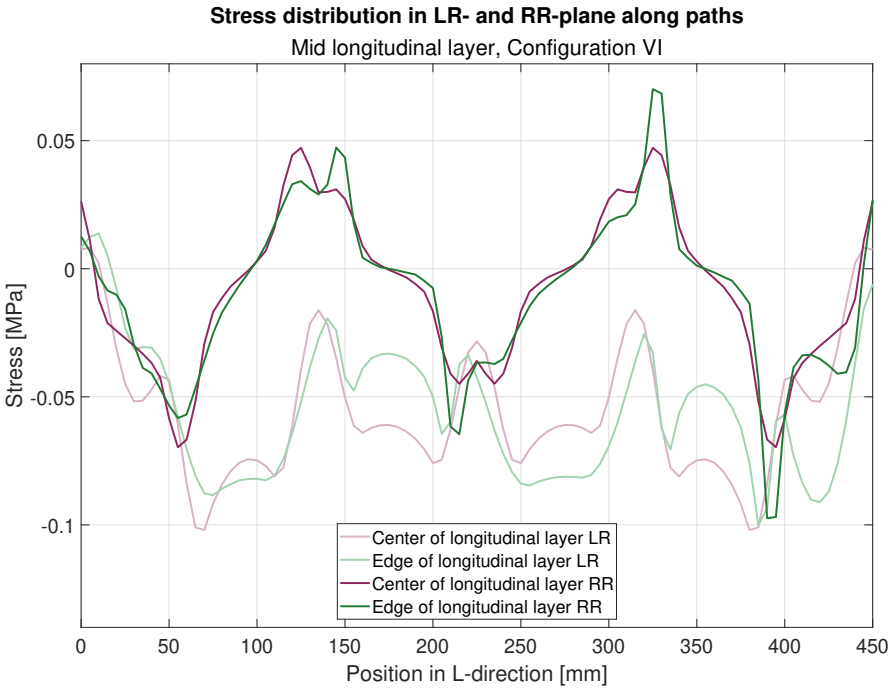
Stress distribution in LR- and RR-plane along paths
Mid longitudinal layer, Configuration VI
Stress [MPa]
Position in L-direction [mm]
Center of longitudinal layer LR
Edge of longitudinal layer LR
Center of longitudinal layer RR
Edge of longitudinal layer RR

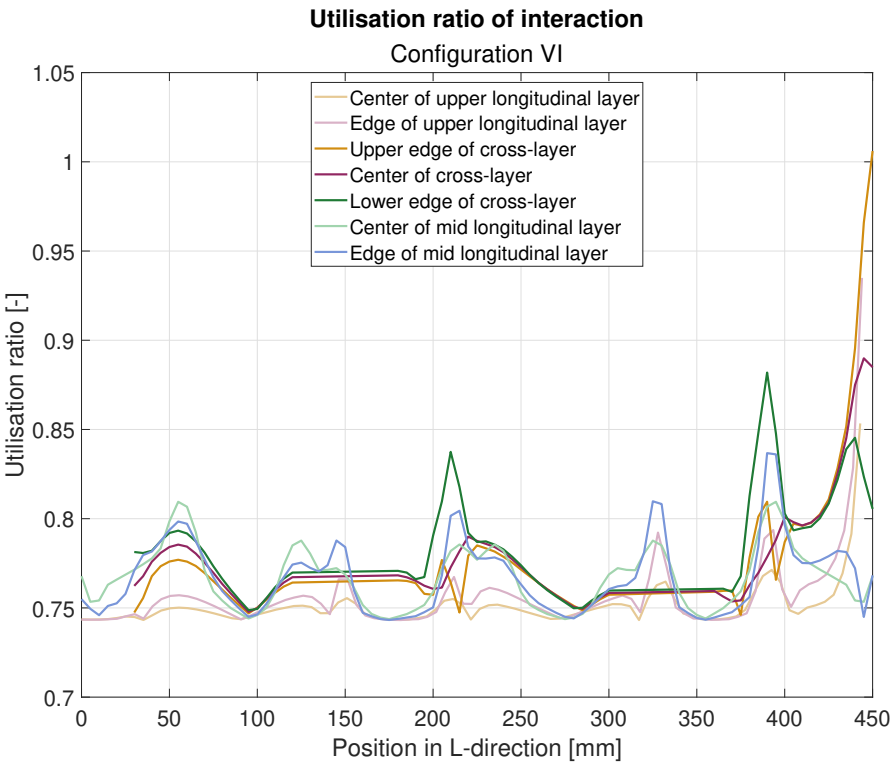
Utilisation ratio of interaction
Configuration VI
Center of upper longitudinal layer
Edge of upper longitudinal layer
Upper edge of cross-layer
Center of cross-layer
Lower edge of cross-layer
Center of mid longitudinal layer
Edge of mid longitudinal layer
Utilisation ratio [-]
Position in L-direction [mm]
1.05
1
0.95
0.9
0.85
0.8
0.75
0.7
0
50
100
150
200
250
300
350
400
450

H.7 Configuration VII

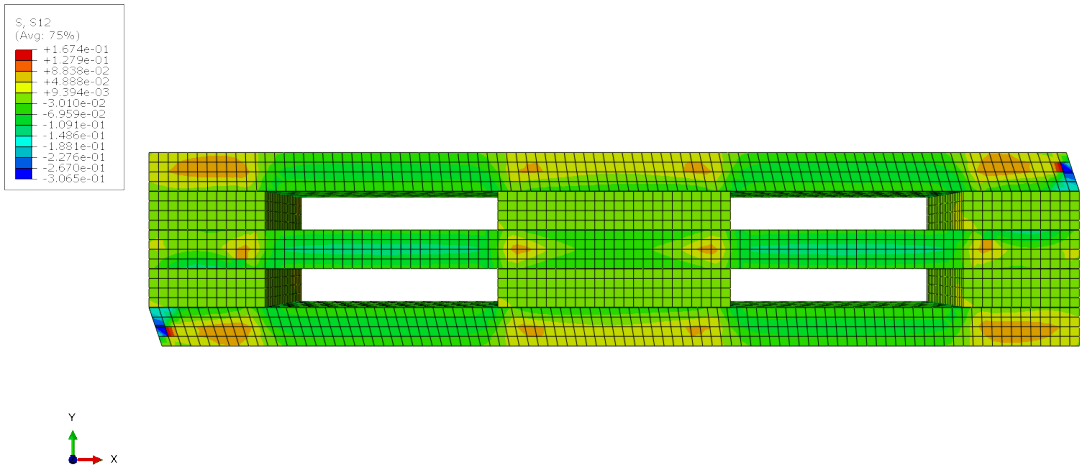

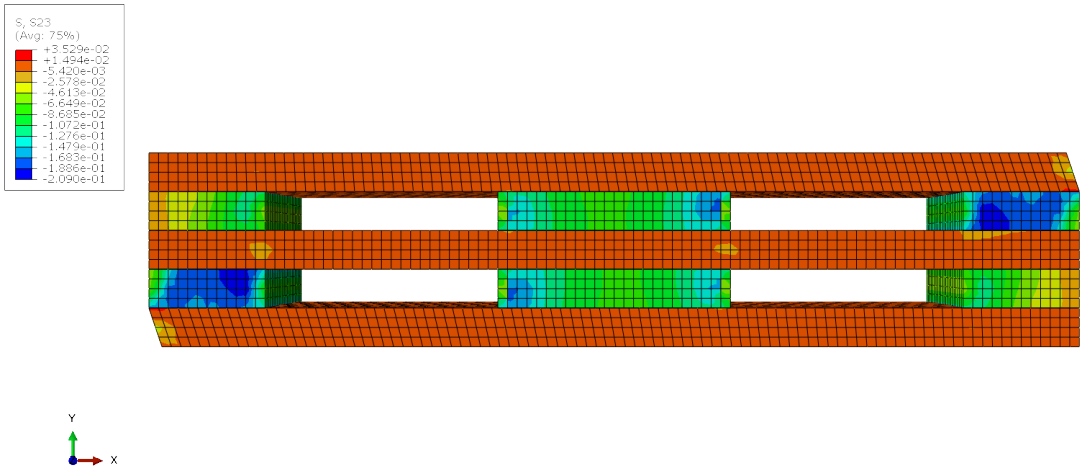

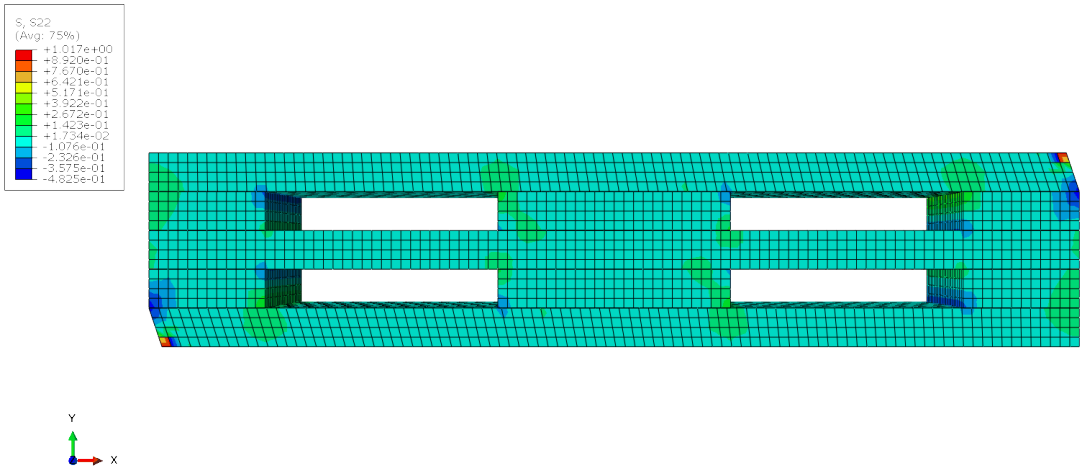

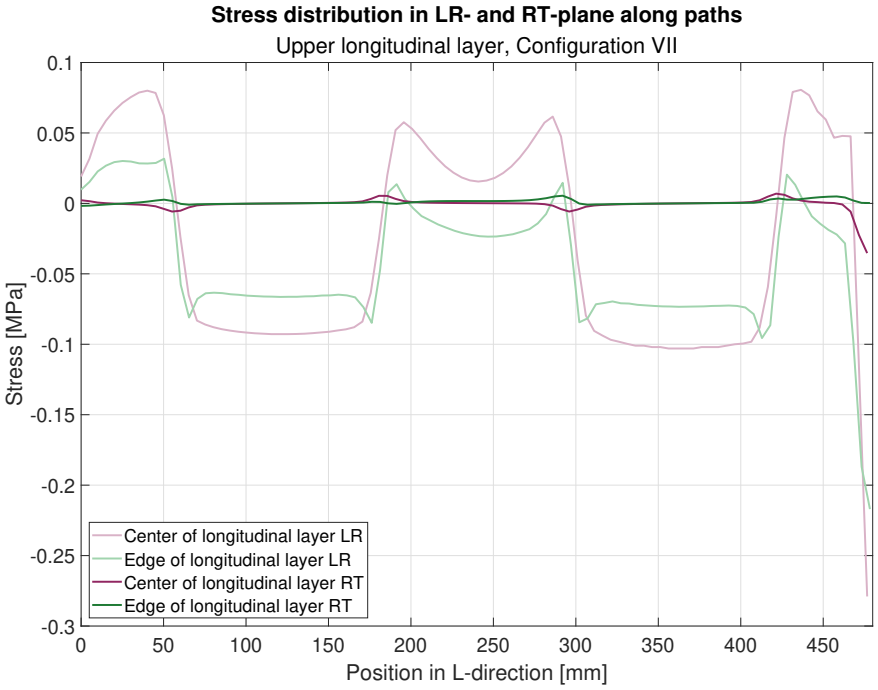
Stress distribution in LR- and RT-plane along paths
Upper longitudinal layer, Configuration VII
Stress [MPa]
Position in L-direction [mm]
Center of longitudinal layer LR
Edge of longitudinal layer LR
Center of longitudinal layer RT
Edge of longitudinal layer RT

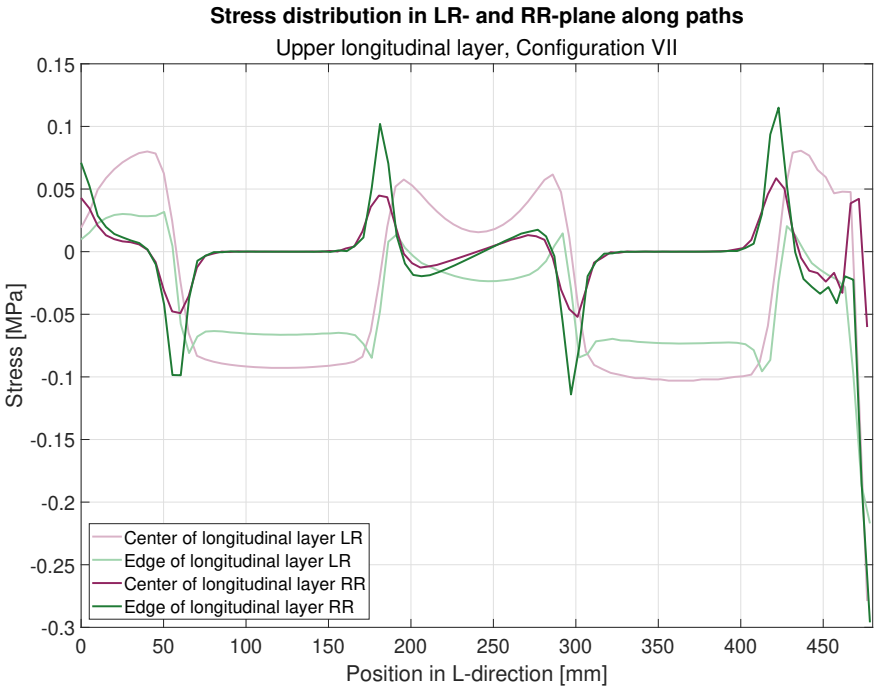
Stress distribution in LR- and RR-plane along paths
Upper longitudinal layer, Configuration VII
Stress [MPa]
Position in L-direction [mm]
Center of longitudinal layer LR
Edge of longitudinal layer LR
Center of longitudinal layer RR
Edge of longitudinal layer RR

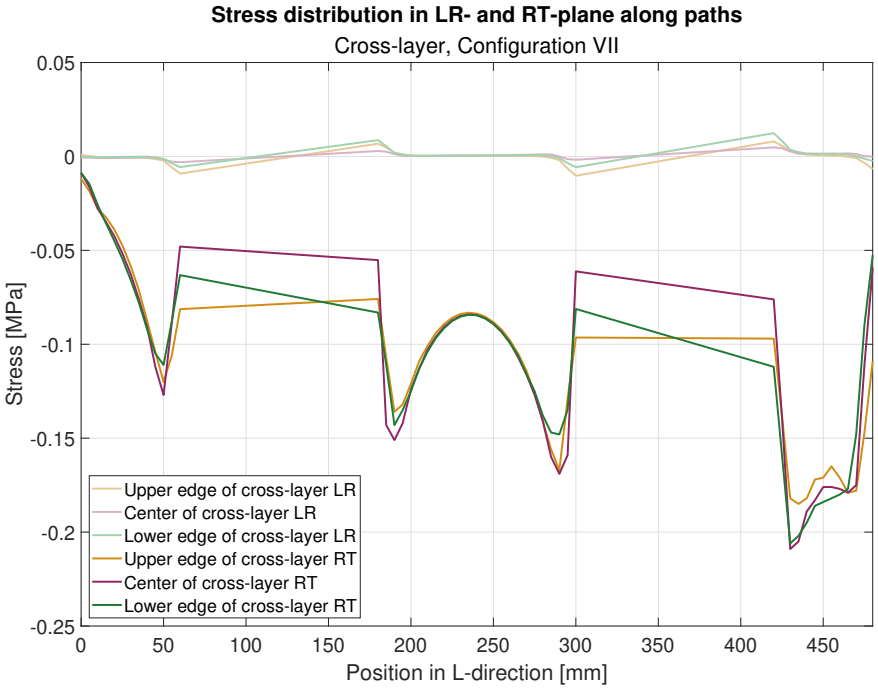
Stress distribution in LR- and RT-plane along paths
Cross-layer, Configuration VII
Stress [MPa]
Position in L-direction [mm]
Upper edge of cross-layer LR
Center of cross-layer LR
Lower edge of cross-layer LR
Upper edge of cross-layer RT
Center of cross-layer RT
Lower edge of cross-layer RT

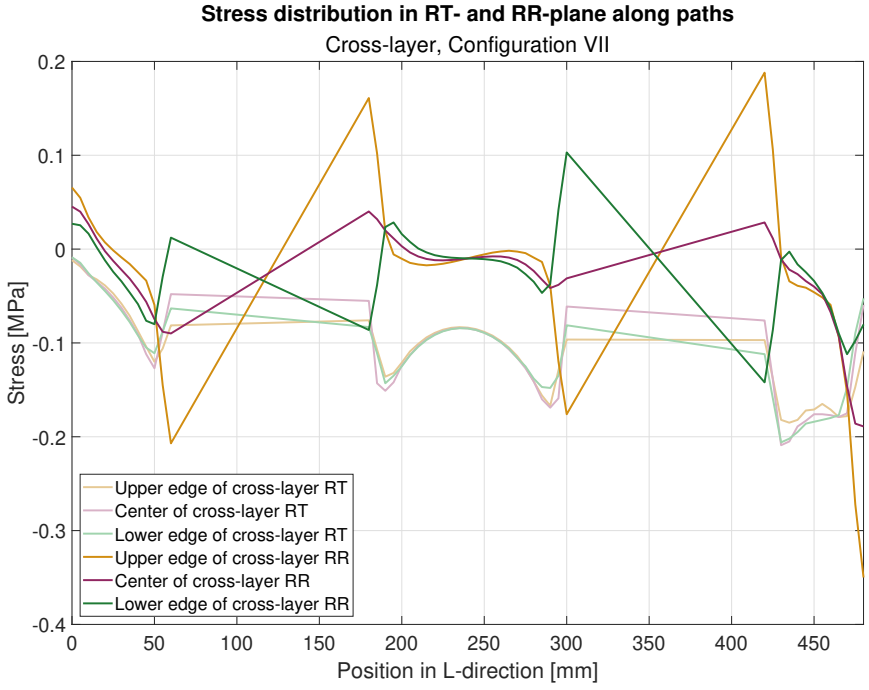
Stress distribution in RT- and RR-plane along paths
Cross-layer, Configuration VII
Stress [MPa]
Position in L-direction [mm]
Upper edge of cross-layer RT
Center of cross-layer RT
Lower edge of cross-layer RT
Upper edge of cross-layer RR
Center of cross-layer RR
Lower edge of cross-layer RR

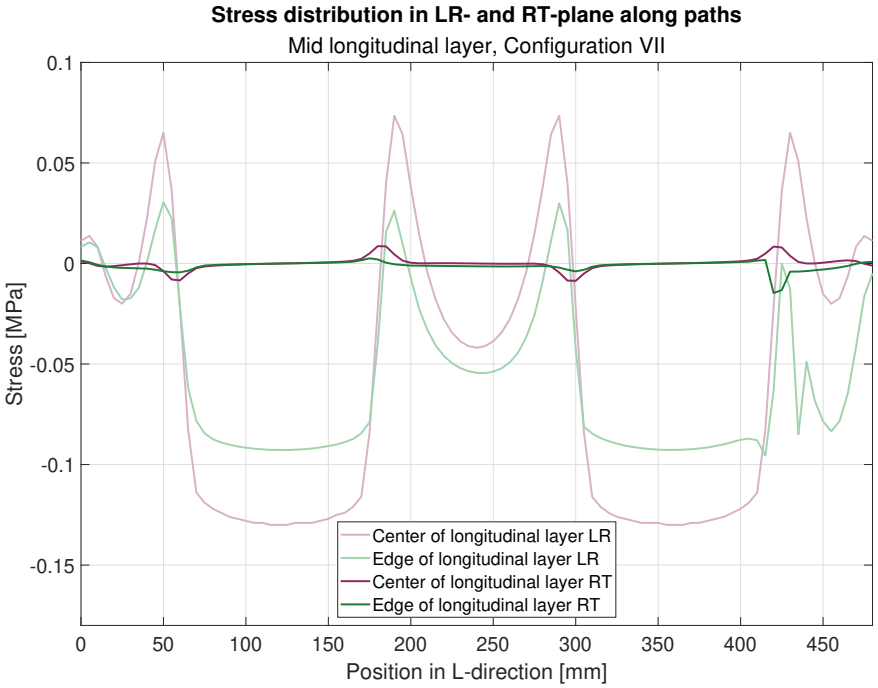
Stress distribution in LR- and RT-plane along paths
Mid longitudinal layer, Configuration VII
Stress [MPa]
Position in L-direction [mm]
Center of longitudinal layer LR
Edge of longitudinal layer LR
Center of longitudinal layer RT
Edge of longitudinal layer RT

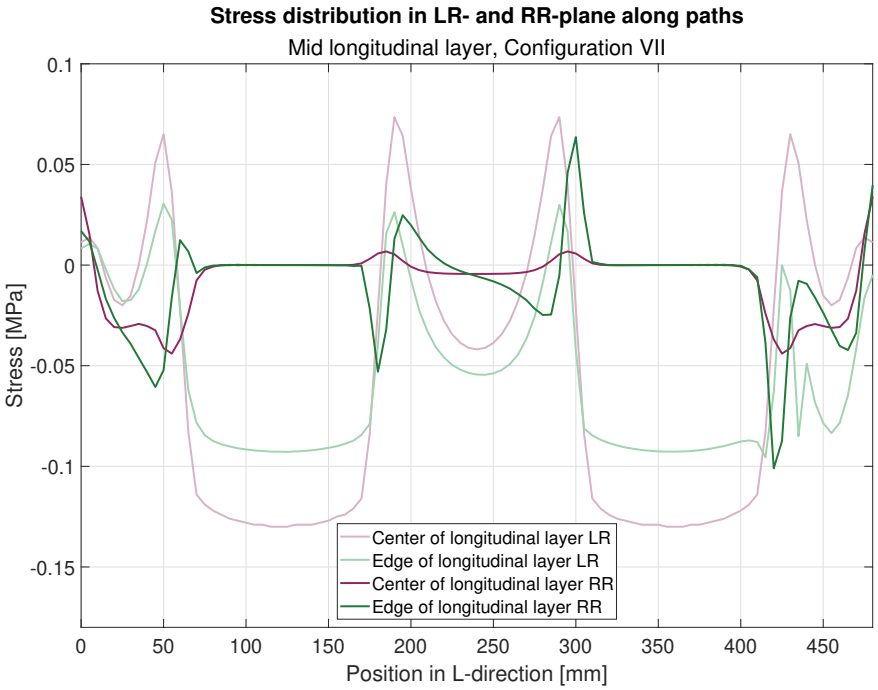
Stress distribution in LR- and RR-plane along paths
Mid longitudinal layer, Configuration VII
Stress [MPa]
Position in L-direction [mm]
Center of longitudinal layer LR
Edge of longitudinal layer LR
Center of longitudinal layer RR
Edge of longitudinal layer RR

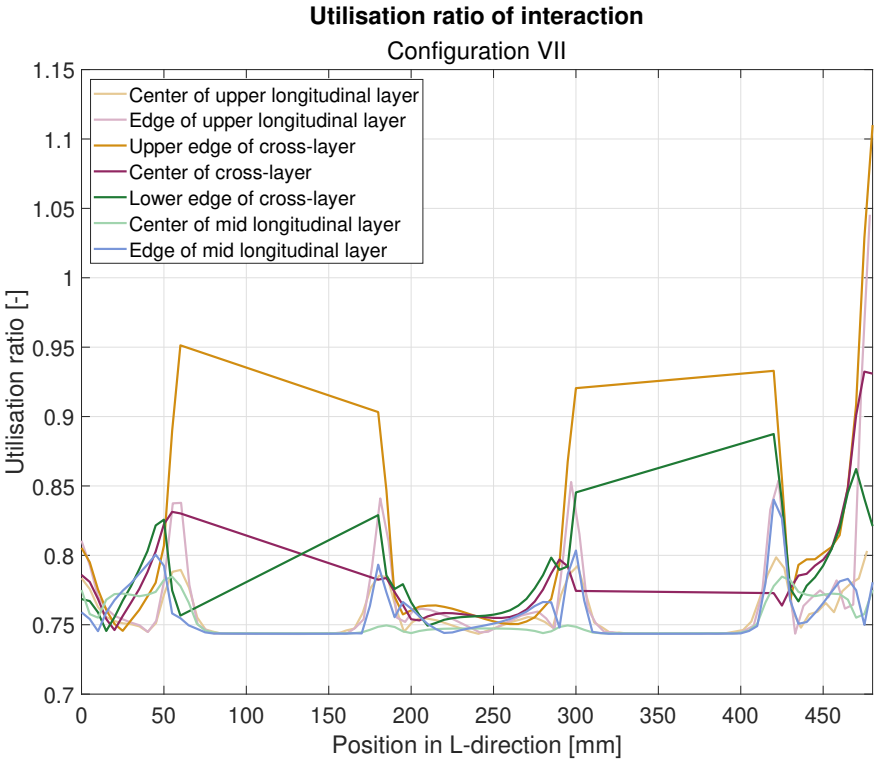
Utilisation ratio of interaction
Configuration VII
Center of upper longitudinal layer
Edge of upper longitudinal layer
Upper edge of cross-layer
Center of cross-layer
Lower edge of cross-layer
Center of mid longitudinal layer
Edge of mid longitudinal layer
Utilisation ratio [-]
Position in L-direction [mm]
1.15
1.1
1.05
1
0.95
0.9
0.85
0.8
0.75
0.7
0
50
100
150
200
250
300
350
400
450

H.8 Configuration VIII

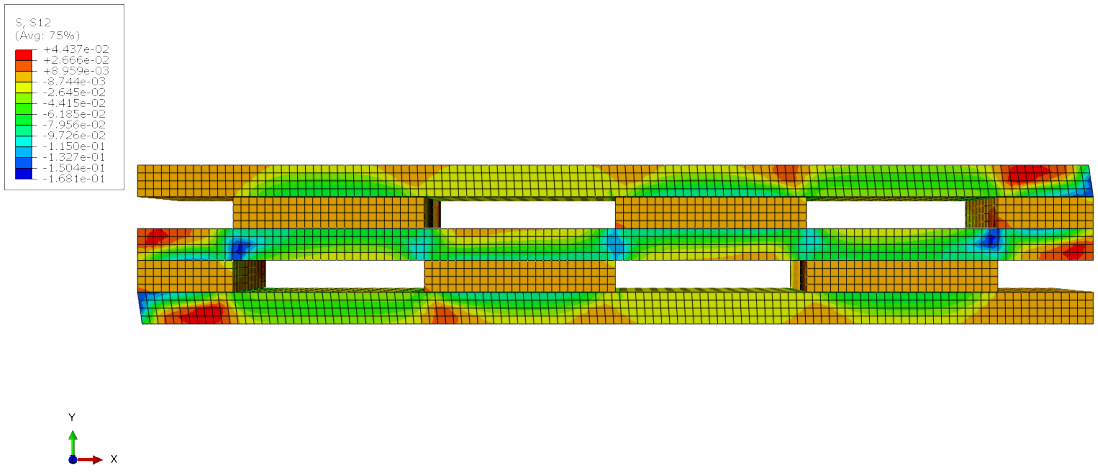

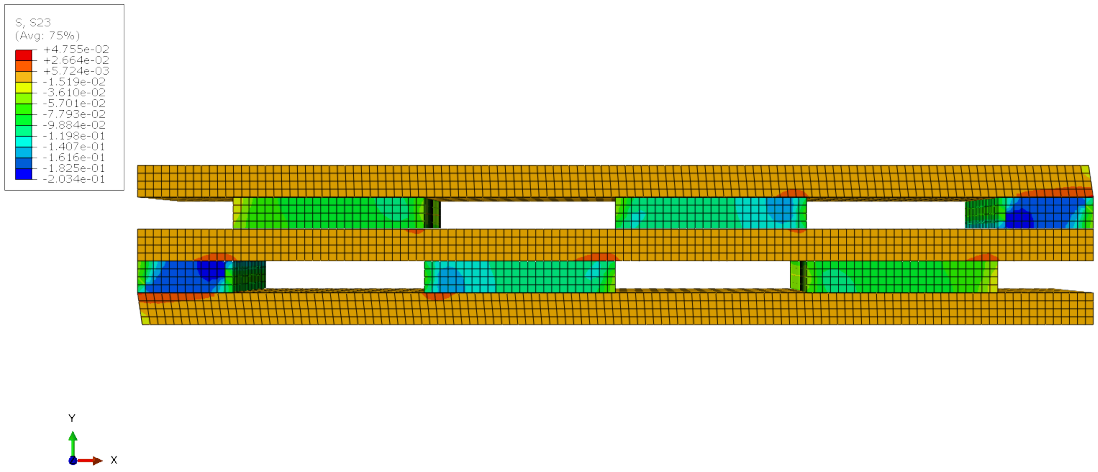

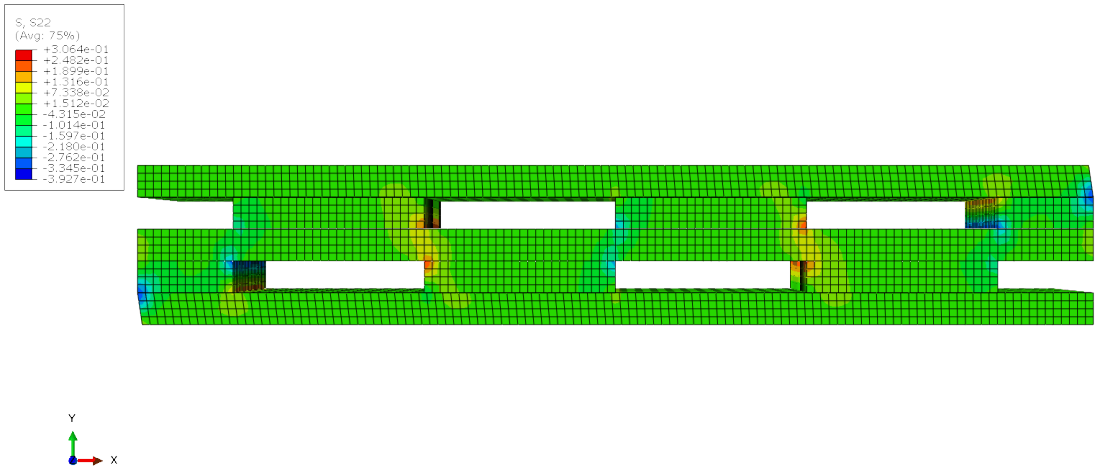

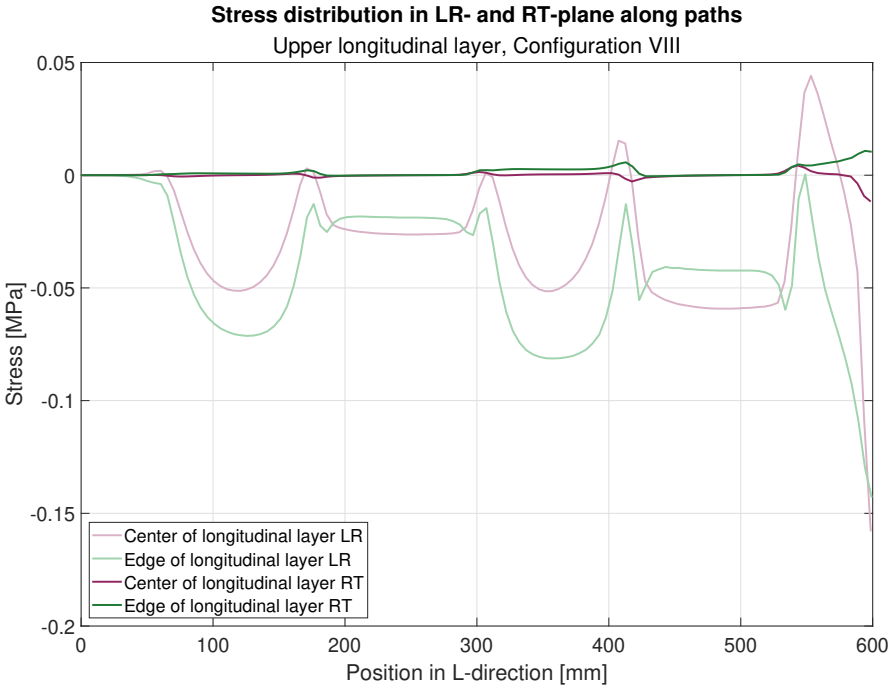
Stress distribution in LR- and RT-plane along paths
Upper longitudinal layer, Configuration VIII
Stress [MPa]
Position in L-direction [mm]
Center of longitudinal layer LR
Edge of longitudinal layer LR
Center of longitudinal layer RT
Edge of longitudinal layer RT

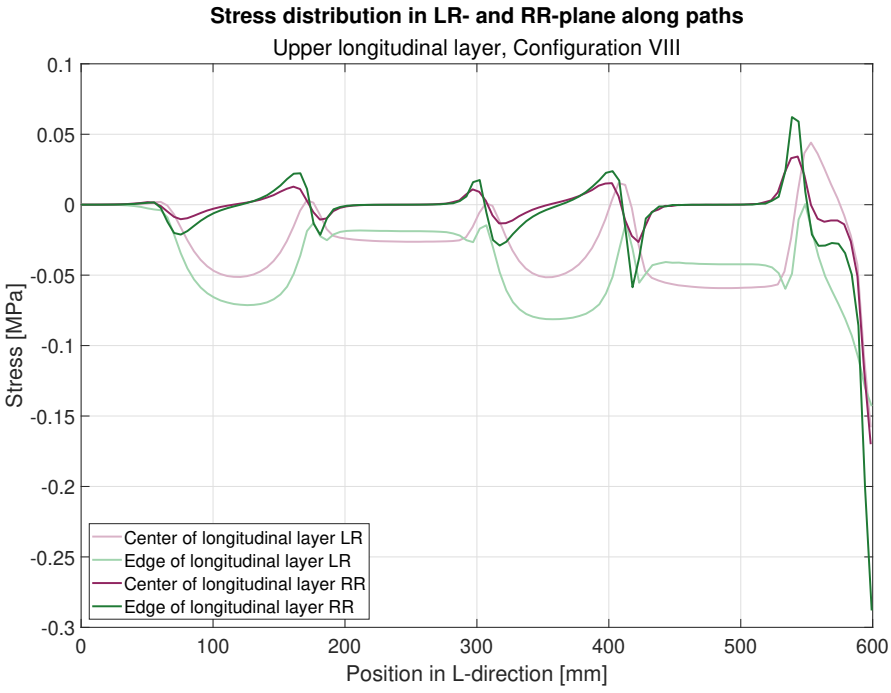
Stress distribution in LR- and RR-plane along paths
Upper longitudinal layer, Configuration VIII
Stress [MPa]
Position in L-direction [mm]
Center of longitudinal layer LR
Edge of longitudinal layer LR
Center of longitudinal layer RR
Edge of longitudinal layer RR

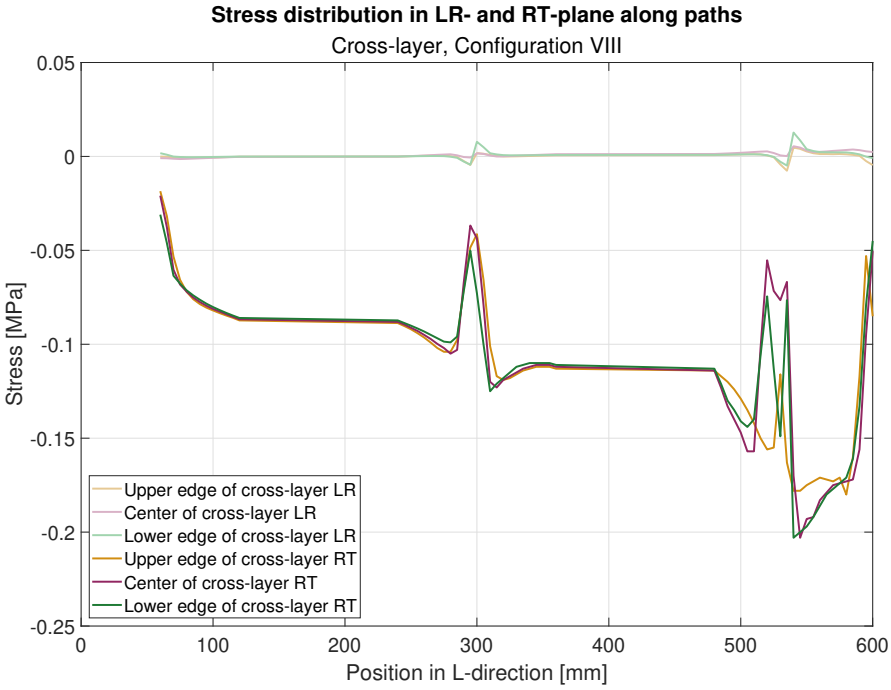
Stress distribution in LR- and RT-plane along paths
Cross-layer, Configuration VIII
Stress [MPa]
Position in L-direction [mm]
Upper edge of cross-layer LR
Center of cross-layer LR
Lower edge of cross-layer LR
Upper edge of cross-layer RT
Center of cross-layer RT
Lower edge of cross-layer RT

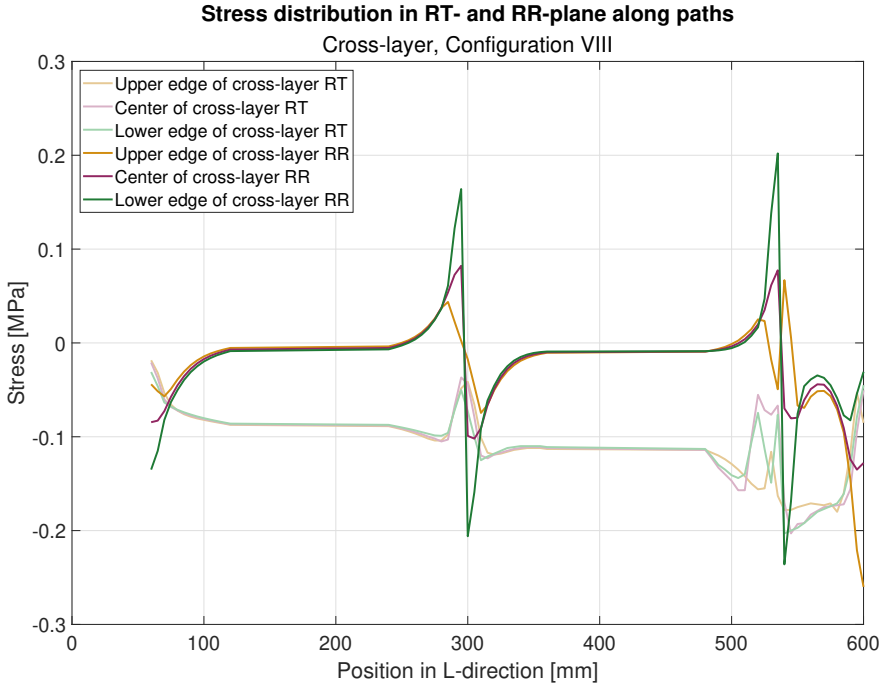
Stress distribution in RT- and RR-plane along paths
Cross-layer, Configuration VIII
Stress [MPa]
Position in L-direction [mm]
Upper edge of cross-layer RT
Center of cross-layer RT
Lower edge of cross-layer RT
Upper edge of cross-layer RR
Center of cross-layer RR
Lower edge of cross-layer RR

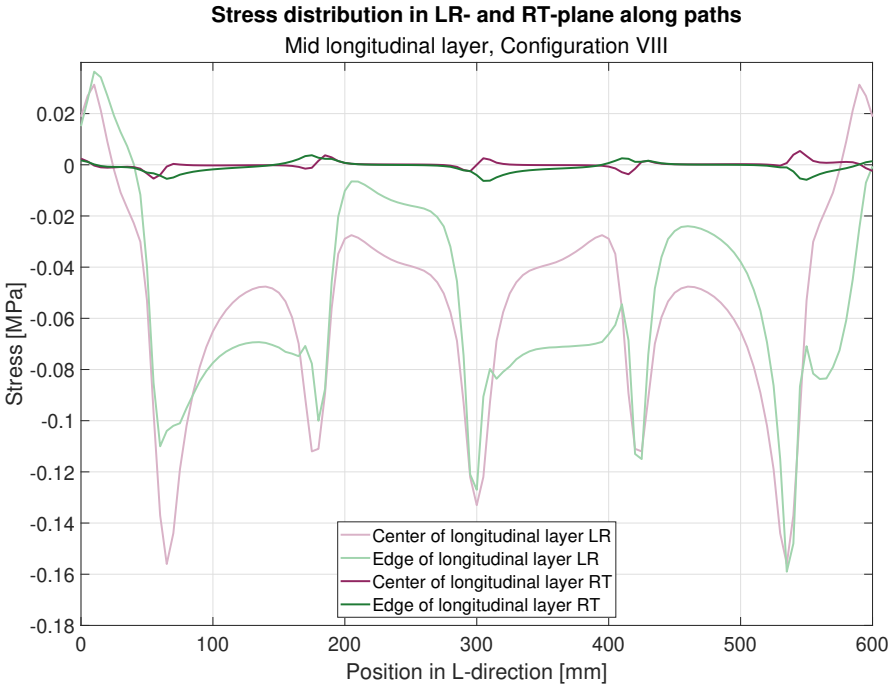
Stress distribution in LR- and RT-plane along paths
Mid longitudinal layer, Configuration VIII
Stress [MPa]
Position in L-direction [mm]
Center of longitudinal layer LR
Edge of longitudinal layer LR
Center of longitudinal layer RT
Edge of longitudinal layer RT

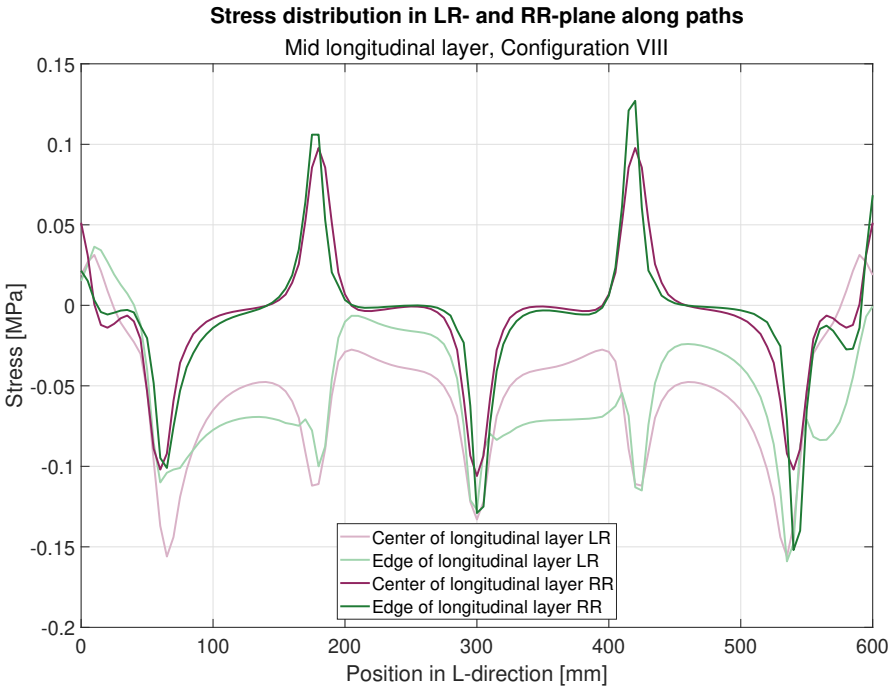
Stress distribution in LR- and RR-plane along paths
Mid longitudinal layer, Configuration VIII
Stress [MPa]
Position in L-direction [mm]
Center of longitudinal layer LR
Edge of longitudinal layer LR
Center of longitudinal layer RR
Edge of longitudinal layer RR

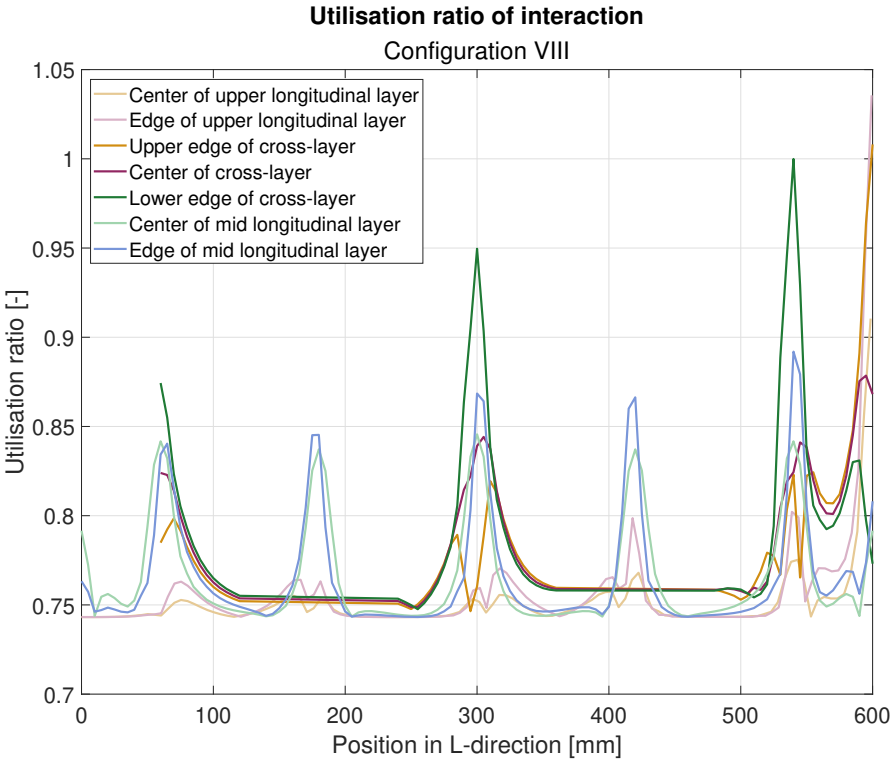
Utilisation ratio of interaction
Configuration VIII
Center of upper longitudinal layer
Edge of upper longitudinal layer
Upper edge of cross-layer
Center of cross-layer
Lower edge of cross-layer
Center of mid longitudinal layer
Edge of mid longitudinal layer
Utilisation ratio [-]
Position in L-direction [mm]
1.05
1
0.95
0.9
0.85
0.8
0.75
0.7
0
100
200
300
400
500
600

H.9 Configuration IX

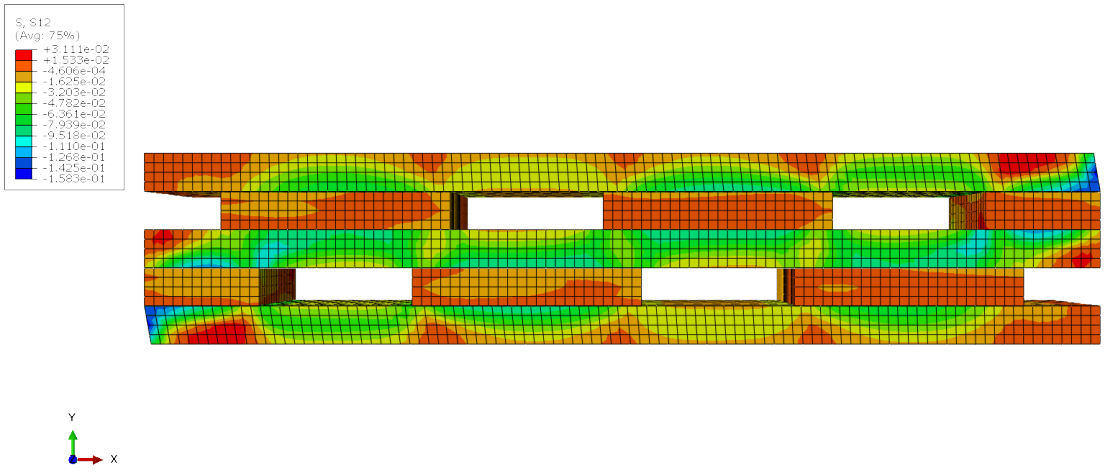

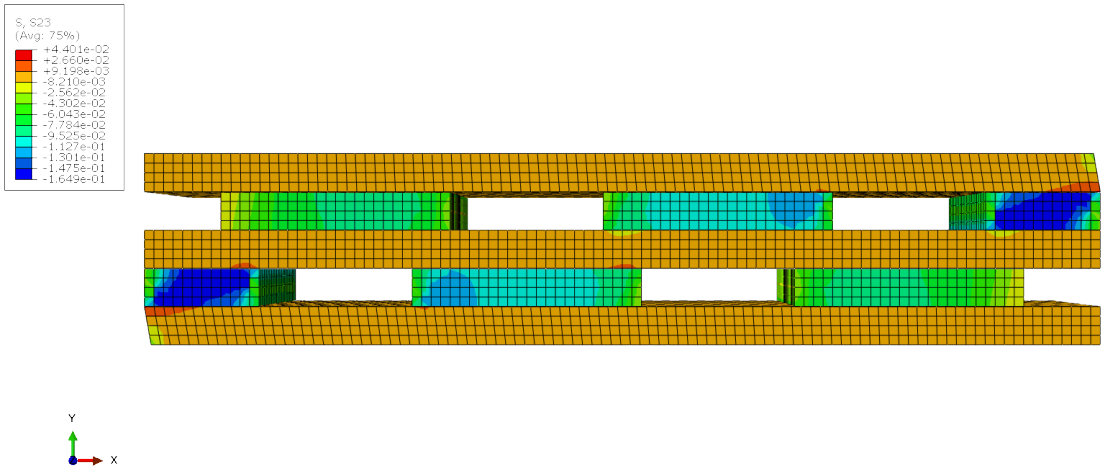

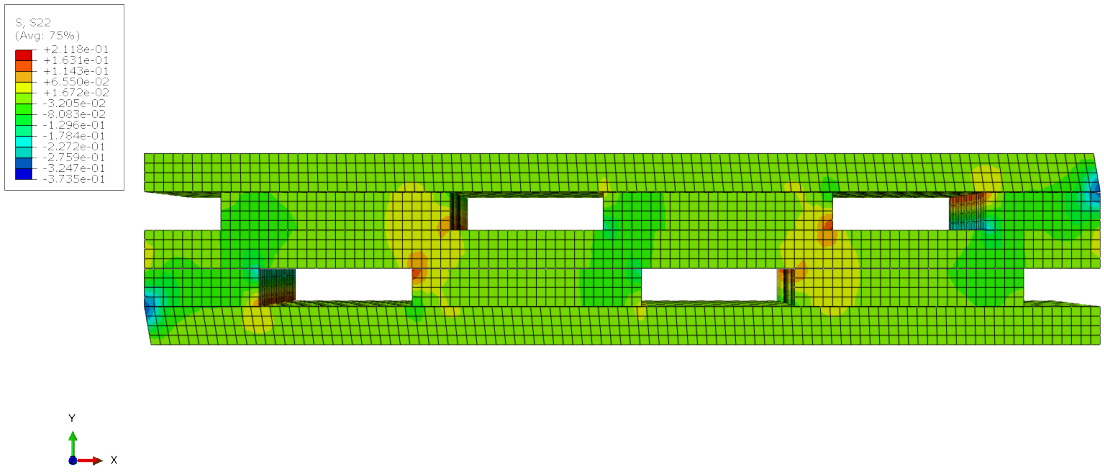

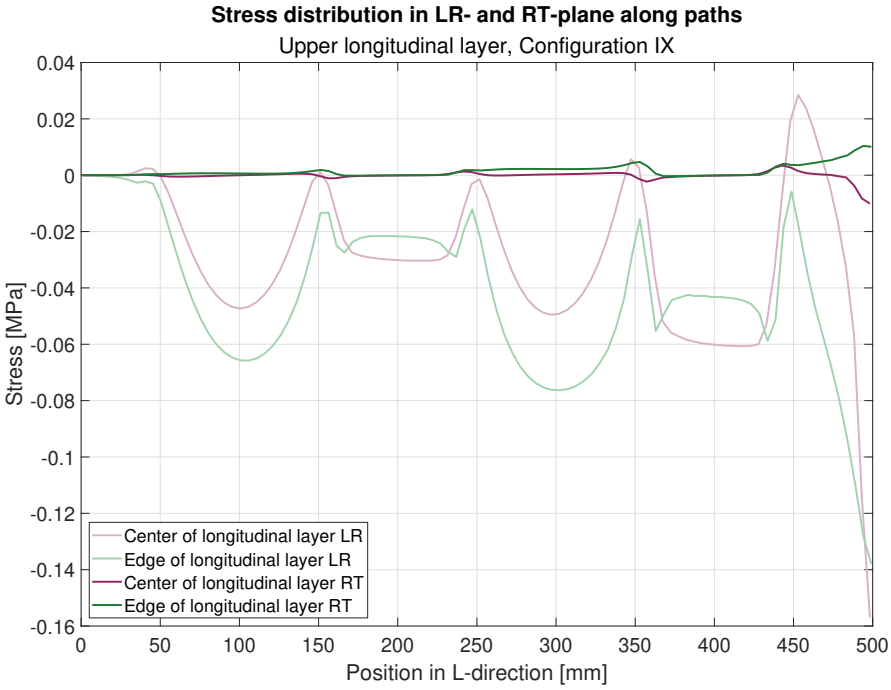
Stress distribution in LR- and RT-plane along paths
Upper longitudinal layer, Configuration IX
Stress [MPa]
Position in L-direction [mm]
Center of longitudinal layer LR
Edge of longitudinal layer LR
Center of longitudinal layer RT
Edge of longitudinal layer RT

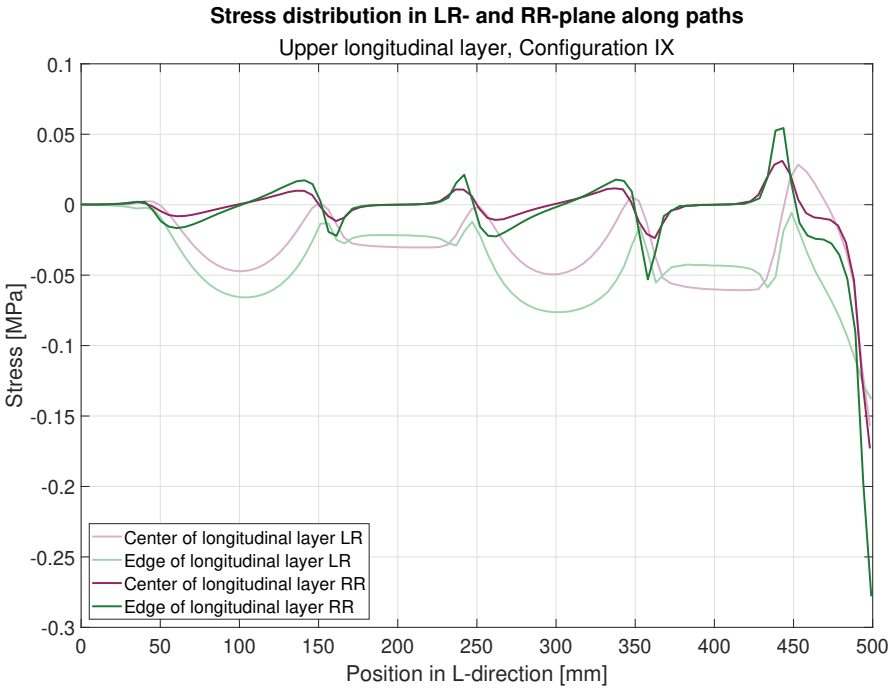
Stress distribution in LR- and RR-plane along paths
Upper longitudinal layer, Configuration IX
Stress [MPa]
Position in L-direction [mm]
Center of longitudinal layer LR
Edge of longitudinal layer LR
Center of longitudinal layer RR
Edge of longitudinal layer RR

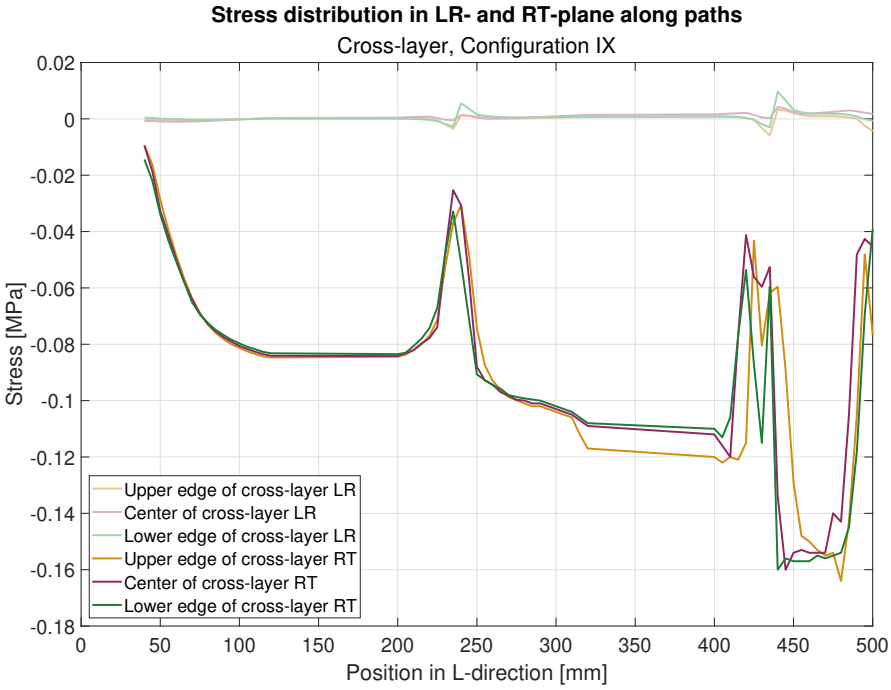
Stress distribution in LR- and RT-plane along paths
Cross-layer, Configuration IX
Stress [MPa]
Position in L-direction [mm]
Upper edge of cross-layer LR
Center of cross-layer LR
Lower edge of cross-layer LR
Upper edge of cross-layer RT
Center of cross-layer RT
Lower edge of cross-layer RT

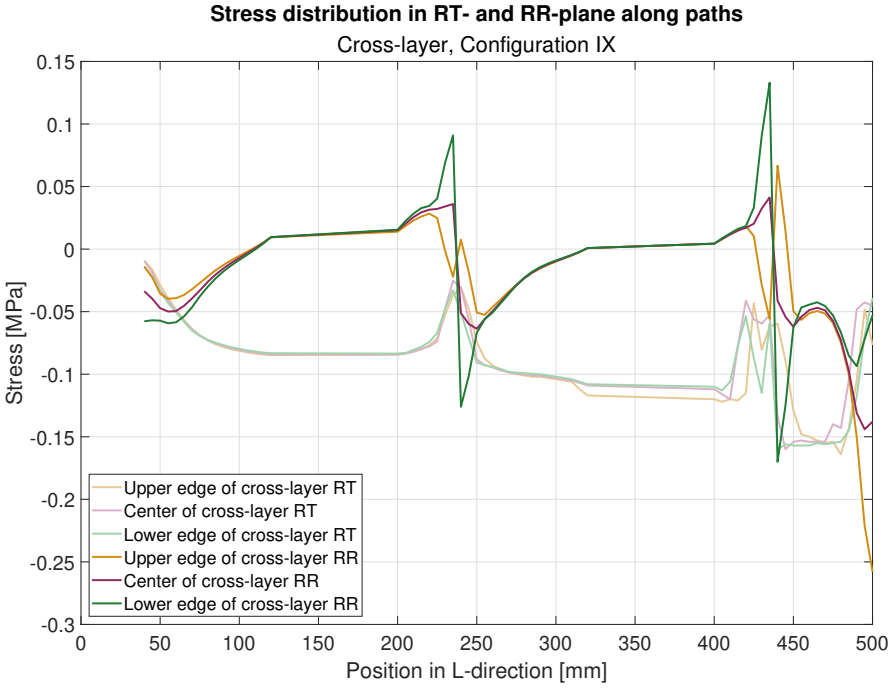
Stress distribution in RT- and RR-plane along paths
Cross-layer, Configuration IX
Stress [MPa]
Position in L-direction [mm]
Upper edge of cross-layer RT
Center of cross-layer RT
Lower edge of cross-layer RT
Upper edge of cross-layer RR
Center of cross-layer RR
Lower edge of cross-layer RR

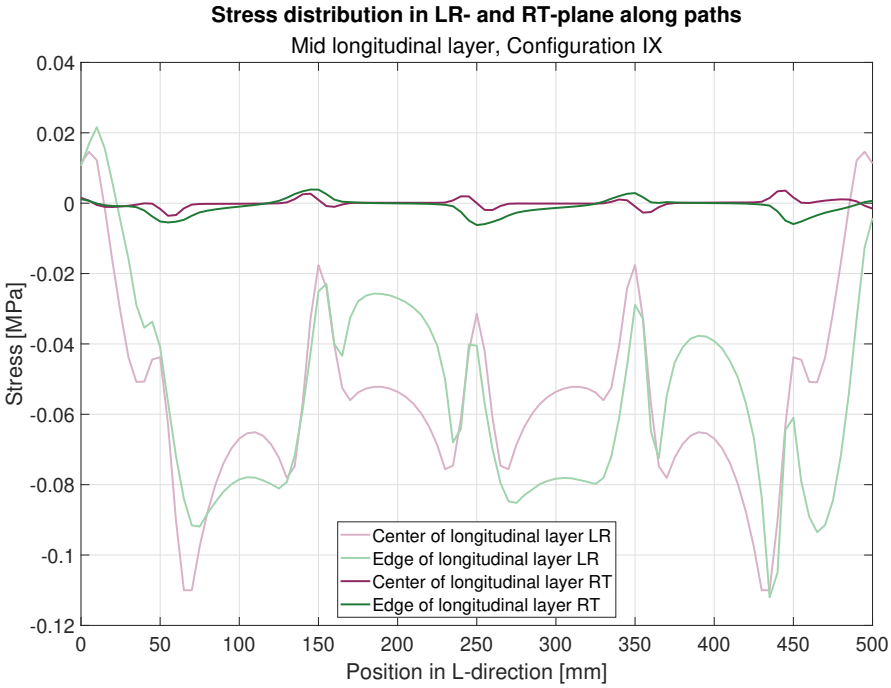
Stress distribution in LR- and RT-plane along paths
Mid longitudinal layer, Configuration IX
Stress [MPa]
Position in L-direction [mm]
Center of longitudinal layer LR
Edge of longitudinal layer LR
Center of longitudinal layer RT
Edge of longitudinal layer RT

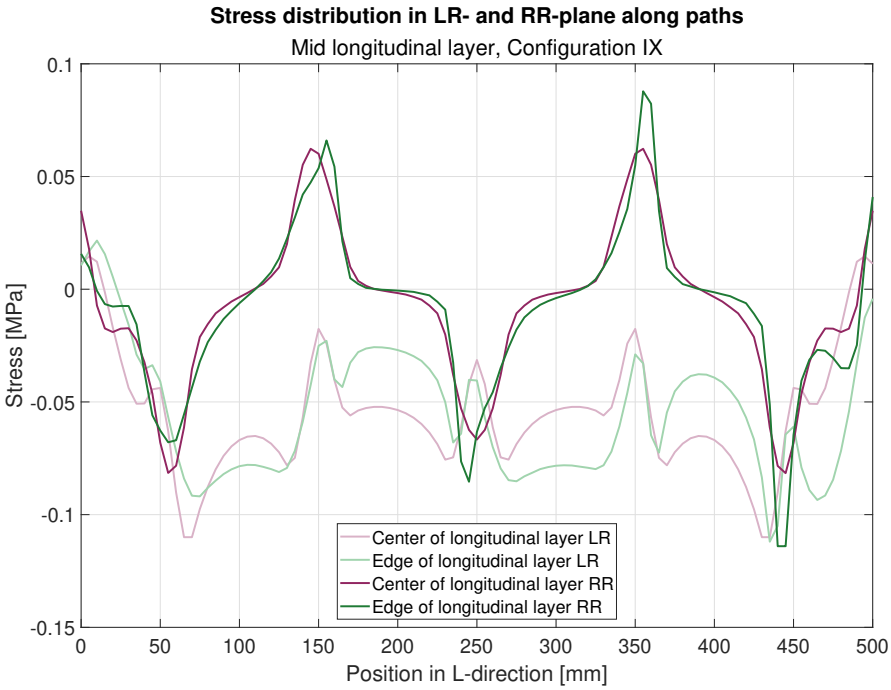
Stress distribution in LR- and RR-plane along paths
Mid longitudinal layer, Configuration IX
Stress [MPa]
Position in L-direction [mm]
Center of longitudinal layer LR
Edge of longitudinal layer LR
Center of longitudinal layer RR
Edge of longitudinal layer RR

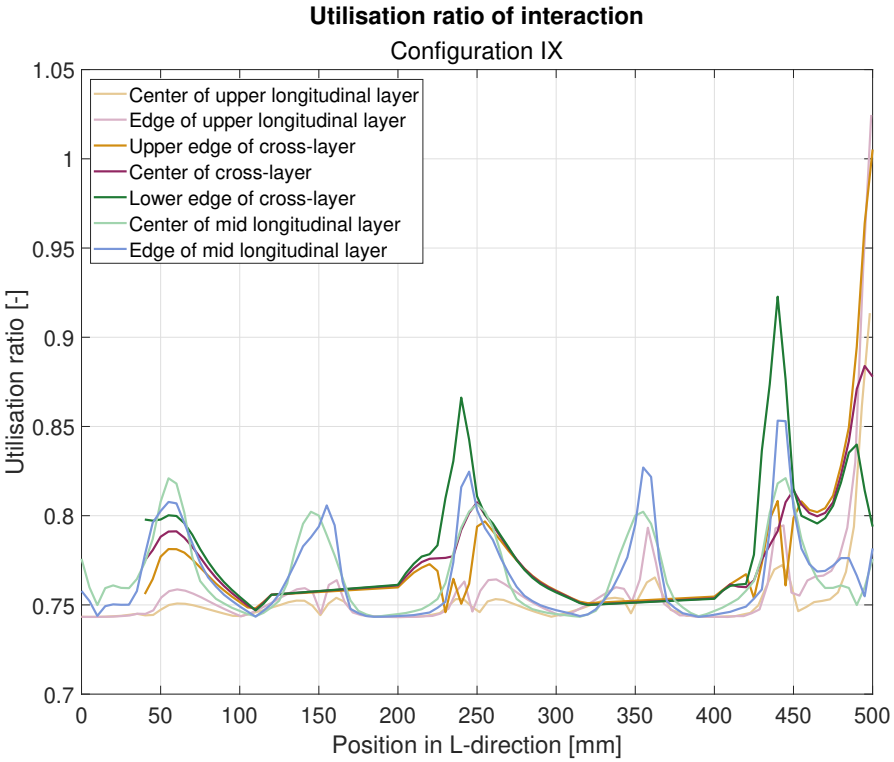
Utilisation ratio of interaction
Configuration IX
Center of upper longitudinal layer
Edge of upper longitudinal layer
Upper edge of cross-layer
Center of cross-layer
Lower edge of cross-layer
Center of mid longitudinal layer
Edge of mid longitudinal layer
Utilisation ratio [-]
Position in L-direction [mm]
1.05
1
0.95
0.9
0.85
0.8
0.75
0.7
0
50
100
150
200
250
300
350
400
450
500

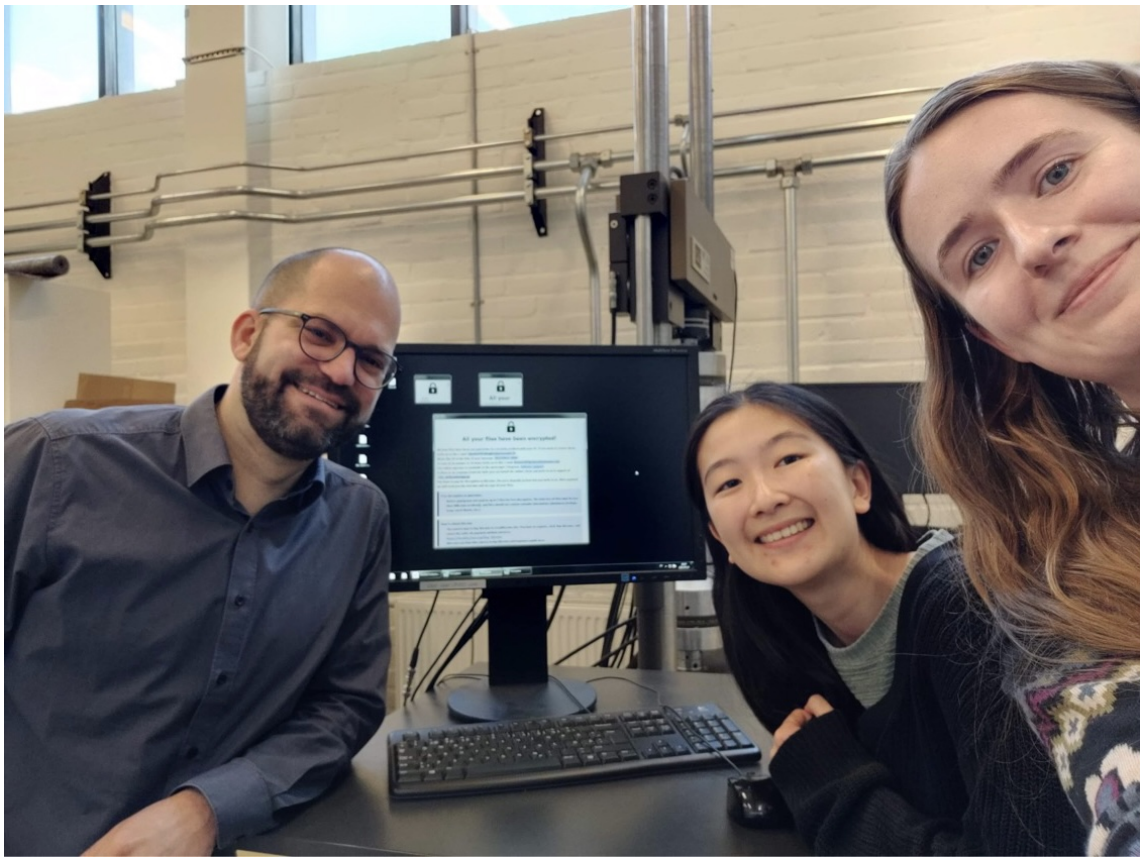

From the left: Robert Jockwer, hacked computer with encrypted data, Linda Xiao, and Anna Moberg. (May 12th 2022)

DEPARTMENT OF ARCHITECTURE AND CIVIL ENGINEERING
CHALMERS UNIVERSITY OF TECHNOLOGY
Gothenburg, Sweden
www.chalmers.se



CHALMERS
UNIVERSITY OF TECHNOLOGY